



DOCTORAL THESIS

**The Development of Photo-Reversible Materials using Azo
Dyes and Natural Polymers**

Kayrel E.K. Edwards

Supervisors: Christopher J. Barrett, Theo G. M. van de Ven

*A Thesis submitted to McGill University in partial fulfillment of
the requirements of the degree of Doctor of Philosophy*

March 2023

©Kayrel E.K. Edwards 2023

Table of Contents

Statement of Objectives.....	viii
Abstract.....	ix
Résumé.....	xi
Acknowledgements.....	xiii
Contribution to Original Knowledge.....	xv
Contributions of Authors.....	xvii
Lists of Figures.....	xx
Lists of Tables.....	xxxii
Lists of Abbreviations.....	xxxiii
1 Introduction and literature review of photo-reversible azo/polymer soft-bonded complexes.....	1
1.1 Abstract and overview.....	1
1.2 Classes of natural polymers.....	3
1.2.1 Cellulose and its derivatives.....	7
1.2.2 Alginates.....	12
1.3 Azo dyes.....	13
1.3.1 Classes of azo dyes.....	15
1.3.2 <i>Trans-cis</i> isomerization.....	18
1.3.3 Spectroscopic techniques and principles of azo dyes.....	22

1.3.4	DFT modeling of <i>trans-cis</i> isomerization of azo dyes.....	27
1.4	Supramolecular chemistry.....	29
1.4.1	Types of intermolecular interaction.....	30
1.4.2	Layer-by-layer assembly.....	32
1.4.3	Other types of design methods.....	36
1.5	Photo-reversible soft-bonded azo/polymer complexes.....	37
1.5.1	Design guidelines for soft-bonded systems.....	38
1.5.2	Optical sensors.....	41
1.5.3	Mechanical behaviour.....	43
1.5.4	Disassembly/reassembly.....	47
1.6	Photo-reversible azo/cellulose-based complexes.....	52
1.7	Scope of this Thesis.....	56
1.8	References.....	60
1.9	Appendix 1: Portion of Regenerative Waste Labs summarized information for sustainable learning portal.....	69
2	Controlled disassembly of azobenzene cellulose-based thin films using visible light...	82
2.1	Abstract.....	83
2.2	Introduction.....	84
2.3	Results and discussion.....	88
2.3.1	LbL assembly of NaCS/BBY thin films.....	88
2.3.2	FTIR spectroscopy.....	90
2.3.3	Influence of pH, ionic strength, and temperature on film stability.....	93
2.3.4	Pump-probe experiments to examine isomerization of BBY.....	95

2.3.5	Confocal Raman spectroscopy.....	97
2.3.6	'Sun and rain' exposure experiment.....	100
2.4	Conclusions.....	103
2.5	References.....	105
2.6	Appendix 2: Supporting information for Chapter 2.....	108
3	Optical and computational study of the <i>trans</i> ↔ <i>cis</i> reversible isomerization of the commercial bis-azo dye Bismarck Brown Y.....	120
3.1	Abstract.....	122
3.2	Introduction.....	124
3.3	Experimental.....	129
3.3.1	Materials.....	129
3.3.2	Pump-probe experiments.....	130
3.3.3	Computational methods.....	131
3.4	Results and discussion.....	133
3.4.1	Commercial BBY absorption profile.....	134
3.4.2	Commercial BBY isomerization.....	136
3.4.3	Commercial BBY kinetics.....	137
3.4.4	Solvent effect.....	140
3.4.5	Recrystallized BBY isomerization and kinetics.....	141
3.4.6	Chrysoidine isomerization and kinetics.....	143
3.4.7	DFT calculations.....	145
3.4.7.1	Equilibrium geometries.....	145
3.4.7.2	Isomerization.....	147

3.4.7.3 Energetics.....	150
3.5 Conclusions.....	152
3.6 References.....	153
3.7 Appendix 3: Supporting information for Chapter 3.....	156
4 Valorization of brown seaweed.....	166
4.1 Abstract.....	168
4.2 Introduction.....	169
4.3 Experimental.....	175
4.3.1 Materials.....	175
4.3.2 Extraction of alginates and cellulose from brown seaweed.....	175
4.3.3 Preparation of alginate-based materials.....	177
4.3.4 Spectroscopies and analyses.....	178
4.3.4.1 Fourier transform infrared (FTIR) spectroscopy.....	178
4.3.4.2 Nuclear magnetic (NMR) spectroscopy.....	178
4.3.4.3 X-ray diffraction (XRD).....	178
4.3.4.4 Polarized light microscopy (PLM).....	179
4.3.4.5 Conductometric titration.....	179
4.3.5 Water solubility.....	180
4.3.6 Oxygen transmission rate (OTR).....	180
4.3.7 Water vapour transmission rate (WVTR) and permeation (WVP).....	180
4.3.8 Mechanical testing.....	181
4.4 Results and discussion.....	182
4.4.1 Extraction yields.....	182

4.4.2	Characterization.....	182
4.4.2.1	NMR spectroscopy.....	183
4.4.2.2	FTIR spectroscopy.....	186
4.4.2.3	Conductometric titration.....	188
4.4.2.4	Xray diffraction analysis.....	189
4.4.2.5	Imaging of fibres, microfibrils and microgels.....	191
4.4.3	Physical and mechanical properties.....	193
4.4.4	Photo-reversible azo/alginate materials.....	197
4.5	Conclusions.....	200
4.6	References.....	200
5	Photo-response of azo dye functionalized cellulose acetate.....	204
5.1	Abstract.....	206
5.2	Introduction.....	207
5.3	Results and discussion.....	212
5.3.1	Characterization of cellulose acetate (DS 1–3)	213
5.3.2	Characterization of Azo-CA polymers.....	214
5.3.2.1	UV-Vis spectroscopy.....	214
5.3.2.2	NMR spectroscopy.....	215
5.3.2.3	FTIR spectroscopy.....	217
5.3.2.4	Surface imaging and azo content.....	218
5.3.2.5	X-ray diffraction patterns.....	221
5.3.2.6	Thermal stability.....	223
5.3.3	Isomerization and kinetics of azo dyes and Azo-CA polymers.....	224

5.3.4	Water contact angle measurements.....	229
5.3.5	Water vapour permeability measurements.....	234
5.4	Conclusions.....	235
5.5	References.....	236
5.6	Appendix 4: Supporting information for Chapter 5.....	240
6	Discussion, conclusions, and future outlook.....	254
6.1	Discussion.....	254
6.2	Conclusions.....	266
6.3	Future outlook.....	269
6.4	References.....	271

Statement of Objectives

The main objective of this Thesis was to develop photo-reversible materials using a range of azo dyes and natural polymers. In Chapter 2, the main aims were to develop a methodology of preparing water-resistant materials using water-soluble starting components, and to control the disassembly of the material using intensities of visible light. In Chapter 3, the main goals were to study in detail the *trans-cis* isomerization of bis-azo dye: Bismarck Brown Y (BBY), used in Chapter 2 to enable a photo-reversible material. Specifically, this optical switching behaviour was explored using pump-probe experiments to measure the kinetics of the *cis* decay of the azo dye BBY in solution and solid-state, and computational modeling to predict the *cis* decay of the azo dye BBY and its mechanism in the gas phase. The main objective of Chapter 4 was to valorize waste brown seaweed (*Sargassum spp.*), by extracting the polysaccharides alginate and cellulose, by preparing novel alginate blends, and a range of photo-reversible materials from the extracted alginate and azo dyes. The main goal of the last Chapter (Chapter 5) was to prepare self-cleaning materials by covalently modifying cellulose-based polymers with azo dyes, specifically to synthesize a range of azo dye functionalized cellulose acetate polymers, and to assess the change in surface wettability and water permeance in response to UV/Vis light.

Abstract

Development of Photo-Reversible Materials using Azo Dyes and Natural Polymers

This Thesis makes contributions towards the fields of optical and smart materials design based on natural polymers. It describes 2 distinct design approaches developed for preparing photo-reversible materials using various azo dyes and natural polymers, towards applications in disassembly/reassembly systems and self-cleaning materials. Generally, petrol-based polymers have been utilized previously to prepare photo-reversible azo-based materials; however due to the negative environmental impacts associated with petrol-based polymers there is a growing demand to prepare materials using bio-based and renewable sources. In Chapters 2–4, photo-reversible materials whose disassembly could be triggered by low intensities of visible light were prepared by layer-by-layer assembly of natural polymers and azo dyes mainly utilizing electrostatic interactions. Expanding on this, in Chapter 5, photo-reversible materials whose surface wettability and water permeance could be controlled by intensities of UV-Vis light were prepared by covalent modification of the natural polymers with azo dyes.

In Chapter 2 we outlined a novel process of preparing photo-reversible materials, using a cellulose-based polymer and an azo dye. In response to low intensities of blue light while being washed, the water-resistant polyelectrolyte multilayered (PEM) material could be gently disassembled back to its water-soluble starting components. In Chapter 3 for the first time, it was shown that the isomerization kinetics of the commercial Bismarck Brown Y (BBY) azo dye when embedded in these photo-reversible materials fit well to a biexponential model and the *cis* decay was measured to be on the time scale of seconds-milliseconds. The results from the DFT modeling

supported our theory that the *trans-cis-trans* isomerization of the azo dye led to the disassembly of the multi-layered films described in Chapter 2. Chapter 4 provided another example of preparing these photo-reversible materials using another natural polymer known as sodium alginate. To valorize the waste brown seaweed (*Sargassum spp.*) polluting Caribbean beaches, alginate and cellulose were extracted, with the extracted alginate being used to make novel blends with arrowroot starch, as alternatives for petrol-based plastics like high density polyethylene (HDPE) and ethylene vinyl alcohol (EVOH). Similar to the cellulose-based polymers in Chapters 2 and 3, the extracted alginate was also used to make photo-reversible PEM films and capsules. Conversely, in Chapter 5, photo-reversible materials were prepared by covalently modifying cellulose and cellulose acetate with azo dyes for applications as self-cleaning hydrophobic materials. The grafting of the cellulose-based polymers with azo dyes greatly reduced the surface wettability of the materials, and using UV-Vis light as a trigger the water permeance of these azo functionalized cellulose-based materials could be altered. In summary, all these examples show the great potential of using natural polymers in the place of petrol-based polymers towards fabricating more sustainable photo-reversible materials for a range of applications.

Résumé

Développement de matériaux photo-réversibles à l'aide de colorants azoïques et de polymères naturels

Cette Thèse apporte des contributions aux domaines de la conception de matériaux optiques et intelligents basés sur des polymères naturels. Elle décrit deux approches distinctes pour préparer des matériaux photo-réversibles en utilisant divers colorants azoïques et polymères naturels, en vue d'applications dans les systèmes de désassemblage/réassemblage et les matériaux autonettoyants. Les polymères à base de pétrole ont été utilisés précédemment pour préparer des matériaux azoïques photo-réversibles; cependant, en raison des impacts environnementaux négatifs associés aux polymères à base de pétrole, il est préférable de préparer des matériaux utilisant des sources biologiques et renouvelables. Dans les Chapitres 2 à 4 de cette Thèse, des matériaux photo-réversibles dont le désassemblage peut être déclenché par de faibles intensités de lumière visible ont été préparés par assemblage couche par couche de polymères naturels et de colorants azoïques en utilisant principalement des interactions électrostatiques. Dans le Chapitre 5, des matériaux photo-réversibles dont la mouillabilité de la surface et la perméance à l'eau peut être contrôlée par l'intensité de la lumière UV-Vis ont été préparés par modification covalente des polymères naturels avec des colorants azoïques.

Dans le Chapitre 2, nous avons décrit un nouveau processus pour préparer de matériaux photo-réversibles en utilisant un polymère à base de cellulose comme composant et le colorant azoïque. Cependant ils pouvaient retrouver ses solubles composants de départ quand les multicouches de polyélectrolytes (PEM) sont exposés à la lumière bleue de faible intensité. Dans

le Chapitre 3 pour la première fois, il a été montré que la cinétique d'isomérisation du colorant azoïque commercial Bismarck Brown Y (BBY) lorsqu'il est intégré dans ces matériaux photo-réversibles correspond bien à un modèle biexponentiel et la désintégration *cis* a été mesurée sur une échelle de temps de quelques secondes-millisecondes. Les résultats de la modélisation DFT fournissent également des informations sur le mécanisme d'isomérisation, ce qui confirme notre théorie selon laquelle l'isomérisation *trans-cis-trans* du colorant azoïque conduit au désassemblage des films multicouches du Chapitre 2. Le Chapitre 4 a fourni un autre exemple de préparation de ces matériaux photo-réversibles en utilisant un autre polymère naturel connu sous le nom d'alginate de sodium. Pour valoriser les déchets d'algues brunes (*Sargassum spp.*) qui polluent les plages des Caraïbes, l'alginate et la cellulose ont été extraits, l'alginate extrait étant utilisé pour faire de nouveaux mélanges avec de l'amidon d'arrowroot, comme alternatives aux plastiques à base de pétrole comme le polyéthylène haute densité (HDPE) et l'éthylène alcool vinylique (EVOH). Comme pour les polymères à base de cellulose des Chapitres 2 et 3, l'alginate a également été utilisé pour fabriquer des films et des capsules PEM photo-réversibles. Finalement, dans le Chapitre 5, des matériaux photo-réversibles ont été préparés en modifiant de manière covalente la cellulose et l'acétate de cellulose avec des colorants azoïques pour des applications comme matériaux hydrophobes autonettoyants. Le greffage des polymères à base de cellulose avec des colorants azoïques a considérablement réduit la mouillabilité de la surface des matériaux, et en utilisant la lumière UV-Vis comme déclencheur, la perméance à l'eau de ces matériaux à base de cellulose fonctionnalisés par des colorants azoïques a pu être modifiée. En résumé, tous ces exemples montrent le grand potentiel de l'utilisation de polymères naturels à la place de polymères à base de pétrole pour fabriquer des matériaux photo-réversibles plus durables pour toute une série d'applications.

Acknowledgements

My experience as a PhD student in the Chemistry department over the last 6 years has allowed me to grow and mature into the well-rounded, enthusiastic researcher that I am today. I was able to complete this journey due to the continued support from my supervisors, colleagues, friends, and family.

I would firstly like to thank my co-supervisors, Dr. Christopher J. Barrett, and Dr. Theo G. M. van de Ven, for their guidance and support throughout this degree. Thank you Dr. Barrett for allowing me to travel to various conferences, and to collaborate with other universities to share my work and hone my research skills. Not only did you encourage any research idea I brought to you, but during the Covid-19 pandemic you supported my research while I was stuck in St. Vincent. Likewise, I extend my sincerest gratitude to Dr. van de Ven who taught me everything I now know about cellulose and provided much guidance on my projects particularly in my last 2 years. I could not have asked for two better supervisors, and for that I will always be grateful.

I would also like to thank the past and current members of the Barrett and van de Ven research groups for their assistance and support. Thank you to Tristan and Victoria for familiarizing me with the Barrett lab, and special thanks to Mikhail who became a close friend as we spent many days mulling over the lasers and dippers trying to get our experiments to work. Thank you to Sierra, Martin, Jane, Yiwei, Hannah, Amin, Roya, and Hadi from the van de Ven group for the knowledgeable group meetings, and assistance with everything cellulose-based. It was really an honor to have the support of 2 research groups and so many brilliant scientists. I would also like to thank Aidan for being the best MATLAB teacher and a great friend, thank you to Violeta for keeping the lab in order and teaching me great synthetic skills, and Jessie and Hariz

for the well-deserved breaks from lab-work to grab coffee or just complain about grad school. Thanks also to the Harrington research group and the McCalla research group for conducting the Raman measurements, access to your microscope, and 3D-printers. Thank you also to the facility managers, particularly Mohini, Robin, Petr, and Alex who made doing characterization fun and were always patient with me. Thank you Chantal for helping me manoeuvre grad school and providing a shoulder to lean on during hard times. Thanks to my collaborators at York university, Dr. Mermut and Dr. Pietro, who provided a lot of computational assistance in this Thesis.

Thank you to the CGSS executive 2020/2021 committee for organizing the fund raiser to help St. Vincent after the volcanic eruption. The support from my colleagues and department was much appreciated. Finally, I would like to thank my family for their continued support and belief in me. Mom, Dad, Aunty Thora, Kairel, K'more, and Keishon, thank you for always being there. I could not have done any of this without the emotional support of my close friends as well; thank you Hasani, Sacy, Felica, and Luzia. You no longer have to hear me complain about working late nights and failing experiments again.

Contributions to Original Knowledge

This Thesis contains a number of original scholarly contributions, with Chapters 2–5 either published, submitted, or in the process of being submitted to peer-reviewed journals at the time of submission of this Thesis. Chapter 2 outlines a novel process of preparing photo-reversible polyelectrolyte multi-layers (PEMs) by combining a bio-based polymer with a small photo-switchable azo dye, Bismarck Brown Y (BBY), *via* soft-bonding interactions. The driving force behind the self-assembly of the water-soluble components to form a water-resistant material, and the subsequent photo-driven disassembly was thoroughly investigated using several analytical techniques such as UV-Vis spectroscopy, FTIR spectroscopy, AFM, confocal Raman spectroscopy and laser pump-probe experiments. A novel ‘sunlight and rainfall experiment’ was designed to evaluate the rate of the disassembly of the PEM films under various simulated environmental conditions. This is the first study to date of a photo-driven disassembly of PEM films using visible light and water. Chapter 2 also introduces the isomerization behaviour of the well used azo dye, BBY, whose properties were previously unreported.

Chapter 3 expands on the pump-probe experiments of the BBY azo dye conducted in Chapter 2, investigating the effect of solvent and the polymer matrix on the isomerization behaviour, and determining the rate constants and *cis* lifetime of the azo dye in the various media. Additionally, Chapter 3 utilizes density functional theory (DFT) calculations to provide a theoretical treatment of the isomerization kinetics and a possible mechanism of the isomerization process. The results obtained from the pump-probe experiments and the DFT calculations show how the presence of impurities, type of solvent, and steric interactions can affect the isomerization of azo dyes.

Chapter 4 was inspired by circumstances surrounding the Coronavirus pandemic from 2020–2021 being stationed in my home country of St. Vincent and the Grenadines for 1 year and observing the brown seaweed polluting the beaches. This Chapter focused on developing a methodology to valorize this waste brown seaweed (*Sargassum spp.*), mainly to convert the raw material into an advanced green material. Two of the main components of brown seaweed, sodium alginate and cellulose, were extracted. Novel blends of alginate were then prepared using another locally produced natural product in St. Vincent: arrow root starch (AS). The extracted polymers were thoroughly characterized and compared to other commercial samples. The mechanical and physical properties of the solvent-cast films were assessed and compared to other bio-based materials and traditional synthetic plastics. The results indicate that these alginate films and blends could replace high density polyethylene (HDPE) and ethylene vinyl alcohol (EVOH) plastics in the marketplace. The extracted alginate was then used to fabricate photo-reversible materials such as capsules and PEM films like those prepared in Chapter 2.

Lastly, Chapter 5 is a deviation from soft-bonding azo/polymer complexes prepared in Chapters 2–4, and instead focuses on covalently modifying the polymer with azo dyes towards making robust self-cleaning materials. While a few azo dye modified cellulose derivatives (*e.g.*, Azo-Cel, Azo-HPC) have been previously prepared, this is the first report of the synthesis of azo dye modified cellulose acetate (Azo-CA), as well as the first study of the of the isomerization of the azo dyes once grafted onto the CA polymers. This report also tested the changes in the surface wettability and water vapour permeance of the fabricated materials in response to UV-Vis light. The results showed that CAs could be successfully modified with azo dyes, which retain their isomerization behaviour in solution. Following exposure to UV light the water permeability of these Azo-CA materials can be altered.

Contributions of Authors

Chapter 1: Introduction and literature review of photo-reversible azo/polymer soft-bonded complexes

Chapter 1 was researched and written entirely by Kayrel E. K. Edwards, with Prof. Barrett and Prof. van de Ven assisting with final minor editing of the text.

Chapter 2: Controlled disassembly of azobenzene cellulose-based thin films using visible light

Reprinted (adapted) with permission from: Edwards, K. E., Kim, M., Borchers, T. H., and Barrett, C. J. “Controlled disassembly of azo dye /cellulose-based thin films using visible light” *Materials Advances*, 2022, 3, 6222–6230.

Project design, material preparation, pump-experiments, UV-Vis spectroscopy, NMR spectroscopy, FTIR spectroscopy, titrations, water contact angle measurements, disassembly experiments as well as the analysis of Raman data were conducted by Kayrel E. K. Edwards. Dr. Tristan Borchers helped construct the pump-probe optical set-up, and assisted with some of the pump-probe experiments of BBY in THF solvent. Mikhail Kim assisted with the design of the ‘sunlight and rainfall experiment’ and the dipping experiments. The initial manuscript was written by Kayrel E. K. Edwards, with Prof. Barrett helping with final editing and manuscript submission.

Chapter 3: Optical and computational study of the *trans* ↔ *cis* reversible isomerization of the commercial bis-azo dye Bismarck Brown Y

Reprinted (adapted) with permission from: Edwards, K. E. K., Mermut, O., Pietro, W. J., and Barrett, C. J. “Optical and computational study of the *trans* ↔ *cis* reversible isomerization of the commercial bis-azo dye Bismarck Brown Y” *Physical Chemistry Chemical Physics*, 2023, 25, 5673–5684.

Conceptualization, methodology, investigation, formal analysis, and writing (original draft) were conducted by Kayrel E. K. Edwards. Prof. William Pietro of York University (where Prof. Barrett spent a year sabbatical in 2021) performed all computational analyses and writing pertaining to the DFT section. The initial manuscript was written by Kayrel E.K. Edwards, with Prof. Barrett, Prof. Mermut and Prof. Pietro helping with final editing and manuscript submission.

Chapter 4: Valorization of brown seaweed

Edwards, K. E. K., Barrett, C. J., and van de Ven, T. G. M. “Valorization of brown seaweed” manuscript in preparation.

Project design, extraction, material preparation, spectroscopies (FTIR, NMR, XRD), conductometric titration, water solubility tests, mechanical testing and WVP measurements were conducted by Kayrel E. K. Edwards. Initial manuscript was written by Kayrel E. K. Edwards, with Prof. Barrett and Prof. van de Ven helping with final editing of the manuscript.

Chapter 5: Photo-response of azo dye functionalized cellulose acetate

Edwards, K. E. K., Barrett, C. J., and van de Ven, T. G. M. “Photo-response of azo dye functionalized cellulose acetate” manuscript in preparation.

Project design, synthesis, water contact angle experiments, water vapour permeability experiments, electrospinning, spectroscopic analyses (NMR, FTIR, UV-Vis, PXRD and TGA), isomerization experiments, and interpretation of SEM-EDS data were conducted by Kayrel E. K. Edwards. Initial manuscript was written by Kayrel E. K. Edwards, with Prof. Barrett and Prof. van de Ven helped with final editing of the manuscript.

Chapter 6: Discussion, conclusions, and future outlook

Chapter 6 was written entirely by Kayrel E. K. Edwards, with Prof. Barrett helping with final editing of the text.

List of Figures

- Figure 1.1** Chemical structures of cellulose and some of its common derivatives.....9
- Figure 1.2** Schematic of the structure and components of brown seaweed, and the chemical structure of sodium alginate.13
- Figure 1.3** (a) Azobenzene can convert between *trans* and *cis* states photochemically, and relaxes to the more stable *trans* state thermally. (b) Simplified state model for azobenzenes. The *trans* and *cis* extinction coefficients are denoted ϵ_{trans} and ϵ_{cis} . The Φ refers to quantum yields of photoisomerization, and γ is the thermal relaxation rate constant.....14
- Figure 1.4** UV-Vis spectra of the 3 classes of azo dyes: azobenzene-type, amino azobenzene-type and pseudostilbene-type.16
- Figure 1.5** Structures of the investigated compounds, **1** – azobenzene; **o-2** – *o*-bis-azobenzene; **m-2** – *m*-bis-azobenzene; **p-2** – *p*-bis-azobenzene.17
- Figure 1.6** A) Plot of the change in absorbance vs. time for 4A4NAB in THF at 30 °C before and after 3 flashes of light are applied to the same solution. B) Plot of $\ln(A_{\infty}-A)$ vs. time for 4A4NAB in different solvents at 25 °C. The red lines for 3-pentanol, acetone, and tetrahydrofuran follow the time scale of the upper x-axis. Only the initial linear portion of these plots is shown.18
- Figure 1.7** Schematic of a simplified pump-probe experimental set up using a UV-Vis spectrometer (probe) and LED (pump) to determine the thermal *cis*-to-*trans* relaxation rate behaviour of azo dyes.23

Figure 1.8 The molecular orbital diagram for azobenzene, including the three highest occupied, three lowest unoccupied, and the nonbonding orbitals of the nitrogen lone pairs...25

Figure 1.9 Top: Schematic depicting layer-by-layer assembly of PEM films, beginning with a negatively charged substrate (glass or silicon) being dipped in a polycation solution. Bottom: Illustration of biologically relevant polycationic and polyanionic polymers used in this study and others from our Group, and their acronyms.34

Figure 1.10 A variety of surface-templated HB polymer materials: HB polymer–polymer (A) and polymer–particle (B) films; core–shell (C), and hollow single-component (D), and two-component (E) hydrogel capsules; as well as hollow capsules, obtained by direct precipitation of HB IPC onto particulate substrates (F).36

Figure 1.11 Example Figures for the design guidelines for Soft-bonded systems. (Left) electrostatically bonded ethylated P4VP polymer and methyl orange azo dye. (Right) Halogen and hydrogen bonded self-assembled azo dyes with bis-pyridine derivatives.....40

Figure 1.12 a) Typical AFM image of a SRG formed on an azo material, b) first order diffraction efficiency as a function of writing time, and c) averaged surface profile from a).....42

Figure 1.13 Plausible mechanism of bending in the hydrogen-bonded CLCP films of azo materials. (a) Network structures of the hydrogen-bonded CLCP films consisting of the copolymers and the crosslinkers. Schematic illustration of molecular alignment in the hydrogen-bonded CLCP film before (b), and after (c) irradiation with UV light.....44

Figure 1.14 A) Schematic representation of photo-responsive guest uptake. B) Schematic illustration of the aggregates formed by the C₁₆mimBr/AzoCOONa system in aqueous solution before and after UV-light irradiation.48

Figure 1.15	Schematic model (a) and photographs (b) of the reversible sol–gel transition of the PAA-mAzo/PAA-b-CD mixture.	51
Figure 1.16	A) Example of electrospun azo-Cel fabric. B) Photos of water droplets on a) an as-spun Azo-Cel fabric (<i>trans</i> isomer): WCA = 120 °, b) the same fabric after UV radiation (<i>cis</i> isomer): WCA = 108 °, and c) the same fabric after visible light irradiation (<i>trans</i> isomer): WCA = 118 °. d) The WCA changes of the Azo-Cel fabric over 5 cycles of UV/visible light irradiations. The plotted WCA values are the mean values of 4 sets of the measurements using 4 different pieces of the Azo-Cel fabric, and the error bars represent their maximum and minimum values.....	54
Figure 1.17	(a) Scheme of PDA formation and reactions between AZO and PDA through Michael addition, leading to covalent linkages, and (b) schematic of the self-cleaning behaviour of a photo-responsive membrane comprising a thin film of AZO and PDA.....	55
Figure S1.1	Examples of (a) polymer matrix, (b) biodegradable polymers, (c) synthetic biodegradable polymers, and (d) natural biodegradable polymers.....	70
Figure S1.2	Direct extraction of biomass to provide biopolymers for use in manufacture of biobased products.	73
Figure S1.3	(a) Requirements of barrier properties for different food packaging applications and a comparison between oxygen/water transition rate of selected biodegradable polymers at 25 μm and food packaging barrier requirements. (b) The oxygen/moisture permeability of different polymers.	78
Figure 2.1	Schematic illustration of layer-by-layer (LbL) assembly to make multi-layered (NaCS/BBY) thin films, and the simulated sunlight and rainfall trigger conditions to assess the disassembly of the films and the chemical structures of the materials used.....	86

Figure 2.2 (Left) Image of multi-layered NaCS/BBY films (50 bilayers) deposited on a glass substrate with distinct red colour of BBY. (Right) UV-Vis spectra of NaCS/BBY on quartz with $\lambda_{max} = 450$ nm, BBY in water $\lambda_{max} = 450$ nm and NaCS in water with $\lambda_{max} = 200$ nm...89

Figure 2.3 IR spectra of BBY only (orange) vs. multi-layered NaCS/BBY films (blue). Inset shows the changes in the N–H stretching mode of BBY only (orange) vs. in multi-layered NaCS/BBY films (blue).91

Figure 2.4 (Top) UV-Vis absorption spectra of NaCS/BBY films in response to change in pH. Between pH 2–10 the $\pi \rightarrow \pi^*$ transition absorption band is at 450 nm and at pH 11–12 there is significant broadening of the absorption band to 385–490nm. (Bottom) Image of the film showing colour change from red (pH 2–10) to orange (pH 11–12) and a schematic of the proposed molecular changes which occur in response to change in pH.....94

Figure 2.5 (A) Pump-probe isomerization plot showing the change in absorbance over time for BBY solution in THF: (I) Pump beam is off, (II) Green box represents when the laser is switched on for 1 s and (III) pump beam is turned off showing thermal back relaxation. (B) Decay of the *cis* isomer with fit with a biexponential function.....96

Figure 2.6 (A) Changes in the Raman spectra of BBY in multi-layered NaCS/BBY thin films with increasing 532 nm laser power (0.1–0.5mW). (B) Raman spectra of BBY only (blue) and NaCS/BBY films (red) upon 1st scan at 0.1 mW 532 nm laser power. (*) represents the characteristic *cis* BBY Raman peaks.98

Figure 2.7 (A): Disassembly of NaCS/BBY films triggered by blue light (460 nm LED, 299 mA, 12.50 V). Upper section of films was left exposed (unmasked) while the lower section was masked. (B): Plot of $\ln A$ vs. t during disassembly process for unmasked (circles) vs. masked

(squares) sections of the films. (C and D): Time resolved UV-Vis spectra of NaCS/BBY films following irradiation with blue light, washed using DI water for unmasked and masked sections, respectively ($t = 168$ hr). (E): Schematic of disassembly of NaCS/BBY thin films under ‘simulated sunlight and rainfall’ experimental conditions.....102

Figure S2.1 (A) AFM used to determine the thickness of NaCS/BBY films deposited on glass substrate (R_q : 1.97 nm). (Top, Left) Image of NaCS/BBY thin film (red) deposited on glass substrate (grey). The middle section of the film was masked with parafilm during film growth and removed after dipping to create a boundary for the height measurements. (Top, Right) 3D view of the surface of the thin film (yellow) onto on glass substrate (red). (Bottom, Left) Step height calculations between the glass substrate (green) and thin film (red). ((Bottom, Right) Step height calculations along one line of the thin film shown in the top, right figure. Measurement parameters: 20 μm , FAA 1.0 V, SP: 568 mV, IG 5, 0.5 Hz, 512×512 . (B) AFM of the surface topology of (Left) bare glass substrate (R_q : 1.97 nm) and (Middle) NaCS/BBY deposited on glass substrate showing a fairly uniform surface. (Right) 3D image of surface and edge of NaCS/BBY film deposited on glass substrate. (C) Confocal Raman optical Images of (Left) NaCS/BBY LbL thin film (Middle) NaCS polymer and (Right) BBY azo dye deposited on quartz substrate. Images were obtained using confocal Raman microscope (Alpha 300R, WITTEC), 100 \times objective. Scale bar = 50 μm . (D) (Right & Middle) SEM images of NaCS/BBY thin film deposited on glass substrate at 2 different areas of interest (scale bars are 20 μm and 10 μm , respectively). (Left) Elemental mapping of NaCS/BBY thin film showing presence of polymer NaCS (S = 6 %) and BBY (N = 14 %) uniformly across film surface.113

Figure S2.2 Plot of max absorbance at 450 nm of BBY with increase in the number of bilayers of NaCS/BBY LbL thin films.....114

Figure S2.3 (A) Shows differences in the contact angle of films of the starting material vs. LbL film. Initial measurements of contact angle are as follows; top: NaCS ($\theta = 21.0^\circ, 20.6^\circ$), middle: BBY ($\theta = 44.8^\circ, 43.7^\circ$) and bottom: NaCS-BBY ($\theta = 61.4^\circ, 61.3^\circ$). (B) Changes in contact angle for BBY film over time. Top: $t = 0$ min ($\theta = 44.8^\circ, 43.7^\circ$), bottom: $t = 1$ min ($\theta = 42.4^\circ, 42.0^\circ$). (C) Changes in contact angle for NaCS-BBY film over time. Top: $t = 0$ min ($\theta = 61.4^\circ, 61.3^\circ$), middle: $t = 2$ min ($\theta = 55.4^\circ, 55.9^\circ$) and bottom: $t = 4$ min ($\theta = 49.4^\circ, 49.5^\circ$).....114

Figure S2.4 XPS analysis of NaCS commercial sample showing the binding energy for different atoms.115

Figure S2.5 Titration of NaOH (50.15 mM) against BBY (2.421 mM). Red line shows titration curve (pH vs. V NaOH), and blue line shows the first derivative.....115

Figure S2.6 IR spectra of the polymer NaCS (blue line) and photo-switch BBY (orange line).116

Figure S2.7 Effect of salt (2 M solution) on the stability of NaCS/BBY thin films.....116

Figure S2.8 Effect of temperature on the stability of NaCS/BBY thin films.....117

Figure S2.9 Change in intensity of Raman signal around 1285 cm^{-1} peak overtime of NaCS/BBY thin films using a 532 nm laser at 0.1 mW power.....117

Figure S2.10 (A) Raman spectra of BBY deposited on quartz substrate excited using a 532 nm laser at 0.1 mW (red), 0.2 mW (blue) and 0.5 mW (black) laser power. As laser power increases, the intensity of *cis* peaks at 1510 cm^{-1} and 612 cm^{-1} increases. (B) Full Raman spectrum of BBY only with 532 nm laser at 0.1 mW laser power. (C) Raman spectrum of NaCS only and (D) full Raman spectrum of NaCS/BBY thin films with 532 nm laser at 0.1 mW laser power.....118

Figure S2.11 AFM disassembly after 2 weeks for a film in DI water under ambient light...118

Figure S2.12 (A) Disassembly of NaCS/BBY films deposited on glass substrate triggered by blue light (460 nm LED, 299 mA, 12.50 V), washed with tap water. Upper section of films was left exposed (unmasked) while the lower section was masked. (B,D) Time resolved UV-Vis spectra of NaCS/BBY films following irradiation with blue light, washed using tap water for unmasked and masked sections, respectively ($t = 0-24$ hr). (C) Graph of $\ln A_{450nm}$ vs. t during disassembly process for unmasked (circles) vs. masked (squares) section of the films.....119

Figure 3.1 Chemical structures of the geometric isomers of Bismarck Brown Y (BBY) and Chrysoidine azo dyes. Chemical structure of polymer NaCS and schematic of layer-by-layer self-assembled NaCS/BBY thin films materials.....126

Figure 3.2 Schematic of the optical pump-probe experimental set up used to determine the thermal *cis-to-trans* relaxation rate behaviour of BBY.....132

Figure 3.3 UV/Vis spectra of crude commercial BBY azo dye in NaCS/BBY film (- black) and water (- red), recrystallized BBY in water (-- red) and Chrysoidine azo dye in water (- green) with $\lambda_{max} = 455-464$ nm.135

Figure 3.4 The absorbance vs time profiles of commercial BBY in (a) ethanol and (b) multilayered NaCS/BBY thin films. Key: (I) Before irradiation, (II) during 1 s pulse with 532 nm laser, (III) *cis* decay in dark.137

Figure 3.5 The decay of *cis* isomer fit to biexponential and monoexponential kinetics of commercial BBY in (a) ethanol and (b) multi-layered NaCS/BBY thin films. The inset shows the residual plot between our least-squares four-parameter biexponential fit and the data.....139

Figure 3.6	(a) Effect of solvent/medium on kinetics of <i>cis</i> decay of crude BBY. Effect of (b) solvent polarity and (c) solvent proticity on rate constants of BBY. Rate values for deprotonated crude BBY shown in brackets.	140
Figure 3.7	The absorbance vs. time profiles of (a) recrystallized BBY in ethanol and (b) Chrysoidine in ethanol. Key: (I) Before irradiation, (II) during 1s pulse with 532nm laser, (III) <i>cis</i> decay in dark. The decay of <i>cis</i> isomer fit to monoexponential kinetics of (c) recrystallized BBY in ethanol and (d) Chrysoidine in ethanol.	143
Figure 3.8	DFT optimized geometries for the three isomers of BBY (a) EE, (b) EZ and (c) ZZ.	146
Figure 3.9	DFT optimized <i>cis-trans</i> isomerization transition-state geometries of BBY (a) EZ-EE and (b) ZZ-EZ.	147
Figure 3.10	DFT prediction of the C–N–N bond angle along the ZZ-EZ reaction coordinate.....	149
Figure 3.11	DFT predicted N–N bond length profile along the ZZ-EZ coordinate.....	149
Figure S3.1	The absorbance vs. time profiles of BBY in solvents (a) DMF, (b) THF, (c) THF/H ₂ O, and (d) H ₂ O. (I) Before irradiation, (II) during 1 s pulse with a 532 nm laser, (III) <i>cis</i> decay in dark.	159
Figure S3.2	The decay of <i>cis</i> isomer fit to biexponential kinetics of BBY in solvents (a) DMF, (b) THF, (c) THF/H ₂ O, and (d) H ₂ O. The inset shows the residual plot between our least-squares four-parameter biexponential fit and the data.	160
Figure S3.3	Mass spectra of crude BBY.	161

Figure S3.4 ^1H - NMR spectra of crude commercial BBY, recrystallized BBY and Chrysoidine azo dyes.	162
Figure S3.5 FTIR spectra of crude commercial BBY, Chrysoidine, recrystallized BBY and crude BBY (deprotonated) azo dyes.	163
Figure S3.6 DFT optimized geometry of the protonated EE (<i>trans</i>) isomer of BBY.....	164
Figure S3.7 Runs ‘2’ and ‘3’ showing the decay of <i>cis</i> isomer fit to monoexponential kinetics of Chrysoidine.	164
Figure S3.8 Energy profile showing a typical monotonic rise from the <i>cis</i> isomer to the activation energy, followed by a monotonic fall to the <i>trans</i> isomer, as a plot of relative Energy vs. CNNC bond angle.	165
Figure 4.1 Illustration of the structure and composition of brown seaweed (<i>Sargassum spp.</i>) and chemical structures of major components: alginate and cellulose.....	174
Figure 4.2 Schematic showing the extraction of the major components: alginate and cellulose from waste brown seaweed collected from St. Vincent.	176
Figure 4.3 (A) ^1H NMR of extracted Na alginate from brown seaweed (<i>Sargassum spp.</i>) vs. commercial Sigma Aldrich in D_2O solvent. (B) ^{13}C Solid-State NMR of brown seaweed, extracted sodium alginate from brown seaweed vs commercial Sigma Aldrich, and extracted cellulose from brown seaweed vs. commercial cellulose kraft pulp.....	184
Figure 4.4 IR spectrum of brown seaweed (black), commercial alginate Sigma Aldrich (blue, dashed), extracted Na alginate (blue), commercial cellulose kraft pulp (red, dashed) and extracted cellulose (red).	186

Figure 4.5	Conductometric titration of extracted Na alginate (with 0.1 mL, 0.5 N HCl) against NaOH (10 mM). Measured degree of substitution (DS) = 0.9, <i>i.e.</i> , COOH content of 5.1 mmol/g.....	189
Figure 4.6	X-ray diffraction patterns of cellulose from brown seaweed (green) <i>vs.</i> cellulose kraft pulp (from wood) (black), and alginate extracted from brown seaweed as a film (red) and blend with arrowroot starch and glycerol (blue).....	190
Figure 4.7	Polarized microscope images of extracted alginate bundles and fibres from brown seaweed deposited on (A) a glass slide and (B) mica coated with PLL and extracted cellulose fibres and microfibrils on (C) a glass slide and (D) mica coated with PLL.....	192
Figure 4.8	Graphs of (A) water solubility, (B) water vapour transmission rate (WVTR) and water vapour permeability (WVP), (C) oxygen transmission rate (OTR), (D) tensile strength and (E) elongation at break of Na alginate films and blends.....	194
Figure 4.9	Formation of water-resistant Ca alginate (A) capsules and (B) straw, (C) azo dye/alginate capsules and (D) azo dye/alginate PEM films.....	198
Figure 5.1	(Top) Schematic of the reaction of cellulose acetate (varying % acetyl content) with azo dyes, and the photo-induced <i>trans-cis</i> isomerization of Azo-CA polymers. (Bottom) Photographs of solvent cast films of cellulose monoacetate (CMA) and cellulose diacetate (CDA), and azo modified cellulose-based polymers: azobenzene CMA (Azo-CMA), azobenzene CDA (Azo-CDA), hydroxy-azobenzene CDA (Ho-Azo-CDA) and azobenzene cellulose (Azo-Cel).	212

Figure 5.2	(A) ¹³ C NMR of Azo-CDA in DMSO-d6 solvent (red) and CDA in solid-state (black). (B) ¹³ C NMR of Ho-Azo-CDA (red) and CDA (black) in solid-state.....	216
Figure 5.3	IR spectrum of CDA (blue) vs. Azo-CDA (orange).....	218
Figure 5.4	SEM images of planar and/or cross-sectional views of (A) CDA, (B) Azo-CDA (solvent-cast), (C) Azo-CDA (electrospun), (D) Azo-CMA (E) Ho-Azo-CDA, and (F) Azo-Cel.	219
Figure 5.5	X-ray diffraction patterns of Cellulose (green), CMA powder (black), CTA powder (blue), CDA powder from Sigma Aldrich (red), Azo-CDA film (magenta), Ho-Azo-CDA film (cyan), and Azo-CMA film (orange).	222
Figure 5.6	TGA traces showing the thermal decomposition temperature (T_d) of starting materials: azo dyes and CA, and azo functionalized CA (Azo-CA) samples.....	223
Figure 5.7	UV-Vis spectra and thermal back relaxation of (A) Ho-Azo-COCl and (C) Ho-azo-CDA in THF. Absorbance measurements were taken at 1 min intervals in the dark. (B) and (D) shows the conversion of the <i>cis</i> isomer of Ho-azo-COCl and Ho-azo-CDA back to its original <i>trans</i> state in the dark.	225
Figure 5.8	Decay of the <i>cis</i> isomers of (A) Ho-Azo-COCl azo dye fit with a monoexponential function and (B) Ho-azo-CDA polymer fit with a biexponential function.....	227
Figure 5.9	(A) Schematic showing the change in surface wettability of azo functionalized cellulose acetate films in response to light. (B) Photograph of the optical set up used to initiate a	

photo-response in thin film and contact angle set up used to measure water contact angle (WCA).
.....230

Figure 5.10 Effect of acetylation of cellulose and grafting of azo dyes onto cellulose and CA polymers on surface wettability (black bars). Purple bars indicate the water contact angle (WCA) of film surface following UV irradiation for $t = 20$ min and blue bars represent the WCA following exposure to ambient visible light for $t = 20$ min.....232

Figure 5.11 Change in water vapour transmission rate (WVTR) and water vapour permeability (WVP) of CA (CDA and CMA) and azo modified CA films (Azo-CDA and Azo-CMA) under ambient light and with exposure to UV light.....235

Figure S5.1 (A) ^1H NMR spectra of CA polymers in DMSO- d_6 or D_2O solvent at various time periods following acetylation of cellulose and consequent hydrolysis of cellulose triacetate (CTA). (B) Determination of degree of substitution (DS) of commercial CA using ^1H NMR spectroscopy, in DMSO- d_6 solvent.249

Figure S5.2 ^1H NMR of azo dyes: precursor Ho-Azo-COOH (blue), synthesized Ho-Azo-COCl and (green) and commercial Azo-COCl (red).250

Figure S5.3 IR spectrum of azo dyes: (blue) commercial Azo-COCl, (orange) synthesized Ho-Azo-COCl, and (yellow) precursor Ho-Azo-COOH.....251

Figure S5.4 IR spectra of cellulose and cellulose acetate with varying % acetyl content...251

Figure S5.5 (A) UV-Vis spectra and thermal back relaxation of azo-CDA in THF solution in the dark following irradiation with UV light for $t = 20$ min. Measurements were taken at $t = 60$

min intervals. Inset shows the decrease in the absorbance band at 450 nm during thermal back relaxation. (B) Conversion of azo-CDA from *cis*-to-*trans* isomer in dark following irradiation with UV light. (C) Plot of first order kinetics $\text{Ln}(A_\infty - A_t)$ vs. t for azo-CDA in THF during *cis* decay.252

Figure S5.6 (A) UV-Vis spectra and thermal back relaxation of Ho-azo-CMA in THF solution in the dark following irradiation with UV light for $t = 20$ min. Measurements were taken at $t = 60$ min intervals. Inset shows the decrease in the absorbance band at 460 nm during thermal back relaxation. (B) Conversion of Ho-Azo-CMA from *cis*-to-*trans* isomer in dark following irradiation with UV light. (C) Decay of the *cis* isomer of Ho-Azo-CMA in THF fit with a monoexponential function.253

List of Tables

Table 1.1	Characteristics of various soft bonds.....	31
Table S1.1	Common-plant-based and petroleum-based materials and their approximate prices.....	71
Table S1.2	Analysis of information of environmentally problematic plastic items.....	72
Table S1.3	Feedstock localities based on highest production capacity for 2018/2019.....	75
Table S1.4	Biomaterial resin and product suppliers list.....	76

Table S1.5	Relative gas permeabilities polymers.....	78
Table S1.6	Mechanical and thermal properties of plant-based and petrochemical-based polymers.....	79
Table S1.7	Suitable applications of various bio-based and biodegradable polymers.....	79
Table 3.1	Geometric parameters of isomers and transitions states.....	145
Table 3.2	DFT calculations of transition state thermochemistry (relative electronic energies, rates).	151
Table 5.1	The kinetics of the thermal back relaxation of the <i>cis</i> isomer of azo dyes and Azo-cellulose-based polymers in THF following irradiation with UV light. (*Ref: Otsuka and Barrett, 2019).	229

List of Abbreviations

AFM	Atomic force microscopy	LbL	Layer-by-layer
Azo-CDA	Azobenzene cellulose diacetate	NaCS	Sodium cellulose sulfate
Azo-Cel	azobenzene cellulose	NMR	Nuclear magnetic resonance
Azo-CMA	azobenzene cellulose monoacetate	OP	Oxygen permeability
BBY	Bismarck Brown Y	PEM	Polyelectrolyte multilayer
CA	Cellulose acetate	PLM	Polarized light microscopy

CDA	Cellulose diacetate	PXRD	Powder x-ray diffraction
CI	Crystallinity index	SEM	Scanning electron microscopy
CMA	Cellulose monoacetate	SFE	Surface free energy
CTA	Cellulose triacetate	TGA	Thermogravimetric analysis
DAC	Dialdehyde cellulose	UV/Vis	Ultraviolet/Visible
DFT	Density Functional Theory	WCA	Water contact angle
EDS	Energy dispersive spectroscopy	WVTR	Water vapour transmission rate
FTIR	Fourier transform infrared spectroscopy		
Ho-Azo-CDA	Azobenzene cellulose diacetate	WVP	Water vapour permeability
Ho-Azo-CDA	Azobenzene cellulose diacetate		
HPC	Hydroxypropyl cellulose		

Chapter 1: Introduction and literature review of photo-reversible azo/polymer soft-bonded complexes

1.1 Abstract and overview

The main objective of this research was the development of novel photo-reversible materials using azo dyes and natural polymers harnessed from bio-based sources such as wood and seaweed. The term '*photo-reversible*' will be used to describe any material capable of undergoing physical and/or chemical change, such as mechanical bending, change in surface hydrophilicity or change in surface wettability, in response to light as an external stimulus, yet which can also be returned to the initial state, undamaged and able to cycle again. These natural polymers studied here as host materials include cellulose and its derivatives, and alginates, which are both highly and cheaply abundant and offer excellent mechanical and physical properties comparable to petrol-based polymers, while having the added advantage of being bio-based and/or biodegradable which limits the negative implications currently associated with traditional petrol-based plastic materials. When combined with azobenzene-based (azo) dyes, these natural polymers can be rendered reversibly responsive to light, with applications towards designing materials for assembly/disassembly and self-cleaning systems.

Throughout this Thesis there will be a focus on using natural polymers, specifically cellulose and its derivatives, and alginate, in fabricating photo-reversible materials. Thus, it is

important to understand what exactly natural polymers are and what advantages they offer as viable alternatives to petrol-based polymers in preparing materials for various applications. Additionally, a brief introduction to azo dyes is needed to have a better understanding of how these molecular photo-switches function in these photo-reversible materials. The different classes of azo dyes, their *trans-cis* geometric isomerization, UV-Vis spectroscopy and pump-probe experiments will be discussed. In addition to experimental work, computational modeling has proven to be a useful tool in predicting the kinetics and mechanism of the thermal *cis* decay behaviour of many azo dyes. As such a brief general introduction to computational modeling, focusing on aspects of density functional theory (DFT) that were used here, will be overviewed.

Many of these azo/polymer materials are formed *via* soft-bonded supramolecular assemblies, and therefore an adequate understanding of supramolecular chemistry is needed. The different types of intermolecular interactions utilized throughout this Thesis, such as electrostatic interactions, hydrogen bonding, and π - π interactions, will be briefly discussed. The main driving force for the assembly of the photo-reversible materials in this Thesis was soft-bonding interactions, described in the earlier Chapters (Chapters 2–4), while covalent modification dominated Chapter 5. Additionally, many design approaches were utilized to prepare a wide variety of materials throughout this Thesis. These included the use of an automated dipper robot to prepare polyelectrolyte multilayers (PEMs) in Chapters 2, 4 and 6, while solvent-casting and/or electrospinning were used to prepare free standing films in Chapters 4 and 5. Each of these techniques will be briefly discussed.

Lastly, a literature review of azo/polymer complexes is described throughout, focusing on the types of supramolecular chemistry, the types of polymers, and classes of azo dyes generally used to fabricate these photo-reversible materials. The relationship between the *trans-cis* isomerization of the azo dyes which act as a molecular photo-switch in these soft-bonded materials, towards applications as optical sensors, mechanical bending, and disassembly/reassembly will also be discussed. To conclude, an overview of azo-functionalized cellulose and its derivatives will be summarized to provide an overview on the development of these azo /cellulose-based materials.

1.2 Classes of natural polymers

As mentioned in the previous section, both petrol-based polymers and natural polymers (**Appendix 1: Figure S1.1**) have been used in the fabrication of photo-reversible azo/polymer materials. However, there is a clear bias based on the research output statistics towards petrol-based polymers such as poly(4-vinylpyridine) (P4VP), polyacrylic acid (PAA) and polymethylmethacrylate (PMMA) which dominate the previous literature reports of traditional synthesis of these materials, compared to natural polysaccharides such as cellulose and their derivatives (see **Section 1.5**). Additionally, when it comes to the preparation of materials for applications outside of optical devices, for example, for use in food packaging (wrappings for meats, fruits, and vegetables), and disposable utensils, cutlery and transport packaging, traditionally petrol-based polymers such as polyethylene (PE), polyethylene terephthalate (PET), polypropylene (PP), polyamide (PA) and polystyrene (PS) are most commonly used. Compared to many natural polymers, these synthetic

polymers have production and manufacturing systems that have already been well established since the 1950s.¹ Additionally, for a very long time the raw material needed to produce these synthetic polymers, which is a leftover byproduct from the crude oil industry, was very cheap compared to other sources.² This made the price per lb. of resins of polymers such as PE and PET very cheap compared to most natural polymer resins, as seen in **Appendix 1: Table S1.1**. However, depending on the starting material used to fabricate these natural polymers the price per lb. can be comparable or even better than that of some of the petrol-based polymers, for example cellulose, starch, and PHA have a lower price than PP and are comparable to PA and PET, as seen in **Appendix 1: Table S1.1**.²

However, due to recent issues concerning petrol-based polymers and traditional plastics, mainly the negative impacts which they can have on the environment and human health, there has been a re-transition effort back to natural polymers as preferable alternatives in applications ranging from packaging to electronics. In 2019, the Canadian Government implemented the first of many to come bans on single-use products traditionally made from petrol-based polymers such as PE, PP, PET and PS. These included many single-use items such as straws, cutlery, food serveware made from problematic plastic, drink six-pack rings, and plastic checkout bags (**Table S1.2**).^{3, 4} The focus now for researchers and manufacturers is to design materials that are economically competitive and sustainable using biomass which can also compete in terms of performance. Additionally, these materials should be processed in an environmentally benign way and products should be designed with their end-of-life in mind, to enable reuse or recycling thereby actively contributing to the foundation of a circular economy.

There is a wide array of bio-based feedstocks that have been used to prepare biopolymers as seen in **Appendix 1: Figure S1.2 and Table S1.3**. Depending on one's locality, different bio-based feedstocks may be more accessible, for example in Canada: in Quebec and British Columbia there are many forested areas from which cellulose can be extracted and converted easily and cheaply into different cellulose derivatives, while in coastal provinces such as British Columbia and the Maritimes biopolymers (such as carrageenan, alginates, cellulose, and chitin) can be harnessed from non-terrestrial sources, such as macroalgae and crustaceans. Corn which mainly grows in Ontario and Quebec is also a common feedstock to produce polylactic acid (PLA), thermoplastic starch (TPS), poly (butylene-co-terephthalate) (PBAT), polybutylene succinate (PBS) and biobased-PET (Bio-PET). Furthermore, biopolymers such as cellulose, polyhydroxyalkanoates (PHA) and PBAT can be extracted or produced from waste-material (saw dust, corn husks, fruit peelings, waste from dairy, etc.) and non-terrestrial sources such as algae, which reduces the demand for land use or competition for food streams. Many of these biopolymers can be converted into bioplastics and other products (**Table S1.4**). A bioplastic can be defined as any plastic-like material that is bio-based and/or biodegradable.⁵

According to a study by the European Bioplastics Association (2022), bioplastics represent about 1 % of the total of 367 Mt of plastic produced annually.⁵ In 2022, bioplastics capacity was 2.23 Mt with a projected capacity of 6.3 Mt by 2027.⁶ Global production capacities of bioplastics by material type in 2022 showed that the largest portion of materials are made from PLA (20.7 %) followed by starch blends (17.9 %), bio-based PE (15 %), and bio-based poly(trimethylene terephthalate) (13.3 %). Regenerated cellulose films only constitute a meager 3.5 % showing that

there is a lot of untapped potential for cellulose and its derivatives towards use as bioplastics. In terms of the market segment of bioplastics by material type, most bioplastics are used in flexible (695.6 Mt) and rigid (376.1 Mt) packaging, a fair portion as textiles (328.9 Mt), and a significantly smaller portion in electronics (57.7 Mt) and as coatings and adhesives (35.2 Mt).⁶

Currently there are very limited governmental regulations and policies controlling the physical properties of biomaterials and biopolymers used. However, there is an abundance of academic research data on the physical and mechanical properties of various polymers and industry standards available.² These properties can affect the performance of the product during its use phase as well as its degradation/ recycling phase. **Appendix 1: Figure S1.3, Tables S1.5 and S1.6** list common biomaterials and petrol-based materials, and their corresponding physical and mechanical properties. We see that cellulose kraft paper and cellulose acetate (CA) with a degree of substitution (DS) of 2.5 has the highest water vapour permeability (WVP) and very high oxygen permeability (OP) compared to other natural polymeric materials.² The tensile strength of cellulose and CA are comparable to PET and better than most other biomaterials, while the elongation at break is poor compared to petrol-based materials and other biomaterials.² Cellulose does not have a T_g or T_m while CA has values that are above 100 °C which might be useful for certain applications.²

These properties help predict the most suitable application for the various biomaterials/ bioplastics as seen in **Appendix 1: Table S1.7** which was taken from the Vancouver BC company Regenerative Waste Labs sustainable learning portal. From this table it is seen that generally starch blends have properties which make them useful as films for food waste bags, groceries, and rigid

materials such as coffee pods. In this Thesis a type of starch abundant in St. Vincent known as arrowroot starch (harvested from the Cassava root), was added as a plasticizer to the extracted alginate to make biopolymers which were made into films and straws. From **Appendix 1: Table S1.7** it is also suggested that cellulose-based polymers can be used to make wrappings for candies and for cutlery, specifically cellulose acetate, which was used in Chapter 5 of this Thesis to make hydrophobic photo-reversible materials.

1.2.1 Cellulose and its derivatives

Cellulose can be classified as a natural polymer since it is derived from natural sources such as wood and algae. It is one of the most abundant natural resources on Earth, and can function well as a sustainable feedstock due to its excellent recyclability, degradability, low cost, and worldwide availability.⁷ Generally, there is around 40 – 50 % cellulose in wood,⁸ located in the plant's cell wall to provide structural reinforcement. Cellulose can also be sourced from seed hairs, for example cotton,⁸ and it can also be synthesized by bacteria.⁷ Cellulose can also be found in algae and depending on the species of algae, there can be anywhere from 1 – 35 % cellulose per dry mass of the algae.^{9,10} Cellulose can also be extracted from waste sources such sawdust, corn husks, and fruit peelings. When extracted from trees, the cellulose fibers must be separated from lignin which is not present in non-terrestrial biomass such as seaweed.

Cellulose can exist in different forms based on the hierarchical structure starting from single nanofibrils (CNF) which can assemble to form cellulose microfibrils (MFC) which can

assemble into fibers.^{7, 8} Additionally, the chemical and mechanical treatment of cellulose can change its length scales and properties of the polymer. For example, TEMPO-mediated oxidation can lead to the production of cellulose nanofibrils (CNF), while treatment with very concentrated sulfuric acid at high temperatures can hydrolyze cellulose resulting in cellulose nanocrystals (CNCs), which can aggregate to form microcrystalline cellulose (MCC). The extraction of cellulose from its main terrestrial biomass, wood, is a well-developed industry, especially here in Canada where there are lots of forested areas. Wood refers to the main tissue of the stems, roots, and branches of “woody” plants, after the bark has been removed.¹¹ Wood’s main components are cellulose, hemicellulose, and lignin. The pulping of wood can be achieved with solutions of sulfurous acid and sulfites, aqueous alkalis, chlorine, and alkali and nitric acid.¹¹ A common method to extract cellulose from wood is the kraft method, which involves the treatment of wood pulp with hot NaOH and Na₂S to produce cellulose kraft pulp.¹² Delignification with bleaching agents can be done *via* chlorination and alkali washing.¹¹ Cellulose can also be regenerated mainly *via* the Lyocell method, and viscose method, *i.e.* dissolved then converted back to insoluble fibrous cellulose.^{7, 12} The viscose process has been banned in North America due to the toxicity of the CS₂ used in the process, while the Lyocell process uses N-methylmorpholine N-oxide (NMMO) as a solvent for cellulose.⁷

The general structure of cellulose is shown below in **Figure 1.1**. Cellulose biopolymers consist of linear chains of D-glucose repeating units which are connected through a high degree of intermolecular hydrogen bonding, rendering the polymer insoluble in water and in most organic solvents, and providing materials with excellent mechanical properties. The cellulose polymer

consists of regions which are amorphous or disordered connected by regions which are highly ordered or crystalline. The degree of crystallinity which can be determined by powder X-ray diffraction (PXRD) differs depending on the type of cellulose, the source from which the cellulose was extracted, and the method of extraction. Generally, cellulose is highly crystalline, with a crystallinity index of up to 80 %, determined by the intensities of the peaks associated with the crystalline regions, characterized by 2 theta angles at 22 ° and the amorphous regions, characterized by 2 theta angles at 18 °.¹¹

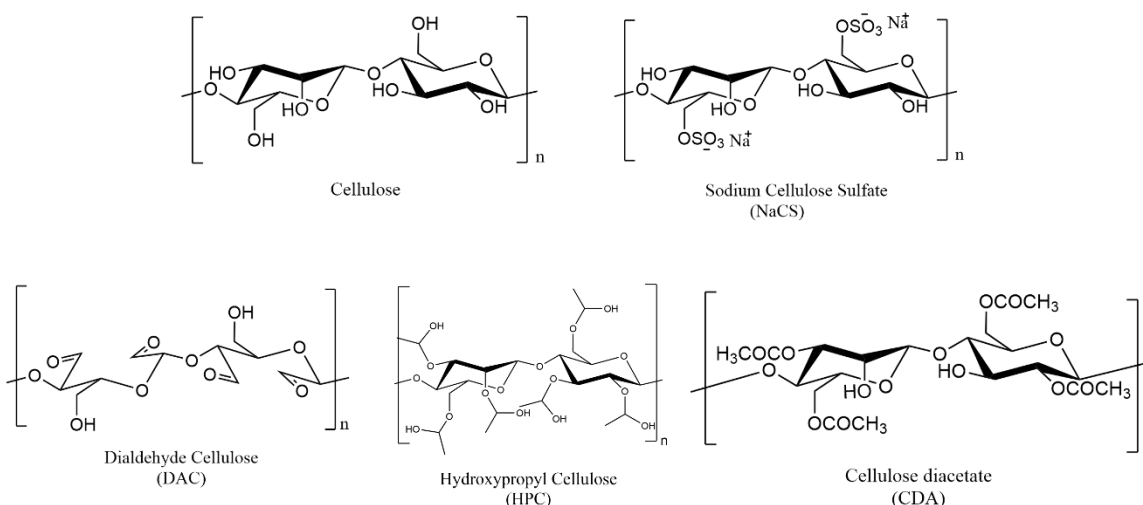


Figure 1.1 Chemical structures of cellulose and some of its common derivatives.

The degree of crystallinity of cellulose can affect its mechanical and physical properties. Kraft paper and cellophane are two of the most widely used forms of cellulose for applications in

paper, packaging, and textiles. Kraft paper in particular has very poor gas and water barrier properties compared to other types of polymeric materials, as well as a high tensile strength (**Appendix 1: Tables S1.4 and S1.5**). Furthermore, the abundance of hydroxyl groups along the cellulose chain allows facile modification of the polymer to create a wide array of derivatives with tailorable properties as seen in **Figure 1.1**. Many of these cellulose derivatives retain the excellent properties of native cellulose such as being biodegradable and biocompatible, while adding additional benefits such as antibacterial properties, flame retardancy, and water solubility.¹³ Water-soluble cellulose derivatives such as commercially available methyl cellulose (MC), hydroxypropyl cellulose (HPC), dialdehyde cellulose (DAC), and sodium cellulose sulfate (NaCS) are of particular interest, as they can be processed under more environmentally friendly conditions. Thanks to their excellent gel-forming properties, these polymers are now well-used in the fabrication of coatings, composites, films, and membranes.¹³

NaCS in particular is interesting due to its high tensile strength in the wet state, its moldability *in situ*, as well as its relatively simple and cost-efficient production, and biocompatibility.¹⁴⁻¹⁶ Recently, even novel edible films for packaging using NaCS and glycerol were developed, fabricated *via* solvent-casting techniques, demonstrating that NaCS could be used as potential degradable coating materials for food packaging.¹⁶ These dense NaCS films formed with an ordered microstructure and were transparent, flexible, and resistant to oils and fats, but not to water.¹⁶ NaCS is also a negatively charged polymer, which can allow it to be assembled into complex structures *via* electrostatic interactions with a polycation, as seen in Chapter 2. Unlike NaCS, HPC is uncharged but has alkyl spacing groups terminated with hydroxyl groups which

allows the polymer to be soluble in water at temperatures below its lower critical solution temperature of 45 °C; above this temperature the polymer entangles and becomes insoluble in water.¹⁷ The presence of the terminal hydroxyl groups could also allow this polymer to assemble into complex structures *via* hydrogen bonding as seen in Chapter 6. Lastly, DAC is an “opened” structured cellulose derivative formed *via* the periodate oxidation of cellulose. This polymer is insoluble in water at RT but solubilizes at elevated temperatures.¹⁸ The presence of aldehyde groups along the polymer chain can allow for the assembly of complex structures *via* hydrogen bonding, or the formation of an imine bond *via* a Schiff base reaction with a primary amine-containing compound, as shown in Chapter 6.

Another common derivative of cellulose is cellulose acetate (CA), formed by the acetylation of cellulose to produce cellulose triacetate (CTA). Lower degrees of substitution can be achieved by hydrolysis of CTA to form cellulose diacetate (CDA) which is acetone-soluble and cellulose monoacetate (CMA) which is water-soluble/dispersible. Commercially available cellulose acetate generally refers to cellulose diacetate with ~ 39 – 42 % acetyl content. CDA has been used since the 1980s in the textile industry, to make films, as contact lenses, and more recently to make superhydrophobic materials. This form of CA also has great film forming ability and mechanical properties. CTA has also been used frequently to prepare liquid crystal displays (LCDs) due to its great film forming properties.

1.2.2 Alginates

Another commonly used natural polymer is alginate (**Figure 1.2**) which is generally extracted from brown seaweed. Seaweeds are macroalgae which similarly to plants, consist of chlorophyll and photosynthesize to make their food. The relative abundance of the different pigments within seaweed results in 3 distinct groups: green seaweed (Chlorophyta), red seaweed (Rhodophyta), and brown seaweed (Phaeophyta). Seaweed is mainly grown and harvested in Asian countries, for use as food, in cosmetics, pharmaceuticals, healthcare, etc. and are mainly constituted of water, up to 85 % of their bodies. They also contain a large percentage of carbohydrates (e.g., alginates, agar, carrageenan, cellulose), proteins, minerals, phenolic compounds, and a small amount of lipids. At present, there are many large unwanted blooms of brown seaweed polluting many Caribbean beaches, which can serve as a raw material for the extraction of these high-valued polysaccharides. While efforts have been made to valorize this waste brown seaweed, for example, for use as fertilizers, packaging, energy and to extract the alginate for use in heavy metal sequestration, there is still more research to be done.

The chemical structure of sodium alginate is shown in **Figure 1.2**, where similar to cellulose the alginate polymer is made up of repeating units of sugars. Here the sugars are mannuronic acid and guluronic acid (instead of glucose) which both have carboxylic acid groups which at neutral pH are deprotonated rendering the polymer negatively charged. These carboxylate anions can complex with metal ions such as calcium to form a hydrogel, or with heavy metals allowing the polymer to be used for heavy metal sequestration for wastewater treatment. Other

common applications of sodium alginate include use as a gelling agent in food, cosmetics and drugs and blending with other compounds to make packaging materials.

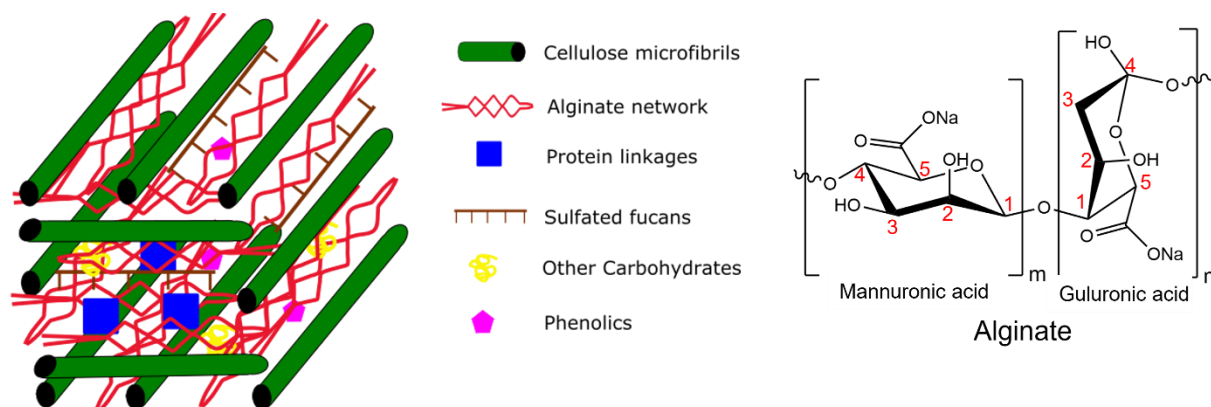


Figure 1.2 Schematic of the structure and components of brown seaweed, and the chemical structure of sodium alginate (adapted from reference ¹⁹).

1.3 Azo dyes

One of the most ubiquitous photo-switches is azobenzene, and its large family of azobenzene-based (azo) dyes, which can isomerize between the E and Z (*trans* and *cis*) stereoisomers upon irradiation (**Figure 1.3**). In other words, photo-isomerization occurs, meaning that the molecule's physical and/or chemical properties can also change significantly upon photo-irradiation. This can occur through a change in E-Z isomerization, through the rotation around the $-N=N-$ bond.²⁰⁻²³ Azobenzenes in general prefer the E-configuration due to its increased stability and lower energy;

therefore, it is presumed at equilibrium in the dark without irradiation that the azobenzene is almost exclusively the E isomer. However, this is not always the case. It should be noted that the Z isomer can be converted back to the E isomer through both photo- and thermal isomerization pathways, so at room temperature a sufficient time is also required to permit remaining *cis* to return back to *trans*, even in the dark (**Figure 1.3**).²³ Isomerization of azobenzene causes large structural changes to the molecule, from a planar nonpolar structure (E) to a polar twisted confirmation (Z). Additionally, para positions of the phenyl rings become 3.5 Å closer upon irradiation.²⁴

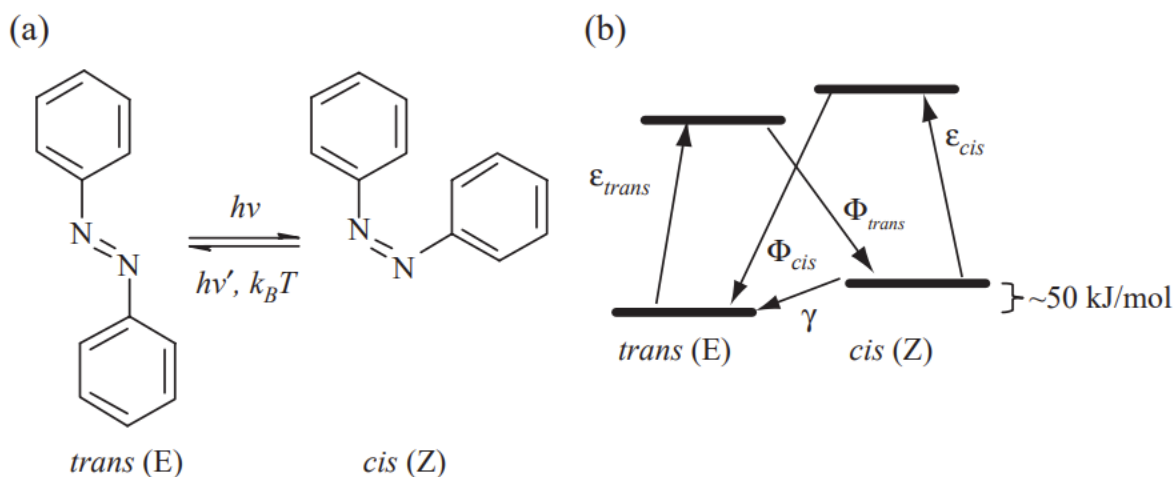


Figure 1.3 (a) Azobenzene can convert between *trans* and *cis* states photochemically, and relaxes to the more stable *trans* state thermally. (b) Simplified state model for azobenzenes. The *trans* and *cis* extinction coefficients are denoted ϵ_{trans} and ϵ_{cis} . The Φ refers to quantum yields of photoisomerization, and γ is the thermal relaxation rate constant (reproduced from reference ²³).

1.3.1 Classes of azo dyes

Since its discovery in 1834, many derivatives and classes of azobenzene-based molecules have been developed.²⁰ Azobenzene derivatives are known to exhibit a characteristic absorption band in their UV-Vis absorption spectra which originates from the $\pi \rightarrow \pi^*$ transition of the azobenzene chromophore. Changing the substituents on the aromatic rings drastically changes the optical properties of azobenzene, giving one the ability to ‘tune’ specific properties such as the *cis* half-life or UV-Vis absorption profile,^{20,21} creating entirely different spectral classes of azo molecules. One can classify these molecules into three spectroscopic classes: azobenzene-type, aminoazobenzene-type, and pseudo-stilbene-type (**Figure 1.4**), based on the ordering of their electronic states, and associated predictive colour and isomerization behaviour. Each class follows different spectroscopic ‘rules’, for instance: azobenzene-type dyes are prominently yellow, while the other two classes are orange, and red respectively.

Azobenzene-type molecules display a low intensity $n \rightarrow \pi^*$ transition activated in the visible region (~ 460 nm), and a higher intensity $\pi \rightarrow \pi^*$ transition with a maximum absorption in the UV region (~ 350 nm) (**Figure 1.4**). When azobenzene contains an electron donating group substituted on a phenyl ring, such as $-\text{NH}_2$ (aminoazobenzene), the $n \rightarrow \pi^*$ and $\pi \rightarrow \pi^*$ transitions appear closer together with their absorbance bands sometimes overlapping in the near visible UV region (~ 400 nm), due to an increase in the π orbital energy and a decrease in the π^* orbital (**Figure 1.4**). Conversely, pseudo-stilbenes have both electron donating and electron withdrawing groups in the 4 and 4’ positions of the two rings resulting in an asymmetric electron distribution

(‘push-pull’), causing inversion of $n \rightarrow \pi^*$ (higher energy) and $\pi \rightarrow \pi^*$ (lower energy) absorption bands with respect to non-substituted azobenzene (**Figure 1.4**), leading to a deep red colour.

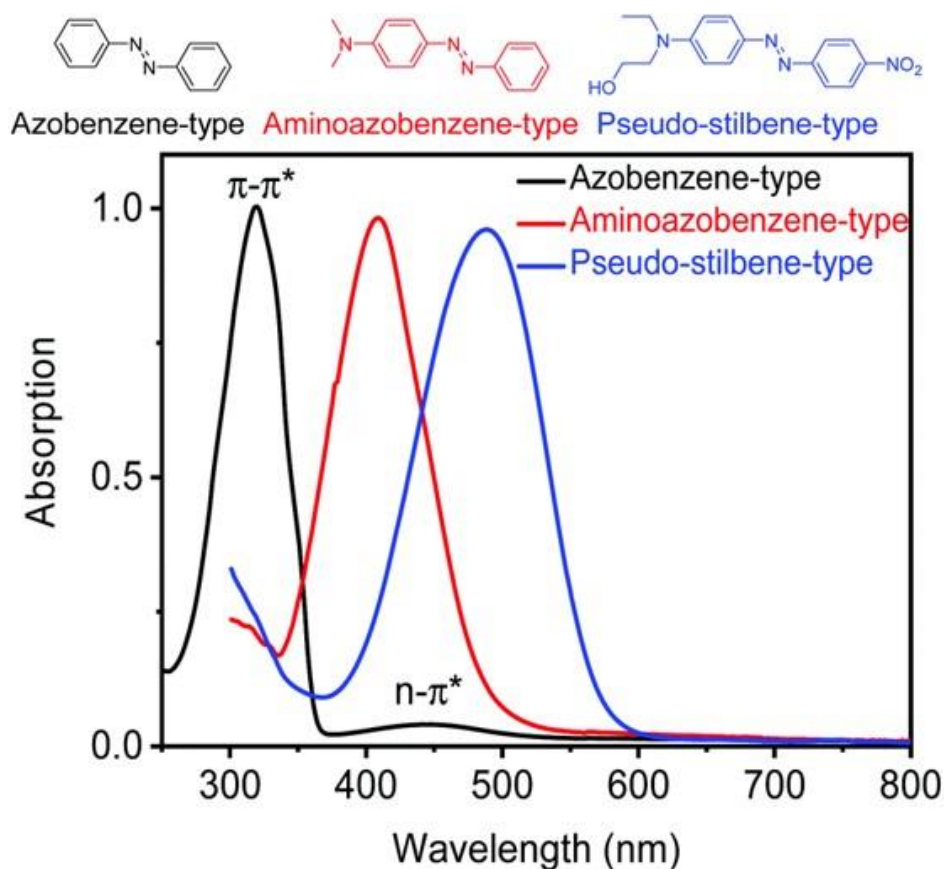


Figure 1.4 UV-Vis spectra of the 3 classes of azo dyes: azobenzene-type, aminoazobenzene-type, and pseudo-stilbene-type (reproduced from reference ²⁵).

Often, a single photo-switch is not enough to enable complex control of a photo-reversible material. Molecules containing more than one azo unit can be termed as oligoazobenzene

molecules, with those containing two azo units per molecule termed as bis-azobenzenes (bis-azos). Having two azo units (N=N bond) per molecule allows for higher loading of azo units in the material without aggregation, and provides a larger volume change upon isomerization.²⁵⁻²⁷ For bis-azos the individual azo units can be connected in meta (*m*-), ortho (*o*-) or para (*p*-) orientation to one another (**Figure 1.5**). Recent work by Boumrifak and colleagues showed that for *m*-bis-azos the individual units are decoupled and behave independently of each other, while interactions between the three rings were observed in *o*-bis-azos and *p*-bis-azos.²⁸

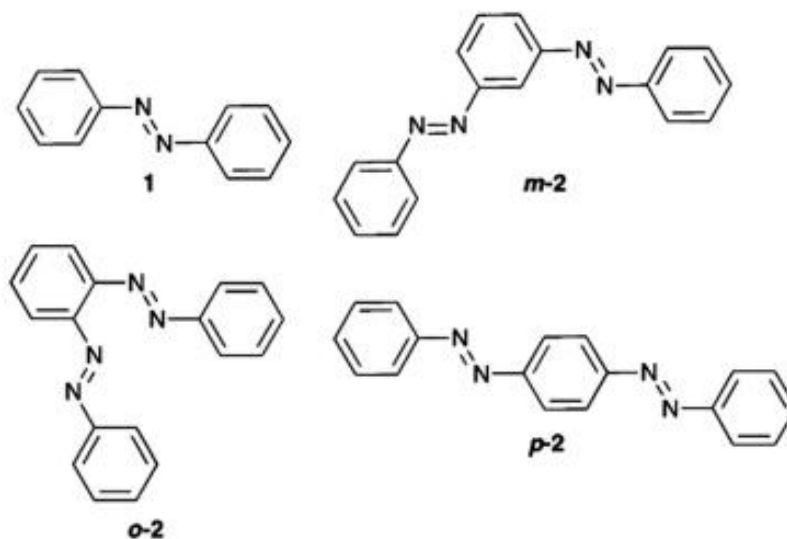


Figure 1.5 Structures of the investigated compounds, **1** – azobenzene; **o-2** – *o*-bis-azobenzene; **m-2** – *m*-bis-azobenzene; **p-2** – *p*-bis-azobenzene (reproduced from reference ²⁶).

1.3.2 *Trans-cis* isomerization

The photo-isomerization of the three spectroscopic classes of azobenzenes, as well as to a limited extent also bis-azos, have been studied in detail both experimentally and computationally. Generally, the *trans* isomer of azo dyes is more stable than the *cis* isomer, and conversion between the two isomeric forms can be achieved *via* the absorption of a photon of light.²² Due to the *cis* isomer being at a higher energy than the *trans* isomer, thermal relaxation from the *cis*-to-*trans* states occurs in the dark. The kinetics of the *cis* decay of azo dyes in solution generally follows a monoexponential decay (**Figure 1.6**), and the rate constant of the thermal relaxation process is affected by the substituents on the aromatic rings.

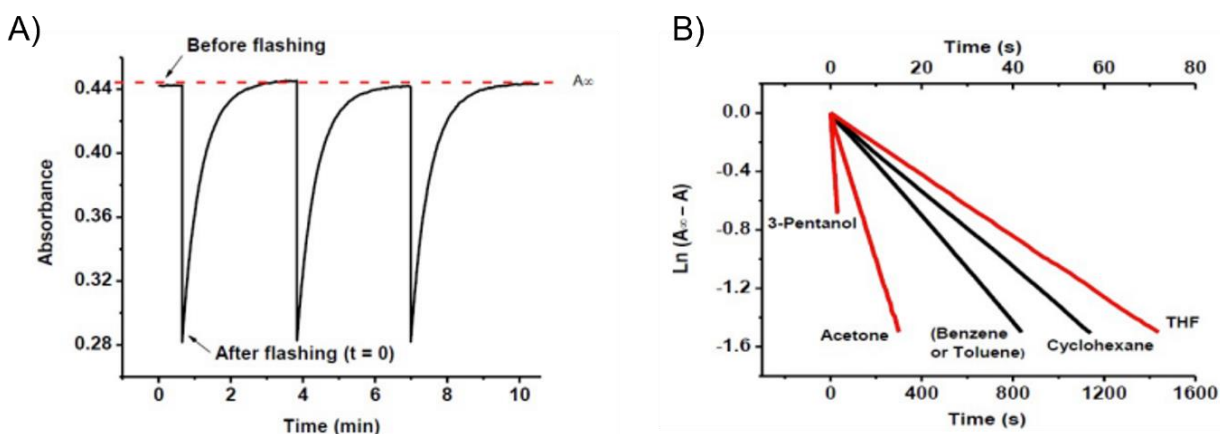


Figure 1.6 A) Plot of the change in absorbance vs. time for 4A4NAB in THF at 30 °C before and after 3 flashes of light are applied to the same solution. B) Plot of $\ln(A_{\infty}-A)$ vs. time for 4A4NAB in different solvents at 25 °C. The red lines for 3-pentanol, acetone, and tetrahydrofuran follow the time scale of the upper x-axis. Only the initial linear portion of these plots is shown (reproduced from reference ²⁹).

Generally, the timescale of the *cis* lifetime of azo compounds is as follows: azobenzene-type (hours), aminoazobenzene-type (seconds), and pseudo-stilbene-type (milliseconds).²² Furthermore, in the case of substituted azo dyes the kinetics of the thermal relaxation of the *cis* isomer is highly dependent on the properties of the solvent.

It is also well known that the local environment of the azo molecule influences the isomerization process. Generally, the *cis* decay of substituted azo dyes, *e.g.*, 4-anilino-4'-nitroazobenzene, 4-aminoazobenzene, Methyl Orange, or Disperse Orange 1, is faster in polar solvents compared to non-polar solvents, as shown in **Figure 1.6b**.²⁹⁻³¹ This is contrary to unsubstituted azobenzenes, where it is generally observed that the rate of the thermal relaxation is independent of the solvent. The differences in the effect of the solvent on the rate constants were shown to be related to the mechanism of the isomerization process.³² Two isomerization mechanisms are typically discussed for azobenzenes: (i) in-plane inversion where one N=N-C angle increases to 180° while the C-N=N-C dihedral angle remains at 0°, and (ii) rotation where torsion around the N=N bond results in a change of the C-N=N-C dihedral angle to 120°.²⁶ A combination of the two processes together has also been reported. Generally, the rotation pathway results in a more polar transition state whose energy can be affected by the surrounding solvent molecules.²⁶

While there have been many reports published on the isomerization of monoazo dyes in solution, much less research exists for bis-azo dyes. Most of the previous research reported on bis-azos in solution has focused on unsubstituted bisazobenzene and has been limited to organic solvents. The timescale of the *cis* decay of unsubstituted bis-azobenzene is greatly affected by the

type of connection between the 3 aromatic rings; *o*-bis-azobenzene (milliseconds), *m*-bis-azobenzene (days) and *p*-bis-azobenzene (hours).²⁶ There have also been a few studies on the kinetics of substituted bisazos. Here, depending on the connection and substituents on the rings, a good fit to either a monoexponential or biexponential model could be observed. For *o*-bis-azo dyes with amino and/or acetamido groups it was observed that the *cis* thermal relaxation was decoupled and proceeded independently for each unit of different timescales.²⁸ The thermal relaxation was fit to a monoexponential decay for the symmetric bis-azo, with a half-life on the millisecond time scale.²⁸ For the asymmetric bis-azo a biexponential fit was used with timescales like that of the monomeric counterparts.²⁸ Robertus and colleagues studied the kinetics of an asymmetric *m*-bis-azo with one ring having a trimethyl-ester based substituent.³³ Both flash photolysis and H-NMR were utilized to observe the kinetics, where the decay was observed to be biexponential.³³ Throughout this Thesis the behaviour of a commonly used commercial bis-azo dye, Bismarck Brown Y (BBY), was investigated for the first time by means of flash photolysis (pump-probe experiments) and confocal Raman spectroscopy.

Since the isomerization of azo and bis-azo dyes results in large structural molecular changes, they are commonly doped into a polymer matrix or grafted onto polymer chains to try and create larger-scale photo-reversible materials for a wide variety of applications. These include medicinal purposes *via* the photo-driven assembly/disassembly, to fabricate surface relief holographic gratings, or photo-actuators, for photo-alignment directors, and as humidity-driven or -sensing devices.³⁴⁻³⁸ These azo dyes once embedded into/onto these polymers behave differently than they would surrounded by other azo molecules in solution.³⁹⁻⁴² Many of these azo/polymer

materials that have been previously studied involved the use of the monoazo dyes such as Disperse Red 1 (DR1) which is a pseudo-stilbene-type molecule, and petrol-based polymers such as polyacrylic acid (PAA) and poly methyl methacrylate (PMMA).³⁹⁻⁴¹ Generally, the thermal relaxation of azo dyes follows first-order kinetics and fits well to a monoexponential model, which will be discussed in more detail in **Section 1.3.3**. However, when grafted onto a polymer, the *cis* decay of the azo molecule can be affected.

The earliest reports of the kinetics of thermal back relaxation of azobenzenes attached as polymeric side chains were in 1972 by Morawetz and Paik, where a monoexponential decay was observed for polymers in solution and in bulk above T_g , but an anomalous fast relaxation component was seen in the glassy state, and ascribed to the relaxation of azo groups trapped in a strained conformation.⁴³ Relaxation curves for these azo-grafted polymers have been fit previously with biphasic decay or Williams-Watts function which models a continuous distribution of relaxation rates reflecting the inhomogeneity of free volume at the strained sites.⁴³ This work was later expanded on by Barrett and colleagues who examined the kinetics of DR1 attached as polymeric side chains, as copolymers and blends cast as films.³⁹⁻⁴¹ They observed that the kinetics were highly dependent on the type of chromophore and type of attachment to the polymer backbone. A biexponential decay was observed for the *cis* \rightarrow *trans* isomerization of azos bound in the side chain of copolymers and blends, above a certain mol ratio of azo.^{39, 40}

Norman and Barrett looked at the kinetics of thermal relaxation of DR1 grafted onto a copolymer, poly (DR1A-co-AA) at various mol ratios dissolved in THF/H₂O co-solvent.⁴¹ DR1, which has good solubility in THF followed a monoexponential decay, however upon addition of

small amounts of water, which is a poor solvent for DR1, the kinetics followed a biexponential decay.⁴¹ As it relates to bis-azos in polymeric matrices, there are very few studies. Vapaavouri and colleagues studied the behaviour of the *p*- and *m*- bis-azo dyes Disperse Yellow 7: *p*-DY7 and *m*-DY7 in solution and when embedded in a poly(4-vinylpyridine) (P4VP) polymer matrix. The *cis* half-life was measured to be on the timescale of minutes, and was observed to be relatively shorter for the dyes when incorporated into solid state films.⁴⁴

1.3.3 Spectroscopic techniques and principles of azo dyes

Many different spectroscopic techniques have been used historically to characterize azo dyes, to observe the *trans-cis* photo-isomerization in real time, and to measure the kinetics of the *cis* thermal relaxation. The main technique utilized is UV-Vis spectroscopy since all azo dyes have the signature azo unit ($-N=N-$ bond) which has a strong absorption in the UV-Vis region. To initiate the conversion from the *trans* to *cis* isomer and observe the *cis* decay of azo dyes, generally pump-probe experiments are used. For fast-switching azo dyes, on the timescale of seconds-milliseconds, a high-powered laser is generally used as the pump beam to briefly trigger photo-isomerization of azo dyes, while a low powered probe beam is used to monitor the change in the concentration of the *trans*-azo dyes before, during and after irradiation. Despite the high sensitivity of this technique, the major drawback is that the set-up requires expensive lasers and associated fast-spectroscopy optical components (shutters, etc.), and lock-in amplifiers to capture and process the fast spectral changes.

A more simplified pump-probe experiment is also commonly used, for slow-switching azo dyes on the timescale of minutes-days. This set-up uses a standard UV-Vis spectrophotometer to produce a continuous probe beam, while the pump beam can be a low powered LED or lamp, irradiating from above over a long time, or even separately, with the sample replaced in the spectrophotometer just before decay measurements are collected (**Figure 1.7**).

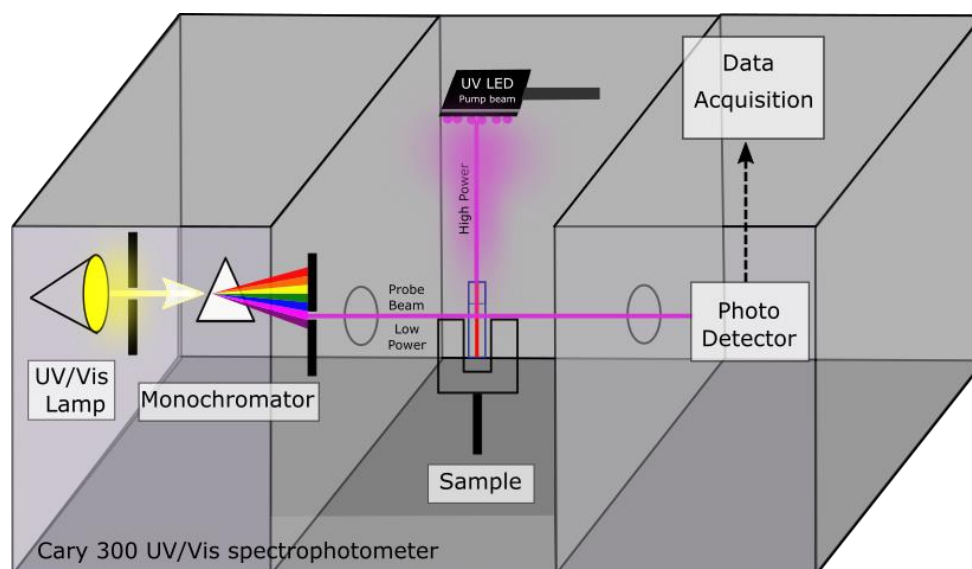


Figure 1.7 Schematic of a simplified pump-probe experimental set up using a UV-Vis spectrometer (probe) and LED (pump) to determine the thermal *cis-to-trans* relaxation rate behaviour of azo dyes.

Both set-ups can be used to measure the isomerization of azo dyes in solution and the solid-state, such as dyes embedded in thin films. Pump-probe experiments using high powered lasers

were used for the research conducted and described in Chapters 2 and 3 of this Thesis to monitor the *trans-cis* isomerization of the faster BBY azo dye, while the more simplified pump-probe experiment using a UV-Vis spectrophotometer was employed for the analysis described in Chapter 5. Other techniques which are used (less frequently) to monitor the *trans-cis* isomerization of azo dyes are NMR spectroscopy, Raman spectroscopy and IR spectroscopy. Compared to these spectroscopies, UV-Vis spectroscopy has the advantage of being a cheap, facile, and quick technique, widely available.

The principle of Ultraviolet/ Visible (UV-Vis) spectroscopy involves the absorption of a photon of light by a molecule, which promotes an electron from the ground state to an excited state. Molecules can have ground state electrons in various orbitals such as the sigma (σ) or pi (π) orbitals or also non-bonding orbitals (n). The absorption of a photon of light can excite an electron from these lower energy levels to higher energy levels (σ^* , π^* and n^*).⁴⁵ Depending on the gap between these energy levels, different wavelengths of light are absorbed, and thus azo dyes with different energy states appear as different colours. **Figure 1.8** shows the molecular orbital diagram for azobenzene.⁴⁵ For azo dyes in particular, the $n\text{-}\pi^*$ and $\pi\text{-}\pi^*$ transitions are of greatest interest, and depending on the wavelengths of these bands in the UV-Vis spectrum, absorption of photons of different energies can result in photo-induced isomerization from *trans*-to-*cis* or *vice versa*, which can be observed by monitoring an increase or decrease in the absorbance at specific wavelengths in the UV-Vis spectrum.

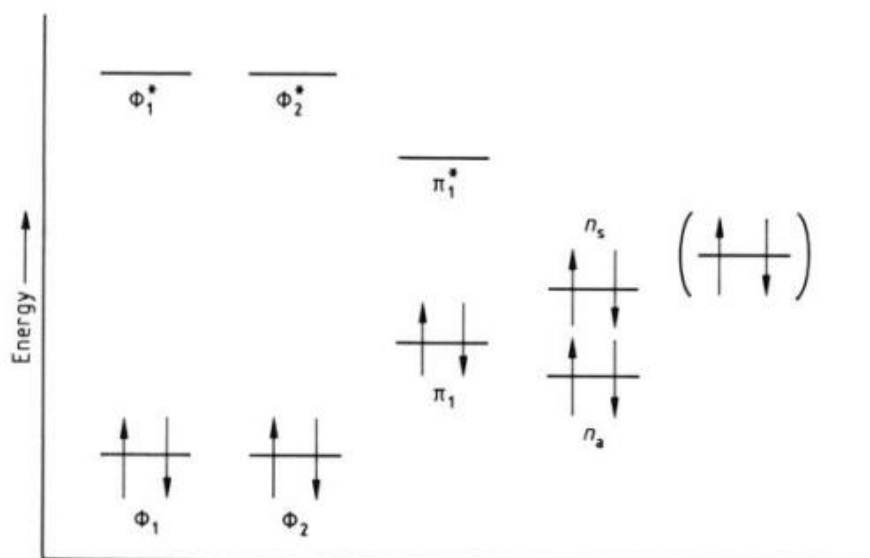


Figure 1.8 The molecular orbital diagram for azobenzene, including the three highest occupied, three lowest unoccupied, and the nonbonding orbitals of the nitrogen lone pairs (reproduced from reference ⁴⁵).

Additionally, depending on the local environment of the azo dye, for example the type of solvent (polarity and proticity) which can result in dimerization association of the azo dyes, a shift in the absorbance band or the appearance of a shoulder can be observed as an indication of intermolecular interactions within the dye-solvent system. According to Lambert-Beer's law (**Equation 1**) the absorbance of the azo dye is directly proportional to the concentration of the species in solution, which initially in the dark is predominantly the *trans* isomer.

$$A = \varepsilon c l \quad (1)$$

Where A is the absorbance, ε is the extinction coefficient of the azo dye, l is the pathlength of the cuvette or glass slide and c is the concentration of the species. By combining Beer's law and the rules of integrated rate laws for first order kinetics,^{40, 43} the kinetics of the *cis* decay of azos can be most easily analyzed. For a first order *cis* \rightarrow *trans* thermal isomerization:

$$\text{Rate} = \frac{d [\textit{trans}]}{dt} = - \frac{d[\textit{cis}]}{dt} = k [\textit{cis}] \quad (2)$$

where $[\textit{trans}]$ and $[\textit{cis}]$ are the concentrations of the *trans* and *cis* isomers, respectively at any time t , and k is the first order rate constant. The rate constant, k , for a monoexponential relaxation curve can be determined from the time dependent absorbance A_t , absorbance immediately after pumping A_0 , and absorbance at infinite time, i.e., complete relaxation back to *trans* A_∞ , using the equation:

$$(A_\infty - A_t) = (A_\infty - A_0)e^{-kt} \quad (3)$$

A plot of $\ln (A_\infty - A_t)$ vs. t should be linear with a slope of $-k$. For samples which deviate from first order kinetics, the experimental A_t relaxation curves were fit to the biexponential equation with 4 fitting parameters:

$$(A_\infty - A_t) = Ae^{-k_a t} + Be^{-k_b t} \quad (4)$$

Like the first-order kinetics, A_∞ and A_t are the absorbance at infinite time and the time dependent absorbance after the pump beam is switched off, respectively. A and B are the relative weighting coefficients, and normalization of these values gives the relative contributions associated with the

processes having rate constants k_a and k_b , respectively. A residual plot and a least-squared fit demonstrated the appropriateness of the biexponential fitting. The lifetime of the *cis* isomer τ , was calculated using **Equation (5)**, where k is the rate constant:

$$\tau = \frac{1}{k} \quad (5)$$

Another important equation for azo dyes is the Arrhenius equation (**Equation 6**). If the rate constant of the *cis* decay of the azo dye is measured at different temperatures, the activation energy, E_a , can be tabulated from the slope of the plot $\ln k$ vs. $1/T$, according to Arrhenius equation shown below:

$$k = A_{rr} e^{-E_a/RT} \quad (6)$$

where k is the rate constant of a first order reaction in this case (s^{-1}), A_{rr} is the pre-exponential factor (s^{-1}), E_a is the activation energy (kJ/mol), R is the universal gas constant ($8.314 \text{ JK}^{-1}\text{mol}^{-1}$) and equal to the product of Avogadro's number and Boltzmann constant, and T is the absolute temperature (K).

1.3.4 DFT modeling of *trans-cis* isomerization of azo dyes

Density functional theory (DFT) is a computational quantum mechanical modeling method which has proven excellent for determining the electronic structure, and thus geometries and interconversions of many-body systems such as isomerizing azo molecules.^{46, 47} It is a powerful

technique that was used in this Thesis to predict the ground states and isomerization pathway of a commercial azo dye, BBY, and to estimate the kinetics and mechanism of the *cis-trans* thermal back relaxation. As easily seen throughout the literature, the opportunity to collaborate with computational modeling experts, and their computations, including DFT and molecular dynamics methods, has allowed experimental researchers to gain a much better understanding of the mechanisms and kinetics of many of their systems studied, such as the basic isomerization process of some of the azo dyes described in this Thesis.^{26, 28, 30, 32, 33, 48, 49}

As a general introductory overview to the computational methods that were employed in Chapter 3, working with our Theoretical Chemistry collaborators, the starting point for this computational chemistry is *ab initio* calculations. For the DFT level of theory, the Kohn-Sham equation is the non-interacting Schrödinger equation or Schrödinger-like equations of approximate systems of non-interacting particles, such as electrons, which generate a similar density to a given system of interacting particles.^{46, 50} The *ab initio* method can be used to calculate different variables such as the molecular geometries, energies, vibrational frequencies, dipole moments, and electron distributions, to name a few. For *ab initio* calculations functionals are used to determine the properties of many-electron systems, that is they describe the function of another function, splitting the energy of the system into several more manageable parts.⁵⁰ The functionals used in Chapter 3 of this thesis were B3LYP, which is a common exchange-correlation functional, well suited to molecules of our size, composition, and behaviour.^{47, 50} The basis set used was the def2-TVZP (triple-split-valence with polarization) basis set, which is one of the Karlsruhe basis sets.^{47, 50} A basis set is “a set of mathematical functions (basis functions), linear combinations of which

approximate molecular orbitals.” “Usually, several basis functions describe the electron distribution around an atom, and combining atomic basis functions yields the electron distribution in the molecule as a whole.”⁵⁰ The def2 basis sets are appealing because they are accurate across much of the periodic table and are available for all elements up to Radon, which is not true for the more common basis sets from Pople and Dunning.⁴⁷ There has been good previous literature of DFT modeling used alongside experiments to acquire theoretical isomerization models of a variety of azo dyes.^{30, 32, 48, 49, 51, 52} Generally, researchers have been able to evaluate the bond length and angle associated with the isomerization of the azo bond and of neighbouring atoms (C–N=N–C) to understand the mechanism of isomerization in more detail, especially since these pico-second (or faster) steps of the overall conversion process are too fast to be able to be observed experimentally.^{30, 49, 51, 52} More discussion of the DFT computational modeling parameters employed is provided in Chapter 3, alongside the results obtained, where there is more appropriate context for explanation.

1.4 Supramolecular chemistry

Supramolecular chemistry is the use of intermolecular forces to form self-assembled networks between molecules. It focuses on weaker interactions beyond the covalent bond, relying on weak interactions between molecules rather than bonds within a molecule. These ‘intermolecular’ bonds can be held together by forces such as ionic interactions, hydrogen bonding, halogen bonding, host-guest interactions, metal coordination, hydrophobic interactions, van der Waals forces, and

π - π interactions.⁵³ These weaker interactions have multiple advantages, most importantly their ability to self-assemble. This ease of synthesis gives some great advantage over traditional chemistry, and ideally the development of new supramolecular materials might help to make intensive and costly organic synthesis an approach of the past. The self-assembly method of supramolecular chemistry also follows a bottom-up approach, inspired by Mother Nature, so if one adopts this approach, one can also mimic the elegant and complex nano-structural control of materials created in nature, which in many ways surpass the materials created by today's engineers. These forces are ubiquitous and when utilized can form hierarchy structures, leading to unique properties such as self-healing, increased strength, increased toughness, and reversible binding. Due to the rich variety of different intermolecular forces, a vast array of materials can be designed to have varying strength or reversibility of bonding depending on the forces used.⁵³

1.4.1 Types of intermolecular interactions

Table 1.1 summarizes the characteristics of the different non-covalent interactions. The strongest non-covalent forces are ionic interactions forming salts.⁵³ These salts are held together by oppositely charged ions (positive and negative), and salts can be considered a full charge transfer, while the sharing of a proton leads to hydrogen bonding. Hydrogen bonds, similar to ionic bonds, are formed through attractive forces between two polar (oppositely partially charged) groups, which form the hydrogen bond between an electron donor and an electron acceptor.⁵⁴

Type of interaction	Strength [kJ mol ⁻¹]	Range	Character
van der Waals	51	short	non-selective, non-directional
H-bonding	5–65	short	selective, directional
coordination binding	50–200	short	directional
“fit interaction”	10–100	short	very selective
“amphiphilic”	5–50	short	non-selective
ionic	50–250 [a]	long	non-selective
covalent	350	short	irreversible

[a] Dependent on solvent and ion solution; data are for organic media.

Table 1.1 Characteristics of various soft bonds (reproduced from reference ⁵³).

The ‘cousin’ of hydrogen bonding is halogen bonding, working in a similar fashion. The halogen bond has the advantage of high directionality and easily tunable strength.⁵⁵ Another useful soft interaction is formed through π - π stacking, which involves orbital overlap of aromatic molecules, and is widely considered one of the weaker interactions. Despite this, π - π stacking is important due to the increased stability it gives a material.⁵⁶ Another widely used non-covalent interaction is the host-guest interaction, involving the association of the guest moiety into the host system, which can be especially dynamic and reversible.⁵⁷

In the following overview multiple materials will be discussed using a wide range of supramolecular chemistry interactions. Importantly, and of great relevance to this Thesis, weak non-covalent bonds can permit supramolecular materials to be responsive to external stimuli. This

can be in the form of mechanical response such as bending, or in the form of reversible binding, such as self-healing, or assembly/disassembly in response to external stimuli. These stimuli can be in the form of pH, heat, humidity, or light, for example. Of these forms of stimuli, light is a preferred method since it isn't reliant on solvent, can generate a response within nanoseconds or faster, can be highly localized in space, and can be removed with ease. Additionally, visible wavelengths of light can be used non-invasively and non-destructively for *in vivo* studies of living cells, tissues, or organisms. Photo-stimulus has been used as a driving force to cause mechanical response,^{58, 59} on-off birefringence,^{23, 60} drug delivery,^{35, 61, 62} as well as other effects. Soft bonding interactions are of particular interest, such as electrostatic interactions and hydrogen bonding, which are both reversible and directional (**Table 1.1**).⁵³ This allows more complex systems to easily assemble and later gently and reversibly disassemble when introduced to a particular stimulus, such as pH, temperature, or salt, without breaking the covalent bonds.⁶³

1.4.2 Layer-by-layer (LbL) assembly

One method commonly used to develop soft-bonded stimuli-responsive materials is layer-by-layer (LbL) self-assembly. LbL assembly involves the sequential adsorption of alternating layers of charged polymers/molecules from aqueous solution onto a substrate *via* an alternating dipping process (**Figure 1.9**).⁶⁴ LbL assembly offers many advantages compared to other forms of film production such as solvent casting, drop casting, and spin-coating; these include increased reproducibility, ease of automated fabrication, and a more homogenous dispersion of the materials resulting in more uniform coatings.⁶³ This technique generally involves the alternate combination

of two oppositely-charged water-soluble components, through successive absorption and over-compensation of charge, reversing the zeta potential of the growing multilayer surface, which results in a water-resistant film of controlled thickness and properties. Material layers are linked to each other in the LbL films through soft, weak attractive forces such as ionic bonding, and hydrogen bonding. If at least one component is a polymer, this increases the number of linkages between the layers, which renders the entire material remarkably stable to re-dissolution and re-conformation, even after long times and high temperatures.

For electrostatically-bonded LbL films, common polyanions include poly(acrylic acid) (PAA) and hyaluronic acid (HA) which can be combined with polycations including poly(allylamine hydrochloride) (PAH) or poly-L-lysine (PLL), to fabricate polyelectrolyte multilayer (PEM) films that can be used as tunable extracellular matrix materials.⁶⁵ The thickness of these PEM films is affected by (i) molecular weight (MW) and concentration of polymer, (ii) pH of the dipping solutions, (iii) ionic strength, and (iv) temperature. Generally, the thickness of PEM films can range from few nanometers to micrometers or more. Atomic force microscopy (AFM) was used as a robust and facile technique to measure the thickness of the PEM coatings prepared, adjacent to a scratch or a step-edge from the deposited soft polymer layers to the hard silicon (or glass) substrate below. This height difference along the boundary edge of the PEM film was used to estimate the thickness of the films, and also provides the advantage of capturing a 2D image of the topography and roughness of the PEM coating, if existing. The AFM mode used in these experiments was tapping mode, whereby the gently oscillating AFM tip comes into contact with the material, changing the amplitude of the oscillating and cantilever deflection which then relays

a signal back to the instrument to adjust its z position, and obtain sensitive information of height and topography.

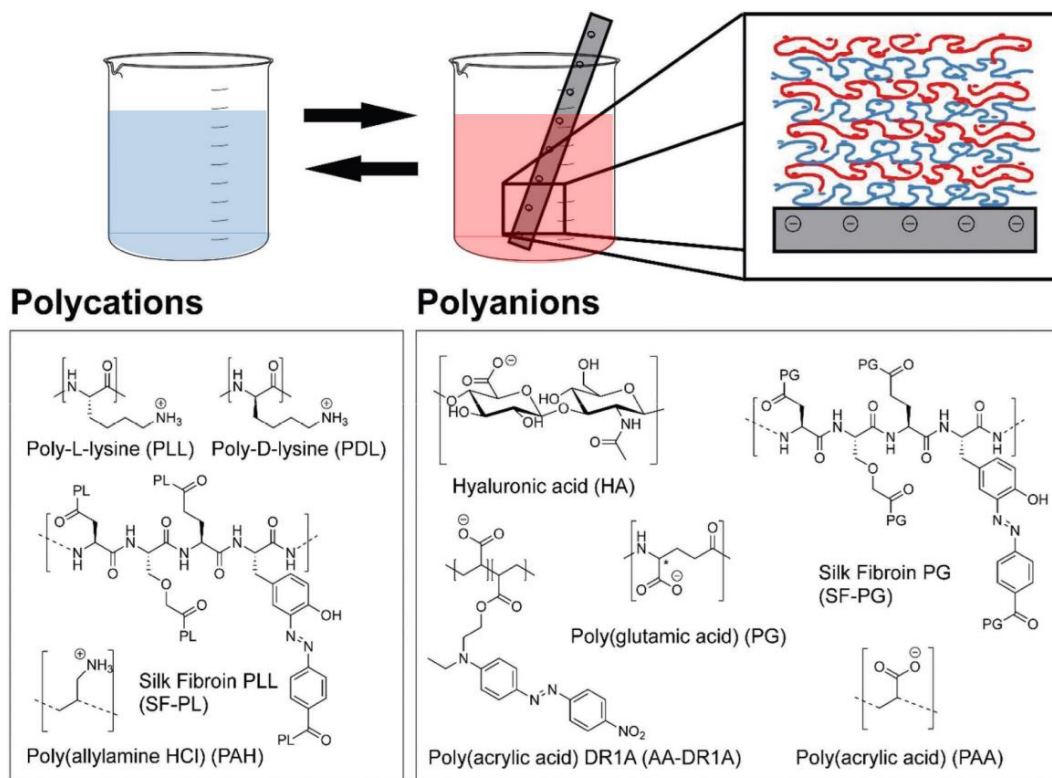


Figure 1.9 Top: Schematic depicting layer-by-layer assembly of PEM films, beginning with a negatively charged substrate (glass or silicon) being dipped in a polycation solution. Bottom: Illustration of biologically relevant polycationic and polyanionic polymers used in this study and others from our Group, and their acronyms (adapted from reference ⁶⁵).

Figure 1.9 shows a schematic of the dipping process used to fabricate these multilayered PEM films and the polycations (which all contain a (+) charged ammonium group) and polyanions

(which contain a (-) charged carboxylate anion group) used in the fabrication process. In addition to common synthetic polymers such as PAA and PAH, **Figure 1.9** also depicts the structures of more natural polymers that can be employed for the LbL process, such as Poly-L- and D-lysine (PLL and PDL), silk fibroin (SF), hyaluronic acid (HA) and poly(glutamic acid) (PG), showing their potential to be used equally, and easily in preparing PEM films. For this Thesis research described, the polycations used were (+) charged azo dyes containing ammonium groups, while the polyanions were (-) charged natural polymers containing sulfate, and carboxylate groups.

Hydrogen bonding has been utilized to prepare a wide range of materials from LbL films consisting of two polymers, films consisting of a polymer and small molecules, and to make hollow capsules and coatings on beads as depicted in **Figure 1.10**. Early sets of hydrogen-bonded (HB) LbL films were commonly prepared using carboxylic acid-containing polymers such as PAA and poly(methacrylic acid) (PMAA), which allowed films to be used for the preparation of pH-sensitive materials.³⁴ More recently, hydrogen-bonded (HB) LbL films have involved polymers containing hydroxyl or amino groups for use as photo-chromic paper, gas barriers, and flame-retardant coatings.⁶⁶⁻⁷⁰ In this Thesis, the hydrogen-bonded PEMs were prepared using amino azo dyes and natural polymers containing hydroxyl, carbonyl, and carboxylic acid groups.

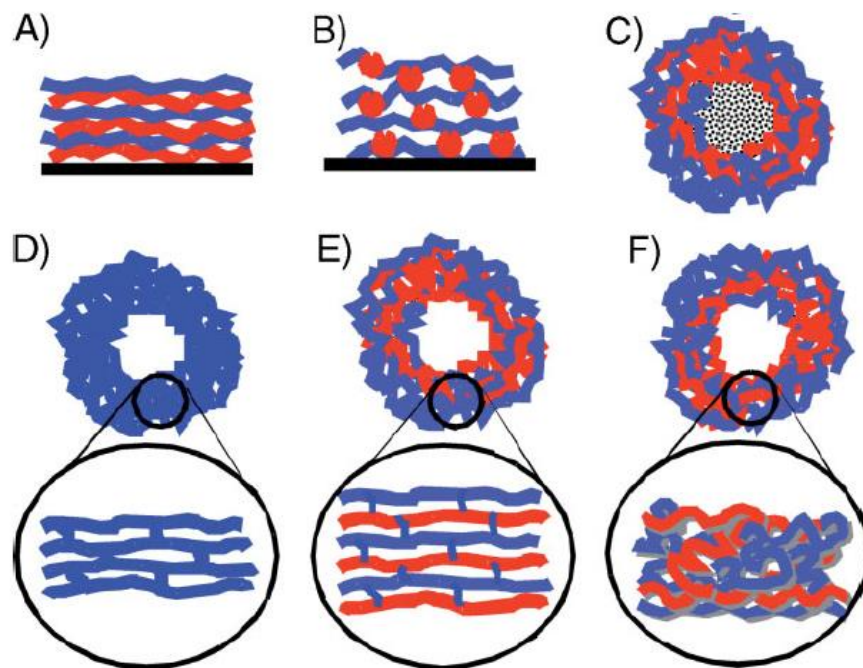


Figure 1.10 A variety of surface-templated HB polymer materials: HB polymer–polymer (A) and polymer–particle (B) films; core–shell (C), and hollow single-component (D), and two-component (E) hydrogel capsules; as well as hollow capsules, obtained by direct precipitation of HB IPC onto particulate substrates (F) (reproduced from reference ⁶³).

1.4.3 Other types of design methods

The other types of design methods used in this Thesis were solvent casting and electrospinning. Solvent casting involves mixing/homogenizing the sample in a ‘good’ solvent, pouring into a glass petri dish, and letting the solvent evaporate over time. Generally, the polarity and volatility of the

solvent and the concentration of the mixture affects the micro-assembly within the film and may not always be reproducible compared to a more controlled technique such as LbL assembly. Electrospinning is also a very useful technique to use when fabricating materials with very rough or ‘woven’ textured surfaces or fabrics, and/or to prepare hydrophobic/super-hydrophobic surfaces. This technique involves pumping a solution of the sample through a tube that feeds into a thin needle at which a high (-) charged voltage (generally - 10 to - 20 V) is applied as the sample is drawn onto a metallic drum that is (+) positively charge (generally + 10 to + 20 V) to create a mesh of fibers and globules depending on the flow rate, concentration of the solution, and volatility of the solvent.^{71, 72} The drawback with this technique is that it requires high voltages and a lot of troubleshooting to get the desired morphology, and is only amenable to certain polymers.

1.5 Photo-reversible soft-bonded azo/polymer complexes

Supramolecular materials containing azo dyes is an emerging and exciting new field, for varying applications such as optical sensors, and photo-mechanical bending of material to fashion light-driven micro robotics and molecular machines. Functional groups can be substituted onto the phenyl ring of azobenzenes making it suitable to form multiple different intermolecular bonds including hydrogen, electrostatic, and halogen, and then optimizing interactions for each application. Additionally, due to the aromaticity of the benzene groups, they can form π - π stacking with other aromatic molecules. Using such functional groups one can engineer a new range of materials, where the strength of the bond, as well as the rate of *cis* half-life, can be optimized to fit

the engineering purpose of the material.⁷³⁻⁷⁶ Limiting the materials described henceforth in essence to polymeric supramolecular azobenzene materials, these materials can be divided usefully into several application categories, including mechanical movement of films, optical sensors, assembly/disassembly of supramolecular polymers, and uptake and release into and out of host-guest interactions.

1.5.1 Design guidelines for soft-bonded systems

There are many design guidelines for the supramolecular assembly of soft-bonded complexes. These include hydrogen bonding, halogen bonding, electrostatic interactions, π - π stacking and metal co-ordination. In Chapters 2 – 4 of this Thesis electrostatic interactions were the main driving force for the PEM films that were fabricated, with hydrogen bonding, π - π stacking and hydrophobic effects as minor soft-bonding interactions present. In Chapter 5, covalent bonding was the main type of bonding utilized. The nature and strength of the different supramolecular interactions can affect different properties of these materials, which has been shown throughout the literature to be important for controlling the desired behaviour of azo/polymeric complexes.

Supramolecular self-assembled systems based on hydrogen bonding is one of the most frequently used soft-bonded systems due to the relatively strong, selective, and directional nature of the hydrogen bonds. Most hydrogen bonded systems are designed in such a way to ensure maximal bonding of the dye to the polymer chain. The most frequently used polymers in the synthesis of hydrogen bonded azo/polymer complexes throughout the literature have been

synthetic polymers consisting of a repeating pyridine backbone, which has a nitrogen with lone pairs capable of acting as a hydrogen bond acceptor.^{44, 74, 77–84} The most common of these polymers are poly(4-vinylpyridine) (P4VP)^{44, 74, 77, 79, 81–84} and its copolymer poly (4-vinylpyridine-co-styrene) (P4VP-co-PS)^{80, 85, 86}. The presence of this nitrogen atom on the polymer facilitates hydrogen bonding with groups such as hydroxyl groups (OH)^{44, 74, 77, 82–84} and carboxylic acids (COOH)^{79, 80, 87} attached to an azobenzene molecule. One of the most popular groups of azo dyes that have been hydrogen bonded with the aforementioned polymers is known as 4-(4-alkylphenylazo) phenols (PAPs) which contains a hydroxyl group (OH) as the substituent on the azobenzene molecule.^{74, 77} Other azo dyes that have been used to form hydrogen-bonded complexes with various polymers are azos containing pyridine (N),⁸⁸ amino groups (NH₂),⁸⁹ amide groups (NHCO),⁹⁰ and cyano groups (CN).⁸⁴ The other polymers which have been used to form hydrogen bonded complexes include polymers containing carbonyl groups (C=O) such as PMMA,^{89, 91} and cyano groups (CN).⁹² These hydrogen-bonded azo/polymer complexes have been used for a plethora of applications and will be discussed in more detail in the next sections.

Halogen bonding is emerging as a useful soft interaction in the production of supramolecular azo/polymer complexes. Features such as high directionality, tunable interaction strength, and donor atom size affect the assembly of these supramolecular systems. There appears to be fewer examples of systems prepared *via* halogen bonding,^{55, 81, 93} compared to hydrogen bonding. This could be because the synthesis of hydrogen bond containing azo dyes is easier or more well established compared to halogen containing azo dyes. The main polymer used to prepare these halogen-bonded complexes was P4VP which has a N atom in the pyridine ring acting as

halogen bond acceptor (**Figure 1.11**).^{55, 81, 93} On the other hand, ionic bonding is used as frequently as hydrogen bonding when fabricating these soft-bonded interactions compared to halogen bonding. In systems where both hydrogen bonding and ionic interactions occur, salt bridges can be formed which help to stabilize the system even more (**Figure 1.11**).

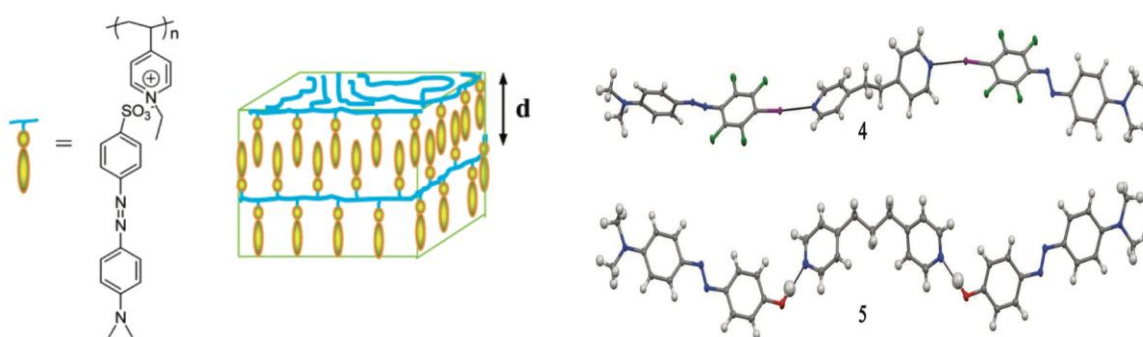


Figure 1.11 Example Figures for the design guidelines for soft-bonded azo systems. (Left) electrostatically bonded ethylated P4VP polymer and methyl orange azo dye (reproduced from reference ⁷⁵). (Right) Halogen and hydrogen bonded self-assembled azo dyes with bis-pyridine derivatives (reproduced from reference ⁵⁵).

Common polymers used to prepare these electrostatically self-assembled materials include PAH,^{94, 95} poly(diallyl dimethylammonium chloride) (PDADMAC),⁹⁶⁻⁹⁸ poly(dimethyl aminoethyl methacrylate) (PDM),⁹⁹ PAA,⁷⁶ PMMA,¹⁰⁰ methylated P4VP,^{60, 101, 102} ethylated P4VP,⁷⁵ poly(1-butyl-vinylpyridinium bromide),^{103, 104} and hyaluronic acid.⁹⁴ These poly(ionic liquids) can provide interesting optical properties due to liquid crystalline nature of the polymeric

matrix. Many of these polymers are coupled to water-soluble azo dyes which come as the salt version, with a negatively charged sulfonate group, for example Methyl Orange,^{60, 75, 101–104} Ethyl Orange,⁷⁸ Brilliant Yellow,⁷³ Niagara Blue⁹⁵ and Amaranth.¹⁰⁵ Since azo dyes contain 2 or more phenyl rings in their structure the occurrence of π - π interactions is very probable, especially at high concentrations of the dye and in a suitable solvent.^{56, 79} This particular interaction can occur across a very large scale and can help further stabilize systems based on the 3 aforementioned interactions. The last type of soft-bonding interaction is the host-guest systems. These also make use of other soft bonding interactions (hydrogen bond, hydrophobic interaction, etc.) to encapsulate the azo dye into the polymeric cavity which is generally a cyclodextrin (CD) and cucurbit[n]uril.^{92, 106–112}

1.5.2 Optical sensors

One further application of azo/polymer materials has been to develop optical sensors. Similar to plants experiencing photo-taxis, optical sensors can respond to light, sensing properties like optical power and intensity, even responding in a mechanical way such as bending towards or away from the light source. To achieve such a response, the molecular design used in the development of these materials is crucial, and optical sensors can be made from materials which show strong birefringence and/or which form surface relief gratings (SRGs). Birefringence is “a directional anisotropy in refractive index”, and photo-alignment in azobenzene systems with polarized light can achieve high levels of induced birefringence.²³

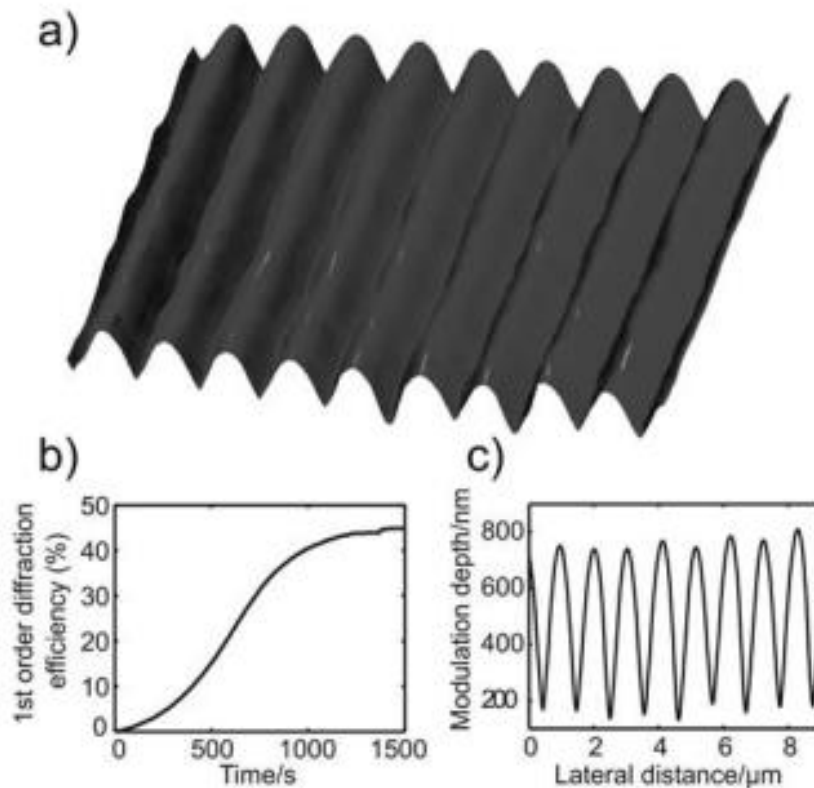


Figure 1.12 a) Typical AFM image of a SRG formed on an azo material, b) first order diffraction efficiency as a function of writing time, and c) averaged surface profile from a) (reproduced from reference ⁸³).

SRGs are formed when there is a large-scale mass transport when thick films made of amorphous azo/polymeric materials are irradiated with a light interference pattern.⁸³ This sinusoidal light interference pattern leads to a sinusoidal surface patterning, and **Figure 1.12** shows an example of a SRG formed from a P4VP (DY7)_{0.5} complex where DY7 is the azo dye Disperse Yellow 7. Over the history of azo/polymeric materials development these two applications have led to many

publications and materials and dye insights, demonstrating the prolificity of these materials towards this application as optical materials and devices.^{55, 73, 78, 79, 81, 83, 91, 96, 99}

In addition to these two now very well researched azo material applications, relevant if lesser-known applications such as for humidity sensors, and optical nanofibers developed through electrospinning have also been prepared and reported.^{38, 60} For example, Schoelch and colleagues harnessed reversible hydrogen bonding to develop an azo/polymer complex sensor by doping the petrol-based polymer polyvinylpyrrolidone (PVP) with the pseudo-stilbene-type azo DR1, which underwent a rapid, drastic, and reversible change in colour upon interaction with aqueous media, or even gentle exposure to humid air. The main driving force behind this colour change was competition of hydrogen donating properties causing displacement of dyes with water molecules, causing disruption and re-forming of antiparallel stacking of molecular dipoles.³⁸ Similarly, Wang and colleagues developed an electrospun fiber, using an ionic polymer/azo complex (methylated P4VP/methyl orange) blended into the petrol-based polymer PMMA. The electrospun fiber showed strong birefringence, and could have potential to serve as ‘artificial tendons’ controlled by light.⁶⁰

1.5.3 Mechanical behaviour

For control over mechanical behaviour of supramolecular materials to be achieved, directional reorientation and or volume change upon photo-irradiation is needed. If the light-induced shape change of these azo/polymer materials on the molecular level can transfer changes on the nano-

level up to the macro-level, then these materials fabricated using a range of soft-bonding interactions can find applications as macroscopic photo-mechanical materials, and light-powered actuators or even ‘robots’.

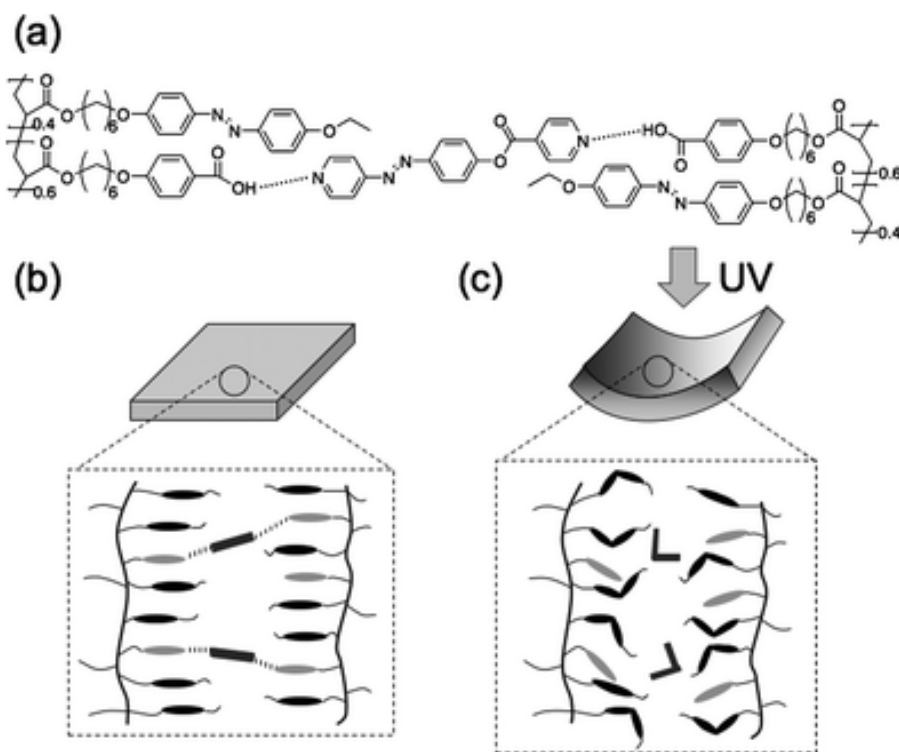


Figure 1.13 Plausible mechanism of bending in the hydrogen-bonded CLCP films of azo materials. (a) Network structures of the hydrogen-bonded CLCP films consisting of the copolymers and the crosslinkers. Schematic illustration of molecular alignment in the hydrogen-bonded CLCP film before (b), and after (c) irradiation with UV light (reproduced from reference 58).

For example, there are a number of examples of azo material actuators formed through hydrogen bonding, ionic bonding, and/or π - π interactions. One recent example is a hydrogen-bonded actuator from a carboxylated polymer containing up to 40 % azo-pyridine grafted onto the polymer, which formed a photo-responsive polymer network that underwent contraction isothermally when photoirradiation was applied as an external stimulus (**Figure 1.13**).⁵⁸ In another example, researchers utilized a natural polymer found in red seaweed known as agarose, to develop a humidity and light driven actuator,⁵⁹ by incorporating poly(ethylene glycol) (PEG)-conjugated azobenzene into the agarose hydrogel, held together through hydrogen bonds between agarose and azo-polymer units. These films were observed to curl away from the source of humidity due to asymmetric swelling and breakage of the hydrogen bonds in the material on the exposed surface. Additionally, as the film was exposed to continuous UV light there was an induced macroscopic bending.⁵⁹

In another example a solar actuator based on hydrogen-bonded azopolymers made from agarose for electricity generation was fabricated.⁹⁰ The researchers drew influence from phototropic plants (plants that respond to sunlight with mechanical motion) to develop a photo-actuator. The aim was to use the contraction ability of the hydrogen bonded azo/polymer films to generate electricity. A fluorinated azo dye was introduced into the agarose matrix which was mechanically coupled with a polyvinyl based piezoelectric transducer with a weight attached to bottom of the film.⁹⁰ The film then was able to transfer photo-stress to the transducer. When light was exposed to the film it generated bending movement that transferred to the polyvinylidene fluoride generator leading to an open circuit alternating voltage signal.⁹⁰

Photo-actuators have also been fabricated through ionic bonding between a negatively charged azobenzene unit, and a positively charged polyelectrolyte, with the azo molecules acting as a crosslinker between polymer chains.^{97, 98} These films developed showed efficient bending when irradiated with UV light. In the first example from Qin and colleagues in 2015, the positively charged polymer PDADMAC was crosslinked with the negatively charged disulfates azo molecule.⁹⁷ The resulting film coiled as it was irradiated with light and relaxed back to its original shape once the light source was turned off.⁹⁷ In a following study by Qin and colleagues in 2017, a multi-responsive actuator was fabricated using again the positively charged PDADMAC polymer but now with a negatively charged tetracarboxylated azo dye, for a photo-bending effect, and the films would also swell in response to humidity or heat.⁹⁸

In addition to ionic bonding, π - π interactions have been used to develop a supramolecular polymer incorporating azobenzene into the repeating units of the polymer.⁵⁶ When irradiated with UV-light, the resulting fibers bend on the nanoscale, unfolding and refolding the fibers.⁵⁶ The researchers constructed helically coiled conformations, by a supramolecular polymer approach; non-covalently ‘stacks’ were produced by assembling cyclic hexamers from barbiturate naphthalene,⁵⁶ which were then held together by π - π interactions due to the aromaticity of the moieties. Azobenzene was introduced into the naphthalene unit, and upon radiation the *trans-cis* isomerization caused defects in the hexamer assembly which changes the organization of the stacks, removing the curvature,⁵⁶ thereby showing that the curvature can be turned on and off *via* UV or visible light.

1.5.4 Disassembly/reassembly

Light can be used to initiate the uptake, storage, and release of a compound by photo-responsive supramolecular polymers. This can be in the form of host-guest systems, micelles and hydrogels for drug delivery systems, or ion transport vessels. These systems can be fabricated by attaching a photo-responsive azo molecule to a polymeric channel large enough to form photo-reversible guest release systems.^{35,61} For example, thin films containing controlled size pores at the molecular level were synthesized by layer-by-layer (LbL) assembly of cationic and anionic pillar[5]arenes, and attaching azobenzene units to the pore outlet (**Figure 1.14a**).⁶¹ Using UV/Vis light, the authors were able to open (*trans* state) or close (*cis* state) the “molecular valve” initiating either guest uptake, storage, or release of *p*-DNB(para-dinitrobenzene). The films were selective for only the para-substituted DNB and not the meta/ortho equivalents. Additionally, the photo-isomerization of the *trans/cis*-azo-polymer system was reversible and could be repeated many times.⁶¹

Another example utilizing the LbL approach of loading cyclodextrin (CD) cargo was by presented by Biang and colleagues in 2017.³⁵ These films were held together by electrostatic forces between the positively charged azo-polymer and the negatively charged PAA.³⁵ The β -CD-RhB was used as a cargo which interacted with the azo compound in a host guest manner, entrapped into the multilayers, until photo-isomerization occurred and the cargo was released from the multilayer using green light.³⁵ Another design motif is that involving micelles, constituted of amphiphilic molecules which arrange themselves in a spherical form in an aqueous solution. Photo-irradiation has been used to control micellization/demicellization, as well as to change the morphology of micelles synthesized by ionically bonding azo dyes to poly (ionic liquids).^{100, 113}

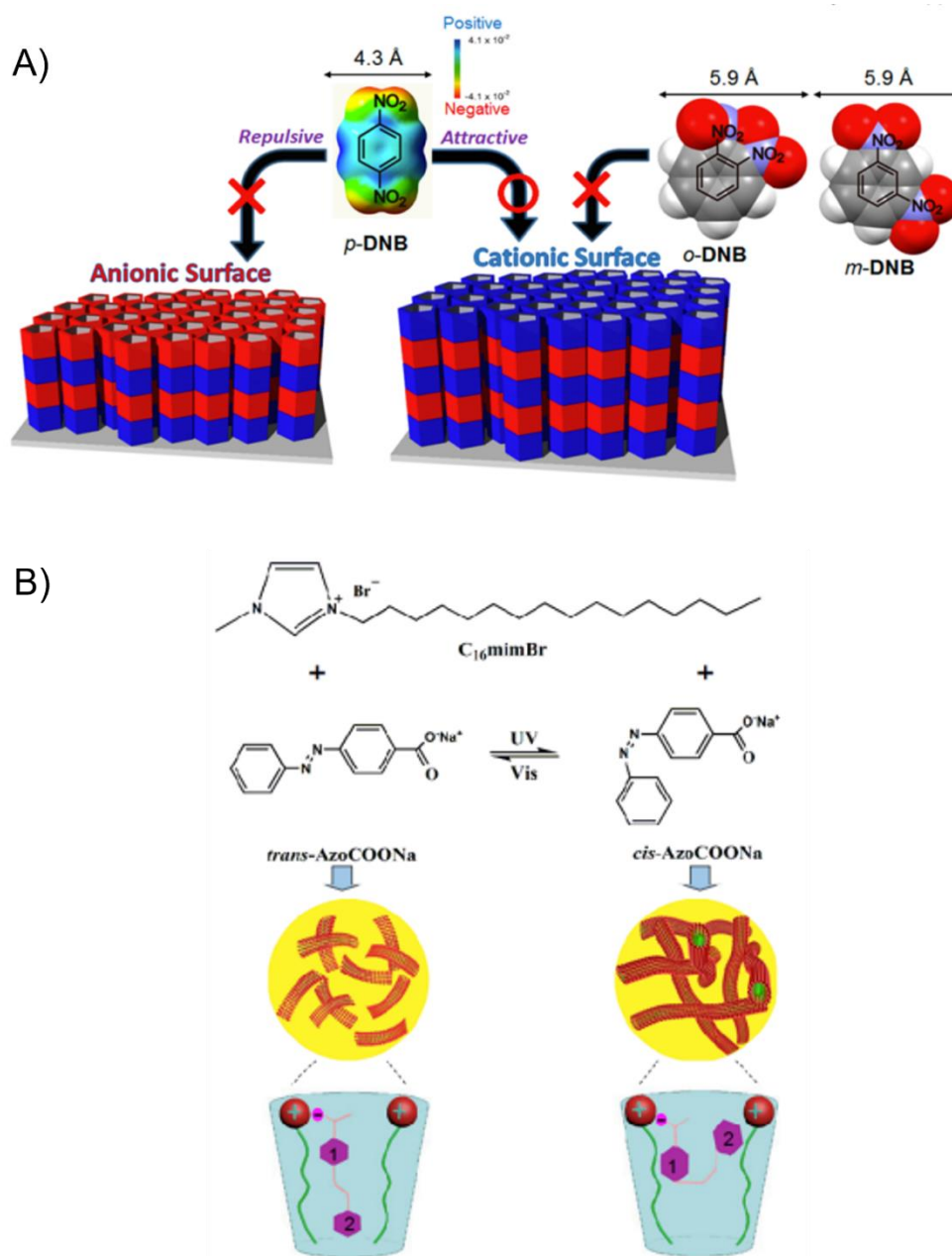


Figure 1.14 A) Schematic representation of photo-responsive guest uptake (reproduced from reference ⁶¹). B) Schematic illustration of the aggregates formed by the C₁₆mimBr/AzoCOONa system in aqueous solution before and after UV-light irradiation (Reproduced from reference ¹¹³).

For example, wormlike micelles with photo-responsive viscoelastic behaviour were formed by a surface-active ionic liquid/azobenzene derivative mixed solution (**Figure 1.14b**).¹¹³ The researchers were able to convert spherical C16mimBr (1-hexadecyl-3-methylimidazolium bromide) micelles into light responsive viscoelastic wormlike micelles by the addition of the dye AzoCOONa (sodium azobenzene 4-carboxylate), then upon UV irradiation the system underwent *trans-cis* isomerization resulting in longer and more entangled wormlike micelles which had an increased viscosity.¹¹³ In another example, thermo- and photo-responsive micelles were prepared from the ionic interaction between 2 triblock copolymers containing PAA, and a positively charged azo dye in a mixture of ionic liquids.¹⁰⁰ Using dynamic light scattering it was observed that irradiation with UV light affects the micellization morphologies, and micellization temperatures of the triblock polymer chains.¹⁰⁰

Another design approach is to use hydrogels, which are water insoluble crosslinked polymer networks that are highly absorbent and capable of holding large amounts of water. Hydrogels can be formed *via* host-guest interactions and electrostatic interactions between polymers and azo dyes. The effect of photo-isomerization can affect the viscosity of hydrogels allowing them to be used as artificial tendons, in drug-delivery systems, and as self-healing materials.^{62, 1091–11, 114, 115} Some of the first examples of these photo-reversible hydrogels were prepared by Tamesue and colleagues in 2010, and involved CD bonded to the rigid structured β -1,3 glucan (CUR), which formed host-guest interactions with the azo functionalized PAA to form a supramolecular hydrogel.¹¹¹ The researchers also studied the formation of a hydrogel between the CD polymer and a diazo dimer. The researchers showed that isomerization of the

supramolecular hydrogel caused a decrease in viscosity of the hydrogel which indicated a dissociation of the azobenzene and the cavity.¹¹¹

In 2012 there were two examples reported where researchers utilized host-guest interactions to develop supramolecular hydrogels that expanded and contracted or separated upon photo-stimuli.^{109, 110} For the hydrogels which expanded and contracted, azo compounds were used as the guest molecules associated to α -CD (host compound) crosslinked *via* methylene bisacrylamide, and expansion-contraction was possible due to the greater association constant of *trans*-azo compounds have compared to *cis*-azo compounds.¹¹⁰ Irradiating flat plates of α -CD-Azo in water showed an expansion (up to 40 %) of the gel, corresponding to the dissociation of the α -CD from the *cis*-azo.¹¹⁰ During irradiation with visible light the plate would shrink corresponding to isomerization of the azo from *cis* to *trans*, and there was also observed bending of the gel to the right when irradiating from the left side with UV light.¹¹⁰ In another example, these same researchers used host-guest interactions between polyacrylamide functionalized with azo (guest) and polyacrylamide functionalized with α and β -CD (host), to develop a photo-regulated macroscopic gel assembly, where upon UV irradiation the gels separated due to steric hindrance of the *cis* isomer and CD and recombined upon irradiation of visible light.¹⁰⁹

In another example by Wang and colleagues in 2015, the polymer PAA was used as the host with tetra-ortho-methoxy-substituted azobenzene as the guest to make hydrogels that released protein in deep tissue using red light (**Figure 1.15**).⁶² The azo dye and CD were covalently linked to side chains of PAA and hydrogels were created through the mixing of *trans* PAA-mAzo and PAA- β -CD, forming in a host guest matter.⁶² Red light irradiation triggered disassembly of *cis*

PAA-mAzo and PAA- β -CD, while blue light showed reassembly, to show that these host-guest complexes could be used for the release of proteins when BSA was loaded into the hydrogel.⁶²

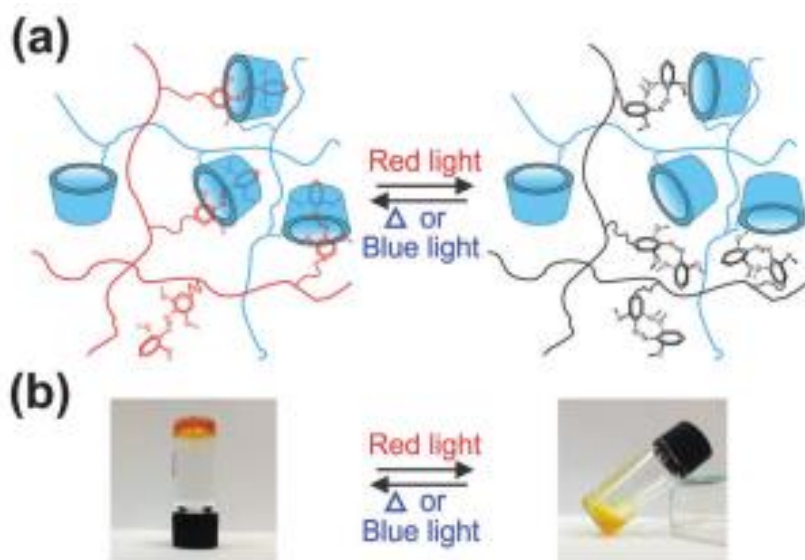


Figure 1.15 Schematic model (a) and photographs (b) of the reversible sol–gel transition of the PAA-mAzo/PAA-b-CD mixture (reproduced from reference ⁶²).

For applications towards self-healing supramolecular hydrogels which mimic natural biological systems, novel host-guest interactions between poly- β -CD and poly-azo showed slower softening effects than the poly-Br-Np and poly- β -CD hydrogel.¹¹⁴ Additionally, it was seen that when the three polymers were mixed to form a hydrogel, competitive binding occurred, and the poly-Br-Np was favored over poly-azo which was further increased when irradiated with UV

light,¹¹⁴ due to the photo-isomerization of the azo unit, allowing for more Np units to bind to the cavity.¹¹⁴ In a last example, supramolecular hydrogels with varying morphologies and different chiroptical reversibility were prepared using the chaperone gelator LHC18 mixed with several achiral azobenzene compounds containing COOH groups, where hydrogen bonds and ionic interactions were formed between the imidazole group of the LHC18 and the COOH groups of the azo moieties, and morphological changes in the nanostructure in the three gels were triggered by UV irradiation.¹¹⁵ Before irradiation, some gels displayed a loosed nanotube structure, while others formed nanosheets, while upon irradiation, two of the samples remained as gels while one collapsed into a sol.¹¹⁵ Additionally, circular dichroism studies showed that the chaperone gel LHC18 transferred its chirality to the azobenzene moieties *via* the supramolecular process.¹¹⁵

1.6 Photo-reversible azo/cellulose-based complexes

Azo dye functionalized cellulose-based materials have been investigated since the 1980s, with the main goal and application of these azo/cellulose-based materials being in the textile industry, to produce brightly coloured fibres, and hydrophobic materials whose surface wettability can change in response to UV/Vis light,^{71, 116} as well as for light to affect techniques such as for chromatographic stationary phases, to change the retention factor of compounds with light.^{117, 118} It was hypothesized that the *trans/cis* photo-isomerization of the azo pendant group changed the efficiency of the resolution of the analyte,¹¹⁷ and this was attributed to the more hydrophilic nature of the *cis* isomer in comparison to the *trans*, where the dipole moments are $\mu = 3 \text{ D}$ and 0 D ,

respectively.¹¹⁹ Additionally, the *trans*-isomer was believed to have a higher-ordered geometric structure due to its liquid-crystalline nature, than the less ordered structure of the *cis*-isomer.¹¹⁷ While not intending to fabricate photo-reversible materials, it should be noted that the dyeing of cotton and acetylated rayon (CA), using azo dyes has been done since the 1950s.^{120, 121} Unlike the previous examples, dyeing of cotton and CA was generally accomplished by doping which involves soft-bonded interactions (hydrophobic and dipole-dipole) between the polymer and the dye.^{120, 121}

While many azo/cellulose-based materials have been fabricated using cellulose and its derivatives such as hydroxypropyl cellulose (HPC),¹²² hydroxypropyl methyl cellulose (HPMC)¹²³ and acetoxypropyl cellulose (APC) derivatives,^{124, 125} very few studies have focused on studying the optics or isomerization of the azo dyes once grafted onto the polymers. Most recent reports of the functionalization of cellulose with azobenzene from Otsuka and Ahmadi-Nohadani in 2019 and 2022, working with our research Group, described the successful isomerization, and associated kinetics of the azo photo-switch once grafted onto the polymer,⁷¹ and explored applications in the field of mechanical bending and hydrophobic textiles.¹¹⁶ These researchers were able to prepare hydrophobic materials (water contact angle, $\theta > 90^\circ$) by functionalizing cellulose with the azobenzene dye and electrospinning the Azo-Cel into fabrics (**Figure 1.16a**),¹¹⁶ and the surface energy of these materials could also be controlled reversibly using UV/Vis light (**Figure 1.16b**). Under visible light irradiation, the surface wettability was induced to be lower (water contact angle, $\theta \sim 117^\circ$) than under UV light (water contact angle, $\theta \sim 108^\circ$).¹¹⁶ Additionally, it was reported

that the *cis* lifetime of the azo unit was significantly longer when covalently bonded to the cellulose polymer, compared to the free unbound azo molecules in solution.⁷¹

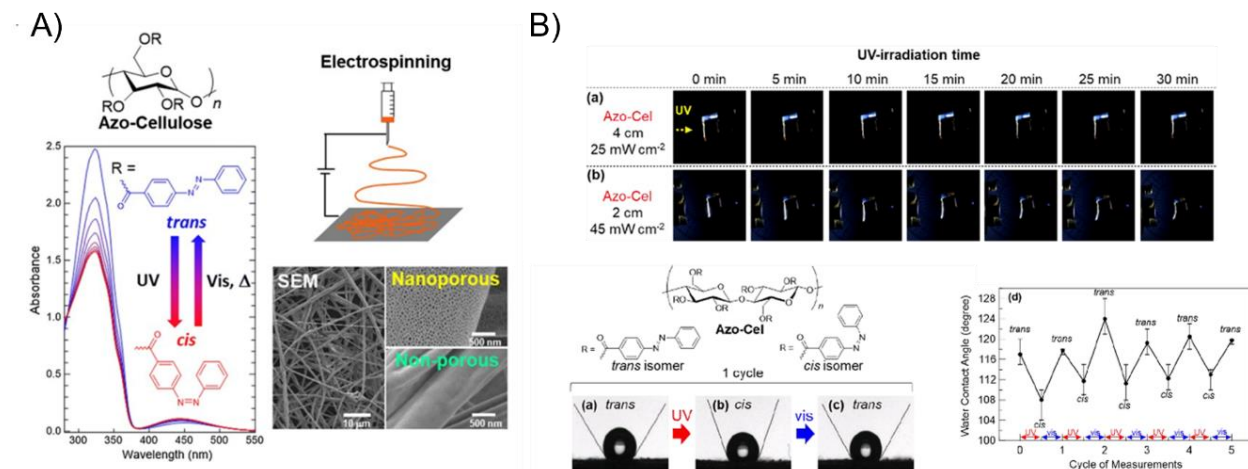


Figure 1.16 A) Example of electrospun Azo-Cel fabric (reproduced from reference ⁷¹). B) Photos of water droplets on a) an as-spun Azo-Cel fabric (*trans* isomer): WCA = 120 °, b) the same fabric after UV radiation (*cis* isomer): WCA = 108 °, and c) the same fabric after visible light irradiation (*trans* isomer): WCA = 118 °. d) The WCA changes of the Azo-Cel fabric over 5 cycles of UV/visible light irradiations. The plotted WCA values are the mean values of 4 sets of the measurements using 4 different pieces of the Azo-Cel fabric, and the error bars represent their maximum and minimum values (reproduced from reference ¹¹⁶).

Since these Azo-Cel materials can significantly and reversibly change their surface wettability in response to light, one potential application outside of textiles could be self-cleaning

materials. An example of such an azo/polymer material using polydopamine (PDA) was recently reported in the literature in 2022.¹²⁶ **Figure 1.17** shows that the material was made using PDA crosslinked with a diaminoazo dye, which when coated onto a urethane filter could dislodge fouling agents in response to UV/Vis light irradiation due to macroscopic movements generated by the *trans-cis-trans* isomerization of the azo dye.¹²⁶ It is quite possible that a similar phenomenon could be achieved with a crosslinked azo/cellulose-based material.

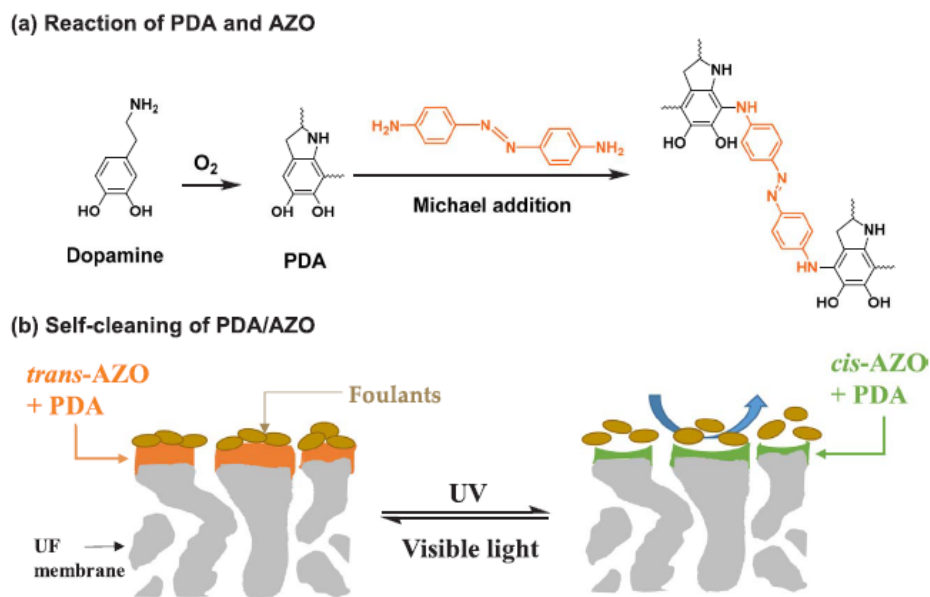


Figure 1.17 (a) Scheme of PDA formation and reactions between AZO and PDA through Michael addition, leading to covalent linkages, and (b) schematic of the self-cleaning behaviour of a photo-responsive membrane comprising a thin film of AZO and PDA (reproduced from reference ¹²⁶).

1.7 Scope of this Thesis

This introduction began by presenting an overview of the current landscape of bioplastics, showing the potential of biopolymers such as cellulose, starch, alginate, etc. to replace traditional petrol-based polymers (PE, PS, PTT, etc.) in a wide range of applications. It also provided a solid background on azo dyes, which can isomerize between the E and Z (*trans* and *cis*) stereoisomers upon irradiation. These changes on the molecular scale can result in large changes in the entire material, allowing azobenzene-containing materials to be developed for a wide variety of shape-changing applications such as drug delivery *via* photo-driven assembly/disassembly, to fabricate surface relief holographic optical gratings, employed as sunlight-driven photo-actuators, for photoalignment, and as humidity driven sensor devices. A review of these photo-reversible azo dye/polymer soft-bonded materials showed that majority of these previous materials were prepared using petrol-based polymers, and in the few cases where these materials were prepared using natural polymers such as cellulose and its derivatives, there were few studies on the isomerization of the azo dyes. This presents an opportunity to develop photo-reversible materials using azo dyes and natural polymers to improve the sustainability of these materials, and to study more in depth the isomerization of the azo dyes both experimentally and using DFT calculations, to better understand the role these azo dyes play in the various photo-driven applications.

The main objective of this Thesis was to develop photo-reversible materials using a range of azo dyes and natural polymers. In Chapter 2, the main aims were to develop a methodology of preparing water-resistant materials using water-soluble starting components, and to control the disassembly of the material using intensities of visible light. Stable multi-layered films

(NaCS/BBY) formed between photo-responsive layers containing the water-soluble BBY azo dye and layers containing a water-soluble cellulose-based polymer were prepared, and their controlled disassembly when triggered by blue light was confirmed and characterized. The resulting polyelectrolyte multilayers (PEMs) were uniform, of 50 bilayers, 390 ± 15 nm thick, held together by weak intermolecular interactions between the hydroxyl and sulfonate groups of NaCS and the amino groups and amine salts of BBY. The thin films were resistant to water over a wide pH and temperature range, however, the disassembly of these LbL films could be triggered on demand using 460 nm blue visible light, confirmed by time-dependent UV-Vis spectroscopy of the photo-disassembly in blue light vs. dark. The isomerization of BBY in solution and thin films under irradiation was confirmed by pump-probe and confocal Raman spectroscopy experiments, respectively. The isomerization of azobenzenes results in significant microstructural changes from a planar, nonpolar structure (E) to a polar, twisted confirmation (Z), resulting in large changes in the material, leading to complete and controlled disassembly back into their water-soluble components reversibly, in principle ready for re-use.

In Chapter 3, the main goals were to study the *trans-cis* isomerization of the bis-azo dye: Bismarck Brown Y (BBY); specifically, using pump-probe experiments to measure the kinetics of the *cis* decay of the azo dye BBY in solution and solid-state, and computational modeling to predict the *cis* decay of the azo dye BBY and its mechanism in the gas phase. The rate constants observed for the thermal *cis-trans* back isomerization permit a determination of how the thermal isomerization is influenced by its local environment. In both solution and when incorporated into multi-layered thin films, the thermal relaxation observed for the commercial azo dye BBY showed

a highly unusual biexponential decay, which clearly demonstrates two distinct isomerization processes. The *cis* decay showed an anomalous fast isomerization process on the timescale of milliseconds, followed by a slower isomerization process with a *cis* lifetime on the order of seconds. It was further observed that the faster isomerization process was influenced more by its local environment than was the slower process. The faster isomerization process also displayed a higher rate constant in aprotic solvents such as THF and DMF compared to that observed in protic solvents such as ethanol and water. Additionally, a higher rate constant was observed in solution compared to the multi-layered thin films where motion of the azo molecules was likely more restricted. Following recrystallization of the BBY azo dye, the more expected monoexponential decay was observed for the *cis* isomer in solution, with a single *cis* lifetime calculated on the timescale of seconds. This timescale corresponded well to values predicted by density functional theory calculations.

The main objective of Chapter 4 was to valorize waste brown seaweed (*Sargassum spp.*), which was done by extracting the polysaccharides cellulose and alginate, followed by the preparation of novel alginate blends, as well as the preparation of a range of photo-reversible materials using the extracted alginate. Over the last decade there has been an influx of pelagic *Sargassum spp.* (brown seaweed) into the Caribbean region, possibly due to climate change. This seaweed can serve as a good candidate for the fabrication of bioplastics because of its high biomass and its ability to grow in a wide range of environments. Additionally, brown seaweed contains polysaccharides such as alginate and cellulose which can be easily and cheaply extracted to prepare bioplastics and a range of other materials. In Chapter 4, using cheap and readily available reagents

such as soda ash, caustic soda, ethanol, and bleach, up to 35 % alginate and 17 % cellulose, were extracted from the waste brown seaweed. The extracted alginate and cellulose were characterized by FTIR spectroscopy, NMR spectroscopy, PXRD, and microscopy. Thin films and straws were prepared using the extracted alginate, and novel blends of the alginate were prepared with natural plasticizers: arrowroot starch, which is abundant and underutilized in St. Vincent, and glycerol. The mechanical properties such as tensile strength (MPa) and elongation at break (%), and physical properties such as water vapour and oxygen permeability of the various films were then assessed. The results indicate that materials made from the extracted alginate are comparable to commercial plastics, particularly HDPE. The incorporation of a photo switchable small molecule azobenzene-based (azo) dye, *via* soft-bonding interactions with the alginate polymers resulted in the fabrication of photo-reversible azo/alginate coatings and capsules which can potentially be used for controlled assembly/disassembly applications.

The main goal of the last Chapter (Chapter 5) was to prepare self-cleaning materials by covalently modifying cellulose-based polymers with azo dyes; specifically, to synthesize a range of azo dye functionalized cellulose acetate polymers, and to assess the change in surface wettability and water permeance in response to UV/Vis light. A series of cellulose acetate polymers with varying degree of acetylation was initially synthesized and thoroughly characterized. It was observed that with increasing acetyl content the water contact angle of the cellulose acetate films increased, as the materials became less hydrophilic. The various cellulose acetate polymers were then covalently modified with azo dyes *via* an esterification reaction and the kinetics of the *trans-cis* isomerization of the grafted azo dyes were assessed. It was observed that generally the *cis*

lifetime of the azo dyes increased when covalently bound to the polymer. Thin films of these azo modified cellulose acetate (Azo-CA) polymers were prepared by solvent-casting and electrospinning, and it was observed that the grafting of the azo dyes onto the cellulose acetate polymers further decreased the hydrophilicity of the material, and increased the water vapour permeance (WVP). The films were subjected to cycles of UV/Vis irradiation and the results showed that while there was no significant change in the water contact angle in response to the UV/Vis irradiation, there was a more pronounced change in the WVP of some of the materials. Chapter 6 provides a summary, and thorough discussion of all the results together as a Thesis, and lastly some general conclusions and future directions of this work.

1.8 References

1. UNEP, Drowning in Plastics – Marine Litter and Plastic Waste Vital Graphics, <https://wedocs.unep.org/xmlui/bitstream/handle/20.500.11822/36964/VITGRAPH.pdf>, (accessed August 2, 2021).
2. R. Shogren, D. Wood, W. Orts and G. Glenn, *Sustainable Production and Consumption*, 2019, **19**, 194–215.
3. ECCC, Single-use Plastics Prohibition Regulations - Technical Guidelines, https://publications.gc.ca/collections/collection_2023/eccc/En14-494-1-2023-eng.pdf, (accessed September 1, 2021).
4. ECCC, Discussion paper: A proposed integrated management approach to plastic products to prevent waste and pollution, <https://www.canada.ca/en/environment-climate-change/services/canadian-environmental-protection-act-registry/plastics-proposed-integrated-management-approach.html>, (accessed September 1, 2021).
5. European-Bioplastics, What are bioplastics?, <https://www.european-bioplastics.org/bioplastics/materials/>, (accessed February 6, 2023).

6. European-Bioplastics, Bioplastics Market Development Update 2022 https://docs.european-bioplastics.org/publications/market_data/2022/Report_Bioplastics_Market_Data_2022_short_version.pdf, (accessed February 6, 2023).
7. D. Klemm, B. Heublein, H. P. Fink and A. Bohn, *Angewandte Chemie International Edition in English*, 2005, **44**, 3358–3393.
8. E. Ott, H. M. Spurline, M. W. Grafflin, N. M. Bikales and L. Segal, *Cellulose and Cellulose Derivatives*, Interscience publishers, New York, 2 Edn., 1954.
9. H. Doh, M. H. Lee and W. S. Whiteside, *Food Hydrocolloids*, 2020, **102**, 105542–105551.
10. A. Mohammed, R. Bissoon, E. Bajnath, K. Mohammed, T. Lee, M. Bissram, N. John, N. K. Jalsa, K. Y. Lee and K. Ward, *Carbohydrate Polymers*, 2018, **198**, 109–118.
11. E. Hagglund, *Chemistry of Wood*, Academic Press Inc., Publishers, New York, 1951.
12. E. O. Fernandez and R. A. Young, *Cellulose*, 1996, **3**, 21–44.
13. Y. Wang, X. Wang, Y. Xie and K. Zhang, *Cellulose*, 2018, **25**, 3703–3731.
14. G. Chen, B. Zhang, J. Zhao and H. Chen, *Carbohydrate Polymers*, 2013, **95**, 332–337.
15. Q.-X. Wu, Y.-X. Guan and S.-J. Yao, *Frontiers of Chemical Science and Engineering*, 2018, **13**, 46–58.
16. G. Chen, B. Zhang, J. Zhao and H. Chen, *Food Hydrocolloids*, 2014, **35**, 476–483.
17. E. Weissenborn and B. Braunschweig, *Soft Matter*, 2019, **15**, 2876–2883.
18. R. Koshani, M. Tavakolian and T. G. M. van de Ven, *ACS Sustainable Chemistry & Engineering*, 2021, **9**, 4487–4497.
19. G. Michel, T. Tonon, D. Scornet, J. M. Cock and B. Kloareg, *New Phytologist*, 2010, **188**, 82–97.
20. H. Rau and S. Yu-Quan, *Journal of Photochemistry and Photobiology A: Chemistry*, 1988, **42**, 321–327.
21. C. J. Barrett, J. I. Mamiya, K. G. Yager and T. Ikeda, *Soft Matter*, 2007, **3**, 1249–1261.
22. A. A. Beharry and G. A. Woolley, *Chemical Society Reviews*, 2011, **40**, 4422–4437.
23. K. G. Yager and C. J. Barrett, in *Polymeric Nanostructures and Their Applications*, ed. H. S. Nalwa, American Scientific Publishers, 2006, ch. 8, pp. 243–272.

24. H. Fliegl, A. Köhn, C. Hättig and R. Ahlrichs, *Journal of the American Chemical Society*, 2003, **125**, 9821–9827.
25. S. Sun, S. Liang, W.-C. Xu, G. Xu and S. Wu, *Polymer Chemistry*, 2019, **10**, 4389–4401.
26. C. Slavov, C. Yang, L. Schweighauser, C. Boumrifak, A. Dreuw, H. A. Wegner and J. Wachtveitl, *Physical Chemistry Chemical Physics*, 2016, **18**, 14795–14804.
27. M. F. S. Teixeira, M. M. Barsan and C. M. A. Brett, *RSC Advances*, 2016, **6**, 101318–101322.
28. C. Boumrifak, C. Yang, S. Bellotto, H. A. Wegner, J. Wachtveitl, A. Dreuw and C. Slavov, *ChemPhotoChem*, 2019, **3**, 411–417.
29. S. Smith and F. B. Abdallah, *Journal of Thermodynamics & Catalysis*, 2017, **08**, 1000181–1000189.
30. A. Georgiev, E. Bubev, D. Dimov, D. Yancheva, I. Zhivkov, J. Krajcovic, M. Vala, M. Weiter and M. Machkova, *Spectrochimica Acta Part A: Molecular and Biomolecular Spectroscopy*, 2017, **175**, 76–91.
31. A. Yano, Y. Konno, E. Kinoshita and R. Yano, *Journal of Photochemistry and Photobiology A: Chemistry*, 2017, **346**, 411–415.
32. N. K. Joshi, M. Fuyuki and A. Wada, *Journal of Physical Chemistry B*, 2014, **118**, 1891–1899.
33. J. Robertus, S. F. Reker, T. C. Pijper, A. Deuzeman, W. R. Browne and B. L. Feringa, *Physical Chemistry Chemical Physics*, 2012, **14**, 4374–4382.
34. Q. Yi and G. B. Sukhorukov, *Soft Matter*, 2014, **10**, 1384–1391.
35. Q. Bian, M. Jin, S. Chen, L. Xu, S. Wang and G. Wang, *Polymer Chemistry*, 2017, **8**, 5525–5532.
36. K. G. Yager and C. J. Barrett, *Macromolecules*, 2006, **39**, 9320–9326.
37. M. Matsumori, A. Takahashi, Y. Tomioka, T. Hikima, M. Takata, T. Kajitani and T. Fukushima, *ACS Applied Materials & Interfaces*, 2015, **7**, 11074–11078.
38. S. Schoelch, J. Vapaavuori, F. G. Rollet and C. J. Barrett, *Macromolecular Rapid Communications*, 2017, **38**, 1600582–1600590.
39. C. Barrett, A. Natansohn and P. Rochon, *Macromolecules*, 1994, **27**, 4781–4786.

40. C. Barrett, A. Natansohn and P. Rochon, *Chemistry of Materials*, 1995, **7**, 899–903.
41. L. L. Norman and C. J. Barrett, *Journal of Physical Chemistry B*, 2002, **106**, 8499–8503.
42. N. Böhm, A. Materny, W. Kiefer, H. Steins, M. M. Müller and G. Schottner, *Macromolecules*, 1996, **29**, 2599–2604.
43. C. S. Paik and H. Morawetz, *Macromolecules*, 1972, **5**, 171–177.
44. J. Vapaavuori, A. Goulet-Hanssens, I. T. S. Heikkinen, C. J. Barrett and A. Priimagi, *Chemistry of Materials*, 2014, **26**, 5089–5096.
45. G. Booth, H. Zollinger, K. McLaren, W. G. Sharples and A. Westwell, in *Ullmann's Encyclopedia of Industrial Chemistry*, Wiley-VCH Verlag GmbH & Co. KGaA, Weinheim, 2012, vol. 11, pp. 676–732.
46. A. D. Becke, *Journal of Chemical Physics*, 1993, **98**, 5648–5652.
47. F. Weigend and R. Ahlrichs, *Physical Chemistry Chemical Physics*, 2005, **7**, 3297–3305.
48. J. Dokić, M. Gothe, J. Wirth, M. V. Peters, J. Schwarz, S. Hecht and P. Saalfrank, *Journal of Physical Chemistry A*, 2009, **113**, 6763–6773.
49. M. Poprawa-Smoluch, J. Baggerman, H. Zhang, H. P. A. Maas, L. De Cola and A. M. Brouwer, *Journal of Physical Chemistry A*, 2006, **110**, 11926–11937.
50. E. G. Lewars, *Computational Chemistry: Introduction to the Theory and Applications of Molecular and Quantum Mechanics*, Springer Dordrecht, 2 Edn., 2011.
51. K. Bujak, H. Orlikowska, J. G. Małecki, E. Schab-Balcerzak, S. Bartkiewicz, J. Bogucki, A. Sobolewska and J. Konieczkowska, *Dyes and Pigments*, 2019, **160**, 654–662.
52. F. He, X. Ren, J. Jiang, G. Zhang and L. He, *Journal of Physical Chemistry Letters*, 2022, **13**, 427–432.
53. C. Faul and M. Antonietti, *Advanced Materials*, 2003, **15**, 673–683.
54. E. Arunan, G. R. Desiraju, R. A. Klein, J. Sadlej, S. Scheine, I. Alkorta, D. C. Clary, R. H. Crabtree, J. J. Dannenberg, P. Hobza, H. G. Kjaergaard, A. C. Legon, B. Mennucci and D. J. Nesbitt, *Pure and Applied Chemistry*, 2011, **83**, 1637–1641.
55. A. Priimagi, G. Cavallo, A. Forni, M. Gorynsztejn–Leben, M. Kaivola, P. Metrangolo, R. Milani, A. Shishido, T. Pilati, G. Resnati and G. Terraneo, *Advanced Functional Materials*, 2012, **22**, 2572–2579.

56. B. Adhikari, Y. Yamada, M. Yamauchi, K. Wakita, X. Lin, K. Aratsu, T. Ohba, T. Karatsu, M. J. Hollamby, N. Shimizu, H. Takagi, R. Haruki, S.-i. Adachi and S. Yagai, *Nature Communications*, 2017, **8**, 15254–15264.
57. H. Guo, J. Yang, J. Zhou, L. Zeng, L. Zhao and B. Xu, *Dyes and Pigments*, 2018, **149**, 626–632.
58. J.-I. Mamiya, A. Yoshitake, M. Kondo, Y. Yu and T. Ikeda, *Journal of Materials Chemistry*, 2008, **18**, 63–65.
59. L. Zhang, H. Liang, J. Jacob and P. Naumov, *Nature Communications*, 2015, **6**, 7429–7441.
60. X. Wang, Q. Zhang, C. G. Bazuin and C. Pellerin, *Macromolecular Symposia*, 2014, **336**, 30–38.
61. T. Ogoshi, S. Takashima and T. A. Yamagishi, *Journal of the American Chemical Society*, 2015, **137**, 10962–10964.
62. D. Wang, M. Wagner, H.-J. Butt and S. Wu, *Soft Matter*, 2015, **11**, 7656–7662.
63. E. Kharlampieva, V. Kozlovskaya and S. Sukhishvili, *Advanced Materials*, 2009, **21**, 3053–3065.
64. G. Decher and J.-D. Hong, *Makromolekulare Chemie. Macromolecular Symposia*, 1991, **46**, 321–327.
65. M. Landry, K. Gu, S. Harris, L. Al-Alwan, L. Gutsin, D. J. De Biasio, Bernie, D. Nakamura, T. C. Corkery, T. T. Kennedy and C. J. Barrett, *Macromolecular Bioscience*, 2019, **19**, 1900036–1900047.
66. W. B. Stockton and M. F. Rubner, *Macromolecules*, 1997, **30**, 2717–2725.
67. Q. Hou, X. Wang and A. J. Ragauskas, *Cellulose*, 2019, **26**, 4787–4798.
68. X. Tian, B. Wang, J. Li, J. Zeng and K. Chen, *Carbohydrate Polymers*, 2017, **157**, 704–710.
69. F. Li, P. Biagioni, M. Finazzi, S. Tavazzi and L. Piergiovanni, *Carbohydrate Polymers*, 2013, **92**, 2128–2134.
70. F. Carosio, M. Ghanadpour, J. Alongi and L. Wagberg, *Carbohydrate Polymers*, 2018, **202**, 479–487.
71. I. Otsuka and C. J. Barrett, *Cellulose*, 2019, **26**, 6903–6915.

72. Y. Zhang, C. Zhang and Y. Wang, *Nanoscale Advances*, 2021, **3**, 6040–6047.
73. O. Kulikovska, L. M. Goldenberg, L. Kulikovsky and J. Stumpe, *Chemistry of Materials*, 2008, **20**, 3528–3534.
74. J. de Wit, G. A. van Ekenstein, E. Polushkin, K. Kvashnina, W. Bras, O. Ikkala and G. ten Brinke, *Macromolecules*, 2008, **41**, 4200–4204.
75. S. Xiao, X. Lu and Q. Lu, *Macromolecules*, 2007, **40**, 7944–7950.
76. S. Xiao, X. Lu, Q. Lu and B. Su, *Macromolecules*, 2008, **41**, 3884–3892.
77. M. Poutanen, O. Ikkala and A. Priimagi, *Macromolecules*, 2016, **49**, 4095–4101.
78. J. E. Koskela, V. Liljeström, J. Lim, E. E. Simanek, R. H. A. Ras, A. Priimagi and M. A. Kostiainen, *Journal of the American Chemical Society*, 2014, **136**, 6850–6853.
79. J. Gao, Y. He, F. Liu, X. Zhang, Z. Wang and X. Wang, *Chemistry of Materials*, 2007, **19**, 3877–3881.
80. T. Kato, N. Hirota, A. Fujishima and J. M. J. Fréchet, *Journal of Polymer Science Part A: Polymer Chemistry*, 1996, **34**, 57–62.
81. J. Vapaavuori, I. T. S. Heikkinen, V. Dichiarante, G. Resnati, P. Metrangolo, R. G. Sabat, C. G. Bazuin, A. Priimagi and C. Pellerin, *Macromolecules*, 2015, **48**, 7535–7542.
82. A. Priimagi, J. Vapaavuori, F. J. Rodriguez, C. F. J. Faul, M. T. Heino, O. Ikkala, M. Kauranen and M. Kaivola, *Chemistry of Materials*, 2008, **20**, 6358–6363.
83. J. Vapaavuori, A. Priimagi and M. Kaivola, *Journal of Materials Chemistry*, 2010, **20**, 5260–5264.
84. X. Wang, J. Vapaavuori, C. G. Bazuin and C. Pellerin, *Macromolecules*, 2018, **51**, 1077–1087.
85. J. del Barrio, E. Blasco, C. Toprakcioglu, A. Koutsioubas, O. A. Scherman, L. Oriol and C. Sánchez-Somolinos, *Macromolecules*, 2014, **47**, 897–906.
86. L. M. Saiz, P. A. Oyanguren, M. José Galante and I. A. Zucchi, *Nanotechnology*, 2014, **25**, 065601–065609.
87. X. Miao, Z. Cheng, B. Ren and W. Deng, *Surface Science*, 2012, **606**, L59–L63.
88. J. Konieczkowska, H. Janeczek, J. Małecki, B. Trzebiecka, D. Szmigiel, A. Kozanecka-Szmigiel and E. Schab-Balcerzak, *Polymer*, 2017, **113**, 53–66.

89. T. I. Burganov, S. A. Katsyuba, T. A. Vakhonina, A. V. Sharipova, O. D. Fominykh and M. Y. Balakina, *The Journal of Physical Chemistry C*, 2018, **122**, 1779–1785.
90. Y. Xiong, L. Zhang, P. Weis, P. Naumov and S. Wu, *Journal of Materials Chemistry A*, 2018, **6**, 3361–3366.
91. L. Philippe, F. Céline and N. Jean-Michel, *Pure and Applied Optics: Journal of the European Optical Society Part A*, 1998, **7**, 71–82.
92. K. Gayathri, S. Balamurugan and P. Kannan, *Journal of Chemical Sciences*, 2011, **123**, 255–263.
93. M. Saccone, V. Dichiarante, A. Forni, A. Goulet-Hanssens, G. Cavallo, J. Vapaavuori, G. Terraneo, C. J. Barrett, G. Resnati, P. Metrangolo and A. Priimagi, *Journal of Materials Chemistry C*, 2015, **3**, 759–768.
94. S. E. Burke and C. J. Barrett, *Macromolecules*, 2004, **37**, 5375–5384.
95. I. Ghosh, B. Das, R. K. Nath, B. Ganguly, B. K. Mishra and A. Pal, *Surface Review and Letters*, 2016, **23**, 1650056–1650065.
96. O. Kulikovska, L. M. Goldenberg and J. Stumpe, *Chemistry of Materials*, 2007, **19**, 3343–3348.
97. C. Qin, Y. Feng, W. Luo, C. Cao, W. Hu and W. Feng, *Journal of Materials Chemistry A*, 2015, **3**, 16453–16460.
98. C. Qin, Y. Feng, H. An, J. Han, C. Cao and W. Feng, *ACS Applied Materials & Interfaces*, 2017, **9**, 4066–4073.
99. X. Wang, J. Vapaavuori, X. Wang, R. G. Sabat, C. Pellerin and C. G. Bazuin, *Macromolecules*, 2016, **49**, 4923–4934.
100. C. Wang, K. Hashimoto, J. Zhang, Y. Kobayashi, H. Kokubo and M. Watanabe, *Macromolecules*, 2017, **50**, 5377–5384.
101. Q. Zhang, C. G. Bazuin and C. J. Barrett, *Chemistry of Materials*, 2008, **20**, 29–31.
102. Q. Zhang, X. Wang, C. J. Barrett and C. G. Bazuin, *Chemistry of Materials*, 2009, **21**, 3216–3227.
103. X. Pan, S. Xiao, C. Wang, P. Cai, X. Lu and Q. Lu, *Optics Communications*, 2009, **282**, 763–768.

104. F. Zhao, J. Wu, Z. Pan, C. Wang, J. Zhang, Y. Zeng and X. Lu, *Optics Communications*, 2012, **285**, 4180–4183.
105. D. Dey, S. A. Hussain, R. K. Nath and D. Bhattacharjee, *Spectrochimica Acta Part A: Molecular and Biomolecular Spectroscopy*, 2008, **70**, 307–312.
106. L. Liu, L. Rui, Y. Gao and W. Zhang, *Polymer Chemistry*, 2014, **5**, 5453–5460.
107. J. Liu, X. Jiang, X. Huang, L. Zou and Q. Wang, *Colloid and Polymer Science*, 2016, **294**, 1243–1249.
108. M. Chen, S. R. Nielsen, T. Uyar, S. Zhang, A. Zafar, M. Dong and F. Besenbacher, *Journal of Materials Chemistry C*, 2013, **1**, 850–855.
109. H. Yamaguchi, Y. Kobayashi, R. Kobayashi, Y. Takashima, A. Hashidzume and A. Harada, *Nature Communications*, 2012, **3**, 603–608.
110. Y. Takashima, S. Hatanaka, M. Otsubo, M. Nakahata, T. Kakuta, A. Hashidzume, H. Yamaguchi and A. Harada, *Nature Communications*, 2012, **3**, 1270–1278.
111. S. Tamesue, Y. Takashima, H. Yamaguchi, S. Shinkai and A. Harada, *Angewandte Chemie International Edition*, 2010, **49**, 7461–7464.
112. I. Tomatsu, A. Hashidzume and A. Harada, *Journal of the American Chemical Society*, 2006, **128**, 2226–2227.
113. Y. Bi, H. Wei, Q. Hu, W. Xu, Y. Gong and L. Yu, *Langmuir*, 2015, **31**, 3789–3798.
114. H. Chen, X. Ma, S. Wu and H. Tian, *Angewandte Chemie International Edition in English*, 2014, **53**, 14149–14152.
115. L. Ji, G. Ouyang and M. Liu, *Langmuir*, 2017, **33**, 12419–12426.
116. H. Ahmadi-Nohadani, S. Nono-Tagne, C. J. Barrett and I. Otsuka, *Macromolecular Rapid Communications*, 2022, **43**, 2200063–2220070.
117. K. Arai and H. Udagawa, *Die Makromolekulare Chemie, Rapid Communications*, 1988, **9**, 797–800.
118. O. Yoshio, S. Hideaki, H. Koichi and I. Masahiro, *Chemistry Letters*, 1986, **15**, 983–986.
119. G. S. Hartley and R. J. W. Le Fèvre, *Journal of the Chemical Society (Resumed)*, 1939, **119**, 531–535.

120. C. L. Bird and M. P. Harris, *Journal of the Society of Dyers and Colourists*, 1957, **73**, 199–202.
121. T. M. Baldwinson, *Journal of the Society of Dyers and Colourists*, 1961, **77**, 246–251.
122. W. Qin, Z. Li, J. Li, L. Zhang, R. Liu and H. Liu, *Cellulose*, 2014, **22**, 203–214.
123. X. Hu, P. J. Zheng, X. Y. Zhao, L. Li, K. C. Tam and L. H. Gan, *Polymer*, 2004, **45**, 6219–6225.
124. S. N. Fernandes, L. E. Aguirre, R. V. Pontes, J. P. Canejo, P. Brogueira, E. M. Terentjev and M. H. Godinho, *Cellulose*, 2015, **23**, 465–476.
125. L. F. Pinto, S. Kundu, P. Brogueira, C. Cruz, S. N. Fernandes, A. Aluculesei and M. H. Godinho, *Langmuir*, 2011, **27**, 6330–6337.
126. S. N. Ramanan, N. Shahkaramipour, T. Tran, L. Zhu, S. R. Venna, C.-K. Lim, A. Singh, P. N. Prasad and H. Lin, *Journal of Membrane Science*, 2018, **554**, 164–174.

1.9 Appendix 1: Portion of Regenerative Waste Labs summarized information for sustainable learning portal

During the course of my Ph.D. Thesis research, I had the opportunity for a three month paid internship through a McGill award, to work with a Canadian company in Vancouver, Regenerative Waste Labs. This invaluable experience allowed me to gain insight into some of the real challenges and opportunities of transitioning academic laboratory research such as my Thesis work, into the ‘real world’ of a sustainable business model, and public perception. Through this internship, I worked with the company to prepare documents for their website, to try and better educate the general public of the goals and mission of this initiative, towards transitioning to more ‘green’ and sustainable alternatives to petrol-based plastics in common consumer products. As such, my Thesis advisors and I felt it important to share some of this documented learning experience, as a natural extension of my academic laboratory research. What follows here is a partial summary of what I produced during this internship, preparing the company’s ‘learning portal’. The goal of the sustainable learning portal was to educate the various stakeholder groups in the circular bioeconomy. The focus was to have been on economically competitive and sustainable bio-sourced materials, including methods to process them in environmentally benign ways, and approaches to designing products with end-of-life properties that enable reuse or recycling, thereby actively contributing to the foundation of a circular bioeconomy. These stakeholder groups include: (i) raw material producers who convert raw materials into resins, (ii) manufacturers who convert resins into products, (iii) retailers who procure packaging *e.g.*, coffee shops, and (iv) users, *e.g.*, customers purchasing a cup of coffee.

Continuum of biomaterials

Biomaterials refer to materials that are bio-based and or biodegradable (**Figure S1.1**).¹ Biomaterials can be grouped into 2 main categories: synthetic vs. natural. Within the natural biomaterials section there are (i) biopolymers extracted from biomass (*e.g.*, cellulose, TPS), and (ii) biopolymers produced by organisms (*e.g.*, PHA, PLA, PGAPCL). Synthetic biomaterials can be **further** divided into (i) aliphatic polyesters (*e.g.*, PBAT, PBS) and (ii) PVA.^{1,2} A review article published in 2019 has good information on market price of different raw materials (**Table S1.1**).³

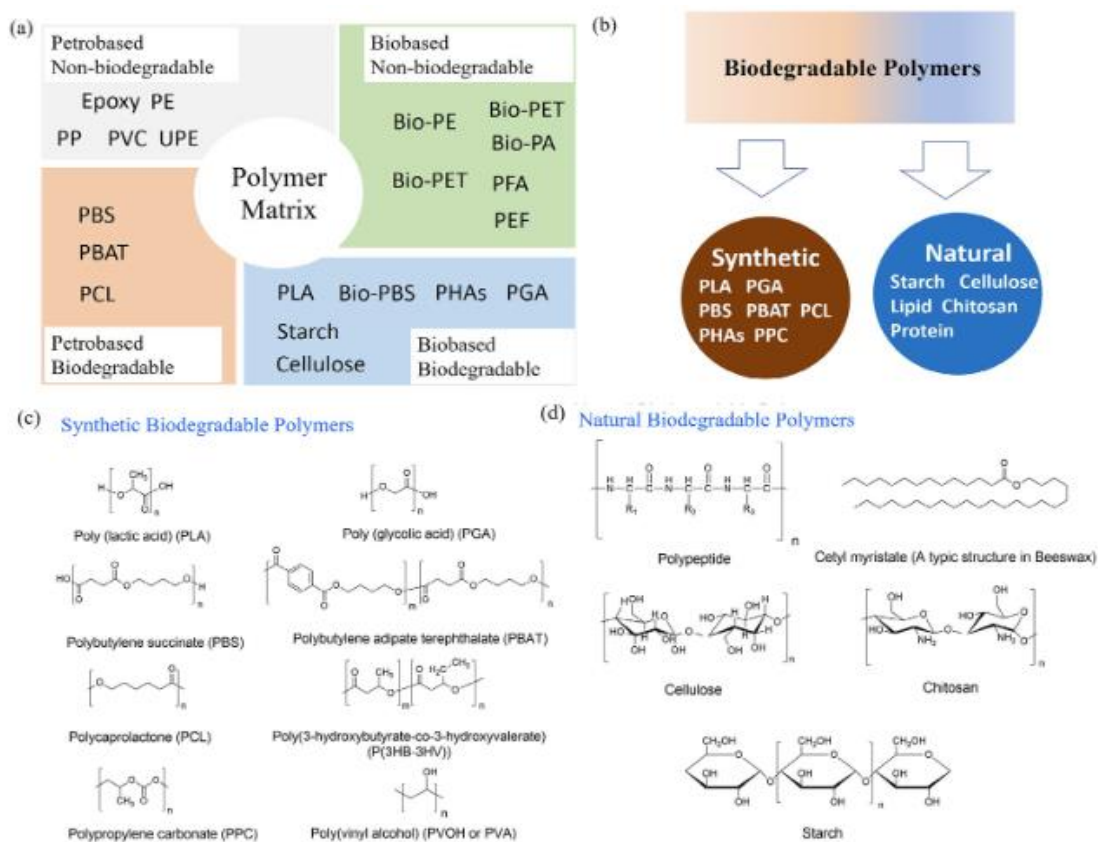


Figure S1.1 Examples of (a) polymer matrix, (b) biodegradable polymers, (c) synthetic biodegradable polymers, and (d) natural biodegradable polymers (reproduced from reference ¹).

Material	Source	Price (\$/lb.)
Lignocellulose fiber	Plant	0.2-0.6
Cellulose esters/ethers	Plant/petrochemical	2-10
Starch	Plant	0.10-1.0
Starch/polymer blends	Plant, petrochemical	1-2?
Polylactic acid (PLA)	Plant	~1.0
Polyhydroxyalkanoates (PHA)	Plant	2-6?
Polybutylene succinate (PBS), polybutylene adipate phthalate (PBAT)	Plant, petrochemical	2-3
Polyamides (Nylon 10, 11)	Castor oil	
Zein	Corn	
Biopolyurethanes	Plant, petrochemical	
Bioepoxies	Plant, petrochemical	
Bio-polyethylene (bio-PE)	Ethanol from corn, sugarcane, etc.	
Bio-polypropylene (bio-PP)		
Bio-polyethylene terephthalate (bio-PET)	Plant sugars	
Polytrimethylene terephthalate (PTT)	Corn glucose, petrochemicals	
Polyethylene furanoate (PEF)	Corn sugars	
PE	Petrochemicals	0.65-0.80
PP	"	0.85-0.95
PET	"	0.85-0.90
PS	"	1.0-1.2
PVC	"	0.85-0.90

Table S1.1 Common-plant-based and petroleum-based materials and their approximate prices (reproduced from reference ³).

Single-Use Plastic guidelines

Raw materials producers in Canada should be aware of the Canadian Environmental Protection Act, 1999 (CEPA) which provides regulations which include managing single-use plastics, including banning, or restricting certain single-use plastics that cause harm, where warranted and supported by scientific evidence. According to Canadian Government legislation, single-use plastic is defined as a product “designed to be thrown away after being used only once”. When characterizing single-use plastics the categories used are: environmentally problematic, recovery problematic and considerations for exemption. Items being considered for a ban or restriction:

plastic checkout bags, stir sticks, six-pack rings, cutlery, straws, and food service ware made from problematic plastic (Table S1.2).⁴

	Environmentally problematic		Value recovery problematic			Exemption considerations	
	Prevalent in environment	Known or suspected to cause environmental harm	Hampers recycling and/or wastewater treatment	Non-recyclable, low or very low recycling rate	Barriers to increasing recycling rate	Performs essential function	No viable alternatives
Plastic checkout bags	✓	✓	✓	✓	✓		
Stir sticks	✓	✓	✓	✓	✓		
Six-pack rings	✓	✓	✓	✓	✓		
Other bags (for example, garbage)			✓	✓	✓		
Snack food wrappers	Some kinds		Some kinds (for example, bioplastics)	✓	✓	✓	
Multi-packaging			✓	✓	✓		
Disposable personal care items			✓	✓	✓		
Beverage bottles and caps	✓	✓					
Contact lenses and packaging	✓			✓	✓	✓	✓
Hot and cold drink cups and lids	✓		✓	✓	✓		
Cigarette filters	✓						✓

Table S1.2 Analysis of information of environmentally problematic plastic items (reproduced from reference ⁴).

Localities

To improve sustainability in the bioplastic packaging supply chain it is necessary to be aware of what feedstocks and which vendors are available within your locality or place of operation.

Purchasing feedstock within your locality curtails transportation cost and helps drive supply and demand within your area. Consult distribution maps of feedstock and bioplastic supplier lists found in **Table S1.3** and **Table S1.4** to be aware of what feedstocks and vendors are available in your locality. A list of bio-based feedstocks is shown below in **Figure S1.2**.

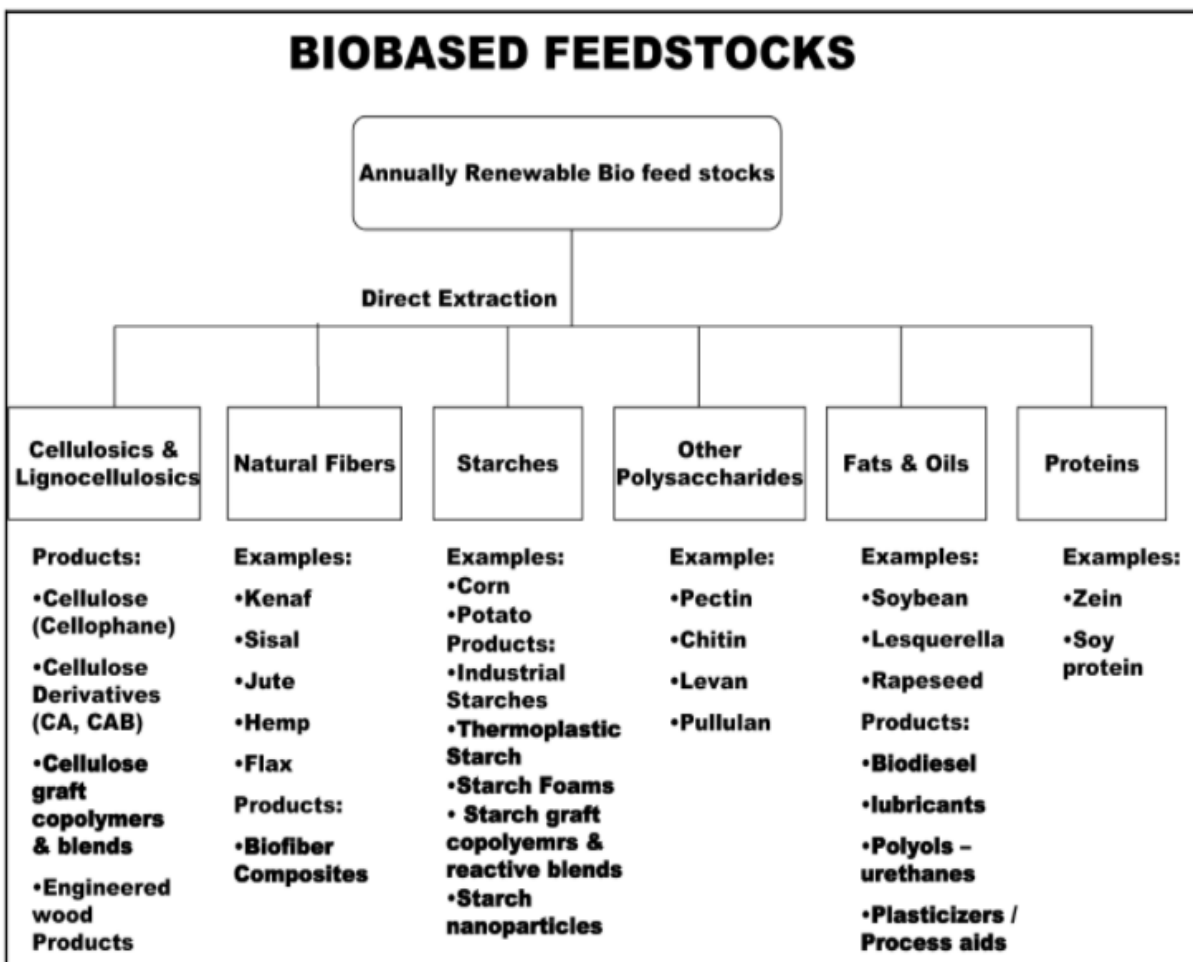


Figure S1.2 Direct extraction of biomass to provide biopolymers for use in manufacture of bio-based products (reproduced from ⁵).

It is important that raw material producers set up facilities close to where feedstocks are available. Additionally, certain feedstocks are used to make specific biomaterials, for example corn is a feedstock for the production of PLA, TPS, PBAT/PBS and Bio-PET. Corn is grown mainly in Ontario and Quebec in Canada, so companies harvesting the corn and its waste products and companies producing PLA resins should set up facilities close to these areas. **Table S1.3** shows a summary of feedstock localities based on highest production capacity in 2018/2019 for the US and Canada.⁶⁻⁸ **Table S1.4** provides a list of biomaterial resin suppliers.⁹ It is important that raw material producers set up facilities that are within the same locality as biomaterial resin and product suppliers.

Feedstock (biomass)	Biomaterials	State/Province with highest production capacity in 2018/2019:	
		Canada	US
Corn	PLA, TPS,PBAT/PBS, Bio-PEF	Ontario, Quebec	Minnesota, Illinois, Iowa Nebraska, South Dakota
Soybean (oil format)	PHA, Bio-PP	Ontario, Quebec, Manitoba	Illinois, Iowa, Minnesota Nebraska, North and South Dakota
Canola (oil format)	PHA, Bio-PP	Saskatchewan , Alberta Manitoba	North Dakota
Wheat (spring, winter, total)	TPS,PBAT,PBS, Bio-PEF	Saskatchewan , Alberta Manitoba	North Dakota, Minnesota Montana, Kansas Washington
Sugarcane	PLA,TPS,Bio-PE, Bio-PET,PBAT,PBS	(Not grown)	Louisiana, Florida
Sugar beets	PLA,PBAT,PBS	Alberta, Ontario	Minnesota, North Dakota Idaho, Michigan
Rice	TPS	*Experimental paddies in Ontario	Arkansas, Louisiana, California
Trees	Cellulose (fibre pulp)	British Columbia, Quebec, Alberta Ontario	Maine, The lake States Lower south and pacific northwest regions
Micro and macro algae	PHB, starch, algae blends	Canada Pacific coast: British Columbia Ontario, Nova Scotia Saskatoon	All across the US, <i>e.g.</i> , California , Florida
Shellfish	Chitin	British Columbia (Pacific Coast) Nova Scotia; PEI; New Brunswick, (Atlantic coast) Quebec	Georgia Basin Washington (Puget Sound)

Table S1.3 Feedstock localities based on highest production capacity for 2018/2019.

Biomaterials	US	Canada
Paper and lignocellulosic fibre pulp	International paper, Georgia Pacific, Weyerhaeuser, Westrock, Rayonier, Domtar, Resolute Forest products, Ecopack	Domtar, Resolute Forest products, Canfor Corporation, Cascades, Celgar, Ecopak, Innofibre, Comet
Cellulose esters/ethers	Eastman, Celanese, Ashland, Dow Dupont, CP Kelco, Rayonier	Nexeo plastics Canada corp
CNC's	Sweet Water Energy, American Process, US forest Products Lab	Celluforce, Anomera , FPInnovations Alberta Innovates , Blue Goose Biorefineries
Starches	Cargill, Ingredion, ADM, Tate and Lyle, BioBag, Natureworks	Ingredion Canada Inc Cerestech , Manitoba starch products Solanyl Biopolymer Inc , ADM
Starch polymer blends	GreenDot Bioplastics, KTM industries	Winpak
PLA	Natureworks, Algix, Total Corbion	BioMatera, Polyferm Canada Terraverdae BioWorks , BASF
PHA (PHB, PHBV)	Danimer Scientific, Newlight Tech, Full Cycle Bioplastics, Mango Materials, Metabolix, MHG Bio, Tephra, RWDC industries	Polyferm Canada Terraverdae BioWorks BASF
Bio-PE	Lyondellbasell	Good Natured Products Competitive Green Technologies
Bio-PP	Lyondellbasell, Braskem	Competitive Green Technologies
Bio-PTF	Dupont, ADM	Not available
Bio-PTT	Dupont, Tate and Lyle	Not available
Bio-PEF	Not available	Not available
PBAT	Algix, Genomatica (BDO), Eastman	Bioamber (succinic acid), BASF, Competitive Green Technologies
Chitin/Chitosan	Agratech, Cruzfoam, Zuchem Ltd, Neuchem, Ebrator Biochemicals, Tidal Vision, Chitolytic	Chitolytic
Algae	AstaReal Inc, Texas A&M Agrilife Research, Qualitas Health, Inc., Total Corbion-AlgaPrime DHA	AlgaeCan Biotech Ltd, AlgaeBloom Technologies, Pond Biofuels, Innofibre

Table S1.4 Biomaterial resin and product suppliers list.

Physical properties to aim for/ performance standards

Currently there are no governmental or industry regulations and policies for physical properties of biomaterials and biopolymers. However, there is an abundance of academic research data on the physical and mechanical properties of various polymers.³ These properties can affect the performance of the product during its use phase as well as its degradation/ recycling phase.

Physical properties to consider include:¹⁰

- moisture/water vapour permeability
- oxygen and carbon dioxide permeability
- mechanical properties include tensile strength, elongation at break, and thermal properties include glass transition temperature, and melting temperature.

Figure S1.3 shows the barrier requirements for different food packaging.¹ **Table S1.5** shows a compilation of the barrier properties of various petrol-based and bio-based polymers,³ while **Table S1.6** shows a compilation of the mechanical and thermal properties of various petrol-based and bio-based polymers.³ **Table S1.7** lists suitable applications of various bio-based and biodegradable polymers based on their barrier, mechanical, and thermal properties from the Regenerative Waste Labs (RWL) website.⁵

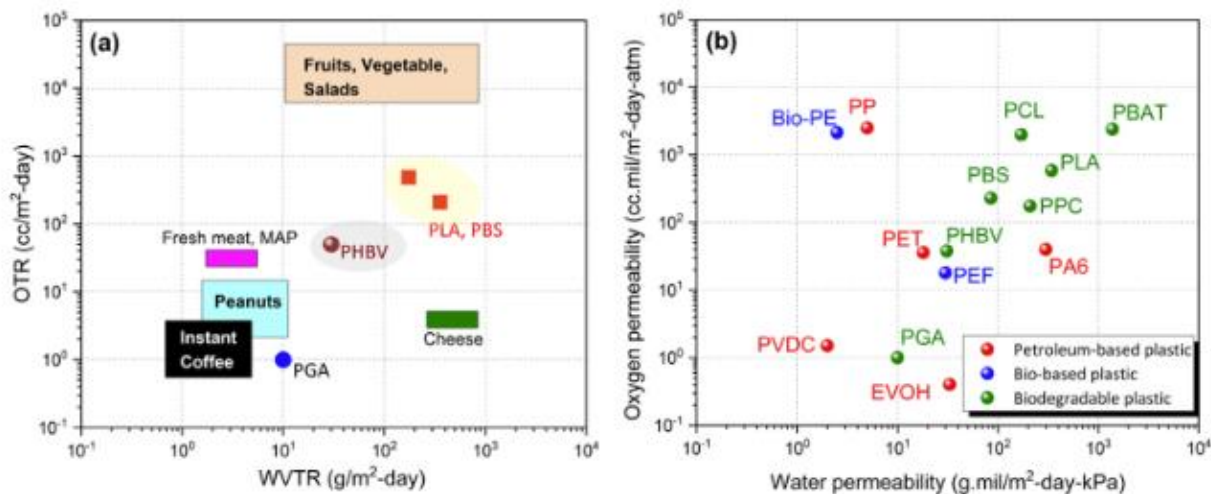


Figure S1.3 (a) Requirements of barrier properties for different food packaging applications and a comparison between oxygen/water transition rate of selected biodegradable polymers at 25 μm and food packaging barrier requirements. (b) The oxygen/moisture permeability of different polymers (reproduced from reference ¹).

Material	Water vapor	Oxygen	Carbon dioxide	References
Kraft paper	High	High	High	Bedane et al. (2012)
Cellulose acetate, DS 2.5	2920	1000		Shogren (1997), Noda et al. (2009)
Corn starch		1		Forssell et al. (2002)
PLA	172	360	1500	Shogren (1997), Aurus et al. (2005), Bedane et al. (2012)
PHBV	21	40		Shogren (1997), Noda et al. (2009)
PBS	330			Shogren (1997)
PEF	6	5	21	Burgess et al. (2015)
PE	5	7000	92,000	Ashley (1985), www.polymerdatabase.com
PP	2	2300	24,000	"
PET	12	60	400	"
PS	80	4000	23,000	"

Relative values are given since measurement conditions vary between studies.

Table S1.5 Relative gas permeabilities polymers (reproduced from reference ³).

Material	Tensile strength (MPa)	Elongation at break (%)	Glass transition temperature (°C)	Melting temperature (°C)	References
Kraft paper	68	3	–	–	Shogren (1999)
Cellulose acetate	90	25	110	230	Sookne and Harris (1945), Mandelkern and Flory (1951)
Corn starch ^a	40	9	112	–	Shogren and Jasberg (1994)
PLA ^b	59	2–7	55	165	Farah et al. (2016), Shogren et al. (2011a,b)
PHA ^c	15–50	1–800	–12–3	100–175	Noda et al. (2009)
PBS	34	560	–32	114	Xu and Guo (2010)
PBAT	22	800	–29	110	Gross and Kalra (2002)
PEF	35–67	3–4	85	211	Knoop et al. (2013)
PTT	49	160	50	228	Kurian (2005), Chen and Patel (2012)
PE	15–30	1000	–125	110–130	www.polymerdatabase.com
PP	36	400	–13	176	"
PET	86	20	72	265	"
PS	30–60	1–5	100	–	"
PVC	52	35	–18	200	"

^aCorn starch was extruded at 20–30% water then equilibrated to 50% r.h.

^bPLA containing 96/4 L/D.

^cPHA containing 85–100% 3-HB, 0–15% other scl, mcl monomers.

Table S1.6 Mechanical and thermal properties of plant-based and petrochemical-based polymers (reproduced from reference ³).

Properties	Film	Rigids (Trays/Cups)	Bottles	Other
Properties	eg. (cut) vegetables and fruits, bread bags, shrink films. Not for long shelf life products, unless barrier laminates are used.	Salads, vegetables, fruits, dairy products, drinking cups, meat. Avoid storage of empty trays and cups at high temperatures.	Not a preferred material. Used in small water bottles and chilled, short shelf life juices and dairy products and wine bottle capsules. Needs barrier materials for further applications	Compostable teabags and coffee capsules. Coated paperboard (coffee cups) and other service ware. Foamed trays and boxes.
Starch Blends	Food waste bags, translucent grocery bags. Vegetables and fruits. Mulch films.	Vegetables and fruits. Coffee capsules.	N/a	Loose fill foams. Service ware. Labels.
Cellulose based	Cellophane, candy wrapping.	N/a	N/a	Some cellulose acetate in cutlery.
Biodegradable polyesters	Grocery bags. Vegetables and fruits. Frozen produce	Vegetables and fruits (non-transparent)	N/a	Biodegradable nets. Coated paperboard. Particle foam. Coffee capsules.
Drop-in-bio-PE	Shopping bags. Various packaging films.	Trays.	Bottles and dairy products shampoo and detergents.	Coated paperboard for packaging of dairy products. Caps and closures.
Drop-in-bio-PET	N/a (yet)	N/a (yet)	Various bottles for soda and water.	N/a (yet)

Table S1.7 Suitable applications of various bio-based and biodegradable polymers (reproduced from the RWL website ⁵).

In addition to the properties above, these properties also need to be considered for resins used in injection moulding: good heat stability, high strength, durability, impact resistance and materials for better compostability.¹⁰ There are currently no Governmental or industry regulations and policies to design materials for better compostability. However, there are recommendations based on scientific research which can help you to design better compostable products. According to previous research, the physical properties of the plastic affects degradation. Better degradation is achieved with:¹⁰

- Greater hydrophilicity
- Presence of heteroatoms (oxygen containing groups, esters, amine, and amides)
- Low crystallinity/more amorphous
- Low melting temperature (T_m)
- Low glass transition temperature (T_g) and
- Low molecular weight (MW)

Degradation can be slowed by annealing the polymer, *e.g.*, PLA, and functional groups such as aliphatic groups (C-H bond), aromatic groups (even though they confer rigidity) also lower the degradation of the product. Aliphatic esters are a good compromise, *e.g.*, PBAT.¹⁰

References

1. F. Wu, M. Misra and A. K. Mohanty, *Progress in Polymer Science*, 2021, **117**, 101395–101435.
2. G. Babak and A. Hadi, in *Biodegradation*, eds. C. Rolando and R. Francisca, IntechOpen, Rijeka, 2013, Ch. 6.
3. R. Shogren, D. Wood, W. Orts and G. Glenn, *Sustainable Production and Consumption*, 2019, **19**, 194–215.
4. ECCC, Discussion paper: A proposed integrated management approach to plastic products to prevent waste and pollution, <https://www.canada.ca/en/environment-climate-change/services/canadian-environmental-protection-act-registry/plastics-proposed-integrated-management-approach.html>, (accessed September 1, 2021).
5. RWL, Embedding Circularity: Sustainable Products and Packaging, <https://rwl-embedding-circularity.thinkific.com/>, (accessed October 5, 2022).
6. Forest Industries: Directory of Primary Forest Industries in Canada, <https://www.canadian-forests.com/forest-industries.html>, (accessed August 10, 2021).
7. Shellfish harvest area quality, <https://www.canada.ca/en/environment-climate-change/services/environmental-indicators/shellfish-harvest-area-quality.html>, (accessed August 11, 2021).
8. US-EPA, Shellfish Harvesting, <https://www.epa.gov/salish-sea/shellfish-harvesting>, (accessed August 11, 2021).
9. Top 50 Bioresins and Bioplastics Suppliers, <https://polymerdatabase.com/Polymer%20Brands/Bioplastic%20Suppliers.html>, (accessed August 11, 2021).
10. P. K. Samantaray, A. Little, A. M. Wemyss, E. Iacovidou and C. Wan, *ACS Sustainable Chemistry and Engineering*, 2021, **9**, 9151–9164.

Bridging Text for Chapter 2: Controlled disassembly of azo dye /cellulose-based thin films using visible light

The first Chapter of this Thesis introduces a novel method of preparing photo-reversible materials that are water-resistant, starting from water-soluble biobased components. Using low intensity visible light as a stimulus, the disassembly of these materials could later be triggered on demand to return the materials back to their aqueous starting components in a non-destructive way. To prepare these photo-reversible materials, polyelectrolyte multilayers (PEMs) were fabricated by assembling the biobased polymer sulfated cellulose (NaCS) with the water-soluble commercial azo dye Bismarck Brown Y (BBY) in a layer-by-layer manner. Generally, PEM materials are fabricated using petrol-based polymers and if an azo dye is incorporated this is done *via* covalently linking the dye to one of the polymeric units. Therefore, this is the first time that such a PEM film was fabricated using a biobased component and a ‘cross-linking’ photo-switch *via* only soft-bonding interactions. The resulting PEM coatings can withstand soaking in high temperatures, very acidic and basic conditions, and up to 1 M salt concentration, allowing potential use in a wide range of packaging applications. A novel simulated ‘sun and rainfall’ experiment designed and conducted in both deionized water and tap water shows that the films disassemble at a faster rate while under irradiation with high intensities of blue light which can trigger the *trans*-to-*cis* isomerization of the azo dye. Additionally, this Chapter confirms and characterizes for the first time the *trans*-*cis* isomerization of the BBY azo dye, which has been studied since the 1860s, by means of confocal Raman spectroscopy and laser pump-probe experiments.

Chapter 2 has been published as a manuscript in a peer-reviewed journal. Citation: Edwards, K. E., Kim, M., Borchers, T. H., and Barrett, C. J. “Controlled disassembly of azo dye /cellulose-based thin films using visible light” *Materials Advances*, 2022, 3, 62226230.

Controlled disassembly of azo dye /cellulose-based thin films using visible light

K. E. Edwards, M. Kim, T. H. Borchers, and C. J. Barrett**

Department of Chemistry, McGill University, Montreal, QC, Canada

2.1 Abstract

In efforts toward designing self-assembled materials that can later be disassembled easily to avoid destruction of component materials during separation and recycling to minimize waste at their end of life, we report the fabrication of robust, water-resistant polymer multilayers whose disassembly could be triggered upon irradiation of wavelengths and intensities of blue visible sunlight. Self-assembled thin films for study were prepared by combining a water-soluble biodegradable polymer, sodium cellulose sulfate (NaCS), and a water-soluble azo dye photo-switch, Bismarck Brown Y (BBY) *via* layer-by-layer (LbL) assembly. The resultant multi-layered materials (NaCS/BBY) were held together by weak intermolecular interactions between the polymeric sulfate groups and the amino groups of the photo-switch, forming robust and water-resistant materials. The photo-disassembly of the films was assessed using ‘rainfall conditions’ and ‘sunlight’ where it was demonstrated that blue visible light could trigger the successful disassembly of the films at a rate of $k_d = 7 \pm 1 \times 10^{-3}$ absorbance units/hr. Optical pump-probe experiments and confocal Raman spectroscopy supported a mechanism that the disassembly was triggered by the *trans*-to-*cis* geometric isomerization of BBY. This method of sunlight- and water-triggered disassembly can in principle allow for recovery of reusable components to be applied as next generation sustainable materials for products and recycling processes.

2.2 Introduction

Society's use of traditional disposable plastics has now clearly become a grave global environmental concern due to their overuse, non-degradability, poor reprocessibility, and toxicity. However, encouraging efforts are being made in such fields as sustainable materials science and bioengineering towards providing low- or non-impact plastic alternatives using naturally-derived polymers. Cellulose for example is one of the most abundant natural resources on Earth, and can function well as a sustainable feedstock due to its excellent recyclability, degradability, low cost and worldwide availability.¹ Over the last few decades much research has focused on the engineering of cellulose into functional materials for uses in medicine and packaging, as well as the processing of nano-cellulose to bulk materials.^{2–6} Cellulose's ability to be used in such a wide variety of applications derives from its complex structure and versatile suite of properties. Cellulose biopolymers consist of linear chains of D-glucose (**Figure 2.1**) repeating units which are connected through a high degree of intermolecular hydrogen bonding, rendering the polymer insoluble in water and in most organic solvents, and providing materials with excellent mechanical properties.

Cellulose can also be easily functionalized to create a wide array of derivatives with tailorable properties. Many of these cellulose derivatives retain the excellent properties of native cellulose such as being biodegradable and biocompatible, while adding additional benefits such as antibacterial properties, flame retardancy, and water solubility.⁷ Water-soluble cellulose derivatives such as commercially available methyl cellulose (MC), hydroxypropyl cellulose (HPC) and sodium cellulose sulfate (NaCS) are of particular interest, as they can be processed under more environmentally friendly conditions. Thanks to their excellent gel-forming properties, these polymers are now well-used in the fabrication of coatings, composites, films and membranes.⁷ NaCS in particular is interesting due to its high tensile

strength in the wet state, its moldability in situ as well as its relatively simple and cost-efficient production, and biocompatibility.^{8, 9} Recently, even novel edible films for packaging using NaCS and glycerol were developed, fabricated *via* solvent-casting techniques, demonstrating that NaCS could be used as potential degradable coating materials for food packaging. These dense NaCS films formed with an ordered microstructure and were transparent, flexible, and resistant to oils and fats, but not to water. Films made from water-soluble polymers can sometimes disassemble before the end of their use however, due to the hydrophilicity of their surfaces.¹⁰

One method of recent interest for developing high-value materials is through layer-by-layer (LbL) self-assembly. LbL assembly involves the sequential adsorption of alternating layers of charged polymers/molecules from aqueous solution onto a substrate *via* a dipping process.¹¹ LbL assembly offers many advantages compared to other forms of film production, such as solvent casting, drop casting, and spin-coating; these include increased reproducibility and a more homogenous dispersion of the fibres resulting in more uniform films.¹² This technique generally involves the combination of two water-soluble components, which when combined result in a water-resistant film. Materials are linked to each other in the films through soft, weak attractive forces such as ionic bonding, hydrogen bonding, or hydrophobic forces. Soft bonding interactions are of particular interest, such as ionic bonding and hydrogen bonding, which are both reversible and directional.¹³ This allows more complex systems to easily assemble and later gently and reversibly disassemble when introduced to a particular stimulus, such as pH, temperature, or salt, without breaking the covalent bonds.¹² Early sets of hydrogen-bonded LbL films were commonly prepared using a carboxylic acid-containing polymer such as polyacrylic acid (PAA) and polymethacrylic acid (PMAA), which allowed films to be used for the preparation of pH-sensitive materials.¹⁴ More recent hydrogen-bonded

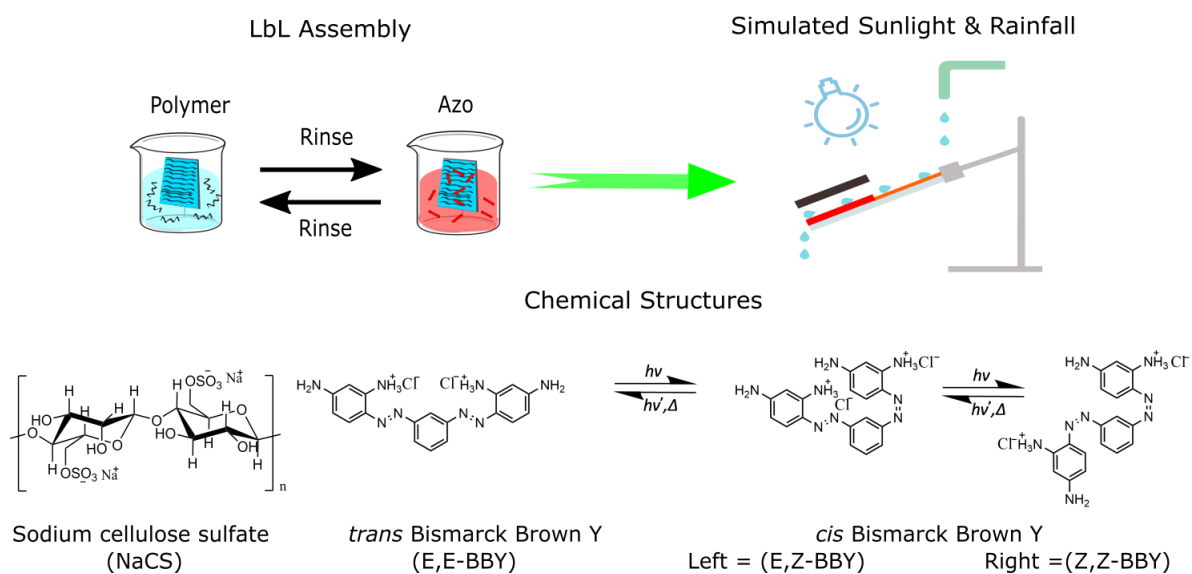


Figure 2.1 Schematic illustration of layer-by-layer (LbL) assembly to make multi-layered (NaCS/BBY) thin films, and the simulated sunlight and rainfall trigger conditions to assess the disassembly of the films and the chemical structures of the materials used.

LbL films involve polymers containing hydroxyl or amino groups for use as photochromic paper, gas barriers, and flame-retardant coatings.^{15–19} For electrostatically-bonded LbL films, common polyanions include PAA and hyaluronic acid (HA) which can be combined with polycations poly (allylamine HCl) or poly-L-lysine, to fabricate polyelectrolyte multilayer (PEM) films that can be used as tuneable extracellular matrix materials.²⁰

Additionally, LbL films and PEM films can be designed to be photo-responsive by covalently attaching a photo-switch to one of the polymers.²¹ Light is often a preferred stimulus since it can be applied precisely and remotely with minimal undesired chemical change otherwise to the host materials. One of the most effective and well-studied photo-switches is azobenzene, which can geometrically isomerize between E and Z (*trans* and *cis*) stereoisomers reversibly upon irradiation. Azobenzene derivatives exhibit a wide characteristic absorption

band in their UV-Vis absorption spectra which originates from the $\pi \rightarrow \pi^*$ transition of the azobenzene chromophore. Adding push-pull substituents on the aromatic rings can drastically change the optical properties of the azobenzene, giving one the ability to ‘tune’ specific properties such as *cis* half-life or UV-Vis absorption profile, optimizing the photo-switching characteristics for a wide variety of specific material applications.^{22, 23} It is also possible to load more than one isomerizing unit into an azobenzene molecule. For example, bisazobenzenes such as Bismarck Brown Y (BBY) (**Figure 2.1**) have two azo units (N=N bonds) per molecule, which allows for higher loading of azo units in the material without aggregation and provides a larger volume change and increased geometrical disruption upon isomerization.²⁴⁻²⁶ BBY ($C_{18}H_{18}N_8 \cdot 2HCl$), which is the dihydrochloride of 4,4’-[1,3-phenylenebis (diazene-2,1-diyl)]di(benzene-1,3-diamine), is one of the few commercially available water-soluble azobenzenes. It has four intermolecular bonding donor/acceptor sites, two of which are protonated. Offering this higher number of intermolecular bonding sites also allows for increased intermolecular interactions between the photo-switch and the polymer, resulting in more stable films when self-assembled.

The isomerization of azobenzene can result in large structural disruption, changing from a planar, nonpolar structure (E) to a polar, twisted confirmation (Z) (**Figure 2.1**). These changes on the molecular scale can result in large changes in the entire material, and azobenzene-containing materials have been developed for a wide variety of shape-changing applications such as drug delivery *via* photo-driven assembly/disassembly, to fabricate surface relief holographic optical gratings, employed as sunlight-driven photo-actuators, for photoalignment, and as humidity driven sensor devices.^{14, 21, 27-31} Generally, these materials are fabricated out of synthetic polymers. However, in response to the negative impact of synthetic polymers on the environment, a shift towards biodegradable and bio-based polymers has received much recent attention.

For the first time, we report here water-resistant self-assembled biobased cellulose materials that can be photo-reversibly dis-assembled and re-solubilized, prepared using a relatively simple and cost-efficient method. Thin multilayer films were prepared by the LbL assembly of two water-soluble components: NaCS, a low toxicity (edible), biobased and biodegradable polymer; and BBY, a photo-reversible azobenzene molecule. The multi-layered thin films (NaCS/BBY) were held together by electrostatic interactions between the anionic polymer and the cationic photo-switch and provided a robust and stable material that was water resistant. Upon blue visible light irradiation in running water however, we were able to trigger and control disassembly of the films, thus returning the material back to its water-soluble starting components, in principle ready for re-use. These new reversibly ‘soft-bonded’ materials could potentially be easily and inexpensively fabricated, as a new class of materials to replace some of the artificial plastics currently used for a variety of thin film or coating applications.

2.3 Results and discussion

2.3.1 LbL assembly of NaCS/BBY thin films

Multi-layered films (NaCS/BBY) comprising a water-soluble biodegradable polymer, sodium cellulose sulfate (NaCS), and a photo-responsive azo dye, Bismarck Brown Y (BBY) were prepared based on the LbL assembly protocols for similar compounds described previously, to produce robust and water-resistant materials.^{15–17} Disassembly of the thin films was then triggered by blue light under ‘simulated sunlight and rainfall’ conditions (**Figure 2.1**). The average thickness of the obtained thin films was 390 ± 15 nm after the deposition of 50 bilayers onto a glass substrate, determined by AFM (**Figure S2.1a**). AFM topology measurements

(**Figure S2.1b**), confocal Raman optical microscopy (**Figure S2.1c**) and SEM imaging (**Figure S2.1d**) confirmed a uniform film surface across various length scales. Elemental mapping of sulfur and nitrogen further confirmed an even distribution of the polymer, sulfated cellulose and the azo dye, Bismarck Brown Y, respectively, across the film's surface (**Figure S1d**). The films were also optically clear and had a deep red appearance due to the characteristic red colour of the BBY dye (**Figure 2.2**).

UV-Vis absorption spectroscopy confirmed that BBY displays a strong absorption band in the visible region ($\lambda_{max} = 450 \text{ nm}$, $\epsilon \geq 32\,000 \text{ Lmol}^{-1}\text{cm}^{-1}$) where the $\pi \rightarrow \pi^*$ and $n \rightarrow \pi^*$ transitions are overlapped (**Figure 2.2**).

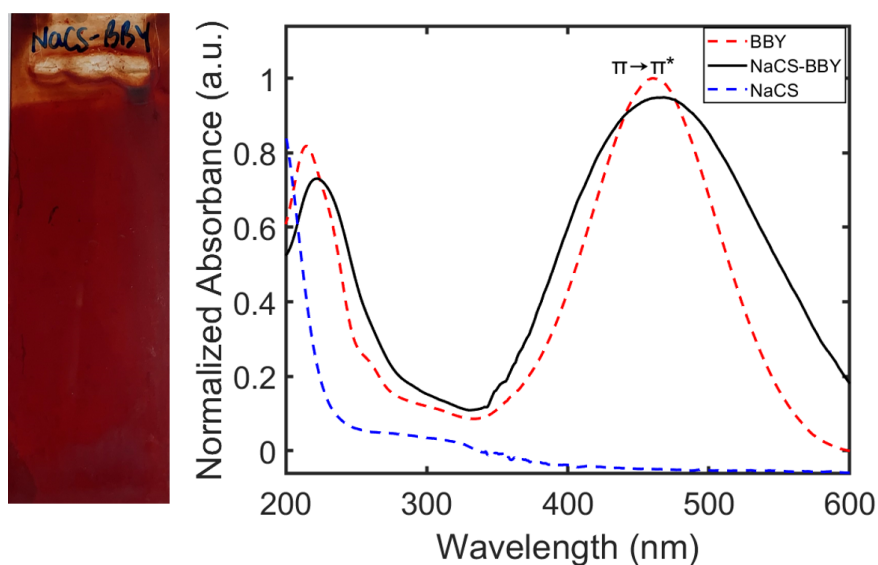


Figure 2.2 (Left) Image of multi-layered NaCS/BBY films (50 bilayers) deposited on a glass substrate with distinct red colour of BBY. (Right) UV-Vis spectra of NaCS/BBY on quartz with $\lambda_{max} = 450 \text{ nm}$, BBY in water $\lambda_{max} = 450 \text{ nm}$ and NaCS in water with $\lambda_{max} = 200 \text{ nm}$.

In the multi-layered films the peak at $\lambda_{max} = 450$ nm was observed to be broader than in solution. This was likely due to intermolecular interactions between the azo and the polymer which affects the electronics of the azo unit (N=N bond) and helps confirm the soft-bonding interactions. UV-Vis absorption spectroscopy also showed two broad peaks for the polymer, with λ_{max} values of approximately 200 nm and 300 nm, consistent with that of cellulose.³² These two absorption bands appear hidden below those of BBY in the multi-layered films (**Figure 2.2**). UV-Vis spectroscopy also showed that the bilayers were deposited linearly by monitoring the increase in the peak at 450 nm which is attributed to the $\pi \rightarrow \pi^*$ transition of *trans* BBY (E, E-BBY) as shown in the Supplementary Information (**Figure S2.2**). The resulting NaCS/BBY films are stable in DI water and contact angle experiments (**Figure S2.3**) revealed that the surface of the films was less hydrophilic than for films of the individual components: NaCS/BBY ($\theta = 61^\circ, 61^\circ$), NaCS ($\theta = 21^\circ, 21^\circ$) and BBY ($\theta = 45^\circ, 44^\circ$). These results support the proposed mechanism that combining two water soluble components in a LbL fashion can render the material less hydrophilic and thus more water resistant, through soft-bonding of the charged hydrophilic groups employed in the electrostatic self-assembly.

2.3.2 FTIR spectroscopy

Multi-layered films are generally held together by weak intermolecular interactions such as hydrogen bonding or ionic bonding.^{12, 20} NaCS is a water-soluble cellulose derivative consisting of hydroxyl groups and negatively charged sulfonate groups, and the degree of substitution (DS) of sulfonate groups on NaCS was determined by XPS analysis to be 1.2, which equates to 7.2 mmol/g (**Figure S2.4**). On the other hand, the azo photo-switch BBY (C₁₈H₁₈N₈·2HCl) has four amino groups attached to the phenyl rings, two of which are protonated to form the acid salt. Titration of BBY against NaOH revealed that BBY displays

a single pK_b value of 8.4 (**Figure S2.5**). The pH of the BBY dipping solution was $pH = 3$, at which BBY is water soluble.

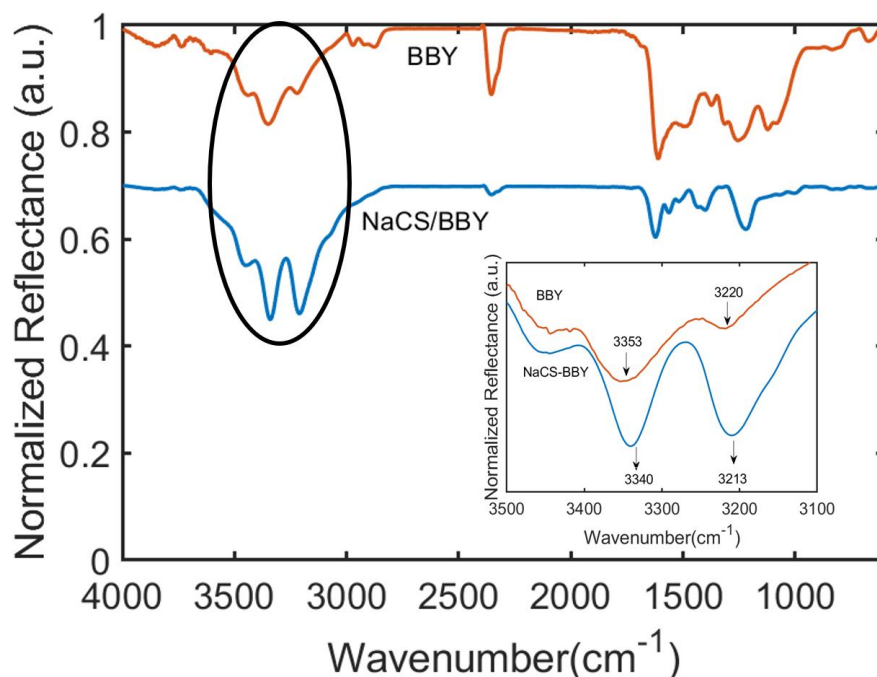


Figure 2.3 IR spectra of BBY only (orange) vs. multi-layered NaCS/BBY films (blue). Inset shows the changes in the N–H stretching mode of BBY only (orange) vs. in multi-layered NaCS/BBY films (blue).

At this pH two of the four amino groups are protonated, facilitating electrostatic interactions with the polymer. FTIR spectroscopy was used to assess the intermolecular interactions in the multi-layered films, with the IR spectrum of the multi-layered film deposited on an aluminium substrate shown in (**Figure 2.3**). The spectrum displays a characteristic N–H stretching of an amine from 3310–3350 cm^{-1} , highlighted by the black circle.^{15, 33} The inset of the IR spectrum shows the two bands which correspond to the free N–H stretch and the intra/intermolecular N–H stretch at 3353 cm^{-1} and 3220 cm^{-1} , respectively, for a solvent-cast film of BBY on an

aluminium substrate (orange line). The shape and size of these peaks are drastically different in the NaCS/BBY spectrum (blue line), as both peaks are shifted to lower energies of 3340 cm^{-1} and 3213 cm^{-1} , with a noticeable increase in the intensity of the latter which is assigned as the intra/intermolecular N–H stretch of the amine group. It is presumed that this is a result of increased intermolecular interactions between the polymer and the azo photo-switch due to the layer-by-layer packing in the multi-layered films. This compares well to early work published by Stockton and Rubner, where they observed similar changes in the IR spectra of polyaniline upon formation of polyaniline/PVP blends and multilayers.¹⁵

Furthermore, in **Figure 2.3**, the peaks between $2800\text{--}3000\text{ cm}^{-1}$ and $2270\text{--}2390\text{ cm}^{-1}$ can be assigned to N–H stretching of different amine salts. Generally, amine salts display N–H stretching between $2800\text{--}3200\text{ cm}^{-1}$, $2700\text{--}3000\text{ cm}^{-1}$ and $2300\text{--}2700\text{ cm}^{-1}$ for primary (NH_3^+), secondary (NH_2^+) and tertiary (NH^+) amine salts respectively.³⁴ BBY is capable of forming all three of these amine salts, since protonation of the four NH_2 groups and the two azo units (N=N bond) is possible. The peaks between $2800\text{--}3200\text{ cm}^{-1}$ were more pronounced for BBY in NaCS/BBY thin films (blue line) compared to bulk BBY (orange line) likely due to electrostatic interaction between the azobenzene photo-switch and the polymer.

The IR spectrum of bulk BBY also showed peaks between $1520\text{--}1625\text{ cm}^{-1}$ which can be assigned to aromatic C=C bending and/or N–H bending of primary and secondary amine salts.^{33, 34} The peaks between $1390\text{--}1440\text{ cm}^{-1}$ were assigned to N–H bending of amines, and $1212\text{--}1274\text{ cm}^{-1}$ to C–N stretching (**Figure 2.3**, **Figure S2.7**). These peaks were also present in NaCS/BBY IR spectrum. The IR spectrum of NaCS showed strong peaks at $3318\text{--}3630\text{ cm}^{-1}$, 1217 cm^{-1} and 985 cm^{-1} which can be assigned to free O–H stretching, ether C–O stretching and alcohol C–O stretching, respectively.³³ There were also two small peaks at 1396 cm^{-1} and 1464 cm^{-1} which can be assigned to sulfonate S=O stretching/ alkane C–H bending.³³ It was

difficult to identify the peaks associated with the polymer in the NaCS/BBY thin films since many of the peaks overlapped with those assigned to BBY.

2.3.3 Influence of pH, ionic strength, and temperature on film stability

LbL films can be sensitive to external stimuli such as pH, ionic strength of the solvent, and temperature. Before conducting the ‘sun and rain’ conditions dis-assembly experiments, we examined the effect of these stimuli on the stability of the thin films. To evaluate the effect of pH, the films were soaked in DI water adjusted from pH 2 to 12 and left out on the lab bench for 1 week under ambient conditions. Films which were immersed in pH 2–10 water did not show any signs of disassembly; the wash water remained colourless and there was no noticeable change in the UV-Vis spectrum of BBY. Conversely, the film submerged in very basic water (pH 11–12) underwent a noticeable colour change from red to orange, and the wash water clearly turned yellow (**Figure 2.4**). There was also a significant change in the UV-Vis spectrum with the broadening of the $\pi \rightarrow \pi^*$ transition absorption band from 450 nm for pH 2–10, to 385–490 nm for pH 11–12 (**Figure 2.4**). It is proposed that at pH 2–10 most of the amino groups of BBY are protonated which favours intermolecular interactions between the polymer and azo compound, and at very basic pH values the amino groups of BBY are deprotonated which disrupts the weak intermolecular forces holding the layers together. This mechanism is supported by the titration results of BBY against NaOH where it was determined that BBY has a pK_b value of 8.4 (**Figure S2.5**). Additionally, the deprotonation of the azo compound is responsible for the colour change from red to orange due to changes in the electrostatic character of the azo unit.

The influence of salt on the stability of the thin films was evaluated by submerging the films in a beaker containing 2 M NaCl solution at RT for 1 week. There was some observed leaching of BBY into the water which turned pale yellow, as well as a slight blue shift in the $\pi \rightarrow \pi^*$ transition absorption band from 450 nm to 445 nm (**Figure S2.7**).

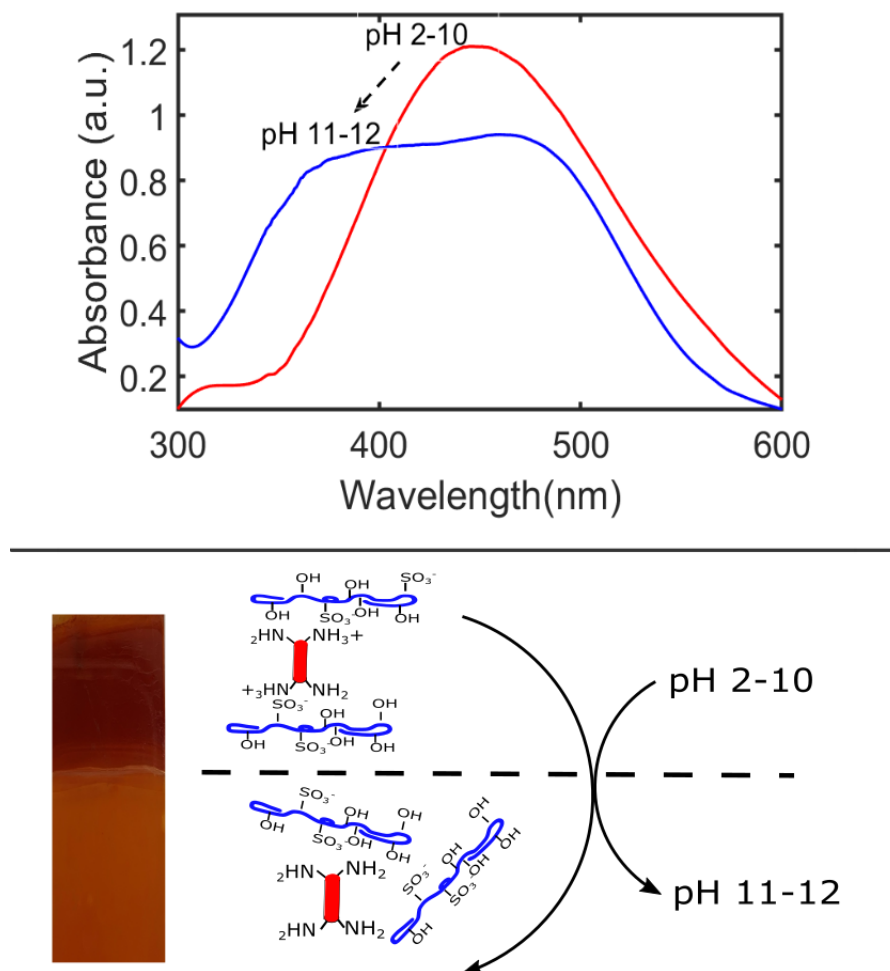


Figure 2.4 (Top) UV-Vis absorption spectra of NaCS/BBY films in response to change in pH. Between pH 2–10 the $\pi \rightarrow \pi^*$ transition absorption band is at 450 nm and at pH 11–12 there is significant broadening of the absorption band to 385–490 nm. (Bottom) Image of the film showing colour change from red (pH 2–10) to orange (pH 11–12) and a schematic of the proposed molecular changes which occur in response to change in pH.

There was also a decrease observed in the absorbance of BBY by 32 % which indicated removal of some (perhaps excess) BBY from the film (**Figure S2.7**), as one might expect salt to disrupt the electrostatic interactions between the positively charged protonated amino groups (NH_3^+) of BBY and the negatively charged sulfonate groups (SO_3^-) of NaCS. Lastly, to assess the impact of temperature on the stability of the thin films, the films were submerged in beakers containing DI water held at RT (21 °C), at 70 °C, and at 100 °C for 1 hour. Films were observed to remain stable at 21 °C and 70 °C but began to partially disassemble at 100 °C. There was a 35 % reduction in the absorbance of BBY in the thin films exposed to this high temperature, and the wash water turned yellow (**Figure S2.8**). At high temperatures hydrogen bonds can suffer degradation, and it is likely that at 100 °C sufficient hydrogen bonds between the amino groups of BBY and hydroxyl groups of NaCS were broken, allowing the film to disassemble. This observation shows that the films are very stable even when exposed to relatively high temperatures, and thus any heating effect which occurs during exposure to 460 nm light in the ‘sun and rain’ conditions experiment should not be expected to play a significant contribution to the disassembly process.

2.3.4 Pump-probe experiments to examine isomerization of BBY

Having established the effects of pH, ionic strength, and temperature of the wash solution on the stability of the films, the *trans-cis* isomerization behaviour of BBY was evaluated using optical pump-probe experiments. The photo-switching of BBY could not be monitored easily with a UV-Vis spectrophotometer, since bisazobenzene photo-switches generally have fast isomerization rates, which makes it difficult to capture the thermal back relaxation of the azo compound in detail, so a separate fast laser setup was constructed. A solution of BBY in THF was pumped by irradiating with 532 nm laser light at a power of approximately 100 mW/cm²

and probed with 488 nm laser (blue light) at low power and the signal monitored over time (Figure 2.5).

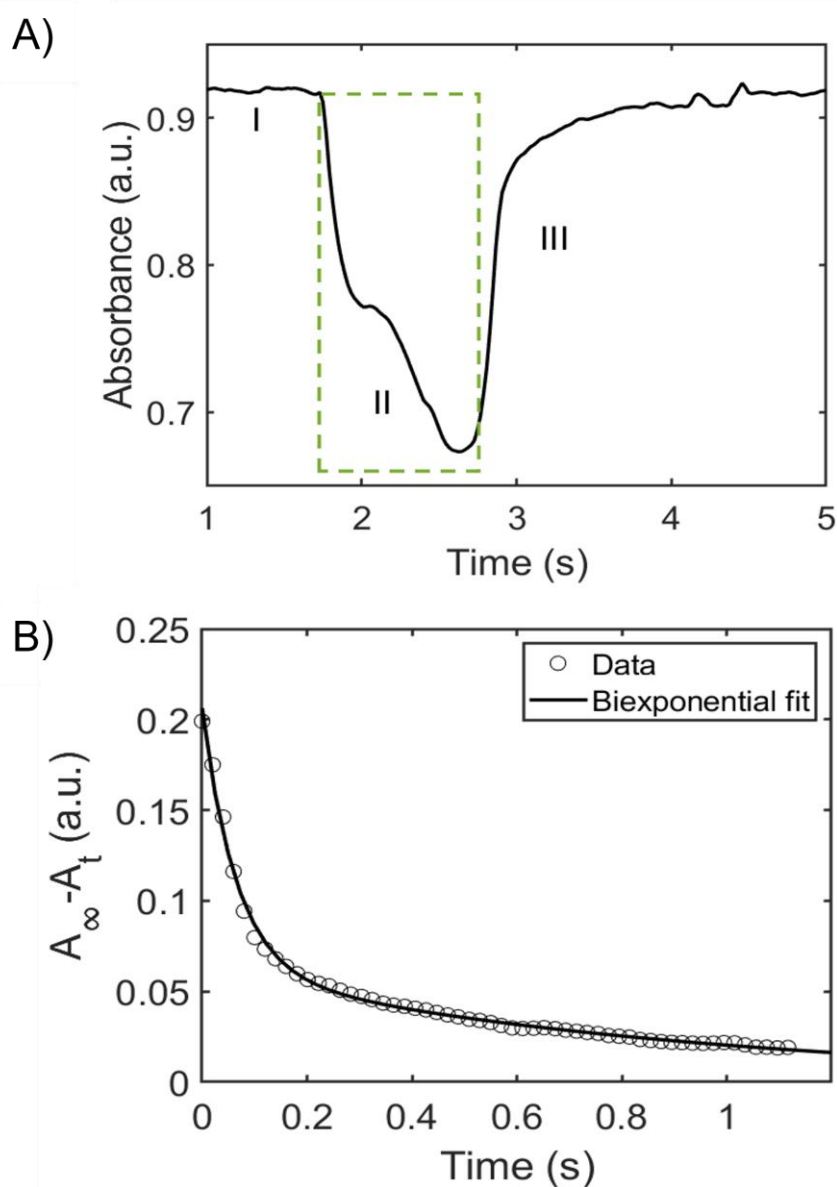


Figure 2.5 (A) Pump-probe isomerization plot showing the change in absorbance over time for BBY solution in THF: (I) Pump beam is off, (II) Green box represents when the laser is switched on for 1 s and (III) pump beam is turned off showing thermal back relaxation. (B) Decay of the *cis* isomer with fit with a biexponential function.

We were able to observe switching from *trans*-to-*cis* states of BBY represented by the green box in **Figure 2.5a**, as well as the thermal back relaxation of BBY in dark which showed a biexponential decay (**Figure 2.5b**). In-depth analysis towards the detailed mechanism of the various BBY isomerizations is the subject of another full study forthcoming.

2.3.5 Confocal Raman spectroscopy

The *trans*-to-*cis* isomerization of BBY when sandwiched in the multi-layered films was confirmed by confocal Raman spectroscopy, which was used to probe changes in the orientation of BBY upon exposure to 532 nm light. For these measurements, multi-layered films were deposited on a quartz substrate and excited with a 532 nm laser at increasing laser power, with a scan rate of 1s/ μm and resolution of 1 spectra/ μm across the width of the thin films (25 mm). Previous studies have shown that the N=N Raman shift of unsubstituted *trans* azobenzene occurs at 1424 cm^{-1} and N=N Raman shift of unsubstituted *cis* azobenzene occurs at 1510 cm^{-1} .³⁵ The Raman shift at 612 cm^{-1} corresponds to the C–N=N–C torsion associated with *cis* azobenzene.³⁵ Additionally, the Raman shifts at 1283 cm^{-1} correspond to C–N stretching, at 1379 cm^{-1} to C–C stretching, at 1574 cm^{-1} to R–C–C stretching (where R = a benzene ring), and at 1612 cm^{-1} to NH₂ scissoring.³⁵⁻³⁷ The first scan of the multi-layered films, which was performed at a relatively low laser power of 0.1 mW, displayed Raman shifts at 482 cm^{-1} , 997 cm^{-1} , 1157 cm^{-1} , 1283 cm^{-1} , 1379 cm^{-1} , and 1612 cm^{-1} as seen in **Figure 2.6a**. As the laser power increased from 0.1 mW to 0.5 mW in 0.1 mW increments, there were notable changes in the spectra, of the appearance of Raman shifts at 612 cm^{-1} and 1521 cm^{-1} and an increase in the intensity of the peak at 1574 cm^{-1} with a simultaneous decrease in the intensity of the Raman shifts at 1283 cm^{-1} and 1612 cm^{-1} . There was also a slight shift in the position of the peak at 1379 cm^{-1} to lower energy observed, and the emergence of a peak at 1296 cm^{-1} . It

is proposed that these changes in the Raman shift are due to a change in the orientation of the BBY molecules from a planar *trans* state to a non-planar *cis* state.^{35, 36}

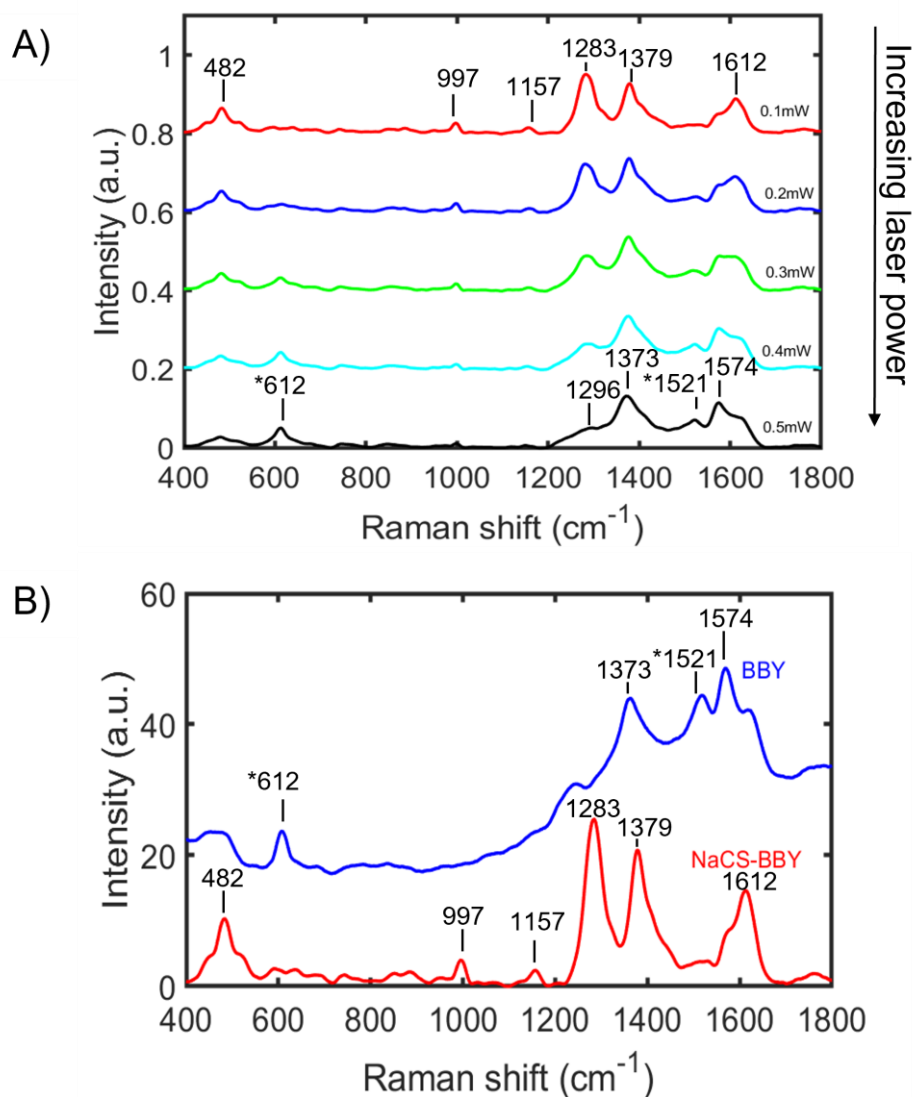


Figure 2.6 (A) Changes in the Raman spectra of BBY in multi-layered NaCS/BBY thin films with increasing 532 nm laser power (0.1–0.5 mW). (B) Raman spectra of BBY only (blue) and NaCS/BBY films (red) upon 1st scan at 0.1 mW 532 nm laser power. (*) represents the characteristic *cis* BBY Raman peaks.

It was also observed that if the 532 nm laser at the lowest power (0.1 mW) was focused on the same spot on a NaCS/BBY thin film for a prolonged period ($t > 50$ s) the Raman signal centred around the peak at 1285 cm^{-1} , which corresponds to C–N stretching, decreased over time. The *trans*-to-*cis* photoisomerization was fit best to a biexponential function (**Figure S2.9**), and detailed optical characterization is the topic of a separate forthcoming paper.

These observations confirm that BBY can undergo isomerization even when bound in multi-layered films, where the free volume is significantly reduced as compared to when in solution. **Figure 2.6b** shows the Raman shifts of BBY molecules only, deposited onto a quartz slide (blue line), which can be considered as ‘free azo’, compared to the Raman shifts of BBY bound in the multi-layered films (red line). It was observed that even at the lowest laser power (0.1 mW) the Raman shifts associated with *cis* BBY at 612 cm^{-1} and 1521 cm^{-1} were present for the ‘free azo’ but were absent/less intense for BBY confined in the multi-layered films. Additionally for the films with BBY only, as the power of the laser increased, the peaks corresponding to *cis*-BBY increased (**Figure S2.10a**). It was also observed that there was considerable fluorescence interference in the Raman spectra of BBY only between $1700\text{--}4000\text{ cm}^{-1}$, not seen in the NaCS/BBY thin films (**Figure S2.10b**). Three peaks at 2914 cm^{-1} , 3201 cm^{-1} , and 3096 cm^{-1} were still able to be identified, can be assigned to N–H stretching.³⁸ **Figure S2.8c** shows the Raman spectrum of NaCS which had Raman shifts at 3495 cm^{-1} , 2959 cm^{-1} , 1065 cm^{-1} , and 831 cm^{-1} which can be assigned to O–H stretching, C–H stretching, asymmetric C–O–C, and symmetric C–O–C/ S=O stretching, respectively.³⁸ The weak Raman shifts at $3203\text{--}3314\text{ cm}^{-1}$, 2910 cm^{-1} , 993 cm^{-1} , and 882 cm^{-1} confirm the presence of NaCS in the multi-layered NaCS/BBY thin films (**Figure. S2.8c**). Due to the high fluorescence signal in the Raman spectra data could not be attained for either the NaCS/BBY thin films or BBY only films when using a red/IR probe (785 nm).

2.3.6 ‘Sun and rain’ exposure experiment

Having established that the photo-switch, BBY, can undergo *trans*-to-*cis* isomerization when in the multi-layered films, an experiment was then constructed to mimic environmental conditions of sunlight and rainfall, to assess the disassembly of the films triggered by blue visible light. The design of the ‘sun and rain exposure’ setup is shown in **Figure 2.1**. The films were clamped under a stream of DI water (pH = 7, T = 21–25 °C, flow rate = 1 L/min). The upper section of the films was left exposed to light while the lower section was covered using a black mask, as a control. The films were irradiated continuously using a 460 nm LED (12 V, 299 mA) light, and the films were removed, dried, and assessed at various intervals, by photographs and UV-Vis measurements of the films taken at each time interval.

Figure 2.7a shows changes in the appearance of the multi-layered films after exposure to blue light and washing with DI water for 1 week (t = 162 hr). While the films did not fully disassemble there was a noticeable decrease in the intensity of the red colour of the films as well as the absorbance of BBY over time. **Figure 2.7c** shows that the absorbance at 450 nm for the unmasked region of the films (section exposed to blue light) decreased by 65 % while **Figure 2.7d** shows that the masked region (control) was stable with a negligible decrease in BBY absorbance. Additionally, during the disassembly process the peaks related to the polymer NaCS became more pronounced ($\lambda = 200$ nm and 300 nm) as more and more of the photo-switch BBY was removed from the films. NaCS was also removed from the films evidenced by the decrease in the absorbance at ($\lambda = 200$ nm and 300 nm) from t = 66–162 hr. **Figure 2.7b** shows a rate plot of Ln absorbance over time (Ln A vs. t), with slope giving the rate of disassembly which follows first order kinetics. The masked/control regions often suffered a decrease in the dark attributed to leaching of excess dye trapped in the assemblies, yet was then stable to disassembly. The average rate of disassembly for the irradiated

(unmasked) section of the films was calculated to be $k_a = 7 \pm 1 \times 10^{-3}$ absorbance units/hr. We also performed a thickness measurement of the unirradiated regions by AFM, further confirming the robustness of the material and water resistance when not irradiated. After 2 weeks of soaking in DI water in the dark, a height measurement of 397 nm was confirmed, from an initial height measurement of $390 \text{ nm} \pm 15 \text{ nm}$ (**Figure S2.11**). This shows that the disassembly of the thin films could be successfully and effectively triggered using 460 nm (blue) light.

The disassembly of the thin films using (Montreal) tap water with $\text{pH} = 8$ (**Figure S2.12**) was also assessed, as this might be more relevant to a cost-effective industrial disassembly process. For films washed with tap water, the upper section of the films was completely disassembled while the bottom masked section remained nearly entirely intact. During the disassembly process the peaks related to the polymer NaCS became more pronounced ($\lambda = 200 \text{ nm}$ and 300 nm) as the photo-switch BBY was removed from the films. Complete removal of the films from the unmasked upper section was confirmed by the disappearance of absorption bands of BBY ($\lambda = 450 \text{ nm}$) and NaCS ($\lambda = 200 \text{ nm}$ and 300 nm). Additionally, there was an observed broadening of the $\pi \rightarrow \pi^*$ transition absorption band of BBY during the disassembly process, possibly due to the presence of salts, trace elements, or other ionic contaminants common in tap water, which can help screen the electrostatic charges holding the multilayer structure together. The rate of disassembly of the films when washed with tap water was also 30-fold faster than when the films were washed with DI water, during irradiation with 460 nm light. The average rates of disassembly of the films were measured to be 0.007 ± 0.001 absorbance units/hr and 0.22 ± 0.02 absorbance units/hr for DI water and tap water, respectively. It is speculated that the high conductivity of tap water, on the order of 1000 Siemens /cm, leads to disassembly behaviour similar to high ionic strength NaCl solutions, as discussed previously.

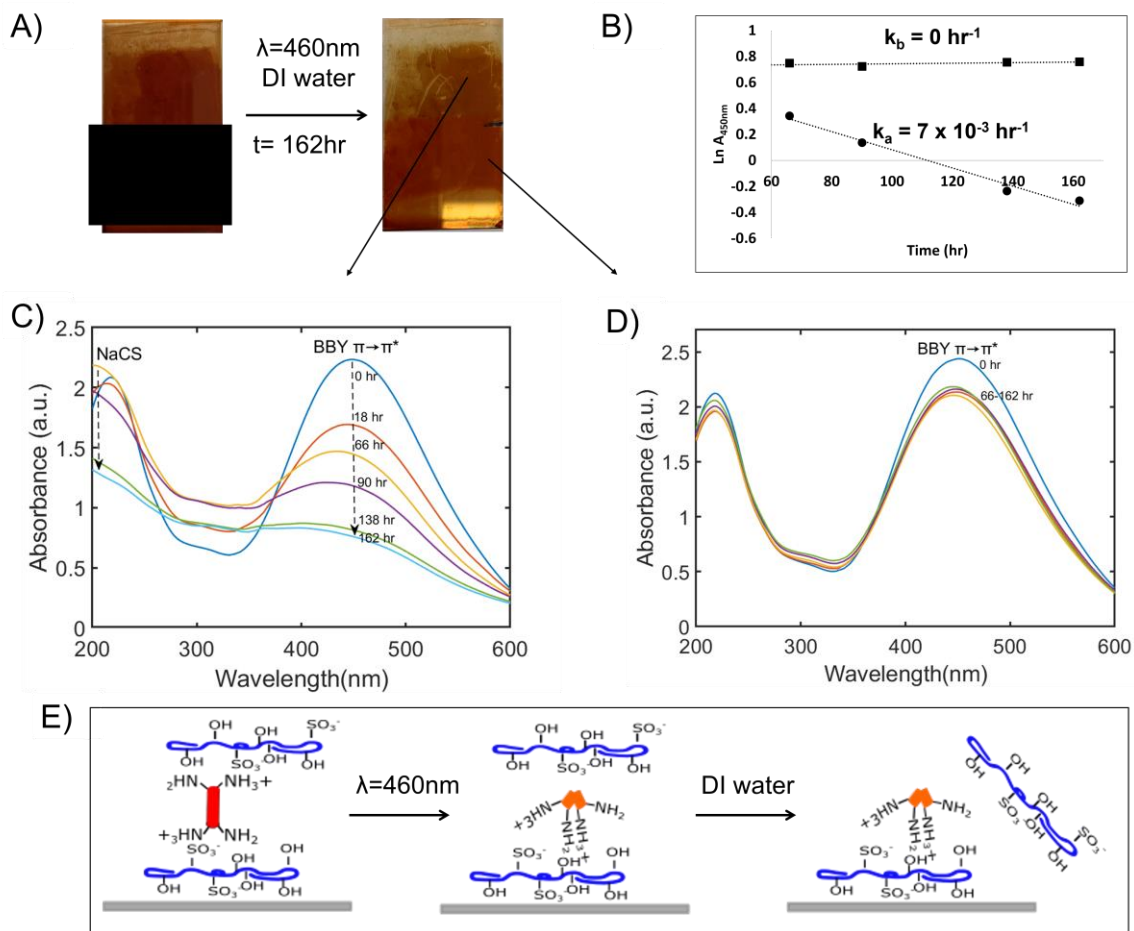


Figure 2.7 (A): Disassembly of NaCS/BBY films triggered by blue light (460 nm LED, 299 mA, 12.50 V). Upper section of films was left exposed (unmasked) while the lower section was masked. (B): Plot of $\ln A$ vs. t during disassembly process for unmasked (circles) vs. masked (squares) sections of the films. (C and D): Time resolved UV-Vis spectra of NaCS/BBY films following irradiation with blue light, washed using DI water for unmasked and masked sections, respectively ($t = 168$ hr). (E): Schematic of disassembly of NaCS/BBY thin films under ‘simulated sunlight and rainfall’ experimental conditions.

To rationalize the observed changes in the UV-Vis spectra during the disassembly process, we propose the following mechanism: Within the multi-layered films, there are many

layers of BBY molecules sandwiched between polymer layers. During irradiation with 460 nm light the upper layers consisting of *trans*-BBY are converted to *cis*-BBY which changes the polarity and geometry of BBY drastically from a planar to a non-planar, twisted molecule. Unsubstituted azobenzene can undergo a change from 9.9 Å to 5.5 Å as it undergoes *trans*-to-*cis* isomerization (a 44 % reduction in length), and more importantly can lead to a significant disruption to the orientational geometry of the bonds holding the structure together.³⁹ These geometric changes have been supported by Density Functional Theory calculations, and a detailed analysis and mechanism of these optical inter-conversions is the subject of a separate study, to be published in parallel. These changes in the geometry and alignment of BBY are proposed to disrupt the electrostatic interactions between BBY and the polymer, leading to the disassembly of the upper layers. As the upper layers are re-solubilized and are washed away, the blue light (460 nm) can penetrate more deeply to lower layers, resulting in further disassembly of the films, layer-by-layer in ‘reverse’ (**Figure 2.7e**). It is of note that the component materials (azo dye, and cellulose polymer) should not suffer any chemical change, or other degradation during this dis-assembly process, so in principle could be completely recycled back into useable starting materials once again, providing a completely sustainable closed-loop waste-free fabrication process, if a suitable separation and recovery process could be developed, also the subject of a separate parallel study.

2.4 Conclusions

Stable multi-layered films (NaCS/BBY) formed between photo-responsive layers and layers containing a cellulose-based polymer were prepared, and their controlled disassembly when triggered by blue light was confirmed and characterized. These results demonstrate the utility

of employing natural polymers in fabricating dynamic, visible light-reversible materials. The water soluble, biodegradable and bio-sourced polymer NaCS, and the water soluble azobenzene photo-switch BBY were assembled into multilayers to form robust, water-resistant, optically clear, and uniform thin films of 50 bilayers, 390 ± 15 nm thick, held together by weak intermolecular interactions between the hydroxyl and sulfonate groups of NaCS and the amino groups and amine salts of BBY. The disassembly of these LbL films however could be triggered on demand using 460 nm blue visible light, confirmed by time-dependent UV-Vis spectroscopy of the photo-disassembly in blue light vs. dark. The isomerization of BBY in solution and thin films under irradiation was confirmed by pump-probe and Confocal Raman spectroscopy experiments, respectively. The isomerization of azobenzenes results in significant microstructural changes from a planar, nonpolar structure (E) to a polar, twisted conformation (Z), resulting in large changes in the material, leading to complete and controlled disassembly back into their water-soluble components reversibly, in principle ready for re-use. Future development work includes the preparation of free-standing films and analysis of physical and mechanical properties of the films: tensile strength, elasticity, and water vapor permeability, and will be the topics of separate forthcoming studies. It is also of great future interest to examine the mechanisms in detail to effectively separate and recover the two components from each other after the disassembly of the films, with detailed optical analysis and DFT calculations, which is being undertaken, to be published separately. Lastly, it is hoped that these new ‘reversibly soft-bonded’ materials can lead in future to a new class of materials that be easily and cheaply fabricated from water-soluble and low-toxicity ‘green’ components, recovered after dis-assembly under gentle environmental conditions, unchanged and ready for re-use, as potential replacements for many of the current single-use artificial plastics.

2.5 References

1. D. Klemm, B. Heublein, H. P. Fink and A. Bohn, *Angewandte Chemie International Edition in English*, 2005, **44**, 3358–3393.
2. P. Sonkaew, A. Sane and P. Suppakul, *Journal of Agricultural and Food Chemistry*, 2012, **60**, 5388–5399.
3. Q. Tarrés, P. Mutjé and M. Delgado-Aguilar, *Cellulose*, 2019, **26**, 6917–6932.
4. J. Wang, D. J. Gardner, N. M. Stark, D. W. Bousfield, M. Tajvidi and Z. Cai, *ACS Sustainable Chemistry & Engineering*, 2017, **6**, 49–70.
5. F. Li, P. Biagioni, M. Bollani, A. Maccagnan and L. Piergiovanni, *Cellulose*, 2013, **20**, 2491–2504.
6. K. Torvinen, J. Sievänen, T. Hjelt and E. Hellén, *Cellulose*, 2012, **19**, 821–829.
7. Y. Wang, X. Wang, Y. Xie and K. Zhang, *Cellulose*, 2018, **25**, 3703–3731.
8. G. Chen, B. Zhang, J. Zhao and H. Chen, *Carbohydrate Polymers*, 2013, **95**, 332–337.
9. Q.-X. Wu, Y.-X. Guan and S.-J. Yao, *Frontiers of Chemical Science and Engineering*, 2018, **13**, 46–58.
10. G. Chen, B. Zhang, J. Zhao and H. Chen, *Food Hydrocolloids*, 2014, **35**, 476–483.
11. G. Decher and J.-D. Hong, *Makromolekulare Chemie. Macromolecular Symposia*, 1991, **46**, 321–327.
12. E. Kharlampieva, V. Kozlovskaya and S. Sukhishvili, *Advanced Materials*, 2009, **21**, 3053–3065.
13. C. Faul and M. Antonietti, *Advanced Materials*, 2003, **15**, 673–683.
14. Q. Yi and G. B. Sukhorukov, *Soft Matter*, 2014, **10**, 1384–1391.
15. W. B. Stockton and M. F. Rubner, *Macromolecules*, 1997, **30**, 2717–2725.
16. Q. Hou, X. Wang and A. J. Ragauskas, *Cellulose*, 2019, **26**, 4787–4798.
17. X. Tian, B. Wang, J. Li, J. Zeng and K. Chen, *Carbohydrate Polymers*, 2017, **157**, 704–710.
18. F. Li, P. Biagioni, M. Finazzi, S. Tavazzi and L. Piergiovanni, *Carbohydrate Polymers*, 2013, **92**, 2128–2134.
19. F. Carosio, M. Ghanadpour, J. Alongi and L. Wagberg, *Carbohydrate Polymers*, 2018, **202**, 479–487.

20. M. Landry, K. Gu, S. Harris, L. Al-Alwan, L. Gutsin, D. J. De Biasio, Bernie, D. Nakamura, T. C. Corkery, T. T. Kennedy and C. J. Barrett, *Macromolecular Bioscience*, 2019, **19**, 1900036–1900047.
21. Q. Bian, M. Jin, S. Chen, L. Xu, S. Wang and G. Wang, *Polymer Chemistry*, 2017, **8**, 5525–5532.
22. H. Rau and S. Yu-Quan, *Journal of Photochemistry and Photobiology A: Chemistry*, 1988, **42**, 321–327.
23. C. J. Barrett, J. I. Mamiya, K. G. Yager and T. Ikeda, *Soft Matter*, 2007, **3**, 1249–1261.
24. C. Slavov, C. Yang, L. Schweighauser, C. Boumrifak, A. Dreuw, H. A. Wegner and J. Wachtveitl, *Physical Chemistry Chemical Physics*, 2016, **18**, 14795–14804.
25. M. F. S. Teixeira, M. M. Barsan and C. M. A. Brett, *RSC Advances*, 2016, **6**, 101318–101322.
26. S. Sun, S. Liang, W.-C. Xu, G. Xu and S. Wu, *Polymer Chemistry*, 2019, **10**, 4389–4401.
27. K. G. Yager and C. J. Barrett, *Macromolecules*, 2006, **39**, 9320–9326.
28. M. Matsumori, A. Takahashi, Y. Tomioka, T. Hikima, M. Takata, T. Kajitani and T. Fukushima, *ACS Applied Materials & Interfaces*, 2015, **7**, 11074–11078.
29. S. Schoelch, J. Vapaavuori, F. G. Rollet and C. J. Barrett, *Macromolecular Rapid Communications*, 2017, **38**, 1600582–1600590.
30. Q. Si, Y. Feng, W. Yang, L. Fu, Q. Yan, L. Dong, P. Long and W. Feng, *ACS Applied Materials & Interfaces*, 2018, **10**, 29909–29917.
31. C. Qin, Y. Feng, H. An, J. Han, C. Cao and W. Feng, *ACS Applied Materials & Interfaces*, 2017, **9**, 4066–4073.
32. H. Orelma, A. Hokkanen, I. Leppänen, K. Kammiovirta, M. Kapulainen and A. Harlin, *Cellulose*, 2020, **27**, 1543–1553.
33. MilliporeSigma IR Spectrum Table & Chart, <https://www.sigmaaldrich.com/CA/en/technical-documents/technical-article/analytical-chemistry/photometry-and-reflectometry/ir-spectrum-table>, (accessed January 4th, 2022).
34. B. Smith, *Spectroscopy*, 2019, **34**, 30–37.
35. C. M. Stuart, R. R. Frontiera and R. A. Mathies, *Journal of Physical Chemistry A*, 2007, **111**, 12072–12080.
36. N. S. Chong, K. Donthula, R. A. Davies, W. H. Ilsley and B. G. Ooi, *Vibrational Spectroscopy*, 2015, **81**, 22–31.
37. T. I. Burganov, S. A. Katsyuba, T. A. Vakhonina, A. V. Sharipova, O. D. Fominykh and M. Y. Balakina, *Journal of Physical Chemistry C*, 2018, **122**, 1779–1785.

38. Horiba Raman data analysis- Raman bands, https://static.horiba.com/fileadmin/Horiba/Technology/MeasurementTechniques/Molecular_Spectroscopy/Raman_Spectroscopy/Raman_Academy/Raman_Tutorial/Raman_bands.pdf, (accessed January 4th, 2022).
39. F. P. Nicoletta, D. Cupelli, P. Formoso, G. De Filpo, V. Colella and A. Gugliuzza, *Membranes (Basel)*, 2012, **2**, 134–197.

2.6 Appendix 2: Supporting information for Chapter 2

2.6.1 Experimental methods

2.6.1.1 Materials

NaCS was purchased from Scientific Polymer (CAT # 023) and BBY was procured from Sigma (LOT 34H3729, $C_{18}H_{18}N_8 \cdot 2HCl$, FW=419.3 g/mol), and was recrystallized before use. Spectroscopic grade THF was purchased from Sigma (CAS # 109-99-9). Sodium chloride salt (CAS # 7647-14-5) was purchased from ACP. NaOH pellets (CAS # 1310-73-2) were purchased from Sigma and 36 % HCl from ACP (LOT # H-6100). The dipping solutions were prepared by dissolving the chemicals in deionized water (MiliQ system). A 10 mM solution of NaCS (molar in terms of a one monomer repeat unit) was prepared (pH = 6.4) and a 3 mM solution of BBY was prepared (pH = 3). The structures of the polymer and dye used are shown in (Figure 2.1).

2.6.1.2 LbL assembly of thin films

Multi-layered films of sodium cellulose sulfate-Bismarck Brown Y (NaCS/BBY) were deposited on glass, quartz, and aluminium substrates. All slide surfaces, excluding the aluminium, which was cleaned with water and acetone, were cleaned using a 'piranha solution' (mixture of sulfuric acid/ hydrogen peroxide). The multilayer deposition process was as follows: The treated substrates were immersed in the polymer solution for $t = 10$ min, followed by three rounds of rinsing with deionized (DI) water (pH = 7) for 1 min each. The films were then immersed in the azo solution for $t = 10$ min, followed by 3 rounds of rinsing with DI water. This dipping process was repeated to form a film with 50 bilayers. The process of LbL assembly is shown in (Figure 2.1).

2.6.1.3 Characterization of LbL NaCS/BBY thin films

UV-Vis spectroscopy: The UV-Vis spectra of BBY in water and NaCS in water were recorded on a Cary 300 Bio UV-Vis spectrophotometer, using a Hellma quartz cuvette (Catalog # 117-100-10-40) with a pathlength of 1 cm, over the range 200–800 nm. The absorption of BBY in the LbL films was then monitored by UV-Vis spectroscopy of the dye's $\pi \rightarrow \pi^*$ transition peak. This was taken directly from films deposited on glass and quartz slides.

FTIR spectroscopy: The Infrared (IR) spectra of a solvent cast BBY film and multi-layered NaCS/BBY films on an aluminium substrate were acquired on a Bruker Hyperion 1000 microscope coupled with the Bruker Vertex 70 FTIR spectrometer (Catalog # : BOPT Hyperion 1000, BOPT Vertex 70). The IR spectra were recorded in reflectance mode over the range 600 to 4000 cm^{-1} , with a resolution of 2 cm^{-1} averaged from 64 scans. The Infrared (IR) spectra of powdered BBY and powdered NaCS were recorded on an FTIR spectrometer (Spectrum II, PerkinElmer, USA) with a single bounce diamond attenuated total reflectance (ATR) accessory employed. The IR spectra was recorded in transmittance mode over the range 400 to 4000 cm^{-1} with a resolution of 1 cm^{-1} averaged over 32 scans.

Confocal Raman spectroscopy: Raman spectra and optical microscopy images of a solvent cast BBY film, a solvent cast NaCS film and multi-layered NaCS/BBY films on quartz substrates were recorded using a confocal Raman microscope (Alpha 300R, WITEC). Measurements were performed using a 532 nm laser at varying power, 100 \times objective (Zeiss, numerical aperture [NA] = 0.9) with a thermoelectrically cooled CCD detector behind a 600-g/mm grating, with integration time: 1 s, scan speed: 1 s/ μm , and resolution: 1 spectra/ μm . Kinetic measurements were performed by monitoring the change in the intensity of the Raman signal near the 1285 cm^{-1} peak for 50 s, at constant laser power of 0.1 mW, focusing on the same spot.

SEM-EDS: The surface (planar view) of the NaCS/BBY thin films deposited on a glass substrate was imaged by high resolution Field Emission Scanning Electron Microscopy (FE-SEM) using a FEI Quanta 450 Environmental Scanning Electron Microscope with EDAX Octane Super 60mm SDD. Elemental mapping was done using the TEAM EDS analysis system. The accelerating voltage used was 10 kV after sputter coating with platinum with a thickness of approximately 7 nm. Other parameters: resolution: 128.9 eV, mag: 6387 and amplitude time: 7.68 μ s.

XPS analysis: the degree of substitution (DS) of NaCS polymer was determined by XPS analysis, performed on a Thermo Scientific K-Alpha, with X-ray source: Aluminium- $k\alpha$, spot size of 400 μ m. Survey scan: pass energy of 200 eV, step size of 1 eV and high-resolution scan (C1s, O1s, S2p, N1s, Na1s): pass energy of 50 eV, step size of 0.1 eV. The software used for data processing was Thermo Avatage (version 5.9914).

Contact angle measurements: the contact angles of the surface of the LbL NaCS/BBY thin films, films of solvent cast NaCS and films of solvent cast BBY on quartz substrates were determined using an optical contact angle goniometer (Model OCA 20, Dataphysics, USA). The sessile drop method was employed, whereby a droplet of water was placed on the sample mounted on a stage, and the image of the drop taken by a high-resolution camera. Images were recorded instantaneously ($t = 0$ s) and overtime ($t = 1$ min, 2 min and 4 min) to allow the drop to equilibrate. The contact angle was then determined using the SCA20 software.

2.6.1.4 Film stability: ionic strength, temperature, and pH

To evaluate the effect of ionic strength of the ‘wash solution’ on the stability of the LbL films, films were soaked in 60mL DI water (pH = 7), tap water (pH = 8) and 2M NaCl(aq) at RT for 7 days. To analyze the effect of pH, films were left in 60 mL DI water of varying pH values (=

2, 4, 7, 8, 9, 10, 11, and 12) to soak for 7 days at RT. The pH of DI water was adjusted using concentrated NaOH and HCl stock solutions. To analyze the effect of heat, films were soaked in 60 mL DI water at RT = 21 °C, 70 °C and 100 °C for 1 hr. The UV-Vis spectra were acquired before and after treatments for all films.

2.6.1.5 Pump-probe isomerization experiments

A solution of BBY in THF in a quartz cuvette (pathlength 1 mm) was probed using a tuneable Ar⁺ laser at $\lambda = 488$ nm at low laser power (1 mW/cm²) and irradiated for 1 s using a 532 nm laser at high laser power (100 mW/cm²). The signal was recorded before, during and after irradiation. Measurements were performed in triplicate.

2.6.1.6 Simulated sunlight and rainfall experiments

‘Sunlight and rainfall’ conditions were simulated to examine the environmental disassembly of the films by light, as shown in (**Figure 2.1**). The films deposited on glass and quartz substrates were clamped under DI water (pH = 7) or (Montreal) tap water (pH = 8), flow rate = 1 L/min, T = 21–25 °C and the bottom section of the films were covered with a black mask. The films were irradiated with visible 460 nm (229 mA, 12.50 V) light. The UV-Vis absorption spectra were recorded from 200–600 nm for quartz slides and 330–600 nm for glass slides. UV-Vis measurements were taken at various intervals. The films were dried under a stream of air for 20 s before each measurement. The simulated sunlight & rainfall experiments were performed in triplicate, and the disassembly rate was calculated according to the **Equation** below:

$$\ln[A_{450\text{ nm}}] = -kt + \ln[A_{450\text{ nm}}]_0$$

2.6.1.7 AFM

Atomic Force Microscopy (AFM) was used to determine the thickness of the films. Films were prepared by applying a parafilm mask to the middle of the glass substrate during the dipping process. The mask was removed following film deposition and the masked area cleaned using ethanol to remove any residue. The thickness of the films was measured as the change in height at the boundary of the films. Measurements were performed at 6 different areas along the film's boundary. Surface topology of the bare glass and NaCS/BBY film deposited on glass were also acquired by AFM. AFM measurements were performed on a MFP3D AFM equipped with molecular force probe controller (Asylum Research – Oxford Instruments) in AC mode in air using ACTA (AppNano) probes. Data processed using MountainsSPIP v. 9.1.9837 (digital Surf). Scan specs: resolution (512×512), Scan rate (0.5 Hz and 1.0 Hz), scan size 5–50 μm .

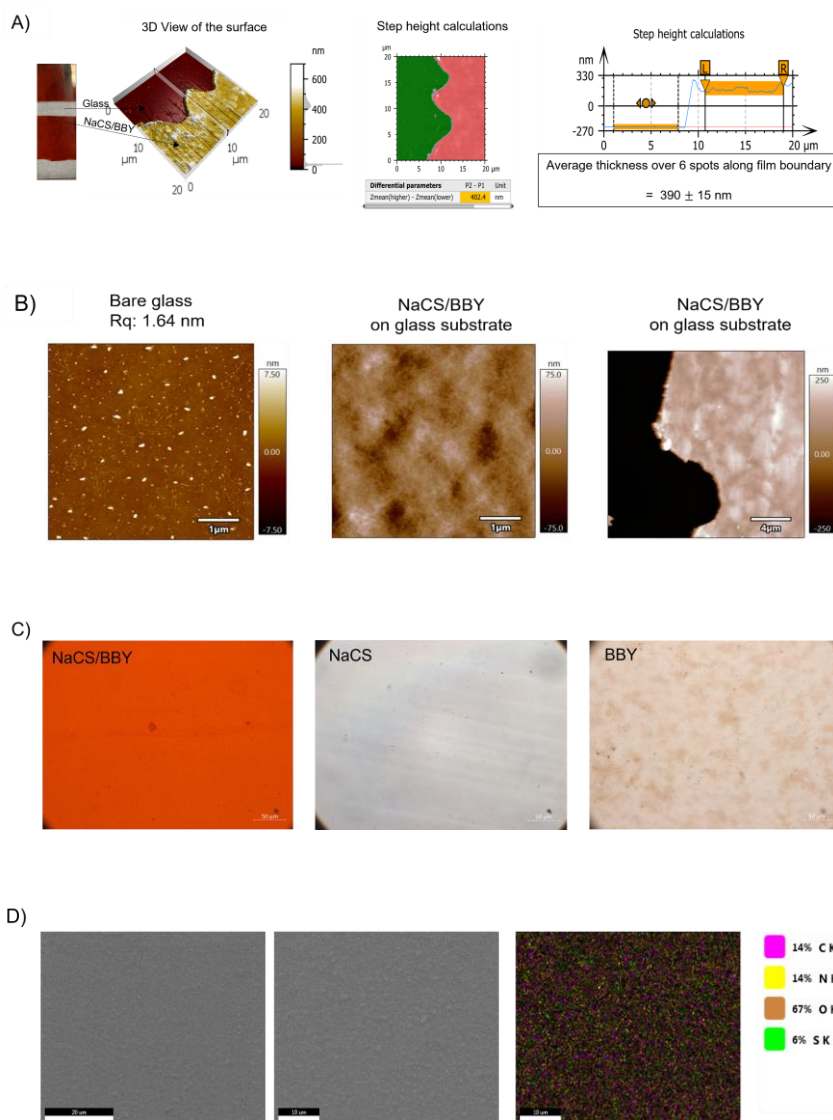


Figure S2.1 (A) AFM used to determine the thickness of NaCS/BBY films deposited on glass substrate (Rq: 1.97 nm). (Right) Image of NaCS/BBY thin film (red) deposited on glass substrate (grey) and 3D view of the surface of the thin film (yellow) onto on glass substrate (red). (Middle) Step height calculations between the glass substrate (green) and thin film (red). (Left) Step height calculations along one line of the thin film shown in the top, right figure. Measurement parameters: 20 μm , FAA 1.0 V, SP: 568 mV, IG 5, 0.5 Hz, 512 \times 512. (B) AFM of the surface topology of (Left) bare glass substrate (Rq: 1.97 nm) and (Middle) NaCS/BBY deposited on glass substrate showing a fairly uniform surface. (Right) 3D image of surface and edge of NaCS/BBY film deposited on glass substrate. (C) Confocal Raman optical Images of (Left) NaCS/BBY LbL thin film (Middle) NaCS polymer and (Right) BBY azo dye deposited on quartz substrate. Images were obtained using confocal Raman microscope (Alpha 300R, WITEC), 100 \times objective. Scale bar = 50 μm . (D) (Right & Middle) SEM images of NaCS/BBY thin film deposited on glass substrate at 2 different areas of interest (scale bars are 20 μm and 10 μm , respectively). (Left) Elemental mapping of NaCS/BBY thin film showing presence of polymer NaCS (S = 6 %) and BBY (N = 14 %) uniformly across film surface.

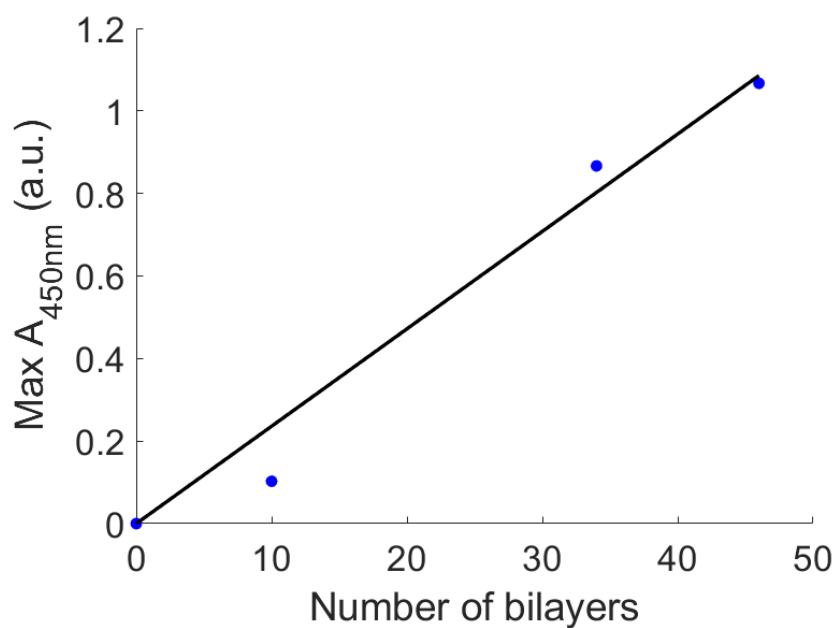


Figure S2.2 Plot of max absorbance at 450 nm of BBY with increase in the number of bilayers of NaCS/BBY LbL thin films.

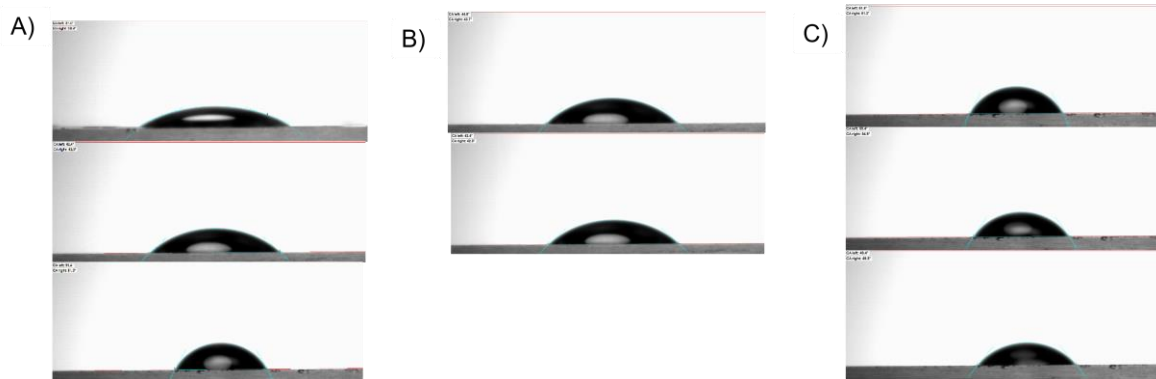


Figure S2.3 (A) Shows differences in the contact angle of films of the starting material vs. LbL film. Initial measurements of contact angle are as follows; top: NACS ($\theta = 21.0^\circ$, 20.6°), middle: BBY ($\theta = 44.8^\circ$, 43.7°) and bottom: NaCS/BBY ($\theta = 61.4^\circ$, 61.3°). (B) Changes in contact angle for BBY film over time. Top: $t = 0$ min ($\theta = 44.8^\circ$, 43.7°), bottom: $t = 1$ min ($\theta = 42.4^\circ$, 42.0°). (C) Changes in contact angle for NaCS/BBY film over time. Top: $t = 0$ min ($\theta = 61.4^\circ$, 61.3°), middle: $t = 2$ min ($\theta = 55.4^\circ$, 55.9°) and bottom: $t = 4$ min ($\theta = 49.4^\circ$, 49.5°).

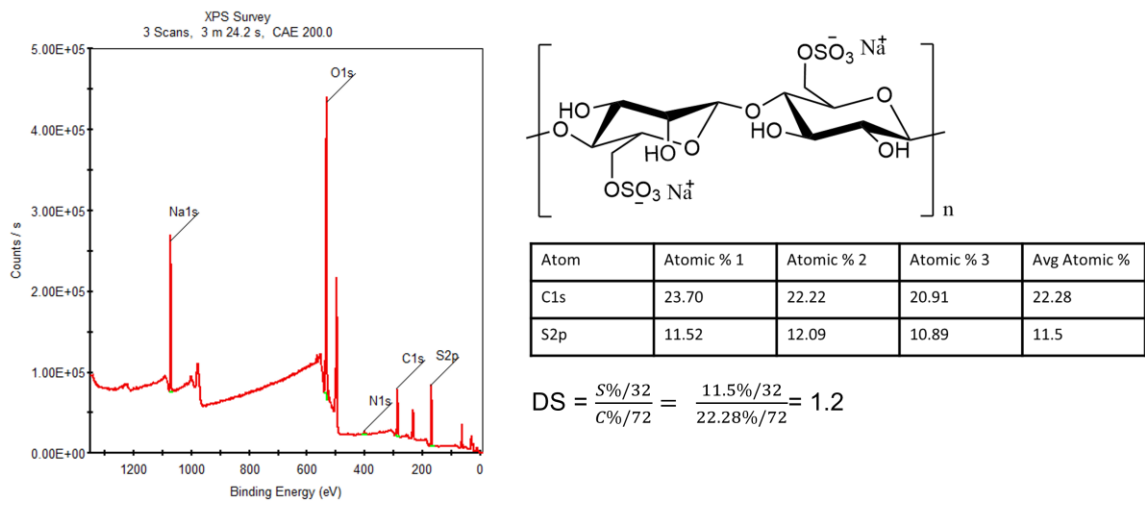


Figure S2.4 XPS analysis of NaCS commercial sample showing the binding energy for different atoms.

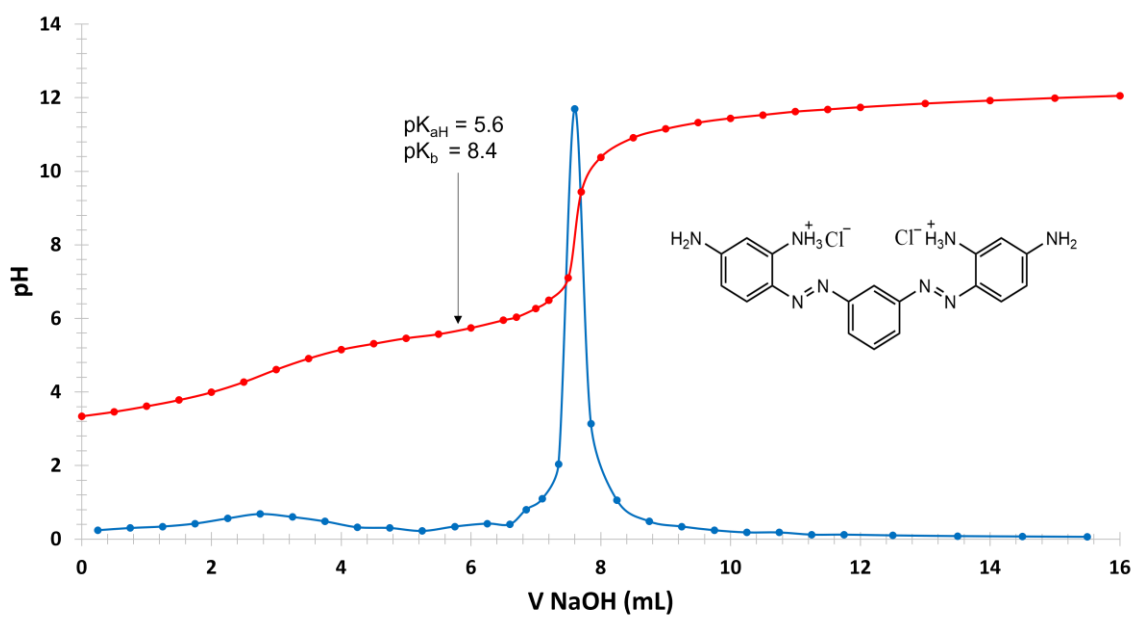


Figure S2.5 Titration of NaOH (50.15 mM) against BBY (2.421 mM). Red line shows titration curve (pH vs. V NaOH), and blue line shows the first derivative.

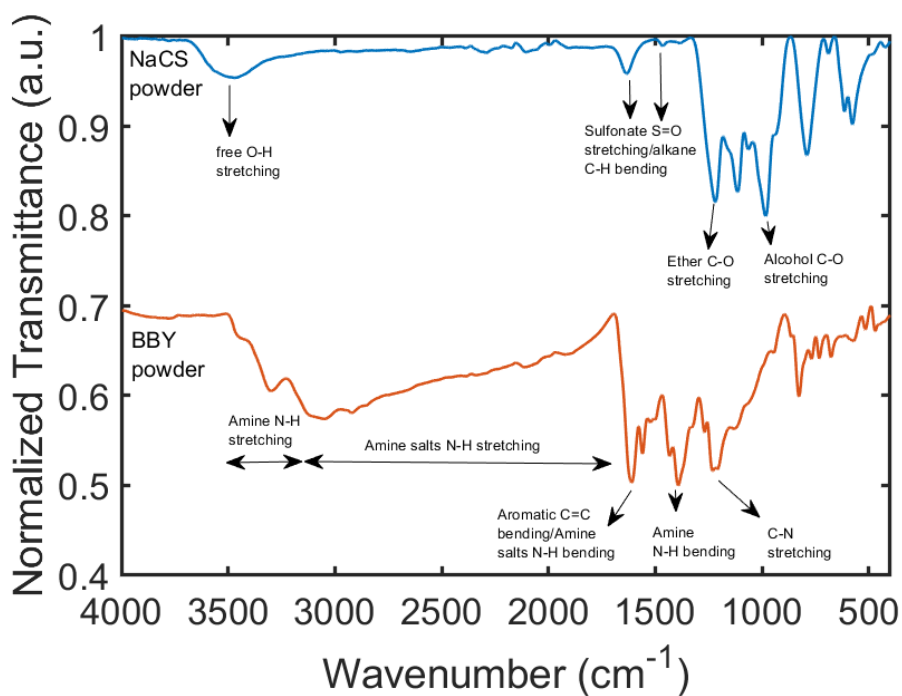


Figure S2.6 IR spectra of the polymer NaCS (blue line) and photo-switch BBY (orange line).

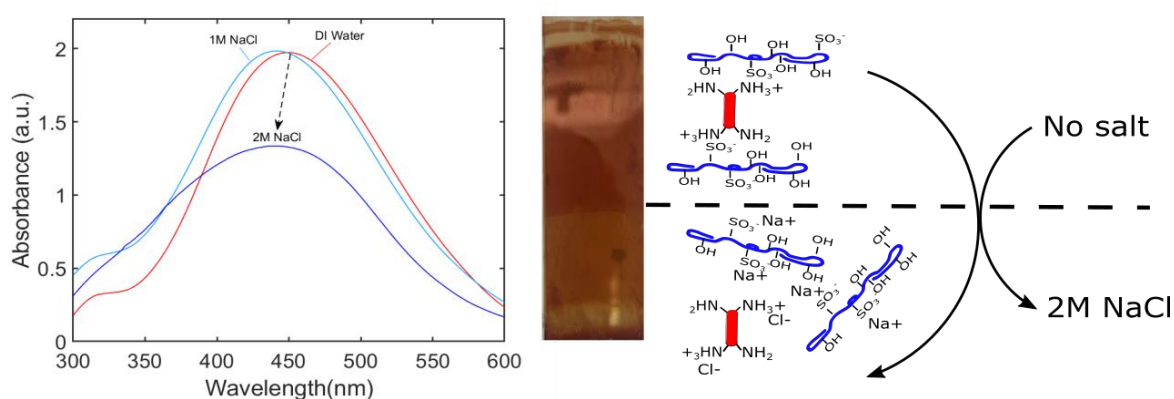


Figure S2.7 Effect of salt (2 M solution) on the stability of NaCS/BBY thin films.

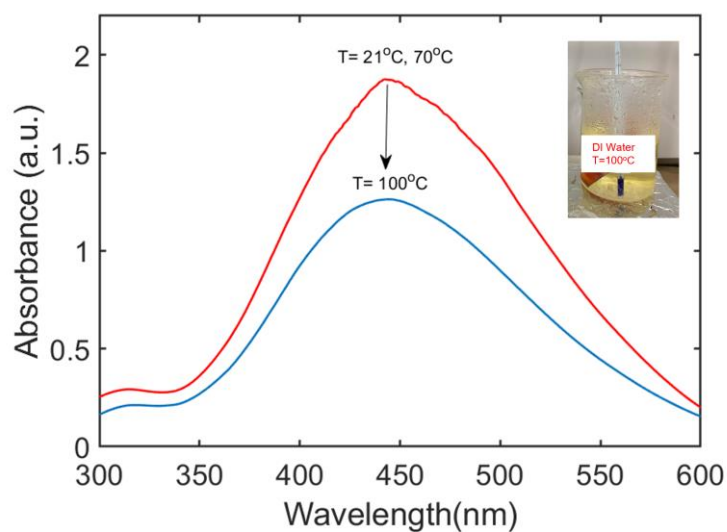


Figure S2.8 Effect of temperature on the stability of NaCS/BBY thin films.

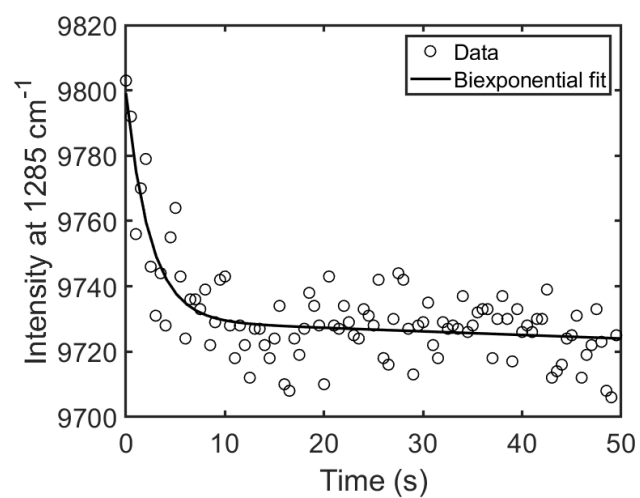


Figure S2.9 Change in intensity of Raman signal around 1285 cm^{-1} peak overtime of NaCS/BBY thin films using a 532 nm laser at 0.1 mW power.

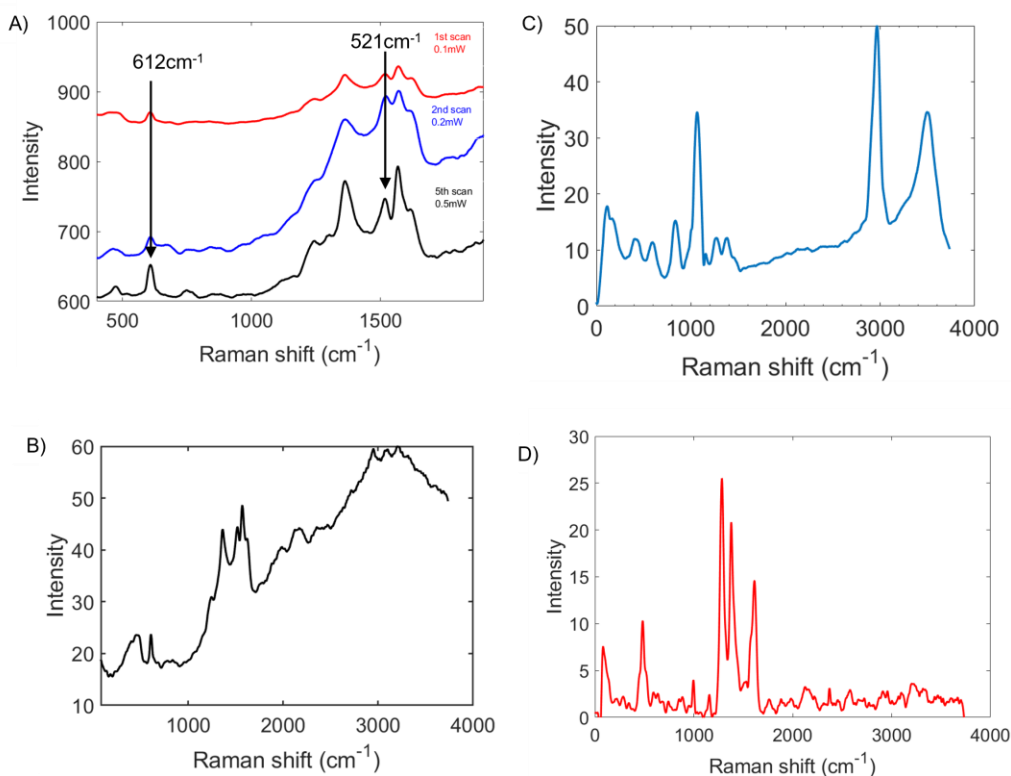


Figure S2.10 (A) Raman spectra of BBY deposited on quartz substrate excited using a 532 nm laser at 0.1 mW (red), 0.2 mW (blue) and 0.5 mW (black) laser power. As laser power increases, the intensity of *cis* peaks at 1510 cm^{-1} and 612 cm^{-1} increases. (B) Full Raman spectrum of BBY only with 532 nm laser at 0.1 mW laser power. (C) Raman spectrum of NaCS only and (D) full Raman spectrum of NaCS/BBY thin films with 532 nm laser at 0.1 mW laser power.

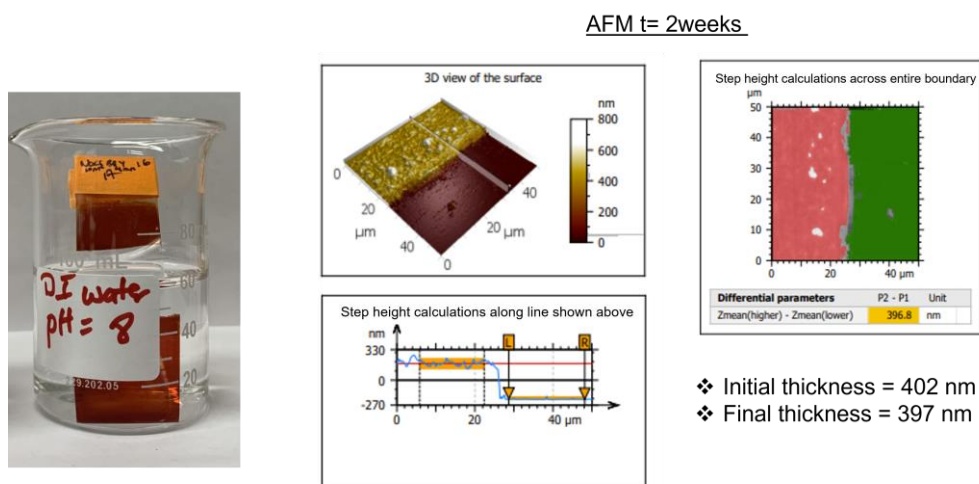


Figure S2.11 AFM disassembly after 2 weeks for a film in DI water under ambient light.

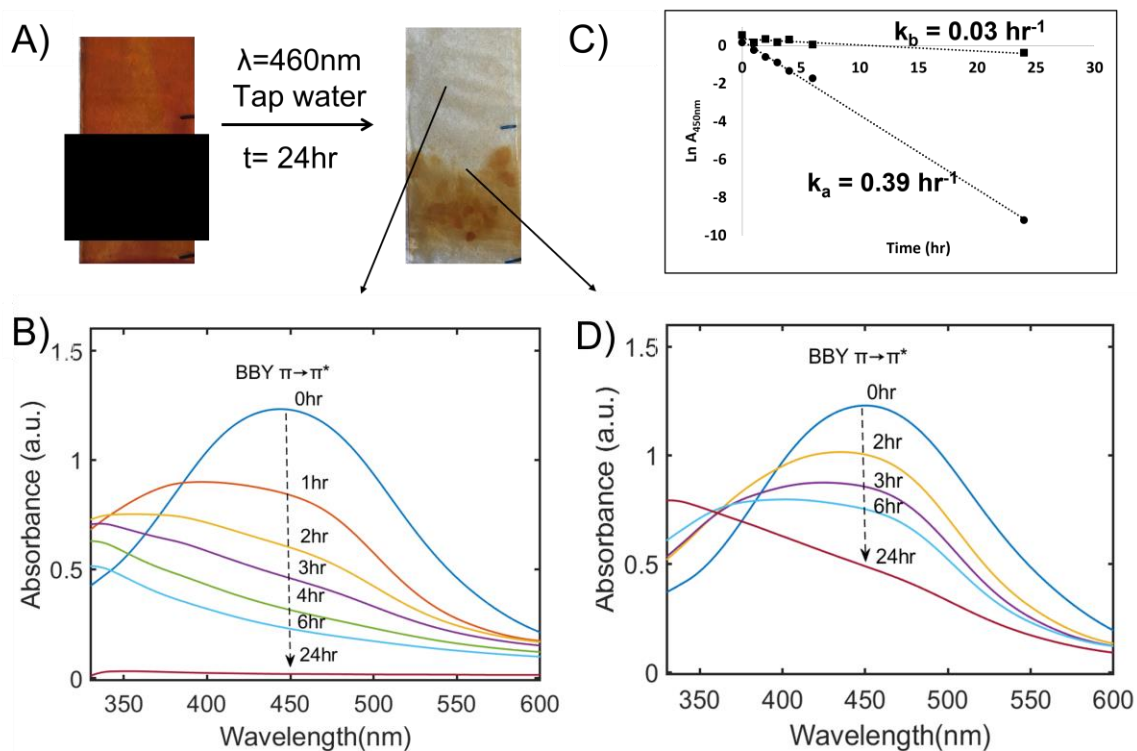


Figure S2.12 (A) Disassembly of NaCS/BBY films deposited on glass substrate triggered by blue light (460 nm LED, 299 mA, 12.50 V), washed with tap water. Upper section of films was left exposed (unmasked) while the lower section was masked. (B, D) Time resolved UV-Vis spectra of NaCS/BBY films following irradiation with blue light, washed using tap water for unmasked and masked sections, respectively ($t = 0\text{--}24\text{ hr}$). (C) Graph of $\ln A_{450\text{ nm}}$ vs. t during disassembly process for unmasked (circles) vs. masked (squares) section of the films.

Bridging Text for Chapter 3: Optical and computational study of the $trans \leftrightarrow cis$ reversible isomerization of the commercial bis-azo dye Bismarck Brown Y

Gaining a better understanding of the isomerization behaviour and kinetics of molecular photo-switches like Bismarck Brown Y (BBY) can allow for its use outside of its more traditional application as dyes or stains, to being utilized as dynamic crosslinkers in photo-reversible materials and optical devices. In the previous Chapter (Chapter 2), we demonstrated the utility of BBY as a photo-reversible crosslinker in multi-layered cellulose-based films. BBY is one of the few commercially available water soluble bis-azo dyes. Its water solubility, low cost, and abundance of protonated amine groups made it an ideal candidate for the fabrication of polyelectrolyte multilayers (PEMs). Upon irradiation with low intensity blue light, the disassembly of the material could be preferentially triggered while in an aqueous environment. Additionally, in Chapter 2, for the first time the *trans-cis* isomerization of BBY was observed directly by means of pump-probe experiments. The isomerization of the azo dye in THF solvent showed that the bis-azo dye could undergo *trans-to-cis* isomerization using green visible light, and that the *cis* reversion followed a highly unusual biexponential decay. While this observation was useful to help confirm the mechanism, a more in-depth study of the isomerization of BBY was clearly needed to understand this unusual thermal relaxation. As such, in this Chapter (Chapter 3) the main objective is to assess the isomerization of the BBY azo dye when embedded in the multi-layered films. Additionally, the influence of the solvent on the isomerization behaviour is evaluated using pump-probe experiments for BBY in protic solvents such as ethanol and water, and aprotic solvents such as DMF and THF. Since the commercial BBY azo dye was found to have a relatively low purity (50 %) as sold, attempted purification of the dye and the subsequent reassessment of the isomerization

behaviour was conducted. This is the first detailed report on the isomerization kinetics of the BBY azo dye. Working with our collaborators in Theoretical Chemistry at York University in Toronto, computational modelling was also undertaken to rationalize the behaviour of this bisazo dye through density functional theory (DFT) methods.

Chapter 3 has been published as a manuscript in a refereed journal. Citation: Edwards, K. E. K., Mermut, O., Pietro, W. J., and Barrett, C. J. “Optical and computational study of the *trans* ↔ *cis* reversible isomerization of the commercial bis-azo dye Bismarck Brown Y” *Physical Chemistry Chemical Physics*, 2023, 25, 5673–5684.

Optical and computational study of the *trans* ↔ *cis* reversible isomerization of the commercial bis-azo dye Bismarck Brown Y

Kayrel E.K. Edwards,^a Ozzy Mermut,^b William J. Pietro,^c and Christopher J. Barrett.^{a,b*}

^aDepartment of Chemistry, McGill University, Montreal, QC, Canada.

^bDepartment of Physics and Astronomy, York University, Toronto ON, Canada.

^cDepartment of Chemistry, York University, Toronto ON, Canada.

3.1 Abstract

The *trans-cis-trans* isomerization behaviour of Bismarck Brown Y (BBY) during and after irradiation with visible light was characterized in detail for the first time by means of optical pump-probe experiments, to study the geometric inter-conversion of bis-azobenzene both in solution and embedded in multi-layered polymeric thin films. The rate constants observed for the thermal *cis-trans* back isomerization permit a determination of how the thermal isomerization is influenced by its local environment. In both solution and when incorporated into multi-layered thin films, the thermal relaxation observed for the commercial azo dye BBY showed a highly unusual biexponential decay, which clearly demonstrates two distinct isomerization processes. The *cis* decay showed an anomalous fast isomerization process on the timescale of milliseconds, followed by a slower isomerization process with a *cis* lifetime on the order of seconds. It was further observed that the faster isomerization process was influenced more by its local environment than was the slower process. The faster isomerization process also displayed a higher rate constant in

aprotic solvents such as THF and DMF compared to that observed in protic solvents such as ethanol and water. Additionally, a higher rate constant was observed in solution compared to the multi-layered thin films where motion of the azo molecules was likely more restricted. Following recrystallization of the BBY azo dye, the more expected monoexponential decay was observed for the *cis* isomer in solution, with a single *cis* lifetime calculated on the timescale of seconds. This timescale corresponded well to values predicted by density functional theory calculations.

3.2 Introduction

Among the most ubiquitous reversible photo-switches are azobenzene-based dyes (azos) , which can isomerize between E and Z (*trans* to *cis*) geometric isomers upon irradiation. The isomerization of azobenzene can result in significant structural changes both on the molecular scale, and also on the macroscale in azo-containing materials when changing from a planar, nonpolar structure (E) to a polar, twisted conformation (Z). Thus, azobenzene-containing materials have been used for a wide variety of applications such as for biomaterial triggering purposes *via* a light-driven assembly/disassembly,^{1,2} photo-control over biological materials and interfaces,^{3,4} for photo-alignment and photo-actuators as 'artificial muscles',^{3,5,6} and as humidity driven sensor devices.⁷ Most recently, azo dyes have been demonstrated to be able to function as photo-switchable crosslinkers in cellulose-based polyelectrolyte multilayer materials (PEMs), allowing the films' disassembly to be triggered by blue visible light while being gently washed with water.⁸ These thin films were held together by weak intermolecular interactions between the positively charged amino groups of the azo dye Bismarck Brown Y (BBY), and the negatively charged sulfate groups of the polymer sodium cellulose sulfate (NaCS).⁸ The dye BBY, first reported in 1866,⁹ is one of the few commercially available water-soluble azobenzene dyes and has been widely used as a biological stain.¹⁰ BBY has also been studied for its potential application as non-linear optic (NLO) materials,¹¹ and electrochemical materials,¹² however detailed optical mechanistic studies, such as the kinetics of the *trans-cis-trans* isomerization of BBY, have yet to be reported.

Azobenzene dyes can be characterized into three spectral types based on the relative energies of their $n-\pi^*$ and $\pi-\pi^*$ states as: azobenzene type, aminoazobenzene type, and

pseudostilbene type, which lead to different isomerization rates and behaviours. Azobenzene type dyes display a maximum absorption in the UV region (~350 nm) with a high intensity π - π^* and a low intensity n - π^* band in the visible region (~460 nm).^{13, 14} The addition of amino groups in the ortho or para positions results in the n - π^* and π - π^* bands coming close or overlapping in the near visible-UV region (~400 nm) due to an increase in the π orbital energy and a decrease in the π^* orbital.¹³ BBY azo dye ($C_{18}H_{18}N_8 \cdot 2HCl$), which is the dihydrochloride of 4,4'-[1,3-phenylenebis(diazene-2,1-diyl)]di(benzene-1,3-diamine), can be classified as an aminoazobenzene-type molecule, with a maximum absorption at ~450 nm.⁸ The last type of azobenzene is the pseudostilbene type, with electron donating and electron withdrawing groups in the 4 and 4' positions and are often referred to push-pull azobenzenes. This phenomenon results in the reversal of the positions of the two bands: the π - π^* band is significantly red shifted past that of the n - π^* .¹⁴

The photo-isomerization behaviour of the three spectroscopic classes of all azobenzene-based (azo) dyes has been studied in detail both experimentally and computationally. Generally, the *trans* isomer of azo is more stable than the *cis* isomer, and conversion between the two isomeric forms can be achieved *via* the absorption of a single photon of light.¹⁵ Due to the *cis* isomer possessing a higher energy than the *trans* isomer, thermal relaxation from the *cis*-to-*trans* states occurs spontaneously in the dark. The kinetics of this *cis* decay generally follows a monoexponential decay, and the rate constant of the thermal relaxation process is affected by the substituents on the aromatic rings.¹⁵ Generally, the timescale of the *cis* lifetime of azo compounds is as follows: azobenzene type (hours), aminoazobenzene type (seconds), and pseudostilbene type (milliseconds).¹⁵ Furthermore, in the case of substituted azo the kinetics of the thermal relaxation

of the *cis* isomer is highly dependent on the properties of the solvent. For example, Joshi and colleagues showed experimentally and computationally that the rate of thermal isomerization of

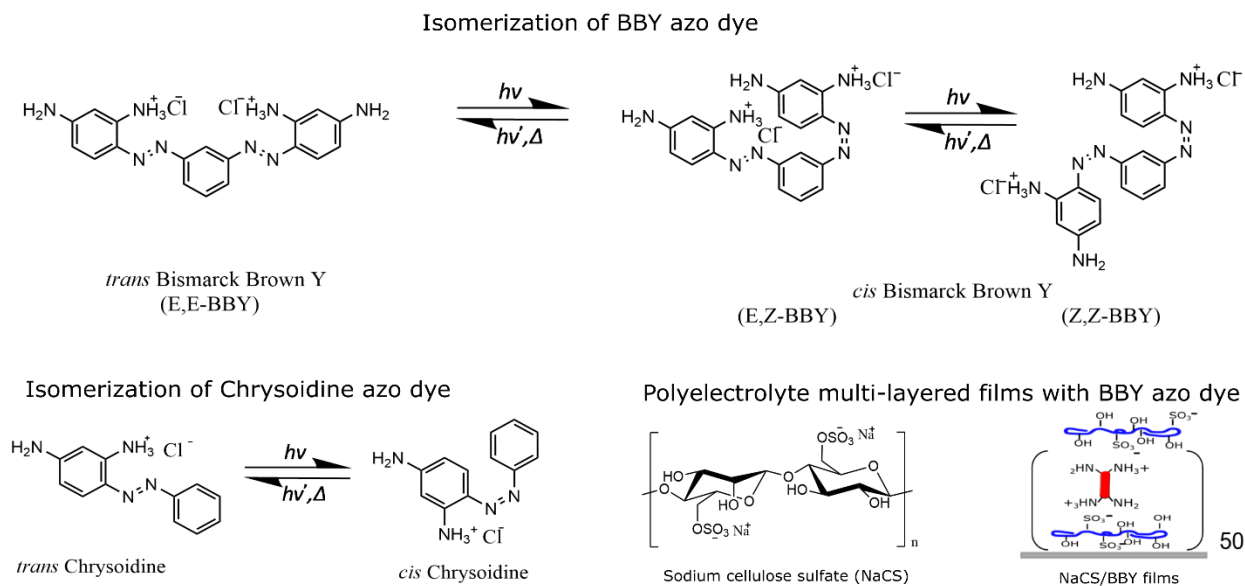


Figure 3.1 Chemical structures of the geometric isomers of Bismarck Brown Y (BBY) and Chrysoidine azo dyes. Chemical structure of polymer NaCS and schematic of layer-by-layer self-assembled NaCS/BBY thin films materials.

aminoazobenzene (AAB) was accelerated in polar solvents compared to non-polar solvents.^{16, 17} These results match well with work reported by other researchers on other azo dyes such as methyl orange and 4-anilino-4'-nitroazobenzene.¹⁸⁻²⁰ This is contrary to unsubstituted azo, where it was observed that the rate of the thermal relaxation was largely independent of the solvent.¹⁵ The differences in the effect of the solvent on the rate constants was shown to be related to the mechanism of the isomerization process.¹⁶ Two isomerization mechanisms are typically proposed

for azo: (i) in-plane inversion where one N=N–C angle increases to 180 degrees while the C–N=N–C dihedral angle remains at 0, and (ii) rotation where torsion of the N=N bond results in a change of the C–N=N–C dihedral angle to 120 °.²¹ Generally, the rotation pathway results in a more polar transition state whose energy can be affected by the surrounding solvent molecules.²¹

BBY azo dye can also be classified as a bis-azobenzene molecule (bis-azo) since it contains two azo units (N=N bond) per molecule. Possessing two azo units per molecule allows for higher loading of azo units in the material without aggregation and provides a larger volume change upon isomerization.^{12, 21–23} For bis-azobenzenes the individual azobenzene units can be connected in meta(*m*), ortho(*o*) or para(*p*) orientation to one another.^{21, 23, 24} Recent work by Boumrifak,²⁴ and by Slavov,²¹ showed that how the azo units are connected matters, as for *m*-bis-azobenzenes the individual units are decoupled and behave independently of each other. Therefore, the isomerization of *m*-bis-azobenzenes resembles that of the monomeric azobenzene.^{21, 24} Experimental results showed that the *cis* decay of *m*-bis-azobenzene in ethanol fit well to a monoexponential model, and the half-life was observed to be on the timescale of > 2 days.²¹ The experimental results were supported by theoretical calculations, and the success of computational modelling, including density functional theory (DFT) and molecular dynamics simulation, has now allowed a far better understanding of the isomerization process of azobenzene molecules.^{19, 25, 26}

There have been few studies reported however on the detailed kinetics of substituted bis-azobenzenes, and these tend to be limited to bis-azos which isomerize using UV light and in organic solvents. For example, Boumrifak and colleagues conducted experimental studies on the thermal relaxation of *o*-bis-azobenzenes with amino and/or acetamido groups, where they observed that the *cis* thermal relaxation was decoupled and proceeded independently for each unit at different timescales.²⁴ The thermal relaxation was fit to a monoexponential decay for symmetric

bis-azobenzenes, with a half-life on the millisecond timescale.²⁴ For the asymmetric bis-azobenzene a biexponential fit was used with timescales similar to that of the monomeric counterparts.²⁴ Robertus and colleagues studied the kinetics of an asymmetric *m*-bis-azobenzene with one ring having a trimethyl-ester based substituent.²⁷ Both flash photolysis and H-NMR were utilized to observe the kinetics, where the decay was observed to be biexponential.²⁷ Vapaavouri and colleagues studied the behaviour of the para- and meta- bis-azo dyes Disperse Yellow 7: *p*-DY7 and *m*-DY7 in solution and when embedded in a poly(4-vinylpyridine) (P4VP) polymer matrix. The *cis* half-life was measured to be on the timescale of minutes and was observed to be shorter for the films.²³

Generally, the thermal relaxation of azobenzenes follows first-order kinetics and decay curves fit well to a monoexponential model. However, when grafted onto or doped into a polymer, the *cis* decay of the azobenzene molecule can become more complex. Such complex kinetics of Disperse Red 1 (DR1), when attached as polymeric side groups, as copolymers, and blends cast as films, was reported.²⁸⁻³⁰ In these examples carbon-based polymers such as polyacrylic acid (PAA) and poly methyl methacrylate (PMMA) were used.²⁸⁻³⁰ It was observed that the relaxation kinetics were highly dependent on the type of chromophore and type of attachment to the polymer backbone. A biexponential decay was observed for the *cis-to-trans* isomerization of azos bound in the side chain of copolymers and blends, above a certain mol ratio of azo.^{29, 30} Complex kinetics were also observed for the thermal relaxation of DR1 grafted onto a co-polymer, poly (DR1A-co-AA) at various molar ratios dissolved in a THF/H₂O cosolvent.²⁸ DR1 which has good solubility in THF followed a monoexponential decay, however upon addition of small amount of water, which is a poor solvent for DR1, the kinetics followed a biexponential decay.²⁸ Other factors which may result in a deviation from first order kinetics are the presence of impurities in the azo dyes

and dimerization of azos due to poor solubility, hydrogen bonding and π - π stacking.^{31, 32} These results demonstrate the strong influence of the solvent and the local environment on the kinetics of azo dyes, and that they can often exhibit strongly non-monoexponential rate behaviour.

Herein, we report for the first time the *trans-cis* isomerization as well as the kinetics of the thermal *cis-trans* relaxation of the water-soluble commercial bis-azobenzene dye BBY, using visible light, both in solution and in the solid-state in multi-layer films. Pump-probe experiments were utilized to characterize the *cis* decay of crude and recrystallized BBY in various solvents, as well as in the solid state, embedded in multi-layered cellulose-based thin films (NaCS/BBY). The *cis* decay curves were fit using both mono- and bi-exponential models, and the rate constants and *cis* lifetimes in various solvents and embedded in multi-layered films were determined. Computational modelling was employed to help rationalize the *trans-cis* isomerization rates and behaviour of BBY and the effect of the local environment on the isomerization process.

3.3 Experimental

3.3.1 Materials

Commercial BBY azo dye was procured from Sigma (LOT 34H3729, C₁₈H₁₈N₈·2HCl, FW = 419.3 g/mol). Chrysoidine was procured from Sigma (LOT BCBW6003, C₁₂H₁₂N₄·HCl, FW = 248 g/mol). Spectroscopic grade THF was purchased from Sigma (CAS # 109-99-9), DMF ACS Reagent Grade from Sigma Aldrich (CAS # 227056), methanol from Fisher (A412-4), ethanol (100 %) from Commercial Alcohols (# PO16EAAN), acetone ACS reagent from Sigma (CAS # 67-64-1) and ethyl acetate from Sigma Aldrich (CAS # 319902). BBY was recrystallized as

follows: the dye was suspended in acetone and after stirring for a few minutes, then the acetone was decanted (it is supposed that the dye has very low solubility in organic solvents). To the flask, ethanol was added, and the slurry was stirred for ~10 minutes. The precipitate (not soluble in ethanol) was removed by filtration and the ethanol solution was concentrated under reduced pressure. The solids from the rotary evaporator were dissolved into a smaller volume of methanol. Ethyl acetate was added with stirring until a slight, persistent turbidity was maintained. Then the flask was placed in a freezer overnight. The next day the precipitate was removed by filtration and the recrystallized BBY dried in an oven at 65 °C for 48 hours.

3.3.2 Pump-probe experiments

The experimental setup used for the isomerization measurements is shown in **Figure 3.2** and is based on previously reported methods.⁸ Solutions of crude and recrystallized BBY in THF (8×10^{-5} M), ethanol, deionized H₂O, and THF/H₂O 50:50 ratio (2×10^{-4} M) were prepared and added to a quartz cuvette (VWR, catalogue # 414004-060, transparent over the range of 300–600 nm studied) with an internal path length of 1 mm. The cuvette was capped to limit the evaporation of solvent. A layer-by-layer (LBL) thin film of Bismarck Brown Y /Sodium cellulose sulfate (NaCS/BBY) was prepared based on work previously reported by the authors.⁸ The probe beam used in the experiment was a circularly polarized 488 nm line from argon laser at low power, (1–5 mW). The pump beam was produced by a 532 nm laser (100 mW) at higher power, with up to 1000 data points acquired in 10s, at 100 data points per second. The sample was pumped for 1 s and the absorbance signal recorded. Measurements were performed at RT (~300 K). For a first order *cis* → *trans* thermal isomerization:

$$\text{Rate} = \frac{d[\textit{trans}]}{dt} = -\frac{d[\textit{cis}]}{dt} = k[\textit{cis}] \quad (1)$$

where [*trans*] and [*cis*] are the concentrations of the *trans* and *cis* isomers, respectively at any time t , and k is the first order rate constant. The rate constant, k , for a monoexponential relaxation curve can be determined from the time dependent absorbance A_t , absorbance immediately after pumping A_0 , and absorbance at infinite time, *i.e.*, complete relaxation back to *trans* A_∞ , using the equation:

$$(A_\infty - A_t) = (A_\infty - A_0)e^{-kt} \quad (2)$$

A plot of $\ln(A_\infty - A_t)$ vs. t should be linear with a slope of $-k$. For samples which deviate from first order kinetics, the experimental A_t relaxation curves were fit to the biexponential equation with 4 fitting parameters:

$$(A_\infty - A_t) = Ae^{-k_a t} + Be^{-k_b t} \quad (3)$$

Like the first-order kinetics, A_∞ and A_t are the absorbance at infinite time and the time dependent absorbance after the pump beam is switched off, respectively. A and B are the relative weighting coefficients, and normalization of these values gives the relative contributions associated with the processes having rate constants k_a and k_b , respectively. A residual plot and a least-squared fit demonstrated the appropriateness of the biexponential fitting. Measurements were performed in triplicate, and the standard deviation was calculated. The lifetime of the *cis* isomer τ , was calculated using **Equation (4)** below, where k is the rate constant:

$$\tau = \frac{1}{k} \quad (4)$$

3.3.3 Computational methods

Restricted Kohn-Sham Density Functional (DFT) calculations were performed with Orca 5.0 using the def2-TZVP (triple-split-valence with polarization) basis set and the B3LYP functional.³³ All

molecular structures were fully geometry optimized.^{34, 35} For geometry-optimized structures, all possible conformers of the benzene rings were investigated to find global minima. Isomerization reaction coordinate profiles were generated by full geometry optimization under the constraint of fixing the C–N=N–C dihedral angle at values between the E and Z optimized angles. The dihedral angle was stepped in increments of 10 ° with 2 ° steps near the transition-state. Activation energies were taken as the saddle point in the reaction coordinate profiles.

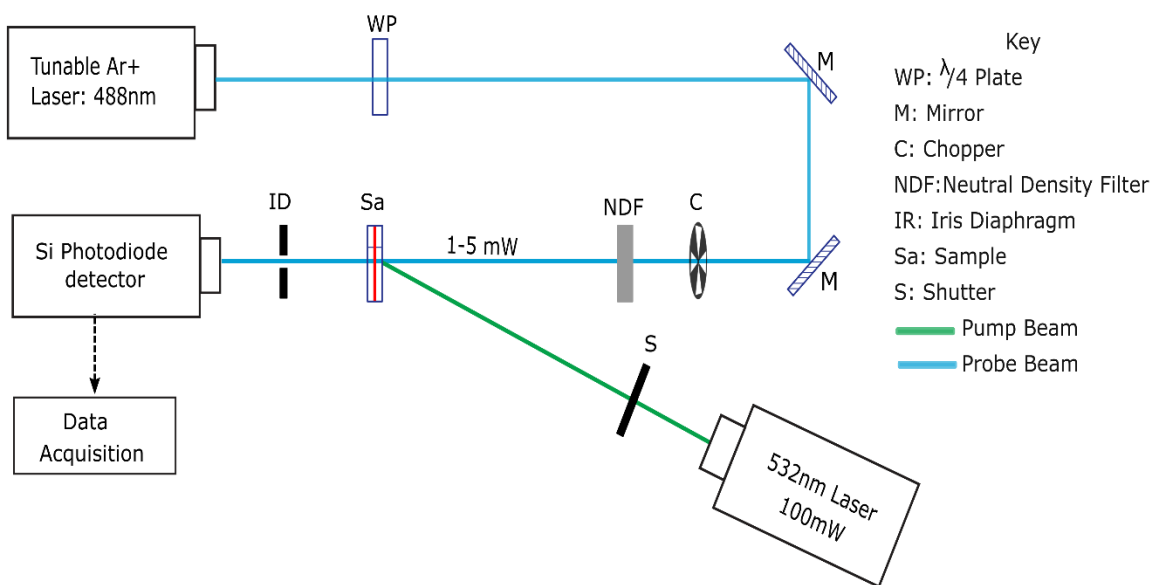


Figure 3.2 Schematic of the optical pump-probe experimental set up used to determine the thermal *cis*-to-*trans* relaxation rate behaviour of BBY.

All barriers were determined by pointwise constrained geometry optimizations along the isomerization reaction coordinate, which was initially assumed to be a dihedral rotation. In all cases, however, the nitrogen atom attached to the centre ring begins a sudden inversion upon

reaching a dihedral of about 82 degrees, and proceeds through the transition state with the C–N–N angle approaching 180 degrees. This mechanism was checked by performing a second set of steps along a reaction coordinate defined by a pure inversion mechanism. In this case, the C–N–N–C dihedral rotates as C–N–N approaches 180 degrees, affording exactly the same transition state in structure and energy. Vibrational analyses were performed on each transition structure to assure the existence of one imaginary frequency, verifying that the geometry resides at a local saddle point. In all cases, animation of the corresponding mode clearly shows inversion through the linear nitrogen.

3.4 Results and discussion

Most water-soluble azo dyes are generally salts, possessing a negatively charged sulfonate group (SO_3^-) in the para or meta positions of the benzene rings. Many FDA approved food dyes contain these sulfonate groups, for example: Sunset Yellow FCF (Yellow No.6), Brilliant blue FCF (Blue No.1), Indigotine (Blue No.2), Allura red AC (Red No.40), and tartrazine (Yellow No.5).³⁶ Another method of preparing water soluble azo dyes is the addition of amine groups to the molecule. One of the most widely-used water-soluble aminoazobenzene dyes is Bismarck Brown, which comes in the form of Bismarck Brown Red (BBR) and Bismarck Brown Y (BBY). Commercially available BBY ($\text{C}_{18}\text{H}_{18}\text{N}_8 \cdot 2\text{HCl}$) contains 4 amino groups, two of which are protonated, and lie ortho to one of the nitrogen atoms of the azo $-\text{N}=\text{N}-$ bond. The protonation of the amine groups of BBY increases its solubility in water but decreases its solubility in organic solvents. The most common use of this azo dye is as a biological stain for imaging in histology experiments,¹⁰ however, there has been recent potential reported for the use of BBY in optical

devices.^{8, 11} Most recently, our group was able to prepare photo-reversible materials where BBY was added as a photo-switchable crosslinker in cellulose-based multi-layered thin films, allowing the films' disassembly to be triggered by low-power visible light while being gently washed with water.⁸ In this work, it was shown that the *cis* decay of commercial BBY in THF followed a biexponential decay.⁸ To better understand the mechanism of this photo-driven disassembly process, the *trans-cis* isomerization of BBY, as well as the kinetics of the *cis* decay, a more detailed study was sought into the optical characterization, and associated computations to rationalize the geometric conversion.

3.4.1 Commercial BBY absorption profile

It was observed by UV-Vis spectroscopy that a solution of crude commercial BBY azo dye in water (pH = 4) displays a strong absorption band in the visible region ($\lambda_{max} = 464$ nm) where the $\pi \rightarrow \pi^*$ and $n \rightarrow \pi^*$ transitions are overlapped (**Figure 3.3**). The absorption of BBY in other solvents was also measured and it was observed that the maximum absorption was somewhat different in various solvents, being more red-shifted in polar/protic solvents (ethanol = 467 nm) compared to non-polar/aprotic solvents (DMF = 452 nm, THF = 453 nm).

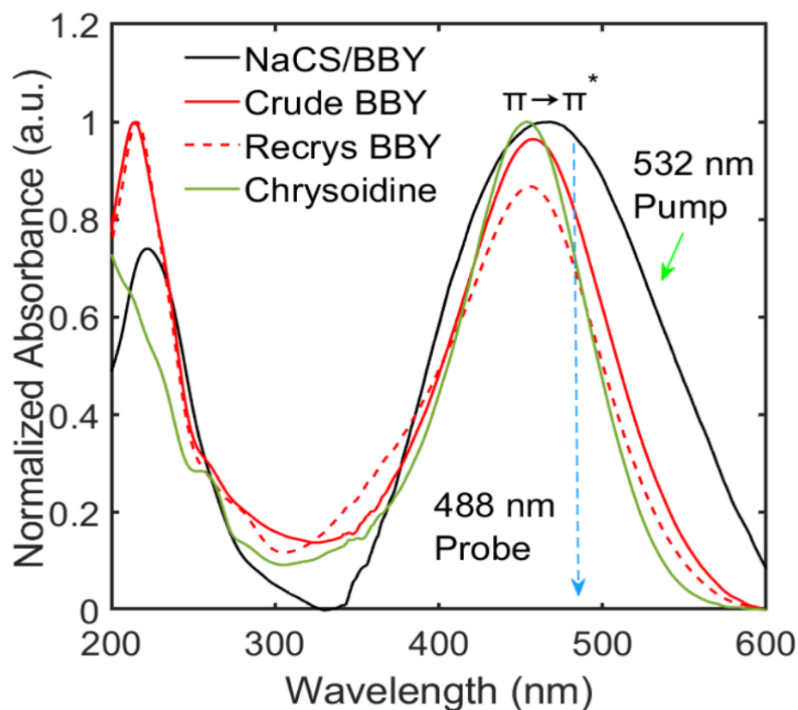


Figure 3.3 UV/Vis spectra of crude commercial BBY azo dye in NaCS/BBY film (- black) and water (- red), recrystallized BBY in water (-- red) and Chrysoidine azo dye in water (- green) with $\lambda_{max} = 455\text{--}464$ nm.

These absorption profiles matched well with the expected absorption of BBY azo dye dissolved in acidified 50 % ethanol ($\lambda_{max} = 454\text{--}460$ nm, $\epsilon \geq 32,000$ Lmol⁻¹cm⁻¹), according to the vendor Sigma Aldrich.³⁷ For the NaCS/BBY thin films, there was an observed broadening of the absorption band of BBY within the thin films ($\lambda_{max} = 450\text{--}460$ nm), possibly owing to the electrostatic interactions between the sulfonate (SO₃⁻) groups of NaCS polymer and the amine groups (NH₃⁺) of BBY azo dye.

3.4.2 Commercial BBY isomerization

For the pump-probe experiments, the sample was probed using a 488 nm (blue) laser wavelength, close enough to the maximum absorbance band of the dye (450–464 nm) and pumped using a 532 nm (green) laser wavelength at high power (100 mW), as this wavelength still overlaps sufficiently with the absorption band of BBY, and the intensity of this laser was high enough to induce an observable *trans*-to-*cis* isomerization of BBY. **Figure 3.4a** displays changes in the absorbance of crude BBY in ethanol solution (i) before irradiation (ii) during 1s pulse with 532 nm laser and (iii) *cis* decay in the dark. Before irradiation the absorbance at wavelength 488 nm was high due to the abundance of *trans*-BBY in solution. During the 1 s pulse with the green laser there was a drastic decrease in the absorbance as *trans*-BBY (EE) was converted to the *cis* isomer (EZ and ZZ). Once the pump beam was switched off, the absorbance increased back to its original value within approximately 1 s as the *trans* isomer was allowed to thermally relax back from the less stable *cis* conformation. The increase in the absorbance during the *cis* decay in the dark was very fast during the first 0.5 s and slower over the next 0.5 s. This photoinduced isomerization and thermal relaxation in the dark was reproducible, with the absorbance consistently returning to its original value for at least three cycles, similar to a result for the isomerization of crude BBY we previously reported in THF.⁸ Pump-probe experiments conducted in other solvents such as DMF, water, and co-solvent THF/water showed similar time-dependent absorption profiles (**Figure S3.1**). **Figure 3.4b** shows the changes in the absorbance of BBY in the multi-layered NaCS/BBY thin films. Similar to BBY in solution, before irradiation the absorbance at 488 nm was at its maximum and decreased during irradiation with the 532 nm laser. Once the pump beam was switched off the absorbance eventually returned completely to its original value in the dark.

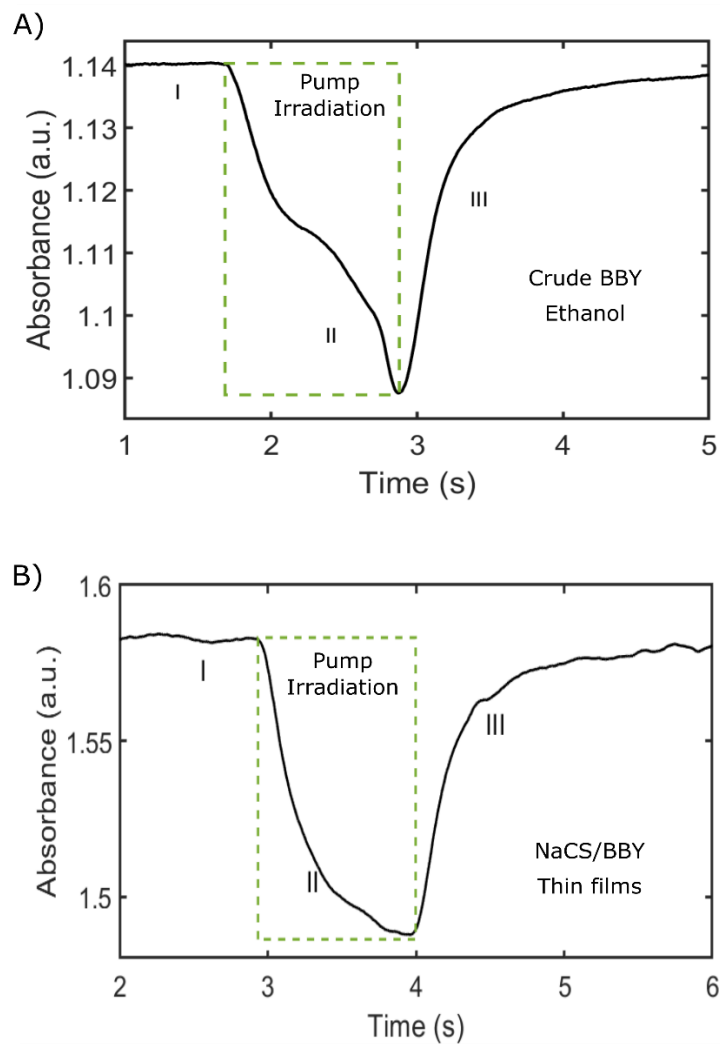


Figure 3.4 The absorbance vs. time profiles of commercial BBY in (a) ethanol, and (b) multilayered NaCS/BBY thin films. Key: (I) Before irradiation, (II) during 1s pulse with 532 nm laser, (III) *cis* decay in dark.

3.4.3 Commercial BBY kinetics

Figures 3.5a and **3.5b** show the change in $(A_{\infty} - A_t)$ over time for crude BBY in ethanol and in NaCS/BBY thin films during the *cis* decay in the dark. Both decay curves show a better fit to the

biexponential function (**Equation 3**) compared to the monoexponential function (**Equation 2**), consistent with our previously reported biexponential decay observed for crude BBY in THF.⁸ The insets of **Figures 3.5a** and **3.5b** show the residual plots between the least-squares four-parameter fit and the data, which indicate a good fit of the biexponential function for both curves. From the fitting parameters, the rate constants k_a and k_b can be extracted as shown in **Figure 3.6a**. For BBY in ethanol it was determined that $k_a = 6.8 \pm 0.8 \text{ s}^{-1}$ and $k_b = 0.92 \pm 0.04 \text{ s}^{-1}$ while in the multi-layered films, both rate constants were slightly reduced where $k_a = 6.1 \pm 0.6 \text{ s}^{-1}$ and $k_b = 0.64 \pm 0.03 \text{ s}^{-1}$.

The *cis* decay of BBY in the other solvents (DMF, THF, THF/water and water) also was fit well with a biexponential function (**Figure S3.2**). Additionally, pump-probe experiments of deprotonated BBY in THF showed a good fit to the biexponential function, with rate constants similar to those of protonated BBY (**Figure 3.6a**). **Figure 3.6a** also shows the *cis* lifetimes which were tabulated according to equation 4. Omitting the fast anomalous isomerization rate (k_a) portion, a comparison of the remaining k_b shows that in all solvents the *cis* lifetime of crude BBY was on the timescale of milliseconds-seconds ($\tau = 0.8\text{--}1.1 \text{ s}$), which is expected for an aminoazobenzene type molecule. The longest *cis* lifetime was reported for NaCS/BBY thin films: $\tau = 1.6 \text{ s}$ while the shortest *cis* lifetime was reported in DMF solvent: $\tau = 0.6 \text{ s}$. There was also no observable difference between the *cis* lifetime of protonated vs. deprotonated BBY in THF ($\tau = 0.8 \text{ s}$). The slight elongation of the *cis* lifetime of BBY in the film can be attributed to the reduced volume of the thin film compared to solution. The local EM environment in these self-assembled systems has also been shown by solid-state NMR studies to change significantly on soft-bonding.³⁸ The geometrical changes of BBY on the molecular scale will be discussed in more detail in the DFT calculations section that follows.

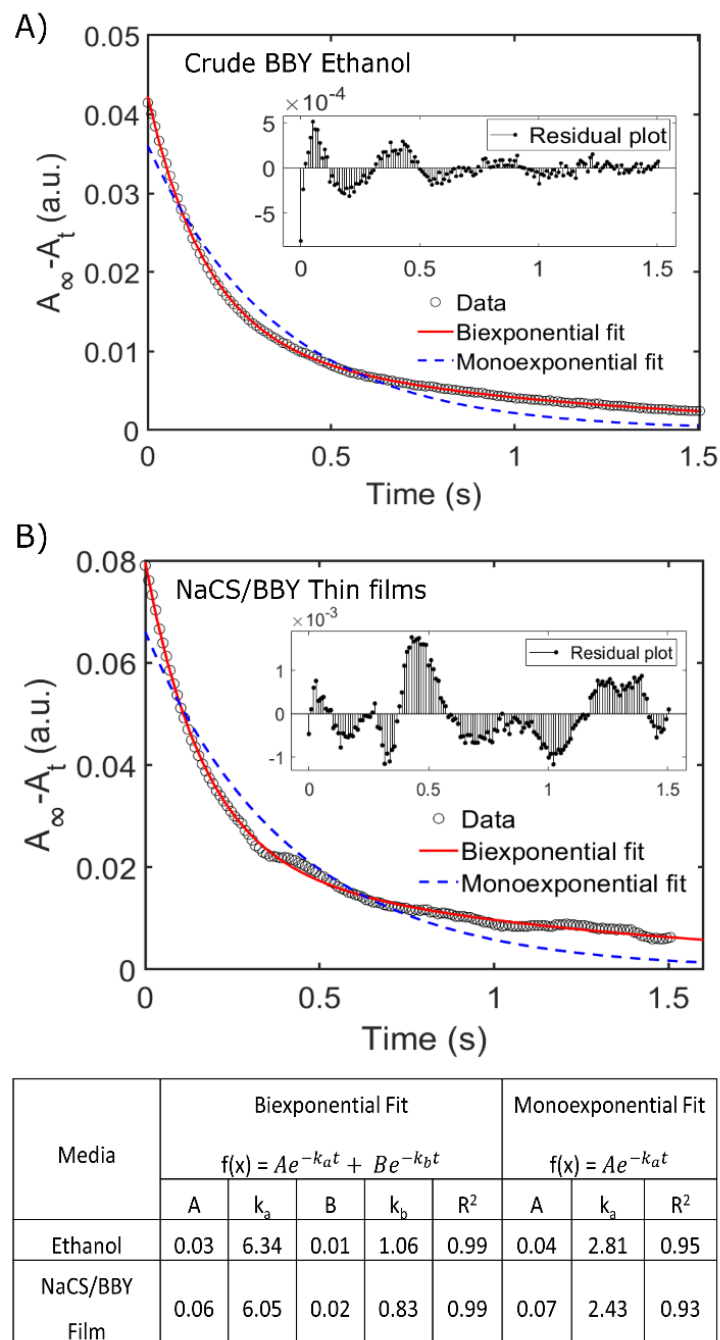


Figure 3.5 The decay of *cis* isomer fit to biexponential and monoexponential kinetics of commercial BBY in (a) ethanol, and (b) multi-layered NaCS/BBY thin films. The inset shows the residual plot between our least-squares four-parameter biexponential fit and the data.

3.4.4 Solvent effect

Figure 3.6a shows details of the two rate constants k_a and k_b for the *cis* decay of crude BBY in various solvents/media. The faster isomerization process had a higher rate constant (k_a) in aprotic solvents such as THF and DMF compared to that observed in more polar and protic solvents such as ethanol and water. While the results indicate a possible relationship between the fast anomalous rate constant k_a with the polarity (**Figure 3.6b**) and proticity (**Figure 3.6c**) of the solvent, there was no observable relationship with the more expected rate constant k_b . This is contrary to previous reports on 4-aminoazobenzene (AAB) where it was observed that the rate constant increased as solvent polarity increased.¹⁶

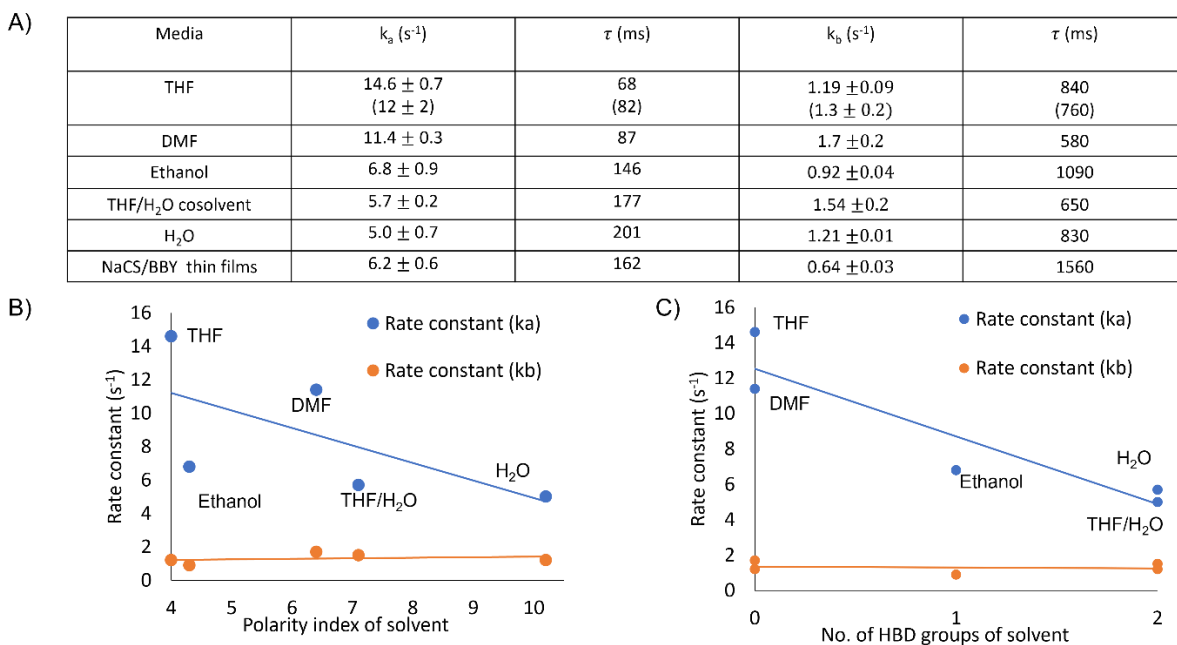


Figure 3.6 (a) Effect of solvent/medium on kinetics of *cis* decay of crude BBY. Effect of (b) solvent polarity, and (c) solvent proticity on rate constants of BBY. Rate values for deprotonated crude BBY shown in brackets. Error analysis: triplicate measurements, same sample.

The results observed for crude BBY azo dye align better with that observed for unsubstituted azobenzene, where the thermal *cis* → *trans* isomerization is independent of solvent polarity and is presumed to occur *via* an inversion pathway.¹⁶ DFT calculations which will be discussed in a later section, support the theory that a likely mechanism of the thermal *cis* → *trans* isomerization of BBY is *via* a combination of rotation and inversion.

3.4.5 Recrystallized BBY isomerization and kinetics

As previously discussed, commercial BBY azo dye is only claimed by the manufacturer to be 50 % pure as sold. Some other commercial azo dyes, such as Disperse Orange 1 (DO1), are also sold with relatively low purity (< 25 %);^{18, 39} therefore purification is standard practice before use, and a simple recrystallization is often sufficient to isolate effectively one single azo species. As a bis-azo however, the impurities in what is sold as BBY are found to contain very similar azo and bis-azo compounds even after standard recrystallization. Also, after traditional column chromatographic separations, multiple similar azo variations still remained, and thus this azo/bis-azo mixture ends up being what is in fact commonly employed as ‘BBY’ in research experiments. In this study, to determine exactly what is being used in most if not all ‘BBY experiments’, the structure and relatively low purity of the crude dye was confirmed by mass spectrometry (**Figure S3.3**), NMR spectroscopy (**Figure S3.4**), and IR spectroscopy (**Figure S3.5**). The mass spectra indicated that the majority of the impurity in the commercial BBY dye consists of another azo dye (2,3,4-triaminoazobenzene),⁴⁰ likely produced during the diazonium coupling reaction (**Figure S3.3**), and with a very similar structure to BBY. Several methods were attempted to purify the crude BBY, including recrystallization, solvent extraction, and column chromatography; however,

the separation of the desired product from the impurity 2,3,4-triaminoazobenzene proved challenging under all usual techniques. The best results were achieved by recrystallization from an organic solvent such as ethanol/methanol using ethyl acetate, however the resulting mass spectra still confirmed that a significant portion of the recrystallization was still the triaminoazobenzene impurity (**Figures S3.3–5**). The presence of this impurity in significant quantities is possibly a contributing cause of the anomalous shorter lifetime observed for the crude BBY commercial azo dye.

A solution of the recrystallized BBY azo dye in water (pH = 4) exhibited a strong absorption band in the visible region ($\lambda_{max} = 455$ nm) which is slightly blue shifted compared to crude BBY in water ($\lambda_{max} = 464$ nm) (**Figure 3.3**). The maximum absorption of recrystallized BBY was also slightly shifted in various solvents (ethanol = 467 nm and DMF = 451 nm). **Figure 3.7a** shows the absorption profile of recrystallized BBY in ethanol during the pump-probe experiments, and **Figure 3.7c** shows the *cis* decay curve which had a good fit to the expected monoexponential function (**Equation 2**). There was only one observable rate constant $k_a = 0.87 \pm 0.08$ s⁻¹ (in ethanol) and the *cis* lifetime of recrystallized BBY was calculated to be on the timescale of seconds ($\tau = 1.1$ s). A good fit to a monoexponential decay was observed in water ($\tau = 0.5$ s), while a good fit to a biexponential decay was observed in DMF ($\tau = 0.3$ s and 1.1 s). Given that BBY is a symmetrical molecule, and the two azo bonds are effectively decoupled from each other, the isomerization of the *cis* (EZ) and (ZZ) isomers should be similar. Therefore, it is expected that the *cis* decay of BBY should follow a monoexponential decay, which was observed in ethanol and water. Additionally, the isomerization of each BBY azo unit should be equivalent to that of the monomeric counterpart, Chrysoidine, whose isomerization kinetics was also measured and will be discussed in the next section.

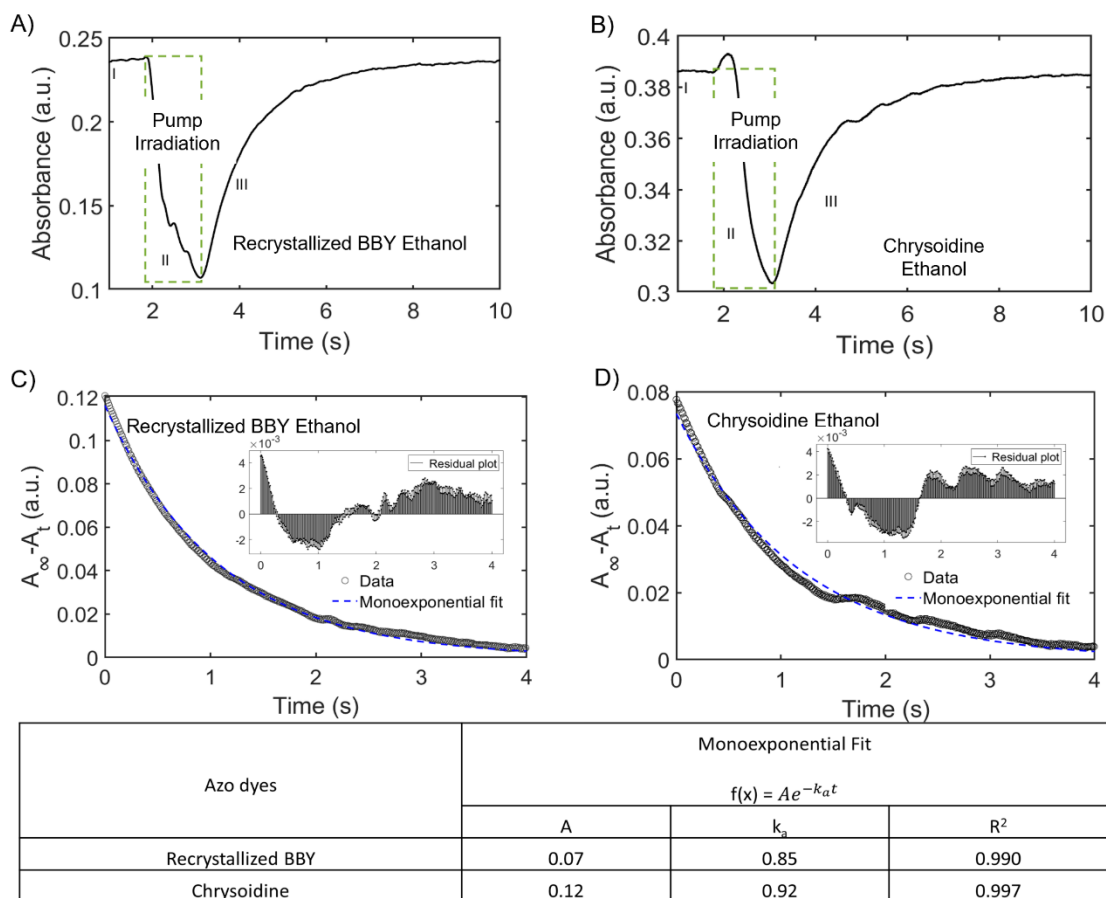


Figure 3.7 The absorbance vs. time profiles of (a) recrystallized BBY in ethanol, and (b) Chrysoidine in ethanol. Key: (I) Before irradiation, (II) during 1s pulse with 532nm laser, (III) *cis* decay in dark. The decay of *cis* isomer fit to monoexponential kinetics of (c) recrystallized BBY in ethanol and (d) Chrysoidine in ethanol.

3.4.5 Chrysoidine isomerization and kinetics

Chrysoidine azo dye (4-phenylazo-m-phenylenediamine. monohydrochloride), also known as Basic Orange 2, is another commercially available water-soluble aminoazobenzene dye whose structure is the monomeric equivalent of the BBY azo dye. The structure and high purity of the

dye was confirmed by various spectroscopic techniques (**Figures S3.3–5**). A solution of the Chrysoidine azo dye in water (pH = 4) has a strong absorption band in the visible region ($\lambda_{max} = 456$ nm) which is similar to the recrystallized BBY in water ($\lambda_{max} = 455$ nm) (**Figure 3.3**). The maximum absorption of Chrysoidine was also slightly shifted in various solvents (ethanol = 459 nm, DMF = 441 nm).

Pump-probe experiments of this azo dye can provide an estimation of the expected *cis* lifetime of a pure sample of BBY azo dye. **Figure 3.7b** shows the changes in the absorbance of Chrysoidine in ethanol, which is similar to the absorption profile observed for BBY. **Figure 3.7d** shows the *cis* relaxation curve in ethanol which has a good fit to the expected monoexponential function (**Equation 2**). There was only one observable rate constant $k_a = 0.79 \pm 0.08$ s⁻¹ (in ethanol) and the *cis* lifetime of Chrysoidine was on the timescale of seconds ($\tau = 1.3$ s). This *cis* lifetime was similar to that calculated for recrystallized BBY ($\tau = 1.1$ s) and crude BBY in ethanol ($\tau = 0.1$ s and 1.2 s). Similarly, to recrystallized BBY, there was a good fit of the *cis* relaxation curve of Chrysoidine to a monoexponential function in water ($\tau = 0.6$ s), and a biexponential function in DMF ($\tau = 0.3$ s and 0.8 s). This indicates that outside of the presence of impurities, other factors such as dimerization or aggregation from π - π stacking, hydrogen bonding, and poor solubility^{31,32,41} can influence the relaxation rates observed for azo dyes. It was previously observed for *p*-hydroxyazobenzene, that the *cis* reversion kinetics in alcohols roughly followed first-order kinetics, while in benzene and toluene the kinetics were unusual.³² Reduced solubility in these non-polar solvents and possible tautomerization were proposed as the cause of this deviation from first-order kinetics.³² For the azo dye DO1, even after purification there was an anomalous fast decay observed in THF and cyclohexane solvents, but not acetone, which the researchers excluded from their plot of $\ln(A_\infty - A_t)$ vs. time in order to get a best fit to a monoexponential decay.^{18,39}

5.4.3 DFT calculations

Computational modelling was undertaken to predict the timescale of the *cis* relaxation of BBY azo dye. While the DFT calculations were performed in the gaseous phase and for the deprotonated form of BBY, the computed energies and rate constants can still provide useful information about the theoretical *cis* lifetime timescale and the likely isomerization pathway.

Parameter	EE	ZZ	EZ-EE TS	ZZ-EZ TS
CNNC dihedral (°)	179.7	11.7	86	86
CNN angle (°)	115.1	125.0	149.1	141.7
r_{NN} (Å)	1.264	1.249	1.249	1.263
$r_{\text{NH}_2\text{NH}_2(\text{para})}$ (Å)	14.07	9.336	14.24	11.43

Table 3.1 Geometric parameters of isomers and transition states.

Equilibrium geometries

Figures 3.8 and **3.9** show the optimized and isomerization transition-state structures, respectively, for each form of Bismarck Brown Y in its most favoured conformer. Important geometric parameters for all species are presented in **Table 3.1**. The two diaminophenylazo moieties in the EZ form are remarkably similar. Moreover, all geometric parameters between the EZ, ZZ, and EE forms are markedly similar. This indicates that the two diaminophenylazo groups are not electronically coupled to each other through the central benzene ring. Each azo group, however, is electronically coupled to both of its rings, as evidenced by the N=N bond lengths. In the EE form, the N=N bond length is 1.264 Å, somewhat longer than a typical N=N double bond (1.23 Å). This elongation can be explained by π -coupling to the benzene rings, which produces a resonance structure with a N–N single bond. π -coupling is somewhat reduced in the ZZ form because of the

non-ideal 11.7° dihedral angle. The nearly planar geometry of the terminal amino groups indicates a high degree of lone-pair delocalization into the rings, as is observed in virtually all aniline-like systems.

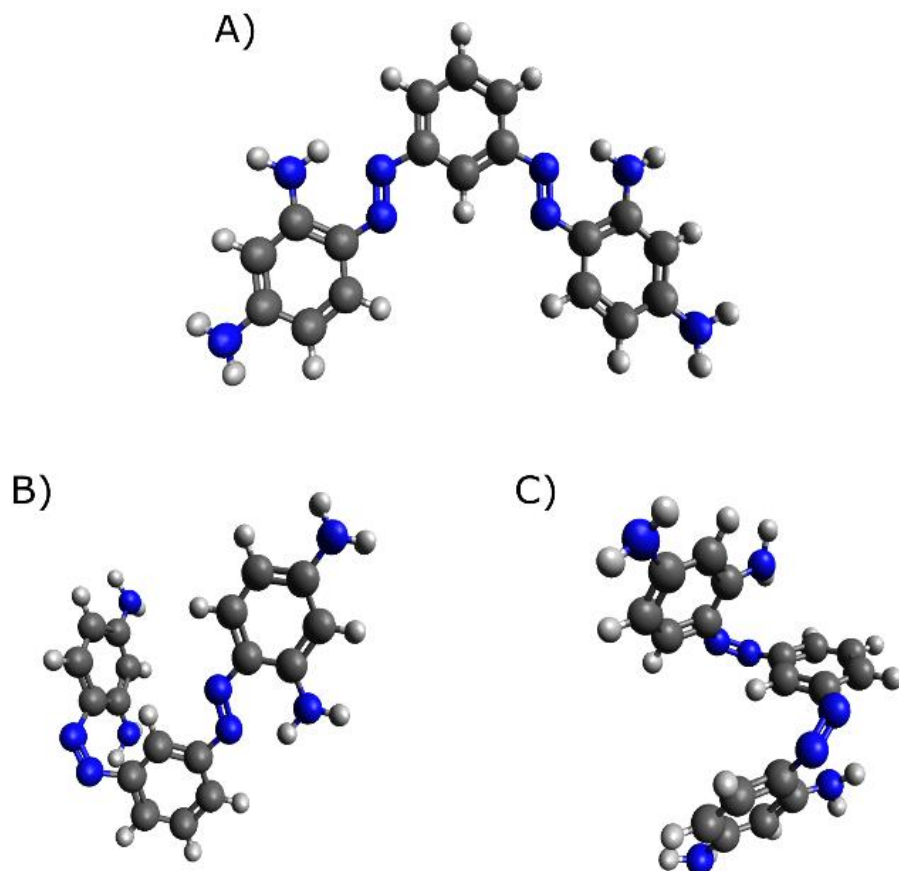


Figure 3.8 DFT optimized geometries for the three isomers of BBY (a) EE, (b) EZ, and (c) ZZ.

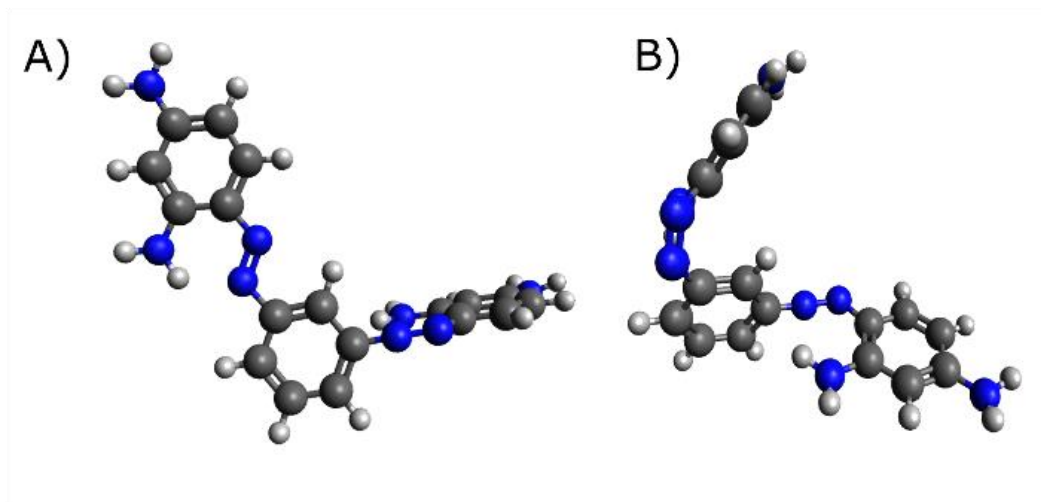


Figure 3.9 DFT optimized *cis-trans* isomerization transition-state geometries of BBY (a) EZ-EE, and (b) ZZ-EZ.

Additionally, the ZZ isomer of BBY is $\sim 5 \text{ \AA}$ shorter in length than the EE isomer, measured by the shortened distance between the para-amino groups in **Table 3.1**. It was hypothesized in a previous study that the cause of the disassembly of water-resistant multi-layered NaCS/BBY films, during irradiation with blue light and washing with water, was due to a change in the geometry and size of the azo dye during isomerization.⁸ It was postulated that this change on the microscale could disrupt the intermolecular interactions holding the films together, leading to disassembly of the entire material.⁸ This length change predicted by DFT of approximately 50 % supports the theory that the *trans-cis* isomerization of BBY was the main cause of the photo-driven disassembly of these PEM films.

Isomerization

The *cis-trans* isomerization mechanism is identical for both the ZZ-EZ and EZ-EE processes, occurring through a combination of rotation and inversion. In the ZZ form, for example, the C–

N=N–C dihedral angle starts at its equilibrium geometry of 11.7° , then begins to rotate about the N=N axis until it reaches 86° . This is the transition state and corresponds to the highest energy along the reaction coordinate. At that point, the mechanism abruptly switches to an inversion. The C–N=N angle (taken from the centre ring) rapidly approaches 180° as the dihedral rotation passes through 90° . The mechanism then switches back to rotation, and the C–N=N–C dihedral angle continues its rotation to the EZ equilibrium geometry of 178.5° . The behaviour of the C–N=N angle along the reaction coordinate is shown in **Figure 3.10**.

An interesting trend is observed in the N=N bond length along the reaction coordinate, as illustrated in **Figure 3.11**. Starting from the *cis* equilibrium geometry, the N=N bond length gradually lengthens as the dihedral angle twists towards the transition state geometry. This is expected, as twisting increasingly misaligns the *p*-orbitals forming the π -bond. However, the elongation trend is reversed when the dihedral angle reaches 86° , the transition state. The azo nitrogen on the centre ring goes planar, and the N=N distance abruptly shrinks to 1.228 \AA , indicating a full, localized double-bond uncoupled with the rings. Once the reaction coordinate passes through the inversion, the N–N distance abruptly expands back to 1.310 \AA , indicating greatly reduced double-bond character. Then, as the rotation continues to the *trans* geometry, the N=N bond length monotonically reduces to its equilibrium value of 1.264 \AA , indicating a double-bond with considerable π -delocalization into the rings. This trend is observed identically for both the ZZ-EZ and EZ-EE isomerizations. The marked similarities in structures and transition state energies involved in the ZZ-EZ and EZ-EE isomerizations further indicate that the two azo moieties are not electronically coupled to each other to any significant degree.

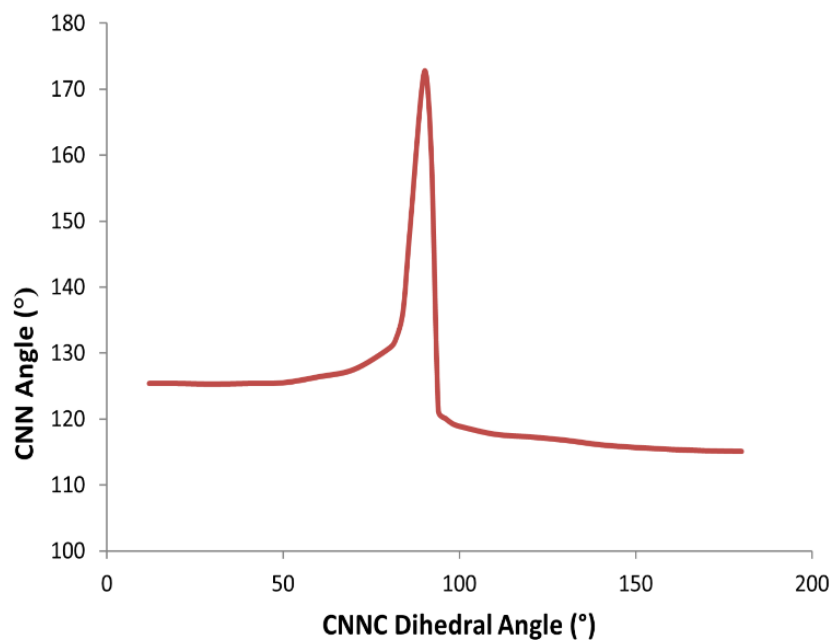


Figure 3.10 DFT prediction of the C–N–N bond angle along the ZZ-EZ reaction coordinate.

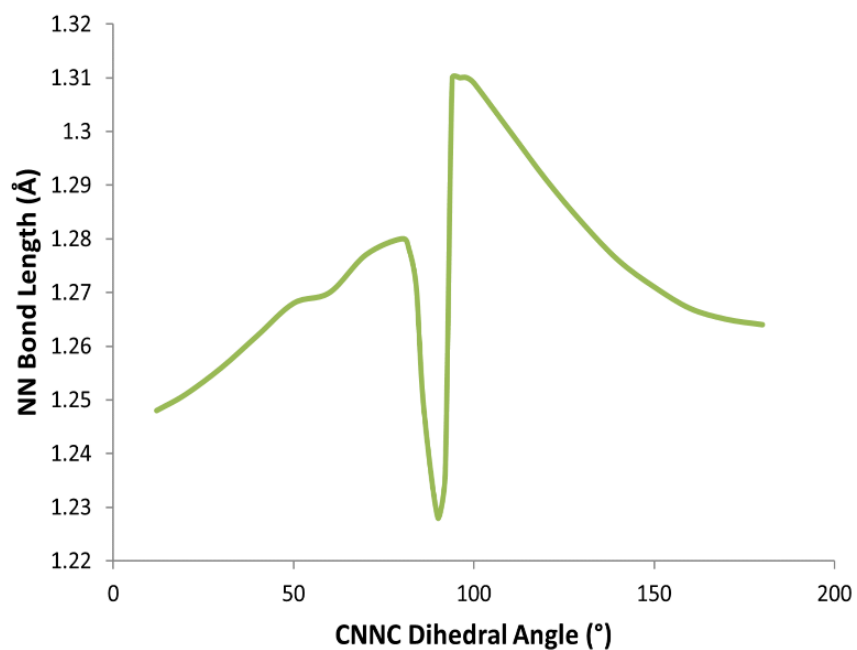


Figure 3.11 DFT predicted N–N bond length profile along the ZZ-EZ coordinate.

The fluctuation in N–N bond length as the isomerization passes through the transition state is interesting. It is caused by a sudden enhancement of pi-bond character between the two nitrogen atoms as the C–N–N angle approaches linearity. This conclusion is supported by the Meyer bond orders presented in the table below. 82 ° and 94 ° are the points immediately before and after the dip, respectively.

CNNC dihedral angle (°)	NN Meyer bond order
82	1.27
90	1.52
94	1.14

Albeit energetically large, we believe that steric effects are at play in the *cis-trans* isomerization, which in the *ZZ* form dominate the differences in isomerization energies. For example, in the *EE* form, both terminal rings are coplanar with the central ring, as pi-coupling is energetically favourable. However, in the *EZ* isomer, the terminal ring on the *cis* side is rotated out of coplanarity with the centre ring, while the terminal ring on the *trans* side remains coplanar. The twisting on the *cis* side is due to steric interactions with the centre ring.

Energetics

Table 3.2 presents relative electronic energies for all isomers and transition states, and *cis-trans* isomerization rate constants.

	Conformation				
	ZZ	TS(ZZ-EZ)	EZ	TS(EZ-EE)	EE
Relative Energy (kJ mol ⁻¹)	183.8	261.5	93.1	171.2	0
k (s ⁻¹)	0.24		0.20		

Table 3.2 DFT calculations of transition state thermochemistry (relative electronic energies, rates).

First-order rate constants were derived at 298 K from the Arrhenius equation using the measured frequency factor of 1×10^{13} seconds⁻¹ for the *cis-trans* isomerization of azobenzene.⁴² From the predicted rate constants, the theoretical *cis* lifetime of BBY is equivalent for both *cis* isomers with $\tau = 4$ s and 5 s for ZZ and EZ, respectively, and is on the order that one would expect for an aminoazobenzene spectral class dye. The theoretical *cis* lifetime of BBY also matched reasonably well with the experimental *cis* lifetime of $\tau = 1.1$ s measured in ethanol.

DFT calculations performed on 2,3',4-triaminoazobenzene indicate its isomerization barrier to be 3.7 kJ/mol higher than that of BBY. Benchmark studies suggest DFT isomerization barriers to be fully reliable to an accuracy of about 6 kJ/mol.⁴³ Therefore, we can conclude that the barriers are the same within a few kJ/mol, however we cannot say definitively which is greater.

5.5 Conclusions

The thermal relaxation of BBY in solution and embedded in polymeric thin films was measured for the first time by means of pump-probe experiments, and the behaviour rationalized with computational DFT modelling. BBY was able to undergo *trans*→*cis* isomerization following irradiation with visible light, and thermally relaxed back to the *trans* isomer in the dark, with a *cis* lifetime on the timescale of milliseconds – seconds. It was observed that the *cis* decay was best fit to a biexponential model in most solvent systems and when embedded in the multi-layered cellulose-based thin films. Two rate constants were measured for the *cis* decay of crude BBY: a fast anomalous isomerization rate (k_a), and a slower more expected rate (k_b). The *cis* lifetime was slightly more prolonged when BBY was in the NaCS/BBY thin films *vs.* in solution. Upon recrystallization the more expected monoexponential decay was observed with a *cis* lifetime of $\tau = 1.1$ s in ethanol. This *cis* lifetime corresponded well to that of the monoazobenzene analogue, Chrysoidine ($\tau = 1.2$ s, in ethanol). The experimental value of the *cis* lifetime of crude and recrystallized BBY also corresponded well with the value predicted by DFT calculations for BBY ($\tau = 4$ – 5 s, gas phase). It is hoped that these advanced purification techniques developed and reported here, and the associated spectroscopic behaviour observed for the various components, will aid some of the many researchers who employ Bismarck Brown azo dyes in their experiments and materials.

5.6 References

1. Q. Yi and G. B. Sukhorukov, *Soft Matter*, 2014, **10**, 1384–1391.
2. Q. Bian, M. Jin, S. Chen, L. Xu, S. Wang and G. Wang, *Polymer Chemistry*, 2017, **8**, 5525–5532.
3. V. Y. Chang, C. Fedele, A. Priimagi, A. Shishido and C. J. Barrett, *Advanced Optical Materials*, 2019, **7**, 1900091–1900116.
4. S. Shinkai, T. Nakaji, T. Ogawa, K. Shigematsu and O. Manabe, *Journal of the American Chemical Society*, 1981, **103**, 111–115.
5. M. Matsumori, A. Takahashi, Y. Tomioka, T. Hikima, M. Takata, T. Kajitani and T. Fukushima, *ACS Applied Materials & Interfaces*, 2015, **7**, 11074–11078.
6. A. Natansohn and P. Rochon, *Chemical Reviews*, 2002, **102**, 4139–4176.
7. S. Schoelch, J. Vapaavuori, F. G. Rollet and C. J. Barrett, *Macromolecular Rapid Communications*, 2017, **38**, 1600582–1600590.
8. K. E. Edwards, M. Kim, T. H. Borchers and C. J. Barrett, *Materials Advances*, 2022, **3**, 6222–6230.
9. C. A. Martius, *Journal für Praktische Chemie*, 1866, **98**, 94–96.
10. G. W. Blaydes, *Stain Technology*, 2009, **14**, 105–110.
11. K. A. AL-Adel and H. A. Badran, *International Journal of Emerging Technologies in Computational and Applied Sciences*, 2014, **8**, 64–68.
12. M. F. S. Teixeira, M. M. Barsan and C. M. A. Brett, *RSC Advances*, 2016, **6**, 101318–101322.
13. H. Rau and S. Yu-Quan, *Journal of Photochemistry and Photobiology A: Chemistry*, 1988, **42**, 321–327.
14. O. S. Bushuyev, M. Aizawa, A. Shishido and C. J. Barrett, *Macromolecular Rapid Communications*, 2018, **39**, 1700253–1700267.
15. A. A. Beharry and G. A. Woolley, *Chemistry Society Reviews*, 2011, **40**, 4422–4437.
16. N. K. Joshi, M. Fuyuki and A. Wada, *Journal of Physical Chemistry B*, 2014, **118**, 1891–1899.
17. Y. Hirose, H. Yui and T. Sawada, *Journal of Physical Chemistry A*, 2002, **106**, 3067–3071.

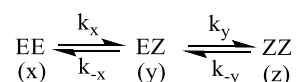
18. S. Smith and F. B. Abdallah, *Journal of Thermodynamics & Catalysis*, 2017, **08**, 1000181–1000189.
19. A. Georgiev, E. Bubev, D. Dimov, D. Yancheva, I. Zhivkov, J. Krajcovic, M. Vala, M. Weiter and M. Machkova, *Spectrochimica Acta Part A: Molecular and Biomolecular Spectroscopy*, 2017, **175**, 76–91.
20. A. Yano, Y. Konno, E. Kinoshita and R. Yano, *Journal of Photochemistry and Photobiology A: Chemistry*, 2017, **346**, 411–415.
21. C. Slavov, C. Yang, L. Schweighauser, C. Boumrifak, A. Dreuw, H. A. Wegner and J. Wachtveitl, *Physical Chemistry Chemical Physics*, 2016, **18**, 14795–14804.
22. S. Sun, S. Liang, W.-C. Xu, G. Xu and S. Wu, *Polymer Chemistry*, 2019, **10**, 4389–4401.
23. J. Vapaavuori, A. Goulet-Hanssens, I. T. S. Heikkinen, C. J. Barrett and A. Priimagi, *Chemistry of Materials*, 2014, **26**, 5089–5096.
24. C. Boumrifak, C. Yang, S. Bellotto, H. A. Wegner, J. Wachtveitl, A. Dreuw and C. Slavov, *ChemPhotoChem*, 2019, **3**, 411–417.
25. F. He, X. Ren, J. Jiang, G. Zhang and L. He, *Journal of Physical Chemistry Letters*, 2022, **13**, 427–432.
26. J. Dokić, M. Gothe, J. Wirth, M. V. Peters, J. Schwarz, S. Hecht and P. Saalfrank, *Journal of Physical Chemistry A*, 2009, **113**, 6763–6773.
27. J. Robertus, S. F. Reker, T. C. Pijper, A. Deuzeman, W. R. Browne and B. L. Feringa, *Physical Chemistry Chemical Physics*, 2012, **14**, 4374–4382.
28. L. L. Norman and C. J. Barrett, *Journal of Physical Chemistry B*, 2002, **106**, 8499–8503.
29. C. J. Barrett, A. Natansohn and P. Rochon, *Macromolecules*, 1994, **27**, 4781–4786.
30. C. J. Barrett, A. Natansohn and P. Rochon, *Chemistry of Materials*, 1995, **7**, 899–903.
31. N. J. Dunn, W. H. Humphries, A. R. Offenbacher, T. L. King and J. A. Gray, *Journal of Physical Chemistry A*, 2009, **113**, 13144–13151.
32. G. Gabor, Y. F. Frei and E. Fischer, *Journal of Physical Chemistry*, 1968, **72**, 3266–3272.
33. F. Weigend and R. Ahlrichs, *Phys Chem Chem Phys*, 2005, **7**, 3297–3305.
34. A. D. Becke, *Journal of Chemical Physics*, 1993, **98**, 5648–5652.
35. C. Lee, W. Yang and R. G. Parr, *Physical Review B Condensed Matter*, 1988, **37**, 785–789.

36. US FDA, Summary of Color Additives for Use in the United States in Foods, Drugs, Cosmetics, and Medical Devices, <https://www.fda.gov/industry/color-additive-inventories/summary-color-additives-use-united-states-foods-drugs-cosmetics-and-medical-devices>, (accessed August 4, 2022).
37. Sigma Aldrich, Product Specification, Bismarck Brown Y, <https://www.sigmaaldrich.com/specification-sheets/335/625/861111-BULK.pdf>, (accessed August 4, 2022).
38. R. N. Smith, L. Reven and C. J. Barrett, *Macromolecules*, 2003, **36**, 1876–1881.
39. S. R. Hair, G. A. Taylor and L. W. Schultz, *Journal of Chemical Education*, 1990, **67**, 709–712.
40. P. O’Leary, in *Science of Synthesis*, eds. C. A. Ramsden and D. Bellus, Georg Thieme Verlag KG, Stuttgart, 2007, vol. 31b, p. 1367.
41. L. C. Abbott, S. N. Batchelor, J. Oakes, J. R. Lindsay Smith and J. N. Moore, *Journal of Physical Chemistry B*, 2004, **108**, 13726–13735.
42. J.-Å. Andersson, *Journal of Photochemistry*, 1983, **22**, 255–261.
43. L. Goerigk, A. Hansen, C. Bauer, S. Ehrlich, A. Najibi and S. Grimme, *Physical Chemistry Chemical Physics*, 2017, **19**, 32184–32215.

3.7 Appendix 3: Supporting information for Chapter 3

3.7.1 Photolysis kinetics analysis

Bismarck Brown Y can undergo two reversible *cis/trans* isomerization processes.



Isomerizations $\text{EE} \rightarrow \text{EZ}$ and $\text{EZ} \rightarrow \text{ZZ}$ are photo-driven. The reverse (*cis-trans*) processes are thermally driven. Concentrations x , y , and z are related to each other through differential **Equation**

(5)

$$\frac{dx}{dt} = -k_x \phi x + k_{-x} y \quad (5)$$

$$\frac{dy}{dt} = k_x \phi x - k_{-x} y - k_y \phi y + k_{-y} z$$

$$\frac{dz}{dt} = k_y \phi y - k_{-y} z$$

where ϕ is the photon flux. We can determine the time profile of all concentrations by solving **Equation (5)**. This is best done numerically by defining a series of incremental time-slices, i , having period Δt , and solving the system numerically as shown in **Equation (6)**. Discretization gives:

$$\frac{x_i - x_{i-1}}{\Delta t} = -k_x \phi x_i + k_{-x} y_i \quad (6)$$

$$\frac{y_i - y_{i-1}}{\Delta t} = k_x \phi x_i - (k_{-x} + k_y \phi) y_i + k_{-y} z_i$$

$$\frac{z_i - z_{i-1}}{\Delta t} = k_y \phi y_i - k_{-y} z_i$$

and collecting time-slices:

$$\left(\frac{1}{\Delta t} + k_x \phi \right) x_i - k_{-x} y_i = \frac{x_{i-1}}{\Delta t}$$

with corresponding expressions for y and z . This system can be solved recursively for each time-slice i , by matrix **Equation (7)**

$$\mathbf{A} \mathbf{C}_i = \frac{1}{\Delta t} \mathbf{C}_{i-1} \quad (7)$$

where \mathbf{C}_i is the concentration vector

$$\mathbf{C}_i = \begin{bmatrix} x_i \\ y_i \\ z_i \end{bmatrix} \quad (8)$$

expressed in expanded form as

$$\begin{bmatrix} \left(\frac{1}{\Delta t} + k_x \right) & -k_{-x} & 0 \\ -k_x \phi & \left(\frac{1}{\Delta t} + k_{-x} + k_y \phi \right) & -k_{-y} \\ 0 & -k_y \phi & \left(\frac{1}{\Delta t} + k_{-y} \right) \end{bmatrix} \begin{bmatrix} x_i \\ y_i \\ z_i \end{bmatrix} = \frac{1}{\Delta t} \begin{bmatrix} x_{i-1} \\ y_{i-1} \\ z_{i-1} \end{bmatrix} \quad (9)$$

3.7.2 Calculation of rate constants

Rate constants, k_x , k_{-x} , k_y , and k_{-y} (**Equation 9**), were calculated from DFT energies of the corresponding species in accordance with transition state theory. The algorithm starts by loading vector C_{-1} with initial conditions ($x = [EE]_0$, $y = 0$, $z = 0$), and evaluating the elements of matrix A . Vector C_i (**Equation 8**) is then determined by recursively solving **Equation (3)** *via* a standard LU decomposition for each time-slice, i .

3.7.3 Pump-probe isomerization spectroscopy data

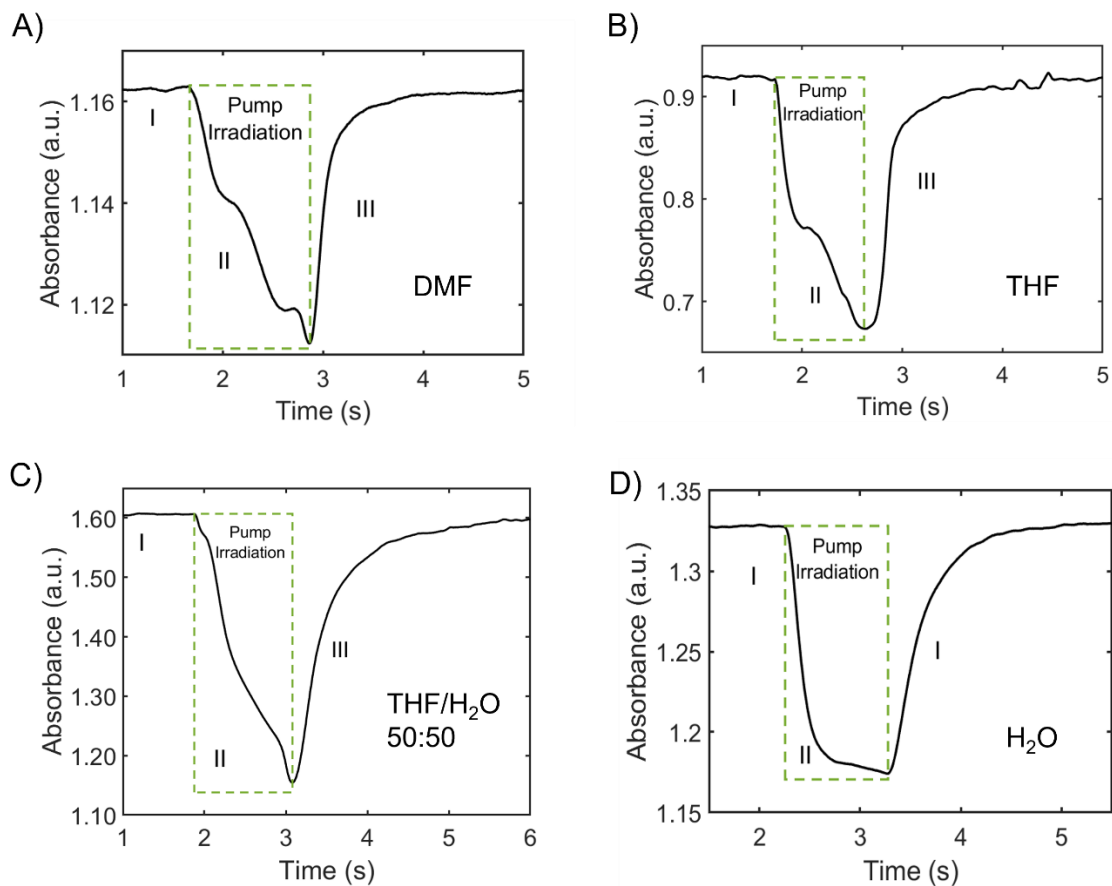


Figure S3.1 The absorbance vs. time profiles of BBY in solvents (A) DMF, (B) THF, (C) THF/H₂O, and (D) H₂O. (I) Before irradiation, (II) during 1s pulse with a 532 nm laser, (III) *cis* decay in dark.

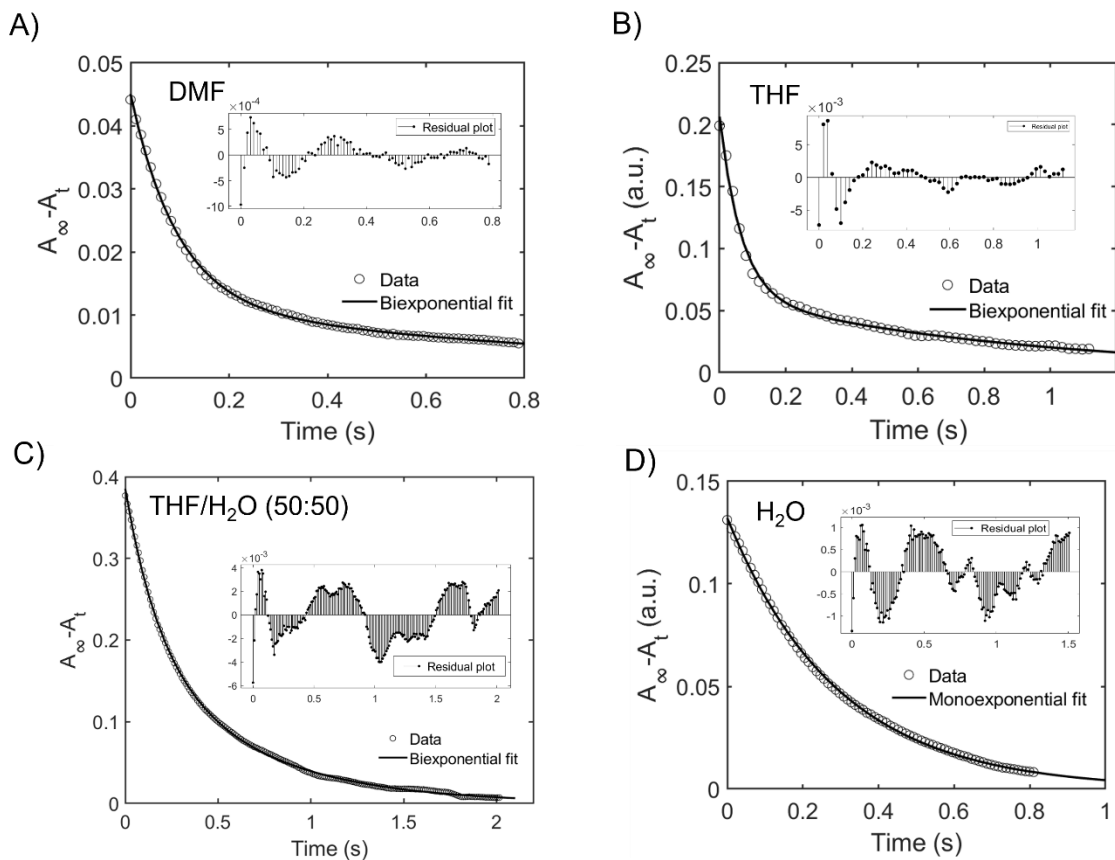


Figure S3.2 The decay of *cis* isomer fit to biexponential kinetics of BBY in solvents (A) DMF, (B) THF, (C) THF/H₂O, and (D) H₂O. The inset shows the residual plot between our least-squares four-parameter biexponential fit and the data.

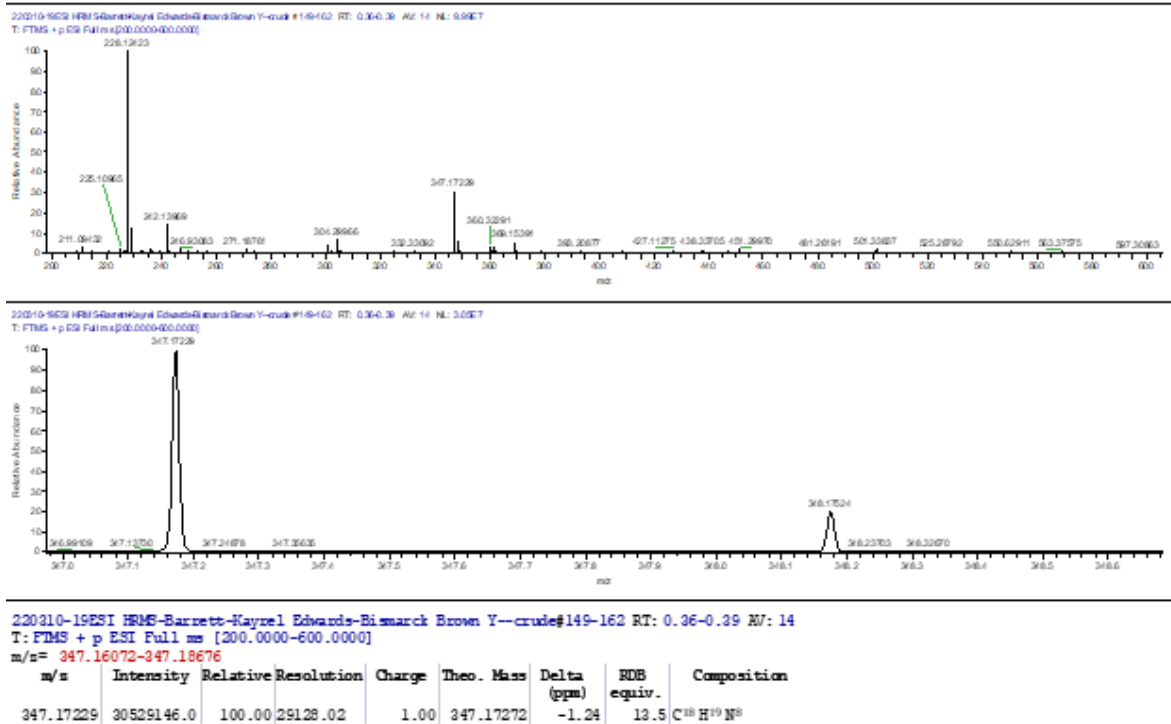


Figure S3.3 Mass spectra of crude BBY.

- Crude BBY (ESI +p, m/z= 347 (C₁₈H₁₉N₈), 228 (C₁₂H₁₄N₅), 242 (C₁₃H₁₆N₅), expected mass (C₁₈H₁₈N₈.2HCl, FW=419.3 g/mol).
- Recrystallized BBY (ESI +p, m/z= 347 (C₁₈H₁₉N₈), 228 (C₁₂H₁₄N₅), 242 (C₁₃H₁₆N₅), expected mass (C₁₈H₁₈N₈.2HCl, FW=419.3 g/mol)
- Chrysoidine (ESI +p, m/z= 213 (C₁₂H₁₃N₄), expected mass (C₁₂H₁₂N₄.HCl, FW=248 g/mol).

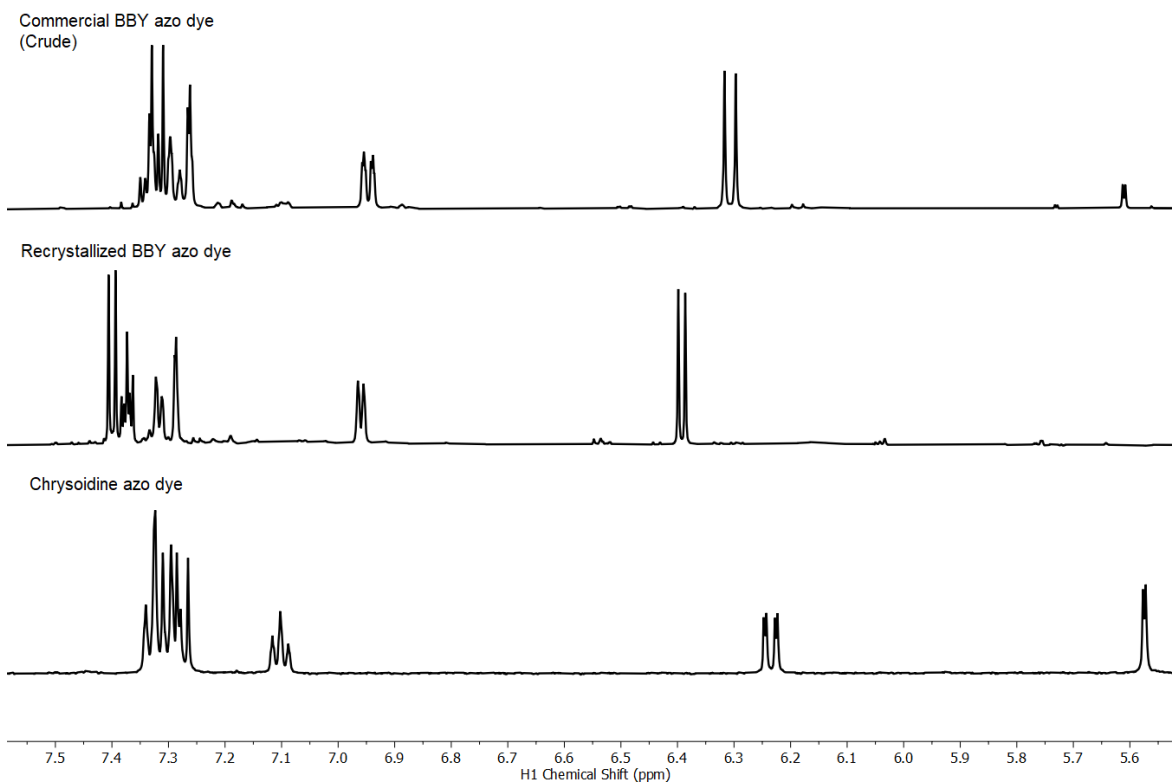


Figure S3.4 ^1H -NMR spectra of crude commercial BBY, recrystallized BBY and Chrysoidine azo dyes.

- Crude commercial BBY azo dye (500 MHz, D_2O) δ 7.37 – 7.24 (m, 4H), 6.98 – 6.92 (m, 1H), 6.31 (d, $J = 9.9$ Hz, 1H)
- Recrystallized BBY azo dye (800 MHz, D_2O) δ 7.40 (d, $J = 9.9$ Hz, 2H), 7.39 – 7.35 (m, 2H), 7.32 (dd, $J = 8.1, 2.2$ Hz, 1H), 7.29 (t, $J = 2.2$ Hz, 1H), 6.96 (dd, $J = 8.0, 2.1$ Hz, 1H), 6.39 (d, $J = 9.9$ Hz, 2H)
- Chrysoidine azo dye (500 MHz, D_2O) δ 7.37 – 7.24 (m, 5H), 7.11 (d, $J = 7.2$ Hz, 1H), 6.24 (dd, $J = 9.9, 2.3$ Hz, 1H), 5.57 (d, $J = 2.3$ Hz, 1H)

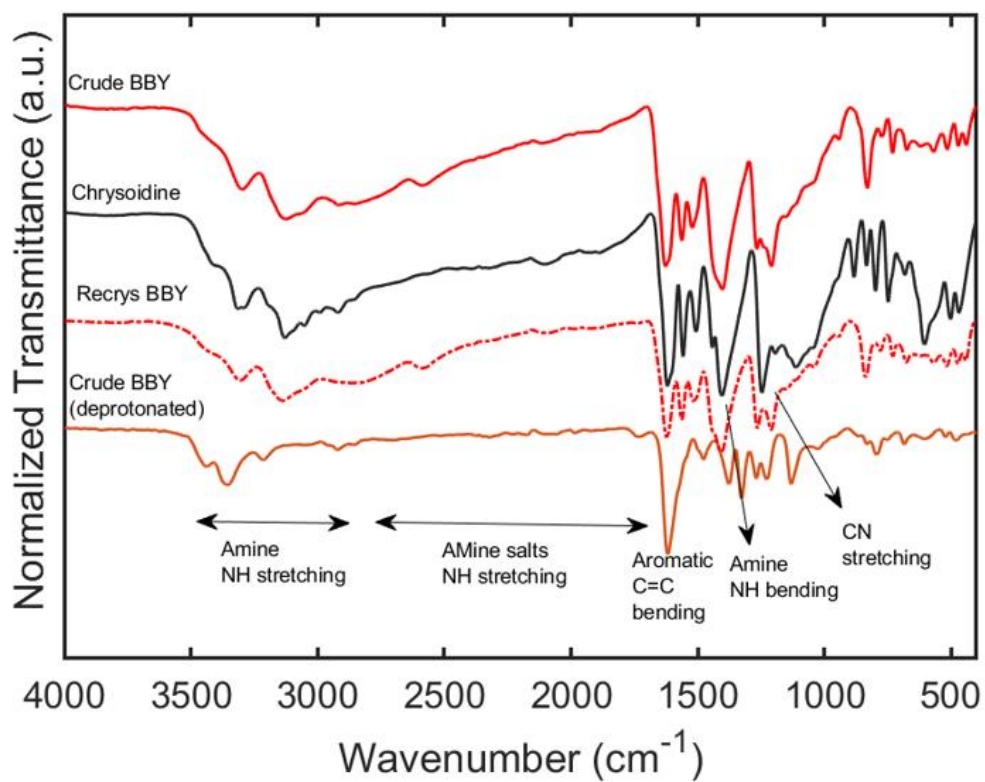


Figure S3.5 FTIR spectra of crude commercial BBY, Chrysoidine, recrystallized BBY and crude BBY (deprotonated) azo dyes.

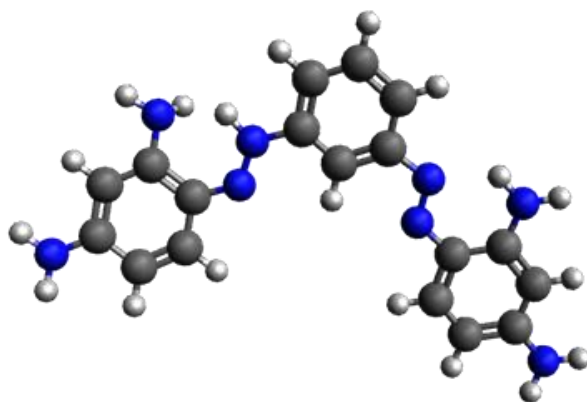


Figure S3.6 DFT optimized geometry of the protonated EE (*trans*) isomer of BBY.

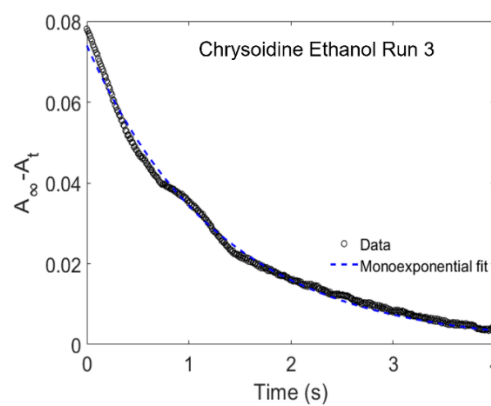
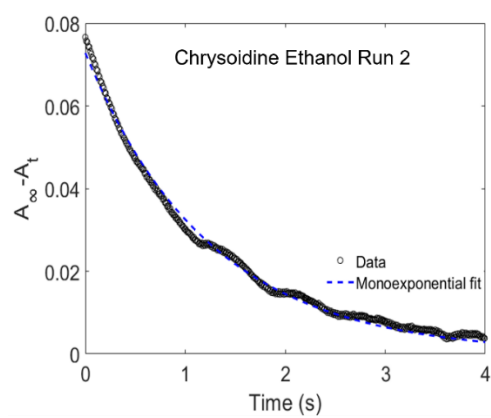


Figure S3.7 Runs '2' and '3' showing the decay of *cis* isomer fit to monoexponential kinetics of Chrysoidine.

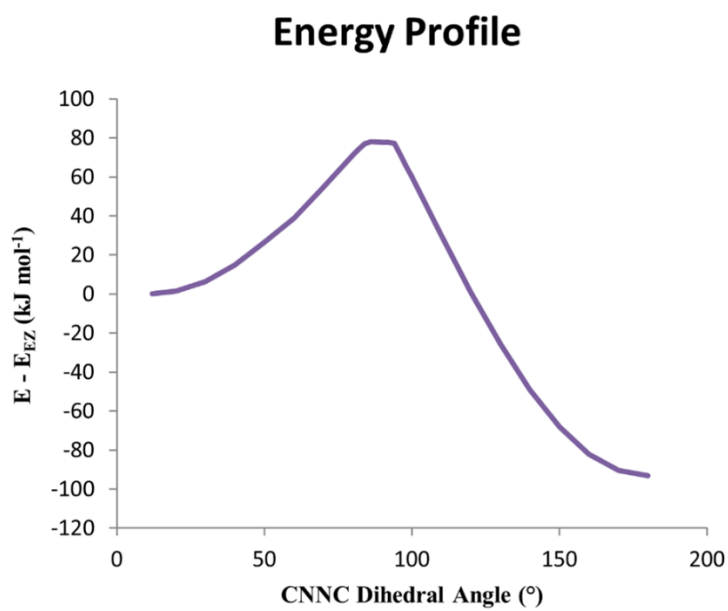


Figure S3.8 Energy profile showing a typical monotonic rise from the *cis* isomer to the activation energy, followed by a monotonic fall to the *trans* isomer, as a plot of relative Energy vs. C–N=N–C bond angle.

Bridging Text for Chapter 4: Valorization of brown seaweed

The research presented in Chapter 4 was inspired by circumstances surrounding the Coronavirus pandemic from 2020–2021, which found me being stationed in my home country of St. Vincent and the Grenadines (SVG) for 1 year and observing the brown seaweed (pelagic *Sargassum spp.*) polluting many of its beaches. This Chapter describes developing a methodology to valorize this waste brown seaweed, with a goal to convert the raw material into an advanced green material. It is my hope that these methods can be extrapolated to other Caribbean islands and coastal provinces in Canada, which also experience an influx of seaweed. Past research in the Caribbean on converting this waste brown seaweed to a high-valued material has focused on conversion to energy *via* combustion, fertilizers, packaging, and extraction of alginates to be used for heavy metal sequestration.

Two of the main components of brown seaweed are alginate and cellulose. In this Thesis Chapter, the goal was to develop a facile method of extracting both alginate and cellulose from the waste brown seaweed in a single scheme, for use in several applications ranging from packaging of food and utensils to fabricating photo-reversible coatings for controlled assembly/disassembly, as an extension to previous Chapters. Improvements were made to already established protocols of extracting alginate and cellulose from *Sargassum spp.*, such as the omission of sulfuric acid and initial bleaching of the brown seaweed, which improved the extraction yields of both polymers. In this Chapter novel blends of the extracted alginate were prepared using another local product of St. Vincent known as arrowroot starch which is mainly used for food. This Chapter has shown that arrowroot starch can work just as well as a plasticizer in alginate films compared to the more commonly used starches such as corn and sago starch. The extracted polymers were thoroughly

characterized, and the mechanical and physical properties of films solvent-cast from these bio-based polymers were assessed. The extracted alginate was also used for the first time to prepare novel azo dye-based photo-reversible materials such as beads/capsules and polyelectrolyte multilayer (PEM) films similarly to the cellulose-based films prepared in Chapter 2.

This Chapter will hopefully highlight a possible route for countries like St. Vincent and the Grenadines to convert a waste-material (brown seaweed) to a value-added product through a facile and inexpensive process, requiring access to only basic lab equipment and readily available reagents such as soda ash, caustic soda, bleach, and ethanol. One potential application of these alginate blends, highlighted by this project, is use as a bioplastic in packaging to replace traditional petrol-based packaging, particularly HDPE. The results presented here show that the mechanical and physical properties of films cast from these alginate blends are comparable to other products currently on the market. By the end of this Chapter, it is hoped that great potential should be clear for this waste brown seaweed to be converted in a facile manner towards a high-valued green material.

Valorization of brown seaweed

K. E. K. Edwards, C. J. Barrett and T. G. M. van de Ven**

Department of Chemistry, McGill University, Montreal, QC, Canada

4.1 Abstract

Over the last decade there has been an influx of pelagic *Sargassum spp.* (brown seaweed) into the Caribbean region, possibly due to climate change. Seaweed is a good candidate for the fabrication of bioplastics because of its high biomass and its ability to grow in a wide range of environments. Herein, we propose a method to valorize waste *Sargassum spp.* collected from St. Vincent and the Grenadines shores to produce bioplastics and photo-reversible materials as an alternative to petrol-based plastics. The extraction of alginate and cellulose from the brown seaweed and characterization by FTIR spectroscopy, NMR spectroscopy, PXRD and microscopy are outlined. Thin films and straws were prepared using the extracted alginate, and novel blends of the alginate were prepared with natural plasticizers: arrowroot starch, which is abundant and underutilized in St. Vincent, and glycerol. The mechanical properties such as tensile strength (MPa) and elongation at break (%), and physical properties such as water vapour and oxygen permeability of the various films were then assessed. The results indicate that materials made from the extracted alginate are comparable to commercial plastics, particularly HDPE. The incorporation of a photo switchable small molecule azobenzene-based (azo) dye, *via* soft-bonding interactions with the alginate polymers resulted in the fabrication of photo-reversible azo/alginate coatings and capsules which can potentially be used for controlled assembly/disassembly applications.

4.2 Introduction

A harrowing quote from the Vice Chancellor of the University of the West Indies (UWI) in Barbados, Sir Hilary Beckles, from a UNEP 2015 report on understanding the spread of Sargassum in the Caribbean states: “overall it would cost the Caribbean region at least US \$120 million and more than 100,000 people to assist the cleanup efforts for the spread of Sargassum in the Caribbean.”¹ The potential as a material of the waste brown seaweed (*Sargassum spp.*) littering the shores of many Caribbean islands towards use as high-value products in the plastic and packaging field is vast. The ability to valorize this waste stream towards use as a raw material for already existing markets ranging from food and energy to packaging could significantly boost the economies of these islands and may also provide a business model for coastal provinces in Canada such as Nova Scotia and New Brunswick which also experience an influx of seaweed (mainly Kelp and Irish Moss) onto their shorelines.²⁻⁴

Since 2011, there has been an influx of free-floating or pelagic brown seaweed into Caribbean waters mainly from the Sargasso Sea.^{1,5,6} This influx has been attributed to an increase in sea temperatures and a decrease in winds.⁶ This influx has also been linked to rising nitrogen content due to pollution from sewage, oil, fertilizers, and global climate change.^{5,6} Normally, the presence of seaweed is beneficial for aquatic life, serving as habitats for fish and invertebrates, being used as nurseries, feeding grounds, and shelter. However, the extreme Sargassum bloom over the last 11 years has negatively impacted many Caribbean islands. According to a recent report by Anne Desrochers in 2020 from the Centre for Resources Management and Environmental Studies (CERMES) of the UWI, Cave Hill campus in Barbados, many sectors such as the Fisheries and Tourism industries have been negatively affected by this ever-growing Sargassum bloom.⁵ For

example, in Barbados in 2015, 42 sea turtles were found dead possibly due to entanglement and compression from the Sargassum on the beaches which serve as a nesting place for the sea turtles.¹ The influx of the Sargassum has also affected the Tourism industry and the surrounding inhabitants, by polluting beaches and giving off a foul odour as the seaweed rots.⁷ The fishing industry is also negatively affected since the dense Sargassum blooms make it difficult for boats to manoeuvre through the waters affecting fishing quotas.¹

Despite the large sum of money predicted to be needed to clean up all the Sargassum in the Caribbean, many valiant efforts have been made towards valorizing this waste brown seaweed. In 2018 the UN Cartagena unit offered monetary support to many Caribbean islands such as Guadeloupe, Martinique, Curaçao, Trinidad, and Barbados, to valorize the Sargassum and use it as a raw material for different applications.⁵ These applications included: food, packaging, fertilizers,⁸ energy *via* anaerobic digestion, combustion and pyrolysis,^{5, 8} heavy metal sequestering^{9, 10} and textiles. Many Caribbean researchers have investigated strategies for optimizing the extraction of alginates,^{6, 11} one of the major components of brown seaweed, while others have studied the use of this alginate to sequester heavy metals for wastewater treatment,^{9, 10} and for electrochemical applications.⁸ Outside of the Caribbean, research into brown seaweed has been prolific, with researchers focusing on valorizing all components of the brown seaweed from the alginates, mineral salts and proteins to cellulose, one of the most abundant natural polymers on earth, usually extracted from terrestrial lignocellulosic biomass such as wood.^{12, 13} Previous work from the authors based in Canada has also investigated the use of alginates blended with hairy nanocellulose for removal of dyes from wastewater.¹⁴

While the most abundant type of seaweed in the Caribbean is the *Sargassum spp.* which can be further divided into *S. fluitans*, *S. natans III* and *S. natans IV* based on slight

morphological differences,¹¹ in other regions of the world, such as East Asia (mainly Japan, South Korea, India, and China), the seaweed industry has focused on other species of seaweed such as Nori and Kelp, mainly used for food.^{15, 16} In the North Atlantic, edible red alga seaweed is harvested in Eastern Canada, Ireland, and Iceland, known as ‘dulse’, a popular, if acquired, local delicacy.^{4, 17} In 2019 the world seaweed production was 35.8 million tons according to the FAO (2021), with most of the seaweed (97 %) being farmed and produced in Asia, and only 3 % harvested from the wild.¹⁷ Seaweed is considered a macroalgae which in many ways is like a plant, containing chlorophyll and photosynthesizing to make their food.¹⁵ The different groups of seaweed are classified based on the pigments which give them their distinct colours: green seaweed (Chlorophyta) contains mostly chlorophyll a and chlorophyll b, red seaweed (Rhodophyta) contains phycobiliprotein and brown seaweed (Phaeophyta) contains fucoxanthin.^{12 15}

According to reports by Baghel most of the seaweed is made up of water, up to 85 % of their bodies.^{12, 18} As it relates to dry mass, the chemical composition of seaweeds is generally constituted of carbohydrates (50 %), lipids (1–5 %), proteins (10–47 %), and minerals (8–40 %).^{12, 18-20} Some researchers also reported the constitution of phenolic compounds (25 %).^{8, 19} Depending on the group, species, and area in which the seaweed is growing the % composition can change. **Figure 4.1** shows an illustration of the structure and composition of brown seaweed. Generally it is understood that brown seaweed has a high % of alginates and cellulose, red seaweed has a high % of agar and green seaweed has a high % of carrageenan.²¹ Together the hydrocolloids found in seaweed: agar, carrageenan, and alginates are great gelling agents²² and are generally exported from Asia to Western countries to be used as food additives, in cosmetics, and in the healthcare and pharmaceutical industries, among others.^{18, 21-24}

Alginates are an interesting class of biopolymers which depending on their counterions (*e.g.*, sodium or calcium) can be water-soluble or insoluble.²⁵ The polymer is constituted of repeating units of mannuronic acid (M) and guluronic acid (G) compared to cellulose whose repeating unit is glucose (**Figure 4.1**).^{23, 25} Depending on the species of the seaweed, the polymer can exist in various proportions of MM, MG, and GG repeating blocks.²¹ The extraction of alginates from *Sargassum* species in the Caribbean and Asian countries has already been well documented in the literature.^{6, 11, 26} The most common method of extraction involved pre-treatment of the brown seaweed with formaldehyde,^{6, 11} or calcium chloride,²⁶ followed by treatment with hydrochloric acid to remove most of the phenolic compounds and pigments, and to convert the predominantly calcium alginate to alginic acid.^{6, 11, 26} The viscous mixture was then treated with sodium carbonate (soda ash) to convert the alginic acid to the water-soluble gel-like sodium alginate which can then be extracted out in the aqueous phase.^{6, 11, 26} The sodium alginate was then precipitated out using excess ethanol,^{6, 11} with an optional bleaching step to remove the residual pigments. The last step involved dialysis to remove the bleach and mineral salts from the alginate, which can then be sold as a food additive,²² or used in the cosmetics or pharmaceutical industries.²³

Much research has focused on the blending of alginates with other bio-based and non-biobased compounds for use in packaging. Alginates have been used to prepare edible packaging,²⁵ and when doped with antimicrobial agents can be used as wound dressings,^{23, 24} and drug delivery systems in the medicinal field.^{23, 24} The polymer can also be blended with other natural compounds to enhance its native properties.^{25, 27, 28} For example, a recent review by Parreidt *et al.* (2018) showed how the addition of antimicrobial agents (*e.g.*, vanillin, lemongrass EO, nisin, etc.) to the alginate packaging could improve or maintain the quality and enhance the shelf-life of fruits, vegetables, meat, seafood, and cheese by altering the barrier and mechanical properties of

the materials.²⁵ Additionally, other studies have shown that the introduction of other natural polymers such as Sago starch,²⁹ and chitosan,³⁰ could alter the physical and mechanical properties of alginate materials.

While the extraction of alginates receives the most attention in the realm of brown seaweed, many researchers have also developed methodologies to extract another valuable polysaccharides such as cellulose from the phycocolloid waste stream. Cellulose is a polymer made up of repeating glucose units linked *via* a beta-(1,4) glycosidic bond.³¹ The chemical structure of cellulose allows it to form many intermolecular hydrogen bonds with other cellulose chains which can organize the polymer into microfibrils and bundles of fibres, resulting in a water-insoluble mechanically robust polymeric network.³² As previously mentioned, cellulose is generally extracted from lignocellulosic biomass such as wood, cotton, hemp, and flax,¹⁸ but over the last decade much interest has been afforded to extracting cellulose from waste streams, such as fruit peelings,³³ sawdust, and now seaweed.³¹ The advantage of extracting cellulose from seaweed is that there are fewer inputs needed, such as no land requirements, fertilizers, pesticides, or freshwater generally needed to grow trees or other terrestrial biomass.^{18, 32} According to a study by Doh, Lee, and Whiteside (2020), the extraction yield of cellulose differs depending on the species and group of seaweed, with the highest yield of 26 % being extracted from the brown seaweeds: Kombu (*Laminara japonica*) and Sargassum (*Sargassum fluitans*), compared to red and green seaweeds.¹⁹ The extracted cellulose was converted to cellulose nanocrystals (CNCs) which could then be used as fillers and reinforcing agents in packaging and other applications.¹⁹

Herein, a method to valorize waste *Sargassum spp.* collected from beaches in St. Vincent and the Grenadines is outlined, to produce bioplastics and photo-reversible materials as an alternative to petrol-based plastics. The extraction of two valuable components: alginate and

cellulose were undertaken in a facile manner to convert the waste starting material into high-value products. Materials ranging from fibers to thin films and straws were fabricated using the extracted alginate. Furthermore, thin films were prepared by blending the alginate with a natural plasticizer known as arrowroot starch, which is also abundant in St. Vincent. The mechanical and physical properties of these alginate materials were assessed to determine the most suitable application for these materials. The incorporation of a photo switchable small molecule azo dye, *via* soft-bonding interactions with the alginate polymers resulted in the fabrication of photo-reversible azo/alginate coatings and capsules which can potentially be used for controlled assembly/disassembly applications.

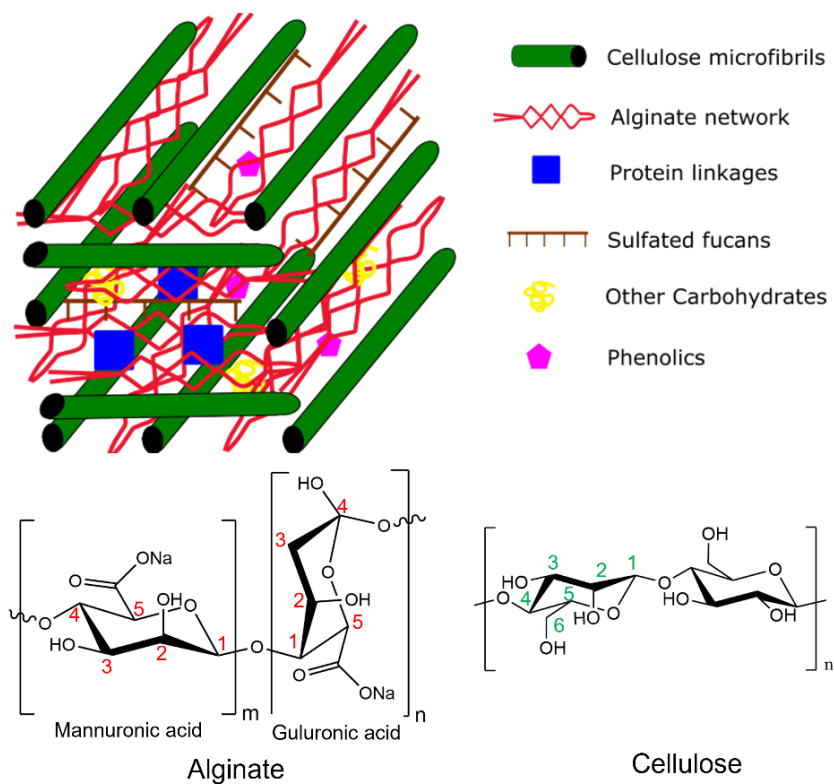


Figure 4.1 Illustration of the structure and composition of brown Seaweed (*Sargassum spp.*) & chemical structures of major components: alginate and cellulose (adapted from reference ²⁰).

4.3 Experimental

4.3.1 Materials

Brown seaweed (*Sargassum spp.*) was gathered from the shoreline of St. Vincent and the Grenadines, at the Rawacou National Park (February 2021). Arrowroot starch (Brand: Nutrela) was purchased in St. Vincent from CK Greaves & Co Ltd. Glycerol (SigmaUltra, > 99 %, CAS # 56-81-5), NaOH pellets (CAS # 1310-73-2), Bismarck Brown Y (BBY) azo dye (LOT 34H3729, $C_{18}H_{18}N_8 \cdot 2HCl$, FW = 419.3 g/mol), Bismarck Brown Red (BBR) azo dye (CAS # 5421-66-9, $C_{21}H_{24}N_8 \cdot 2HCl$, FW = 461.4 g/mol) and sodium alginate (viscosity: 200–400 cps, CAS # 9005-38-3) were purchased from Sigma Aldrich. Sodium carbonate (CAS # 497-19-8) was purchased from Fisher Scientific, hydrochloric acid (certified 0.498–0.501 N, catalog # SA50-1) was bought from Fisher Chemical, and ethanol (100 %) from Commercial Alcohols (# PO16EAAN). Lavo Pro 6 bleach (6 % w/v sodium hypochlorite) was purchased from Staples, ON, Canada. Kraft pulp which was extracted from softwood was supplied by FPInnovations (Quebec, Canada).

4.3.2 Extraction of alginates and cellulose from brown seaweed

The brown seaweed (*Sargassum spp.*) was washed to remove sand and other debris, and then dried in the open sun. The dried seaweed was then crushed and parcelled and shipped to Montreal Canada for extraction and analysis at McGill Chemistry. The extraction process of sodium alginate and cellulose from the brown seaweed is outlined below in **Figure 4.2** according to previously established protocols, with slight modifications.^{11, 12, 26} Brown seaweed (20 g) was dried in an oven overnight at 60 °C and then treated with 300 mL of sodium carbonate (3 % w/v, 9 g) for 2 h at 80 °C to convert calcium alginate to water-soluble sodium alginate. The viscous mixture was strained and the extracted gelatinous sodium alginate in the aqueous layer separated from the solid residue.

Sodium alginate was then bleached using 200 mL of 6 % w/v sodium hypochlorite (Lavo Pro 6 bleach) and precipitated out using an excess of ethanol, strained, and dried overnight in an oven at 60 °C. The mass of the crude yellow sodium alginate was 11 ± 5 g (avg. 55 % dry mass of seaweed; error analysis for 5 extraction results). The product was purified by dissolution in DI water followed by precipitation with ethanol and drying overnight in an oven at 60 °C. The extracted alginate was then dialyzed for 4 days to remove excess bleach and salts. The final mass of extracted sodium alginate was 7.0 ± 3.5 g (avg. 35 % dry mass of seaweed; error analysis for 2 extraction results). The residual seaweed from the alginate extraction was then treated with 50 mL NaOH (0.5 M) and heated for 3 h at 65 °C to remove any residual alginate, proteins, and phenolic compounds from the cellulose. The cellulose was then washed with DI water to neutralize the polymer. The extracted cellulose was then bleached with 20 mL of the hypochlorite solution and washed several times with distilled water. The extracted cellulose was dried overnight in oven at 65 °C with a resultant mass of 3.4 g (17 % dry mass of seaweed).



Figure 4.2 Schematic showing the extraction of the major components: alginate and cellulose from waste brown seaweed collected from St. Vincent.

4.3.3 Preparation of alginate-based materials

Thin films of the extracted sodium alginate were made by dissolving 2 g of Na alginate in 80 mL DI water and then solvent casting onto a ceramic or glass dish and air drying overnight. The dried films were peeled off from the plate. Novel blends containing sodium alginate, arrowroot starch and glycerol in (1:1:1 ratio, total mass 2.1 g) were prepared in a similar manner as described above. Blend solutions containing starch were heated to 100 °C to solubilize the mixture before solvent casting. All films were kept in a desiccator at RH 60 % and RT = 21–23 °C for 3 days before any analyses were conducted.

Water-resistant alginate materials were made by immersion in 5 wt. % calcium chloride solution or 1 wt. % Bismarck Brown R (BBR) azo dye solution for 10 min. Spherical beads were prepared by dripping a 2.5 wt. % sodium alginate solution into the calcium chloride solution or the BBR azo dye solution with mild stirring. The resulting beads/capsules were then freeze-dried. Straws were prepared by wrapping the alginate film around a cylindrical mold, using water to ‘glue’ the film together. The straws were then submerged in the calcium chloride or azo dye solutions and washed with distilled water and dried in an oven at 30 °C for 3 days. Polyelectrolyte multilayer (PEM) coatings were made according to previous methods by the authors.³⁴ Cleaned glass slides was submerged in a 0.03 wt. % alginic acid solution (pH = 5) for $t = 10$ min, followed by three rounds of rinsing with deionized (DI) water (pH = 7) for 1 min each. The slides were then immersed in the Bismarck Brown Y (BBY) azo dye solution (pH = 5) for $t = 10$ min, followed by 3 rounds of rinsing with DI water. This dipping process was repeated to form a film with 50 bilayers.

4.3.4 Spectroscopies and analyses

4.3.4.1 Fourier transform infrared (FTIR) spectroscopy

The infrared (IR) spectra of ground brown seaweed, and the extracted components: sodium alginate and cellulose, as well as commercial alginate from Sigma and cellulose kraft pulp, were recorded on an FTIR spectrometer (Spectrum II, PerkinElmer, USA) with a single bounce diamond attenuated total reflectance (ATR) accessory employed. The IR spectra were recorded in transmittance mode over the range 400 to 4000 cm^{-1} with a resolution of 1 cm^{-1} averaged over 64 scans. The components in the bleach and NaOH extracts from the brown seaweed were assessed using 64 and 24 scans in a similar manner as outlined above. A schematic of the components of the brown seaweed based on the FTIR data is shown in **Figure 4.1**.

4.3.4.2 Nuclear magnetic resonance (NMR) spectroscopy

^1H NMR spectra of the extracted sodium alginate from the brown seaweed and commercial sodium alginate from Sigma were acquired using a Varian 500 MHz spectrometer with solvent D_2O . Solid-State ^{13}C NMR of the brown seaweed and its extracts compared to commercial samples were carried on a Varian VNMRS 400 MHz NMR spectrometer, using a 4 mm probe, with cross polarization at a magic angle spinning of 54.74°. Samples were spun at 13 kHz with 3092 scans with an acquisition time of 30 ms and a delay of 3 s.

4.3.4.3 X-ray diffraction (XRD)

The crystallinity of powdered cellulose extracted from the brown seaweed, cellulose kraft pulp, and films of the extracted alginate and alginate blends were acquired on a Bruker Discover D8 two-dimensional diffractometer, with $\text{Cu K}\alpha$ radiation ($\lambda = 1.54 \text{ \AA}$) and VANTEC 2D detector.

Measurements were made for $2\theta = 5-50^\circ$, with a step interval of 0.02° . The characteristic planes (200) and (110) of cellulose I were assigned according to other established protocols,³⁵ and the crystallinity determined using the **Equation (1)**³⁵ below:

$$CI (\%) = \left(\frac{I_{max} - I_{min}}{I_{max}} \right) \times 100 \quad (1)$$

Where CI is the crystallinity index (%), I_{max} is the intensity of the maximum peak at plane 200, and I_{min} is the intensity of the minimum peak at plane 110.

4.3.4.4 Polarized light microscopy (PLM)

Images of individual microfibrils, fibres and microgels of the extracted cellulose and sodium alginate were taken using a polarized light microscope (Zeiss Scope A1 Axio) equipped with a Axiocam 596 colour camera, with 50× and 100× objectives, with a rotatable stage. Images were processed using the Zen Blue software.

4.3.4.5 Conductometric titration

The degree of substitution (DS) of the carboxylic content of the extracted sodium alginate from the brown seaweed was measured using conductometric titration. Sodium alginate (53 mg) dissolved in 100 mL water, adjusted with 0.1 mL 0.5 N HCl, was titrated against 10 mM NaOH to obtain the pH and conductivity curves as seen in **Figure 4.5**. From the intercepts the carboxyl content was determined to be 5.1 mmol/g which is approximately a DS ~ 1.

4.3.5 Water solubility

The water solubility of the various alginate films and blends was assessed using the method outlined by Fazilah *et al.* (2011), with slight modification.²⁹ Films were cut into strips of 2 cm × 3 cm and stored in a desiccator with silica gel (RH 0 %) for 1 week before measurements were taken. The initial mass of the films was taken to the nearest 0.0001 g. The samples were placed in a beaker with 80 mL deionized water and agitated for 1 h at RT (21–25 °C). The mixture was filtered using a Whatman No.1 filter, dried at 60 °C to constant weight. This was repeated in triplicate. The water solubility was calculated using **Equation 2** below:

$$\text{Water solubility (\%)} = \left(\frac{\Delta w}{w_i} \right) \cdot 100 \quad (2)$$

where Δw is the weight loss of film (g) and w_i is the original weight of the film (g).

4.3.6 Oxygen transmission rate (OTR)

The OTR ($\text{cm}^3 \text{ m}^{-2} \text{ day}^{-1}$) of the alginate films and blends was measured using an OX-TRAN® 2/22 (H) (MOCON, USA) machine. During testing the temperature was kept at 23 °C and gas at 0 % RH. Experiments were performed in duplicate on samples of dimensions 5.64 cm^2 and thickness 0.1–0.2 mm.

4.3.7 Water vapour transmission rate (WVTR) and permeation (WVP)

The WVTR and WVP tests were performed according to the ASTM E96 upright cup test with slight modifications.³⁶ A vial was filled with dried calcium chloride and a strip of the thin film was placed between two circular disks on top of the flask. The initial mass was recorded, and the

vial placed in a humidity chamber with saturated salt solution (22 °C, 58 % RH). The mass was taken every 24 h for 1 week and WVTR calculated based on the **Equation 3** below:

$$WVTR (cm^3m^{-2}day^{-1}) = \left(\frac{w}{t}\right)(A^{-1}) \quad (3)$$

where w is the weight loss (g) converted to volume loss (cm^3) given that the density of water is $1 gcm^{-3}$, t is the time (days), and A is the area of the film (m^2). The WVP can then be calculated using **Equation 4** below:

$$WVP (gm^{-1}s^{-1}Pa^{-1}) = WVTR \cdot d \cdot (\Delta p^{-1}) \quad (4)$$

Here d is the thickness of the film (m), and Δp is the vapour pressure difference of the saturated salt solution (2 kPa, at 295 K).

4.3.8 Mechanical testing

The mechanical properties of the alginate films and blends were acquired based on previously established protocol by Fazilah *et al.* (2011),²⁹ and the ASTM D882 standard for tensile properties of thin plastic sheetings.³⁷ The films were cut into rectangular strips of dimension 25 mm × 75 mm, and thickness 0.10–0.22 mm, measured using a tmi® testing machine (model 49-70) in triplicate. The tensile stress (MPa) and elongation at break (%) were obtained by extending the film, which was gripped at 30 mm, at a rate of 1.5 mm/s until the film ruptured at the centre. Measurements were performed on six samples each and the average tabulated. The machine used was an Instron Mini 44 (gripper CAT # 2710-004).

4.4 Results and discussion

4.4.1 Extraction yields

Two strategies were undertaken to extract sodium alginate from waste brown seaweed (*Sargassum spp.*); the first method entailed bleaching the brown seaweed as the first step. A major drawback to this method was the reduced overall yield of the extracted alginate. Upon bleaching it was observed that the dry mass of the seaweed was reduced by 44 % before treatment with the soda ash to extract the alginate. Inspection of the components extracted during the bleaching process revealed that their identity was determined to be predominantly alginates as observed by the FTIR spectroscopy. This loss of sodium alginate in the bleach solution led to a poor crude yield of < 31 % compared to the crude yield of 55 % which could be achieved if bleaching was done before the first precipitation of the alginate using ethanol. Moreover, even when the seaweed was bleached prior to alginate/cellulose extraction, subsequent bleaching was still required to remove the persistent brownish colour after treatment with soda ash and again after the cellulose extraction. Therefore, the second method involving no initial bleaching of the seaweed and only bleaching of the extracted alginate and extracted cellulose was used since this method utilized less bleach and resulted in higher extraction yields of alginate from the waste brown seaweed. The extraction yields of both alginate (35%) and cellulose (17%) in this study were comparable to those previously reported at 17–30 % for alginates^{6, 11} and 10–17 % for cellulose.¹²

4.4.2 Characterization

The successful extraction of sodium alginate and cellulose from the *Sargassum* brown seaweed was confirmed by several spectroscopic techniques, including liquid and solid-state NMR and FTIR spectroscopy, and XRD.

4.4.2.1 NMR spectroscopy

The NMR of waste brown seaweed (*Sargassum spp.*) was observed in the solid-state as seen in **Figure 4.3b**. ^{13}C SS-NMR showed strong bands corresponding to possibly two of the major components of the brown seaweed: alginates and cellulose. The peak at 176 ppm corresponded to the carboxylate anion (COONa) typical of alginates. The broad peaks between 100–110 ppm corresponded to the C1 of the sugars involved in the glycosidic bond for either the alginates, cellulose or sulfated fucans. The convolution of peaks between 60–80 ppm represented the C2–C6 of the different sugars present in the seaweed, mainly the alginates and cellulose.

For the extracted sodium alginate both liquid (**Figure 4.3a**) and solid-state (**Figure 4.3b**) NMR was used to confirm the structure as well as high purity of the samples using the method outlined in the experimental section. Sodium alginate forms a viscous solution and can even gel when dissolved in water, so for liquid NMR very dilute systems were used. Liquid NMR was not used for cellulose since it has limited solubility in many common NMR solvents. Based on previous reports, sodium alginate is constituted of repeating units of mannuronic acid and guluronic acid compared to cellulose whose repeating unit is glucose. Depending on the species of the seaweed, the ratio of the M/G units differ. Generally, for alginate polymers, ^1H NMR spectrum should have peaks between 3.5–5.2 ppm, with an expected peak at 5.08 ppm corresponding to G-1, and 4.70 ppm corresponding to M-1 (where 1 represents the C1 involved in the pyranose bond connecting the sugar units together into a chain). **Figure 4.2a** shows the ^1H NMR spectrum of sodium alginate extracted from the waste brown seaweed (*Sargassum spp.*) with peaks at: δ 4.96 (G-1), 4.37 (G-5), 4.11, 4.03, 3.95, 3.92 (G-2,3,4), 3.83, 3.67, 3.58, and 3.56 ppm (M-2,3,4).

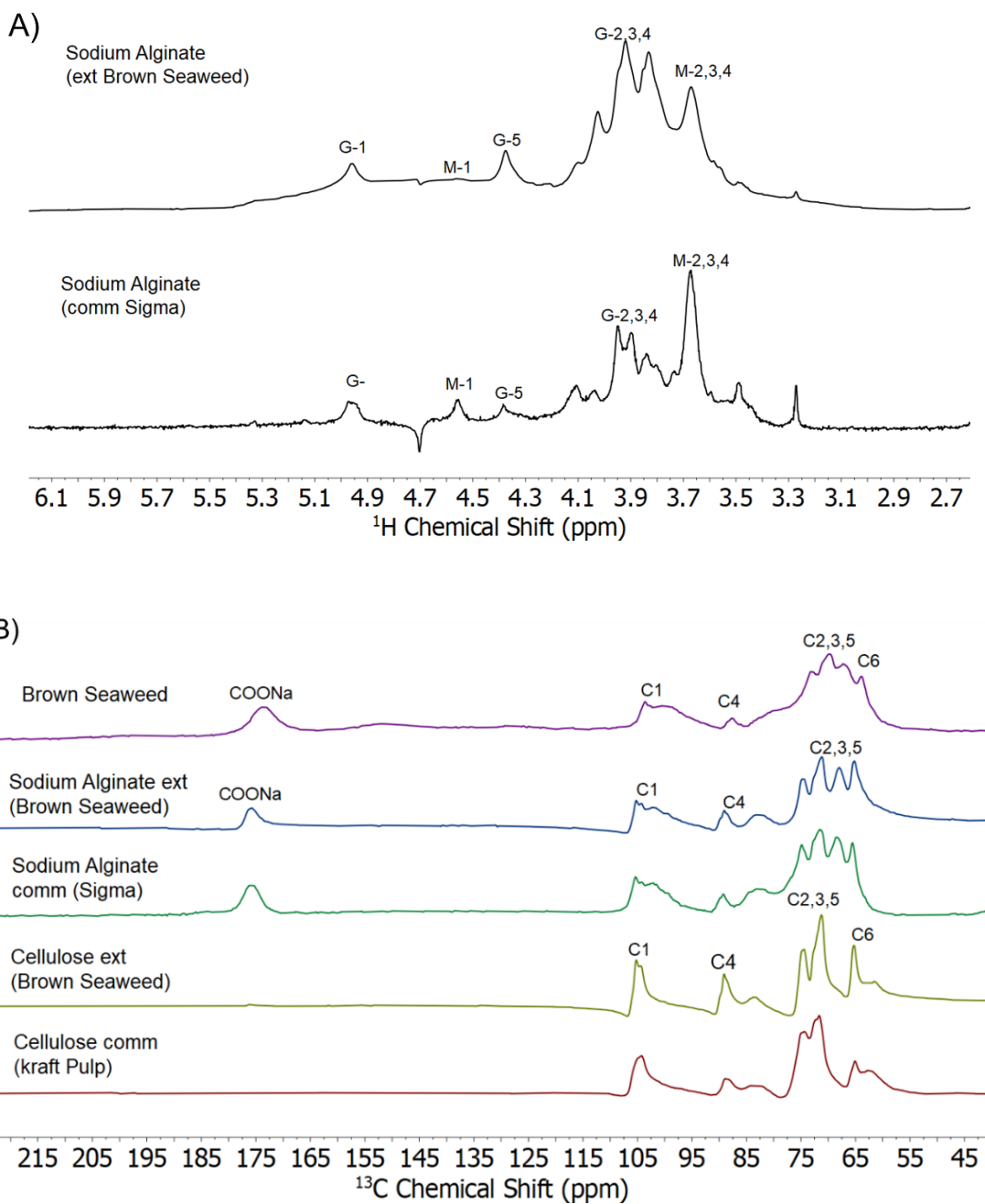


Figure 4.3 (A) ^1H NMR spectra of extracted Na alginate from brown seaweed (*Sargassum spp.*) vs. commercial Sigma Aldrich in D_2O solvent. (B) ^{13}C Solid-State NMR of brown seaweed, extracted sodium alginate from brown seaweed vs. commercial Sigma Aldrich, and extracted cellulose from brown seaweed vs. commercial cellulose kraft pulp.

There was also a very small peak at 4.70 ppm corresponding to M-1. This indicated that the alginate extracted from the brown seaweed (*Sargassum spp.*) was made up more of guluronic acid compared to mannuronic acid. The spectrum matched well with that of commercial sample from Sigma and previous work by other authors.³⁸ In the commercial sample, the M-1 and M-2,3,4 peaks were more pronounced, indicating a higher degree of M/G in the commercial Sigma sample which more than likely originated from East Asia compared to the sample extracted from the *Sargassum* brown seaweed located in St. Vincent in the West Indies.

In addition to liquid NMR, solid-state NMR, with magic angle spinning (MAS) can give well resolved peaks for the different carbons in the alginate and cellulose-based samples.³⁸ **Figure 4.3b** shows the solid-state ¹³C NMR spectra of the extracted alginate vs. a commercial sample from Sigma. The extracted sodium alginate matched very well to the alginate sample from Sigma. The presence of the carboxylate anion (COONa) was observed at 176 ppm, with 3 peaks for C1 at 105 ppm, 104 ppm, and 101 ppm possibly due to the M and G sugars. There were also two peaks at 84 ppm and 83 ppm corresponding to C4, and several peaks between 65–83 ppm corresponding to C2, C3, and C5. The absence of peaks at 60 ppm and 65 ppm which is observed for C6 on the pyranose ring for cellulose confirmed the high purity of the extracted alginate. For the extracted cellulose from the *Sargassum* brown seaweed, the spectrum matched well with cellulose kraft pulp, which was extracted from softwood, with the expected peaks observed for C1–C5 between 70–110 ppm. There were two peaks observed at 60 ppm and 65 ppm, corresponding to C6 which is expected for cellulose. The ratio of these two peaks representing C6 were different for cellulose extracted from waste *Sargassum* brown seaweed compared to cellulose kraft pulp extracted from wood. There was a very small peak at 176 ppm, which indicated that the cellulose was not 100 %

pure, and there might still be some residual alginate or glycoproteins in the extracted sample compared to the sample from wood (where the major contaminant would be lignin).

4.4.2.2 FTIR spectroscopy

The IR spectrum of dried brown seaweed is shown in **Figure 4.4**. The spectrum resembled that of the extracted alginate and cellulose, with some additional peaks not found in the spectra of these two individual components, indicating the presence of other compounds within the brown seaweed. There was a strong and broad peak observed at 3265 cm^{-1} which corresponded to the O–H stretch of the alcohols and carboxylate anion groups of the various carbohydrates in the brown seaweed.

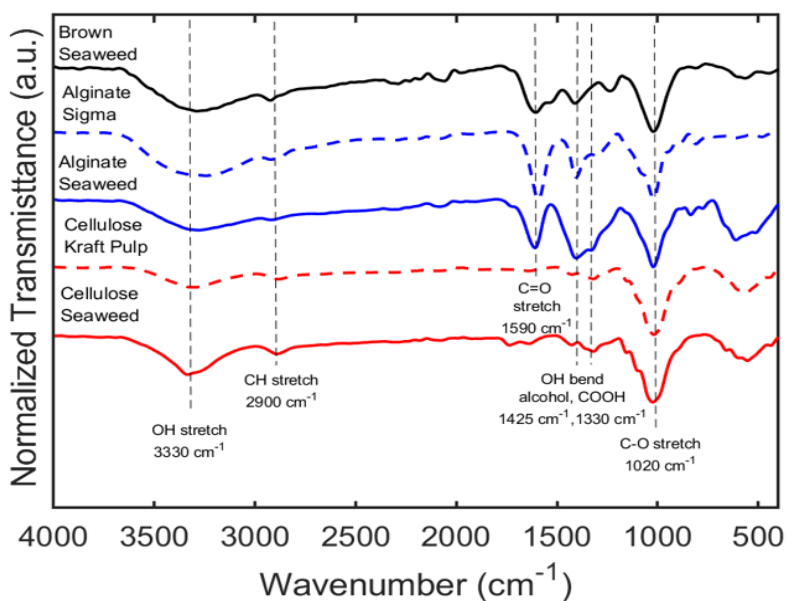


Figure 4.4 IR spectra of brown seaweed (black), commercial alginate Sigma Aldrich (blue, dashed), extracted Na alginate (blue), commercial cellulose kraft pulp (red, dashed), and extracted cellulose (red).

There was also a broad stronger peak at 1024 cm^{-1} due to the C–O stretch of the ether group characteristic of the of sugar units of the various carbohydrates, such as cellulose, alginate and sulfated fucans. There were also weaker, broad peaks observed at 2900 cm^{-1} which corresponded to the C–H stretch of the various polysaccharides, 1590 cm^{-1} which corresponded to the C=O stretch of the carboxylate anion of alginates, 1520 cm^{-1} which corresponded to the C=C stretch of the polyphenols, 1422 cm^{-1} , 1380 cm^{-1} , and 1330 cm^{-1} which can correspond to either the O–H bend of the sugar alcohols, or the O–H bend of carboxylate anion/carboxylic acid, and/or the S=O stretch of sulfates of the sulfated fucans. Analysis of the various bleach, and base residuals during the extraction processes confirmed the presence of largely alginates or glycoproteins in the bleach residue, and sulfated fucans or calcium carbonate in the NaOH residue.

The successful extraction of sodium alginate from the waste brown seaweed was confirmed by IR spectroscopy (**Figure 4.4**) with peaks corresponding to 3265 cm^{-1} (O–H stretch of carboxylate anion), 1602 cm^{-1} (C=O stretch of carboxylate anion), 1422 cm^{-1} (O–H bend of alcohols), 1330 cm^{-1} (O–H bend of carboxylic acid), 1024 cm^{-1} (C–O stretch of ether). The presence of the peak at 1330 cm^{-1} indicated that not all the carboxylic groups of the alginate was in the form of the carboxylate anion (with a Na^+ counterion), but some also existed in the acid form. There were also peaks in the fingerprint region seen for the cellulose polymers: 878 cm^{-1} and 514 cm^{-1} , which could indicate some residual cellulose still present in the extracted alginate sample. The IR spectrum of the extracted alginate matched well with that of commercial sodium alginate from Sigma, with the Sigma sample having a weaker peak at 1330 cm^{-1} indicating most of the sample existed as the carboxylate anion form, which is preferable when making the water-soluble form of the alginate polymer (**Figure 4.4**).

The IR spectrum of the extracted cellulose showed very weak peaks in the region characteristic of alginates and the sulfated fucans between 1200–1800 cm^{-1} . There was a sharper peak at 3330 cm^{-1} representing the O–H stretch of the alcohols and possibly a N–H stretch from residual glycoproteins. This contamination of the extracted cellulose was observed in other works, for example Doh (2020) observed peaks in their cellulose spectra at 1427 cm^{-1} and 1507 cm^{-1} which they attributed to the C=C stretch of the aromatic hydrocarbons of small amounts of polyphenols present in the seaweed. For our cellulose sample, the peaks at 2918 cm^{-1} and 1030 cm^{-1} corresponded to the C–H stretch and C–O stretch of the pyranose rings. The spectrum matched well to that of cellulose kraft pulp, with the fingerprint region having a peak at 555 cm^{-1} . The cellulose kraft pulp also had very weak peaks between 1200–1800 cm^{-1} due to less contamination from lignin and proteins, assuming a more rigorous extraction of the cellulose from softwood. Generally, the extraction of cellulose from wood in North America involves treatment with hot sodium hydroxide and sodium sulfide. Other methods such as the viscose process, which involves treatment with sodium disulfide, has been banned in this part of the world, due to the toxicity of sodium disulfide.³⁹

4.4.2.3 Conductometric titration

Conductometric titration was used to estimate the carboxylic content of the extracted alginate from the waste *Sargassum* brown seaweed (**Figure 4.5**). This method involves monitoring the change in conductivity and pH during titration of the alginate (converted to alginic acid upon addition of 0.1 mL of the stronger acid, hydrochloric acid) with a strong base, in this case sodium hydroxide. The titration curve showed that the extracted alginate polymer has a $\text{pK}_a = 4$ (the pH at which half the carboxylic acid groups are protonated) which is corresponds well with previously published

values of $pK_a = 3-4$.⁴⁰ Using the difference in the volume of sodium hydroxide taken at the intercepts of the curve, it was estimated that the extracted alginate has a carboxylic acid content of 5.1 mmol/g which equates to a degree of substitution (DS) of approximately 1 (**Figure 4.5**). This value matches well with the expected DS of alginates which is usually DS = 1, or 1 carboxylic group per mannuronic or guluronic repeating ring.

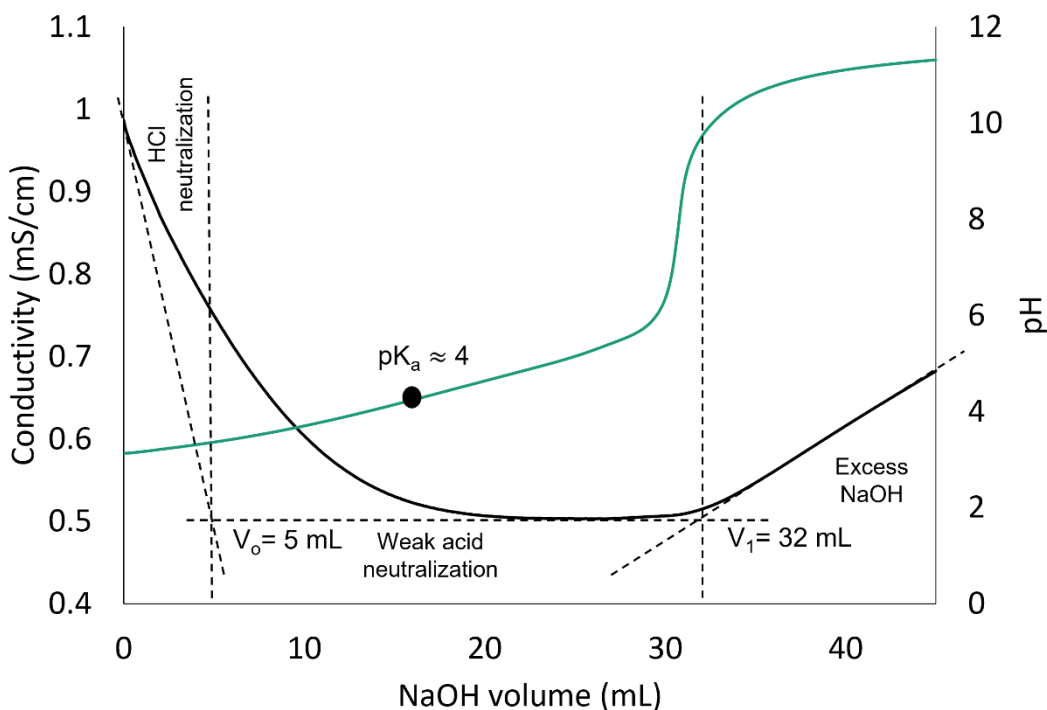


Figure 4.5 Conductometric titration of extracted Na alginate (with 0.1 mL, 0.5 N HCl) against NaOH (10 mM). Measured degree of substitution (DS) = 0.9, *i.e.*, COOH content of 5.1 mmol/g.

4.4.2.4 X-ray diffraction analysis

Calculating the ratio of the peak with highest intensity ($\sim 23^\circ$) and the minimum intensity ($\sim 17^\circ$) provides an estimation of the crystallinity of the extracted cellulose and alginate from the waste

brown seaweed according to **Equation 1**. **Figure 4.6** shows the X-ray diffraction patterns of cellulose from brown seaweed vs. cellulose from kraft pulp harnessed from softwood. Using **Equation 1**, the crystallinity of the two cellulose samples was found to be very similar: cellulose from kraft pulp being 56 % and cellulose from brown seaweed being 53 %. Both cellulose samples could be classified as cellulose I, based on previous reports.³⁵ Additionally, the sodium alginate extracted from the brown seaweed when solvent cast as a thin film was semi-crystalline with a crystallinity of 37 %.

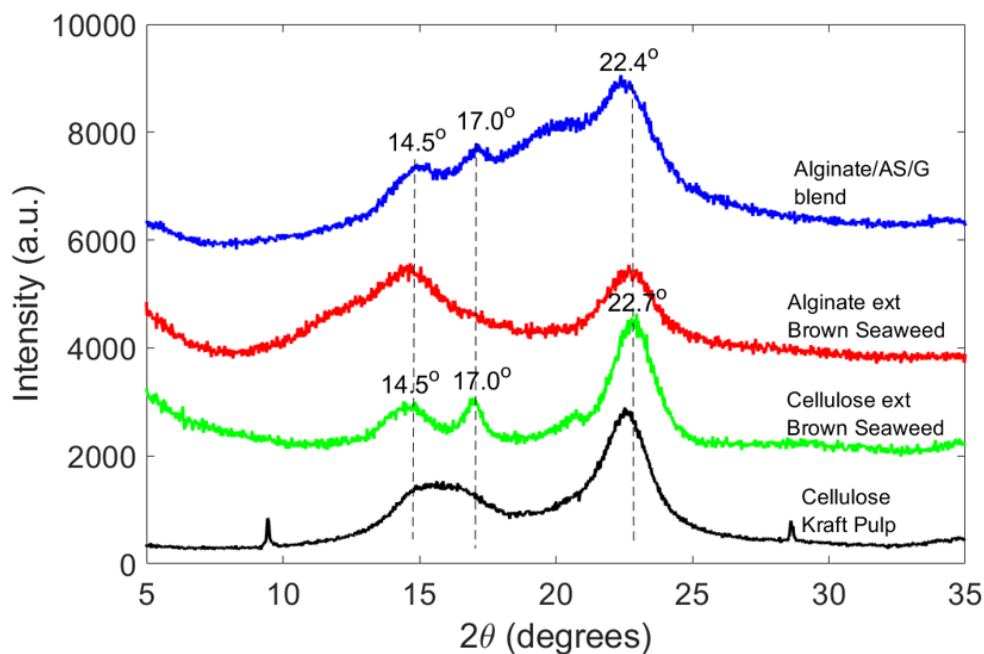


Figure 4.6 X-ray diffraction patterns of cellulose from brown seaweed (green) vs. cellulose from kraft pulp (from wood) (black), and alginate extracted from brown seaweed as a film (red), and a blend with arrowroot starch and glycerol (blue).

When blended with the plasticizers arrowroot starch and glycerol, the crystallinity was maintained at 33 %, with additional peaks appearing at 17 ° and 20 ° due to the inclusion of the starch, which

is constituted of amylose and amylopectin,^{29, 41} bearing a similar resemblance to cellulose polymeric chains and can assemble into crystalline domains.

4.4.2.5 Imaging of fibres, microfibrils, and microgels

Samples for polarized light microscopy (PLM) were prepared by depositing a few microliters of 0.01 wt. % solution of the extracted cellulose and extracted alginate on to a clean glass slide and on mica coated with Poly-L-lysine (PLL) which is positively charged. Both the cellulose and alginate should have a net negative charge and therefore better disperse and adhere as individual fibrils to the positively charged PLL coated mica in comparison to glass which is neutral or slightly negatively charged. Using the technique PLM different length scales of the alginate and cellulose polymers could be visualized (**Figure 4.7**). Both polymers appeared to be birefringent and displayed different colours when the stage was rotated between 0–90°.

For the alginate samples deposited on the bare glass, a large alginate network consisting of bundles of microfibrils, about 100 µm wide and 300 µm long, was clearly visible (**Figure 4.7a, top**). What appeared to be smaller alginate fibres were also observed; these were approximately 2 µm wide and 90 µm long (**Figure 4.7a, bottom**). The fibres were oriented in different directions and birefringent as seen by the various blue and yellow colours. For the alginate sample deposited on the mica strip coated with PLL (+), smaller individual microfibrils on the length scale of 0.5–1 µm and 10–20 µm long were observed (**Figure 4.7b**). There were also many spherical microgels observed that were made up of entangled alginate fibres ranging from 1–15 µm in diameter (**Figure 4.7b**). For the cellulose sample deposited on bare glass, entangled cellulose microfibrils were observed about 1 µm wide and 150 µm long (**Figure 4.7c, top**) as well as individual fibres 1 µm wide and 100–150 µm long (**Figure 4.7c, bottom**). For the cellulose deposited on the mica coated

with PLL a fibrous network could be visualized with individual fibres 500 nm wide and 2–10 μm long (**Figure 4.7d**).

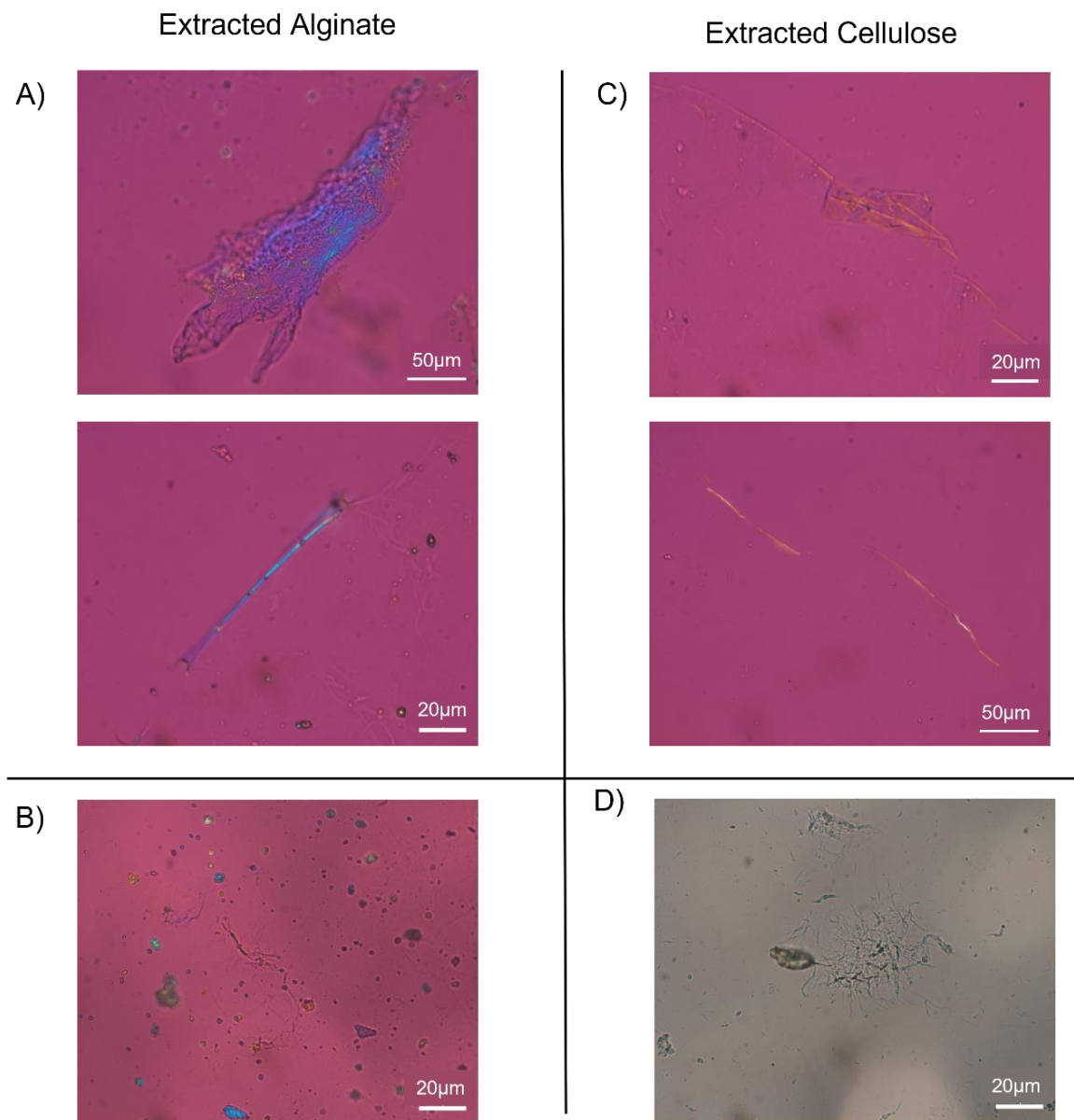


Figure 4.7 Polarized microscope images of extracted alginate bundles and fibres from brown seaweed deposited on (A) a glass slide, and (B) mica coated with PLL, and extracted cellulose fibres and microfibrils on (C) a glass slide, and (D) mica coated with PLL.

4.4.3 Physical and mechanical properties

The mechanical properties such as the tensile strength and elongation at break give an indication of how strong and extensible films cast from the extracted alginate will be. This is a very important parameter when considering a material for use in packaging, as it needs to either withstand the load of groceries if being used as a bio-based alternative to traditional single-use plastic bags, or it needs to be flexible and extensible if being used as food wrappings. Other important properties to consider are the physical properties of materials made from the alginate polymer, such as water solubility and barrier properties like water vapour transmission rate (WVTR) and permeability (WVP), and oxygen transmission rate (OTR). The latter two properties play an important role in determining the correct application of the alginate materials; for example, fruits and vegetables can withstand high barrier transmission rates ($\text{WVTR} > 100$ and $\text{OTR} > 10^4 \text{ cm}^3 \text{ m}^{-2} \text{ day}^{-1}$) while meats require low-medium barrier transmission ($\text{WVTR} = 1\text{--}5$ and $\text{OTR} = 10\text{--}100 \text{ cm}^3 \text{ m}^{-2} \text{ day}^{-1}$).⁴²

To assess the physical and mechanical properties of the extracted sodium alginate, free-standing thin films were solvent cast from an aqueous mixture of (i) alginate only and (ii) alginate blended with natural plasticizers arrow root starch and glycerol. Since sodium alginate is water-soluble, films were also submerged in a solution of calcium chloride to render the materials insoluble in water. The water solubility of the 4 samples was assessed as seen in **Figure 4.8a** and it was found that as expected the water solubility of the sodium alginate films was the highest ($94 \pm 1 \%$); however, the addition of the plasticizers to the sodium alginate significantly lowered the water solubility to a value of $2.0 \pm 0.5 \%$. The reason for this was due to starch's low solubility at RT in water, as heating to $100 \text{ }^\circ\text{C}$ is necessary to solubilize this polymer. Additionally, treatment

of both the alginate films and blends with calcium chloride resulted in fully water insoluble films (0 %) (Figure 4.8a).

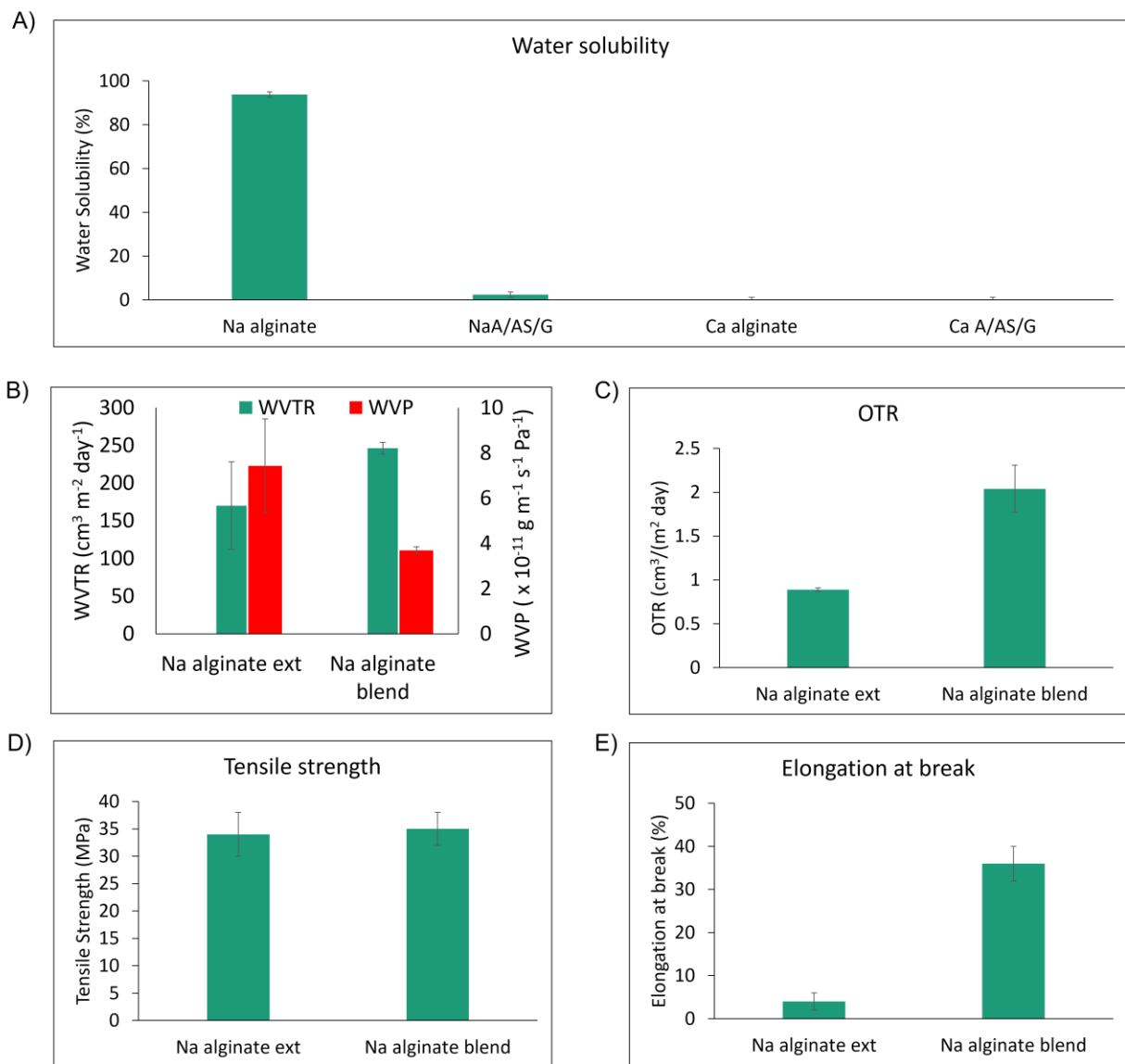


Figure 4.8 Graphs of (A) water solubility, (B) water vapour transmission rate (WVTR) and water vapour permeability (WVP), (C) oxygen transmission rate (OTR), (D) tensile strength, and (E) elongation at break of Na alginate films and blends. Error analysis: 3–6 replicates, same batch.

It has already been shown that the type of counterion affects the properties of alginates. Generally, monovalent cations like sodium have the size and valency to interact with carboxylate anion regions of the MG-block sequences of the alginate polymers in such a way that the polymer chains can still very effectively become solvated.^{21, 23, 25} However, in the presence of larger divalent cations such as calcium, the organization of the carboxylate anion groups of the alginate is such that there is greater complexation leading to gelling of the alginate network and insolubility in water.^{21, 23, 25} These results indicate that for applications requiring a material that is resistant to water, treatment of alginate films with calcium chloride or blending with plasticizers arrowroot starch (and glycerol) are adequate strategies to accomplish this.

As it relates to the barrier properties, WVTR and WVP (which takes into consideration the thickness of the films) were assessed using an inhouse set up. The films were between 0.10–0.20 mm thick and the measurements were taken over a 1-week period, in triplicate, using different pieces of films. The results indicate that the sodium alginate blends had a slightly higher WVTR than the sodium alginate only films, while the alginate blends had a lower WVP compared to the alginate only films (**Figure 4.8b**). Both films had a WVTR in the range of 100–300 cm³ m⁻² day⁻¹, which according to a review by Shogren (2019) falls in the range associated with materials used in packaging coffee, peanuts, and cheese.⁴² Other polymeric materials in this range are ethylene vinyl alcohol (EVOH) and high-density polyethylene (HDPE).⁴² Both alginate films and blends also had a WVP in the range of 3–7 × 10⁻¹¹ g m⁻¹ s⁻¹ Pa⁻¹ (**Figure 4.8b**). For the oxygen barrier properties of the sodium alginate films and blends it was observed that the blends had almost double the OTR than the alginate films only. For both films the range for the OTR was between 1–2 cm³ m⁻² day⁻¹ (**Figure 4.8c**). These values are comparable to other polymer materials such as polyglycolic acid (PGA), polyvinylidene chloride (PVDC), EVOH and corn starch.⁴² The range of

the OTR of the extracted alginate materials makes them suitable for the packaging instant coffee and peanuts.⁴²

As it relates to the mechanical properties of the extracted alginate films and its blends with the arrowroot starch and glycerol, the results indicate a moderate tensile strength that was approximately the same for both samples ~ 35 MPa (**Figure 4.8d**), showing that the addition of the plasticizers to the alginate film did not negatively impact its strength, however, the results indicated that the films were more extensible following plasticization, going from ~ 4 % to 36% elongation at break, approximately a 9 fold increase in its extensibility (**Figure 4.8e**). The mechanical properties of the alginate films were nearly identical to that reported by Fazilah *et al.* (2011) which had a tensile strength of 35 MPa and an elongation at break of 6 %.²⁹ These values were also similar to that of corn starch which has a reported tensile strength of 40 MPa and an elongation at break of 9 %. The mechanical properties recorded for the alginate/ arrow root starch/glycerol blend was comparable in terms of tensile strength to the alginate/sago starch blend prepared by Fazilah *et al.* (2011) (33 MPa),²⁹ and was much better in terms of extensibility, since their film only had a % elongation at break of 2.5 %, ²⁹ compared to the 36 % recorded for the films used in this study. The tensile strength and elongation at break of the alginate/arrowroot starch/glycerol films were comparable to that of HDPE, which has a tensile strength of 19–31 MPa and an elongation at break of 20–50 %.⁴² Similarly, the alginate only films from this study are comparable to polystyrene and PLA which have a tensile strength of 31–49 MPa⁴³ and 21–60 MPa,⁴² respectively, and an elongation at break of 2–3 %⁴³ and 3–6 %, ⁴² respectively.

Outside of replacing HDPE, EVOH, etc. in packaging materials with the extracted alginate from the waste brown seaweed, the dried unprocessed seaweed itself can potentially be used as cat-litter to replace conventional materials such as bentonite (clay) which has been reported to

absorb up to 1000 % its weight in water.⁴⁴ The authors also reported on hematite pellets bonded with starch and bentonite with water absorption capacity of 637 %.⁴⁴ The water absorption of the brown seaweed in this study was measured by soaking approximately 1.5 g of the dried seaweed in 100 mL water for 3 days and measuring the change in mass. The water absorption of the brown seaweed was measured to be 366 ± 18 % which while not as high as bentonite is still very high. The use of the unprocessed *Sargassum spp.* as a bio-based and biodegradable alternative for cat litter is another facile way of valorizing this waste brown seaweed.

4.4.4. Photo-reversible azo/alginate materials

The goal of this section was to highlight the versatility of the extracted alginate from the waste brown seaweed towards making various 3D materials, from beads/capsules to straws and polyelectrolyte multilayer (PEM) thin films. It is well known that when a solution of sodium alginate is dripped into a solution of calcium chloride, the ion exchange which occurs between the sodium and calcium cations results in an instantaneous gelling effect leading to the production of calcium alginate microbeads.⁴⁵ A similar process was attempted with the extracted sodium alginate, whereby a 1 wt. % solution of the polymer was dripped into a 5 wt. % calcium chloride solution to form hydrated calcium alginate beads of diameter 3–5 mm (**Figure 4.9a**). The freeze-dried calcium alginate beads had approximately half the diameter of the hydrated samples, *i.e.*, 1 – 3 mm.

In addition to making water-resistant calcium alginate capsules, water-resistant calcium alginate straws were prepared by rolling up a thin film made of sodium alginate and submerging into a 5 wt. % calcium chloride solution (**Figure 4.9b**). Following the ban of many single-use items such as straws, utensils, etc. by the Canadian Government in 2019, the “rat race” to find

suitable replacements for these materials have been underway. Some suitable alternatives have been metal straws, straws made from the bio-based polymer polylactic acid (PLA) and paper (cellulose) straws. However, poor performance and high prices have left consumers unsatisfied. The use of a waste component, such as the *Sargassum spp.* to make these water-resistant calcium alginate straws can be a viable solution to some of these problems.

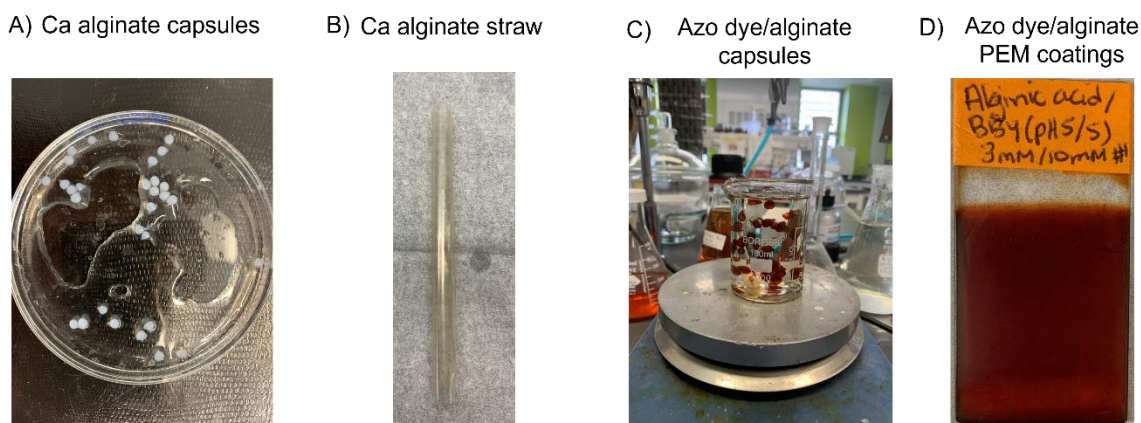


Figure 4.9 Formation of water-resistant Ca alginate (A) capsules and (B) straw, (C) azo dye/alginate capsules, and (D) azo dye/alginate PEM films.

In addition to the fabrication of water-resistant materials by exchanging the sodium counterion with calcium, water-resistant photo-reversible materials were also prepared. A similar method to make photo-reversible beads was attempted by dripping an alginate solution (1 wt. %) into a BBR azo dye solution (2 wt. %), which can act as a photo-reversible crosslinker for the alginate polymer (**Figure 4.9c**). It was shown in a previous study that a similar Bismarck Brown dye, BBY, can undergo reversible *trans-cis* isomerization in response to intensities of visible light and could act as a reversible crosslinker in cellulose-based materials.³⁴ Photo-reversible capsules

were formed *via* electrostatic interaction of the carboxylate anion of the alginate polymer with the amino groups of the BBR azo dye. The hydrated diameter of the BBR/alginate capsules was 1–2 mm; however, these capsules were not stable once removed from water and collapsed in on themselves. When freeze dried, the diameter was larger than when hydrated with an average diameter of 3–5 mm. Future studies will evaluate the use of these photo-reversible beads/capsules as delivery systems, disassembled using intensities of visible light, salinity, temperature, and/or pH.

In addition to photo-reversible capsules, photo-reversible PEM films were prepared using the extracted alginate polymer and one of the Bismarck Brown azo dyes, BBY (**Figure 4.9d**), according to a previous method developed by the authors.³⁴ In the previous method layer-by-layer films were prepared starting from water soluble components, negatively charged sulfated cellulose, and positively charged BBY azo dye. In this work the same azo dye BBY was used as the positively charged component, and the negatively charged component was the extracted sodium alginate polymer from the waste brown seaweed. Stable films were formed when both dipping solutions were adjusted to pH = 5, at which the BBY azo dye is protonated and some of the carboxylic group of the alginate is also deprotonated. It was observed that after deposition of 50 bilayers, there was an intense red colour observed for the alginate/BBY film (absorbance > 2) (**Figure 4.9c**). Additionally, AFM measurements used to obtain the average thickness of the films showed an average step height calculation of ~ 0.3 μm for the PEM films. Similar to the NaCS/BBY films previously prepared by the authors, it is proposed that these alginate/BBY films can be studied for use as photo-reversible water-resistant biobased coatings for applications from packaging or optics.

4.5 Conclusions

This work has demonstrated the ability of waste brown seaweed (*Sargassum spp.*) to be used as the starting material to fabricate various bio-based materials such as films, straws and photo-reversible PEM films and capsules, to potentially be used for packaging applications. The influx of this pelagic *Sargassum spp.* (brown seaweed) into the Caribbean sea has resulted in many challenges for the region; however, as outlined above there are many ways in which this waste material can be valorized. The extraction of a high value hydrocolloid known as sodium alginate (~35 % yield) was achieved in a facile manner using readily available reagents such as soda ash, ethanol, and bleach. Materials made from this extracted alginate had the required physical and barrier properties to replace other bio-based and synthetic polymeric materials. In addition to the extracted alginate, cellulose, one of the most highly valued polymers on earth was extracted from a non-terrestrial source in adequate yield (~17 % yield), providing another avenue to harness this polymer. The incorporation of a photo switchable small molecule azo dye, *via* soft-bonding interactions with the alginate polymers resulted in the fabrication of photo-reversible materials which in the future can be tested for their potential use in controlled assembly/disassembly applications, such as drug delivery systems.

4.6 References

1. UNEP, Understanding the spread of Sargassum in the Caribbean, <https://www.unep.org/cep/resources/factsheet/understanding-spread-sargassum-caribbean>, (accessed July 15, 2021).

2. Emerging Species Profile Sheets, Department of Fisheries and Aquaculture, <https://www.gov.nl.ca/ffa/files/research-development-fdp-pdf-marine-plants.pdf>, (accessed September 10, 2022).
3. J. Goldsmit, R. W. Schlegel, K. Filbee-Dexter, K. A. MacGregor, L. E. Johnson, C. J. Mundy, A. M. Savoie, C. W. McKindsey, K. L. Howland and P. Archambault, *Frontiers in Marine Science*, 2021, **18**, 742209–742227.
4. T. Chopin and R. Ugarte, The Seaweed Resources of Eastern Canada, <https://chopinlab.ext.unb.ca/articles/files/2006.SeaweedResourcesofCanada.pdf>, (accessed October 4, 2022).
5. A. Desrochers, S. Cox, H. A. Oxenford and B. Tussenbroek, *Sargassum Uses Guide: A resource for Caribbean researchers, entrepreneurs and policy makers* Centre for Resource Management and Environmental Studies (CERMES), University of the West Indies, Cave Hill Campus, Barbados, 2020.
6. A. Mohammed, A. Rivers, D. C. Stuckey and K. Ward, *Carbohydrate Polymers*, 2020, **245**, 116419–116427.
7. Caribbean, Alliance, for, Sustainable, Tourism and (CAST), Sargassum A Resource Guide for the Caribbean, <https://repository.oceanbestpractices.org/handle/11329/1288>, (accessed July 17, 2021).
8. T. M. Thompson, B. R. Young and S. Baroutian, *Renewable and Sustainable Energy Reviews*, 2020, **118**, 109564–109577.
9. C. Mohammed, S. Mahabir, K. Mohammed, N. John, K.-Y. Lee and K. Ward, *Industrial & Engineering Chemistry Research*, 2018, **58**, 1417–1425.
10. Y. Vijaya, S. R. Popuri, V. M. Boddu and A. Krishnaiah, *Carbohydrate Polymers*, 2008, **72**, 261–271.
11. A. Mohammed, R. Bissoon, E. Bajnath, K. Mohammed, T. Lee, M. Bissram, N. John, N. K. Jalsa, K. Y. Lee and K. Ward, *Carbohydrate Polymers*, 2018, **198**, 109–118.
12. R. S. Baghel, P. Suthar, T. K. Gajaria, S. Bhattacharya, A. Anil and C. R. K. Reddy, *Journal of Cleaner Production*, 2020, **263**, 121359–121367.
13. K. Truus, M. Vaher and I. Taure, *Proceedings of the Estonian Academy of Sciences, Chemistry*, 2001, **50**, 95–103.
14. M. Tavakolian, H. Wiebe, M. A. Sadeghi and T. G. M. van de Ven, *ACS Applied Materials & Interfaces*, 2020, **12**, 5040–5049.
15. V. Stiger-Pouvreau, N. Bourgougnon and E. Deslandes, in *Seaweed in Health and Disease Prevention*, Eds: J. Fleurence and I. Levine, Academic Press, 2016, , pp. 223–274.

16. F. Ferdouse, S. Løvstad Holdt, R. Smith, P. Murúa and L. Yang, *The global status of seaweed production, trade and utilization*, Food and Agriculture Organization of the United Nations, Rome, Italy, 2018.
17. J. Cai, A. Lovatelli, J. Aguilar-Manjarrez, L. Cornish, L. Dabbadie, A. Desrochers, S. Diffey, E. Garrido Gamarro, J. Geehan, A. Hurtado, D. Lucente, G. Mair, W. Miao, P. Potin, C. Przybyla, M. Reantaso, R. Roubach, M. Tauati and X. Yuan, *Seaweeds and microalgae: an overview for unlocking their potential in global aquaculture development*, FAO Fisheries and Aquaculture Circular No. 1229, Rome, 2021.
18. R. S. Baghel, C. R. K. Reddy and R. P. Singh, *Carbohydrate Polymers*, 2021, **267**, 118241–118253.
19. H. Doh, M. H. Lee and W. S. Whiteside, *Food Hydrocolloids*, 2020, **102**, 105542–105551.
20. G. Michel, T. Tonon, D. Scornet, J. M. Cock and B. Kloareg, *New Phytologist*, 2010, **188**, 82–97.
21. H. P. S. Abdul Khalil, T. K. Lai, Y. Y. Tye, S. Rizal, E. W. N. Chong, S. W. Yap, A. A. Hamzah, M. R. Nurul Fazita and M. T. Paridah, *Express Polymer Letters*, 2018, **12**, 296–317.
22. D. Saha and S. Bhattacharya, *Journal of Food Science and Technology*, 2010, **47**, 587–597.
23. M. Szekalska, A. Puciłowska, E. Szymańska, P. Ciosek and K. Winnicka, *International Journal of Polymer Science*, 2016, **2016**, 1–17.
24. K. Y. Lee and D. J. Mooney, *Progress in Polymer Science*, 2012, **37**, 106–126.
25. T. S. Parreidt, K. Müller and M. Schmid, *Foods*, 2018, **7**, 170–178.
26. S.-Y. Chee, P.-K. Wong and C.-L. Wong, *Journal of Applied Phycology*, 2010, **23**, 191–196.
27. A. Hambleton, F. Debeaufort, A. Bonnotte and A. Voilley, *Food Hydrocolloids*, 2009, **23**, 2116–2124.
28. M. Makaremi, H. Yousefi, G. Cavallaro, G. Lazzara, C. B. S. Goh, S. M. Lee, A. Solouk and P. Pasbakhsh, *Polymers (Basel)*, 2019, **11**, 1594–1612.
29. A. Fazilah, M. Maizura, A. Abd Karim, K. Bhupinder, B. Rajeev, U. Uthumporn, and S. H. Chew, *International Food Research Journal*, 2011, **18**, 1027–1033.
30. M. S. Nair, A. Saxena and C. Kaur, *Food Chemistry*, 2018, **240**, 245–252.
31. A. Mihranyan, *Journal of Applied Polymer Science*, 2011, **119**, 2449–2460.

32. N. Wahlström, U. Edlund, H. Pavia, G. Toth, A. Jaworski, A. J. Pell, F. X. Choong, H. Shirani, K. P. R. Nilsson and A. Richter-Dahlfors, *Cellulose*, 2020, **27**, 3707–3725.
33. H. Tibolla, F. M. Pelissari and F. C. Menegalli, *LWT - Food Science and Technology*, 2014, **59**, 1311–1318.
34. K. E. Edwards, M. Kim, T. H. Borchers and C. J. Barrett, *Materials Advances*, 2022, **3**, 6222–6230.
35. H. A. Foner and N. Adan, *Journal of the Forensic Science Society*, 1983, **23**, 313–321.
36. R. Mustapha, A. Zoughaib, N. Ghaddar and K. Ghali, *Energy*, 2020, **195**, 117057–117067.
37. *Standard Test Method for Tensile Properties of Thin Plastic Sheeting*, ASTM International D882-10, USA, 2010.
38. F. Lianes, F. Sauriol, F. G. Morin and A. S. Perlin, *Canadian Journal of Chemistry*, 1997, **75**, 585–590.
39. P. D. Blanc, *Fake Silk: The Lethal History of Viscose Rayon*, Yale University Press, 2016.
40. F. Abasalizadeh, S. V. Moghaddam, E. Alizadeh, E. Akbari, E. Kashani, S. M. B. Fazljou, M. Torbati and A. Akbarzadeh, *Journal of Biococial Engineering*, 2020, **14**, 8–30.
41. A. Aprianita, T. Vasiljevic, A. Bannikova and S. Kasapis, *Journal of Food Science and Technology*, 2014, **51**, 3669–3679.
42. R. Shogren, D. Wood, W. Orts and G. Glenn, *Sustainable Production and Consumption*, 2019, **19**, 194–215.
43. L. Bastarrachea, S. Dhawan and S. S. Sablani, *Food Engineering Reviews*, 2011, **3**, 79–93.
44. J. McDonald and S. K. Kawatra, *Mineral Processing and Extractive Metallurgy Review*, 2017, **38**, 250–253.
45. P. Lee and M. A. Rogers, *International Journal of Gastronomy and Food Science*, 2012, **1**, 96–100.

Bridging Text for Chapter 5: Photo-response of azo dye functionalized

cellulose acetate

It is an exciting goal of applied research for one to imagine a material capable of cleaning itself in response to an external stimulus. Such a material in theory would be capable of more efficient and longer use, and reuse many times over, saving on resources, time, and money. For instance, self-cleaning materials offer large-scale potential applications in ultra-filtration membranes for wastewater treatment where they could unclog pores, or as anti-fouling coatings for the hulls of ships. Movement of stimuli-responsive molecules on the microscale, for example *via* the *trans-cis* isomerization of attached geometrically isomerizing azo dyes, might translate to significant reversible surface changes on the macroscale. These changes may appear in the form of mechanical bending, change in surface roughness, or a change in the surface hydrophilicity or surface energy. The two latter changes can affect the wettability of the surface as well as the adsorption of fouling agents, with continuous toggling between these two different states (*trans* and *cis*) of the material potentially dislodging fouling agents.

In previous Chapters (2–4), the focus was on developing photo-reversible azo dye/cellulose-based materials *via* soft-bonding interactions, while in this Chapter, the focus will now be on making more robust self-cleaning materials by covalently modifying cellulose-based polymers with azo dyes, to prevent any potential leeching of the azo dyes into the environment. The chemical modification of cellulose, hydroxypropyl cellulose, hydroxypropylmethyl cellulose, and acetoxypropyl cellulose with azo dyes has already been reported in the literature, however, there have been only two studies to date (from our research group) on the isomerization of an azo dye grafted onto the cellulose polymer only, with no isomerization studies reported on the other

cellulose esters and ethers. This Chapter represents a first report on the fabrication of such photo-reversible azo/cellulose acetate materials and their isomerization behaviour.

Photo-response of azo dye functionalized cellulose acetate

K. E. K. Edwards, C. J. Barrett and T. G. M. van de Ven**

Department of Chemistry, McGill University, Montreal, QC, Canada

5.1 Abstract

Herein, for the first time we report on the fabrication of photo-reversible cellulose acetate materials by covalent modification with azo dyes, towards preparing self-cleaning materials. A series of cellulose acetate polymers with varying degree of acetylation was initially synthesized and thoroughly characterized. It was observed that with increasing acetyl content the water contact angle of the cellulose acetate films increased, as the materials became less hydrophilic. The various cellulose acetate polymers were then covalently modified with azo dyes *via* an esterification reaction and the kinetics of the *trans-cis* isomerization of the grafted azo dyes were assessed. It was observed that generally the *cis* lifetime of the azo dyes increased when covalently bound to the polymer. Thin films of these azo modified cellulose acetate (Azo-CA) polymers were prepared by solvent-casting and electrospinning, and it was observed that the grafting of the azo dyes onto the cellulose acetate polymers further decreased the hydrophilicity of the material, and increased the water vapour permeance (WVP). The films were subjected to cycles of UV/Vis irradiation and the results showed that while there was no significant change in the water contact angle in response to the UV/Vis irradiation, there was a more pronounced change in the WVP of some of the materials.

5.2 Introduction

The fabrication of materials whose surface wettability can be tuned using an external stimulus such as UV/Vis light is of interest for the preparation of smart, self-cleaning materials. Recently, materials prepared from polydopamine covalently modified with azo dyes showed potential application as self-cleaning materials.¹ The *trans-cis* isomerization of the azo dyes resulted in the cleaning of filtration membranes coated with the azo-polydopamine material, in response to UV/Vis irradiation.¹ It is then of great interest to explore whether a similar phenomena might be achieved with cellulose-based materials covalently modified with azo dyes. Cellulose can be used to prepare materials with controlled hydrophilic surfaces due to the abundance of hydroxyl groups along the polymer chain.² Cellulose is one of the most abundant natural resources on Earth and works as a sustainable feedstock due to its recyclability, degradability, low cost, and worldwide availability.² Over the last few decades applied research has mainly focused on the engineering of cellulose into functional materials for use in medicine, filtration and packaging, as well as the processing of nanocellulose to bulk materials.³⁻⁷ Cellulose's ability to be competitive in such a wide variety of applications comes from its fascinating structure and properties, as a biopolymer consisting of linear chains of D-glucose repeating units which are connected through a high degree of intermolecular hydrogen bonding, rendering the polymer strong and stable and insoluble in most organic solvents and water.⁸

Cellulose can also be easily functionalized to create a wide array of derivatives with different properties. Many of these cellulose derivatives retain the properties of native cellulose such as being biodegradable and biocompatible, while having additional beneficial properties such as antibacterial properties, flame retardancy, and water solubility.⁸ The wettability of cellulose can

be easily altered by chemical treatment, for *e.g.*, by functionalization with acetal groups to form cellulose acetate (CA).^{9, 10} The wettability of cellulose can also be altered by the addition of hydrophobic sizing agents such as alkenylsuccinic anhydride (ASA) and alkylketene dimer (AKD),^{11, 12} or by coating or chemical modification with fluorinated compounds.^{11, 13-15} Surface wettability is an important property when designing materials for applications such as filtration membranes, anti-fouling materials, self-cleaning materials, and protective textiles.¹⁶ Generally, the surface wettability of a material can be evaluated by measuring the static contact angle (θ) which can be determined from the surface free energy (SFE) of the corresponding solid and liquid.^{10, 16} Various wetting models exist to equate the SFE to θ , such as the Young model,^{17, 18} which is based on the assumption that a chemically homogenous surface is totally smooth, and the Wenzel and Cassie-Baxter models which introduce surface roughness and heterogeneity as two critical factors affecting surface wettability.^{10, 16}

Cellulose acetate (CA) is a very versatile derivative of cellulose, whose % acetyl content dictates the physical and mechanical properties of the polymer. The addition of 1 acetyl group to the anhydrose glucose unit (AGU) at the C6/C2/C3 positions results in a water-soluble form of CA known as cellulose monoacetate (CMA), generally with an acetyl content of 18 %.^{19, 20} Commercially available CA generally refers to the form of CA with 39–42 % acetyl content, known as cellulose diacetate (CDA).²¹ CDA has been used commercially since the 1800s in the textile industry, and since the 1900s to make photographic films, as contact lenses, and more recently to make superhydrophobic materials.^{22, 23} The other common form of CA is known as cellulose triacetate (CTA) where all the hydroxyl groups on cellulose are substituted with acetyl groups, generally with an acetyl content 60 %.^{24, 25} Throughout the literature, it was observed that the surface of films solvent cast from CA were less hydrophilic than native cellulose films, and it

was observed that the more acetal groups per glucose repeat unit of cellulose the less hydrophilic the surface of the materials.⁹ An analysis of the literature showed the following trend; as the degree of substitution (DS) of acetal groups increased from 38 % to 45 % acetyl content, there was a decrease in surface wettability and SFE, indicative by the increase in the advancing contact angle, $\theta = 64^\circ$ to 69° , respectively,⁹ compared to that of cellophane ($\theta = 34^\circ$).²⁶ Measurements of the wettability of lower (< 38 %) and higher (> 45 %) degrees of acetylation of cellulose have yet to be conducted.

The dyeing of CA using azo dyes via doping has been done since the 1950s, mainly for use in the textile industry to add colour to fabrics.^{27, 28} The main driving force for the interaction between the azo dyes and CA fibres was hydrophobic interactions and dipole-dipole interactions.^{27, 28} More recently, researchers have reported functionalizing cellulose and cellulose derivatives with azo dyes for a variety of applications. Azobenzene in addition to being a dye is a ubiquitous photo-switch which can isomerize from E-Z (*trans* to *cis*) geometrical isomer upon irradiation with UV light. Azobenzene derivatives are known to exhibit a characteristic absorption band in their UV-Vis absorption spectra which originates from the $\pi \rightarrow \pi^*$ transition of the azobenzene chromophore. Changing the substituents on the aromatic rings drastically changes the optical properties of the azobenzene, giving it the ability to ‘tune’ specific properties such as *cis* half-life or UV-Vis absorption. Light is a preferred stimulus since it can travel long distances, be highly localized in time and space, and is able to penetrate many (transparent) material barriers without any damaging chemical change. The ability to tune the physical and mechanical properties of a polymer using an external stimulus such as light is generally greatly advantageous from an applied standpoint, since these methods are less cost intensive and do not generate as much waste.

The functionalization of cellulose using azobenzene to prepare Azo-cellulose (Azo-Cel) can be dated back to the 1980s for potential application as a switchable stationary phase for high performance liquid chromatography and thin layer chromatography, as an absorbent in the photo-regulation of the retention factor of different analytes.^{29, 30} Generally, an esterification reaction between the hydroxyl groups of cellulose and acyl chloride azobenzene dyes in the presence of pyridine results in successful grafting of the azo dye onto the cellulose-based polymer.²⁹⁻³¹ Etherification of cellulose,³² HPC,³³ and glycosides,³⁴ and modification of lignin³⁵ with azo dyes has also been reported in the literature. It is hypothesized that the *trans/cis* photo-isomerization of the azo pendant group changed the efficiency of the resolution of the analyte in these previous studies. This was attributed to the more hydrophilic nature of the *cis* isomer in comparison to the *trans*, where the dipole moments are $\mu = 3.0$ D and 0 D, respectively.³⁶ Additionally, the *trans* isomer is believed to have a higher-ordered geometric structure due to its liquid-crystalline nature, than the less ordered structure of the *cis* isomer.³⁰

Recent reports on the functionalization of cellulose with azobenzene from Otsuka *et al.* from our research group focused for the first time on studying the kinetics of the azo photo-switch once grafted onto the polymer and applying these Azo-dye-functionalized cellulose (Azo-Cel) materials towards mechanical bending and photo-induced changes in surface wettability.^{31, 37} The researchers were further able to achieve robust hydrophobic materials by electrospinning the Azo-Cel into fabrics.^{31, 37} The surface energy of these materials could be controlled using UV/Vis light.³⁷ Additionally, the researchers reported that the *cis* lifetime of the azo unit was significantly longer when covalently bond to the cellulose polymer compared to the free unbound azo molecules in solution.³¹ Other researchers have also prepared a range of cellulose functionalized with azobenzene derivatives using an ionic liquid,³⁸ where the characteristics of the azo cellulose-based

material and its functionality could be driven by the structures developed at the nanoscale.³⁸ Other cellulose esters and ethers such as hydroxypropyl cellulose (HPC),³⁹ hydroxypropylmethyl cellulose (HPMC),⁴⁰ and acetoxypopyl cellulose (APC),^{38, 41} have also been functionalized with azobenzene dyes to prepare novel photo-responsive cellulosic materials. To our knowledge, CA has not been functionalized with azobenzene or other azo dyes, and there is thus great potential for such a modification to be introduced to CA. Past research on the modification of CA with other hydrophobic small molecules shows the great potential for this azo modification to be completed, to attempt to reversibly alter the wettability of cellulose. For example, it has been shown that the addition of hydrophobic pendant groups such as perfluoro alkoxy silanes onto CA polymer in addition to electrospinning the polymer could render the material superhydrophobic ($\theta > 150^\circ$).²²

In this work, CAs with varying % acetyl content were first prepared by acetylation of kraft pulp (cellulose) with acetic acid, followed by hydrolysis based on previously established protocols,^{19, 21, 25, 42} to obtain a range of cellulose acetate (CTA, CDA and CMA) as shown in **Figure 5.1**. The physical and thermal properties of the of CA polymers were then assessed. CDA and CMA were then functionalized with 4-(phenylazo) benzoyl chloride (Azo-COCl) and 4-(4-hydroxyphenylazo) benzoyl (Ho-Azo-COCl) to prepare photo-reversible materials, following previous literature protocols with some modifications (**Figure 5.1**). The grafting of the azo dyes onto the polymers was confirmed by various spectroscopic techniques. The kinetics of the *trans/cis* photo- and thermal isomerization were assessed, as well as photo-induced changes in surface wettability and WVP. These properties are important to assess if these photo-reversible materials are to be useful for self-cleaning applications.

5.3 Results and discussion

The versatility of cellulose as a polymer is such that its physical and chemical properties can be easily tuned by the simple addition of a small molecule such as an acetyl group or a photo-switchable azobenzene molecule. The preparation of various CA polymers and the subsequent functionalization of these polymers with azo dyes will be discussed in detail, and changes in the optical and surface properties of these Azo-CA materials are investigated *via* the reversible *trans-cis* isomerization behaviour of these azo molecules.

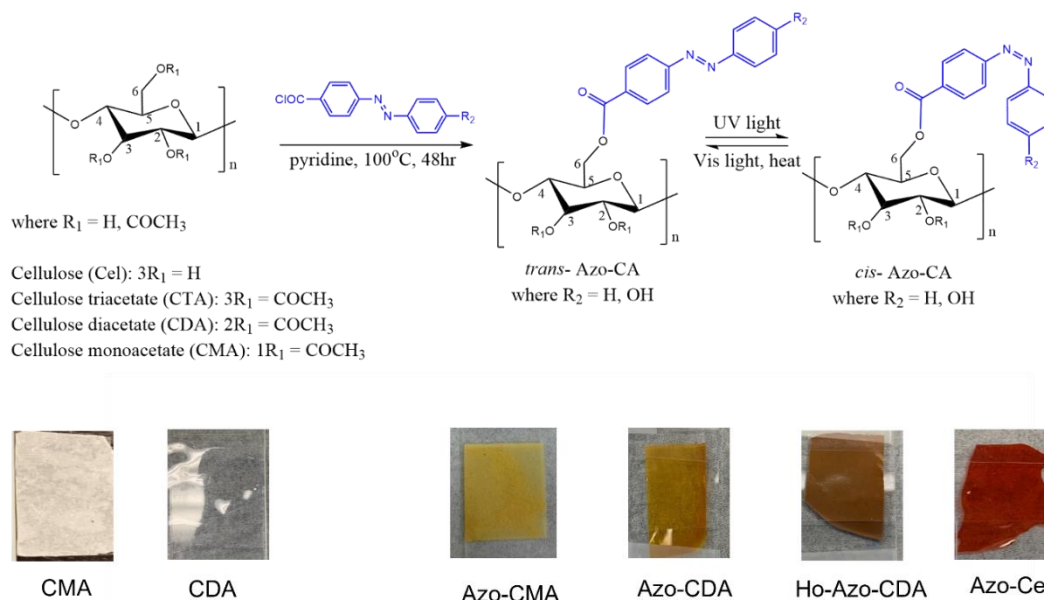


Figure 5.1 (Top) Schematic of the reaction of cellulose acetate (varying % acetyl content) with azo dyes, and the photo-induced *trans-cis* isomerization of Azo-CA polymers. (Bottom) Photographs of solvent cast films of cellulose monoacetate (CMA) and cellulose diacetate (CDA), and azo modified cellulose-based polymers: azobenzene CMA (Azo-CMA), azobenzene CDA (Azo-CDA), hydroxy-azobenzene CDA (Ho-Azo-CDA) and azobenzene cellulose (Azo-Cel).

5.3.1 Characterization of cellulose acetate (DS 1–3)

Cellulose acetates with varying DS starting from cellulose kraft pulp were successfully prepared by acetylation followed by hydrolysis (**Figure 5.1**). To achieve a more homogenous product, generally cellulose is fully acetylated to CTA followed by a hydrolysis to systematically remove the acetal groups to achieve lower degrees of substitution (*e.g.*, CDA and CMA).¹⁹ While the industrial production of CTA and CDA has been refined for many years,²³ the production and use of CMA has not garnered much attention due to the difficulty in achieving a fully water-soluble homogenous product.¹⁹ CTA (DS 2.5) and CMA (DS 0.8) were prepared using the method outlined above, while CDA (DS 2.3) was purchased from Sigma Aldrich,⁴³ and the resulting polymers characterized using H^1 NMR spectroscopy and FTIR spectroscopy, as shown in the **Supplementary Information Figures S5.1 and S5.4**. The synthesized CTA was soluble in DCM, a solvent selective for the triacetate form, while commercial CDA was soluble in acetone and the synthesized CMA was partially soluble in water, and all polymers were soluble in DMSO. The addition of acetyl groups to cellulose during the acetylation process was confirmed by the presence of acetyl protons (CH_3) between 1.8–2.2 ppm in the H^1 NMR spectra of CA, which were absent for the cellulose polymer (**Figure S5.1a**). The cellulose spectrum only had the characteristic pyranose protons between 3.5–5.5 ppm. During the hydrolysis process to convert CTA to CMA, the peaks between 1.8–2.2 ppm changed; the peak corresponding to the proton attached to C3 at 1.8 ppm was diminished, while the peaks associated with C2 (1.95 ppm) and C6 (2.1 ppm) were still intense (**Figure S5.1a**). These results correspond well to those from a previous study by Olaru (2001).⁴²

These changes in the NMR spectra were consistent with the changes observed in the IR spectra (**Figure S5.4**). The characteristic peaks of a cellulose polymer are as follows: 3315 cm^{-1}

(O–H stretch, alcohol), 1225 cm⁻¹ (C–O stretch, ester), and 1022 cm⁻¹ (C–O stretch, ether). Upon acetylation, there were new peaks observed at 1730 cm⁻¹ (C=O stretch, ester), 1365 cm⁻¹ (C–H stretch), and 1225 cm⁻¹ (C–O stretch, ester) which signify conversion of the cellulose polymer to CTA (**Figure S5.4**). During the hydrolysis process the intensity of these peaks diminished as the polymer was converted to a lesser substituted form, *i.e.*, CMA. The IR spectrum of commercial CDA is also shown for comparison, with also has the characteristic peaks of CA observed for our synthesized samples (**Figure S5.4**). Thin films of CA polymers were prepared by solvent casting from DCM for CTA, THF for CDA and DMSO for CMA (**Figure 5.10**). It was observed for CTA, the films formed were very brittle and broke apart if over-manipulated. For CDA, the films produced were more optically clear, flexible, and stable compared to CTA. For CMA, the films formed resembled filter paper (cellulose), were white, flexible, and more stable than CTA films.

5.3.2 Characterization of Azo-CA polymers

5.3.2.1 UV-Vis spectroscopy

The grafting of the azo dyes onto the CA polymers was confirmed by UV-Vis spectroscopy. Previous reports have shown that azobenzene-type dyes, such as Azo-COCl, have a maximum absorption in the UV region (300–350 nm) which originates from the $\pi \rightarrow \pi^*$ transition, with a smaller absorption in the visible region (400–500 nm) which originates from the $n \rightarrow \pi^*$ transition.³¹ This allows monitoring of the grafting of the azo dyes onto the cellulose-based polymers by UV-Vis spectroscopy. These azobenzene-type dyes also have a characteristic orange colour owing to the wavelength of light that is absorbed. In a previous study by Otsuka *et al.* (2019), it was shown that the unbound azo dye azobenzene acyl chloride (Azo-COCl) has a maximum absorption at 332 nm in THF,³¹ while in this study it was observed that the unbound azo

dye hydroxy-azobenzene acyl chloride (Ho-Azo-COCl) was more red-shifted to 375 nm. For the CA samples in this study modified with the Azo-COCl dye, λ_{max} for the azo dye was observed at 325 nm and 329 nm, *i.e.*, blue-shifted by 7 nm and 3 nm for Azo-CDA and Azo-CMA, respectively. This was similar to the shift previously observed for Azo-Cel sample prepared by Otsuka and colleagues (2019).³¹ For the CA polymers modified with hydroxy azobenzene (Ho-Azo-COCl), λ_{max} for the azo dye was blue-shifted by a higher magnitude, *i.e.*, 19 nm and 31 nm for Ho-Azo-CDA ($\lambda_{max} = 356$ nm) and Ho-Azo-CMA ($\lambda_{max} = 344$ nm), respectively. These shifts in the maximum absorbance bands of the azo dyes when bound to the polymer compared to when unbound in solution are indicative of successful covalent attachment. Generally, when an azo dye is grafted onto a polymer the maximum absorption band is shifted due to changes in the electronics of the dye by either the addition or withdrawal of electron density to/from the azo ($-N=N-$) bond by the polymer.^{31,44} Additionally, the concentration (c) of the azo dyes grafted onto the polymer was measured using the maximum absorbance in the UV-Vis spectra, according to the Beer-Lambert law, $A = \epsilon c l$, where A is the absorbance, ϵ is the extinction coefficient and l is the pathlength (1 cm). Using this equation, it was determined that the weight % of azo dye in the Azo-CDA sample was 9 % (w/w) and for Ho-Azo-CDA was 2 % (w/w), measured for 1 sample each. The other samples had limited solubility in THF and therefore this method could not be used to accurately determine the concentration of azo dyes.

5.3.2.2 NMR spectroscopy

The grafting of the azo dyes onto the CA polymers was confirmed by NMR spectroscopy and matched well with the spectra observed for Azo-Cel by a previous study conducted by Otsuka *et al.* (2019).³¹ **Figure 5.2a** shows the carbon NMR spectra of CDA compared to Azo-CDA in DMSO- d_6 solvent, showing the evolution of peaks between 110–168 ppm, corresponding to the

aromatic carbons of the azo dye. These peaks were just as pronounced as the peaks corresponding to the polymer: C=O (170 ppm), C1 (102 ppm), C2–C5 (75–91 ppm), C6 (64 ppm) and CH₃ (21 ppm).

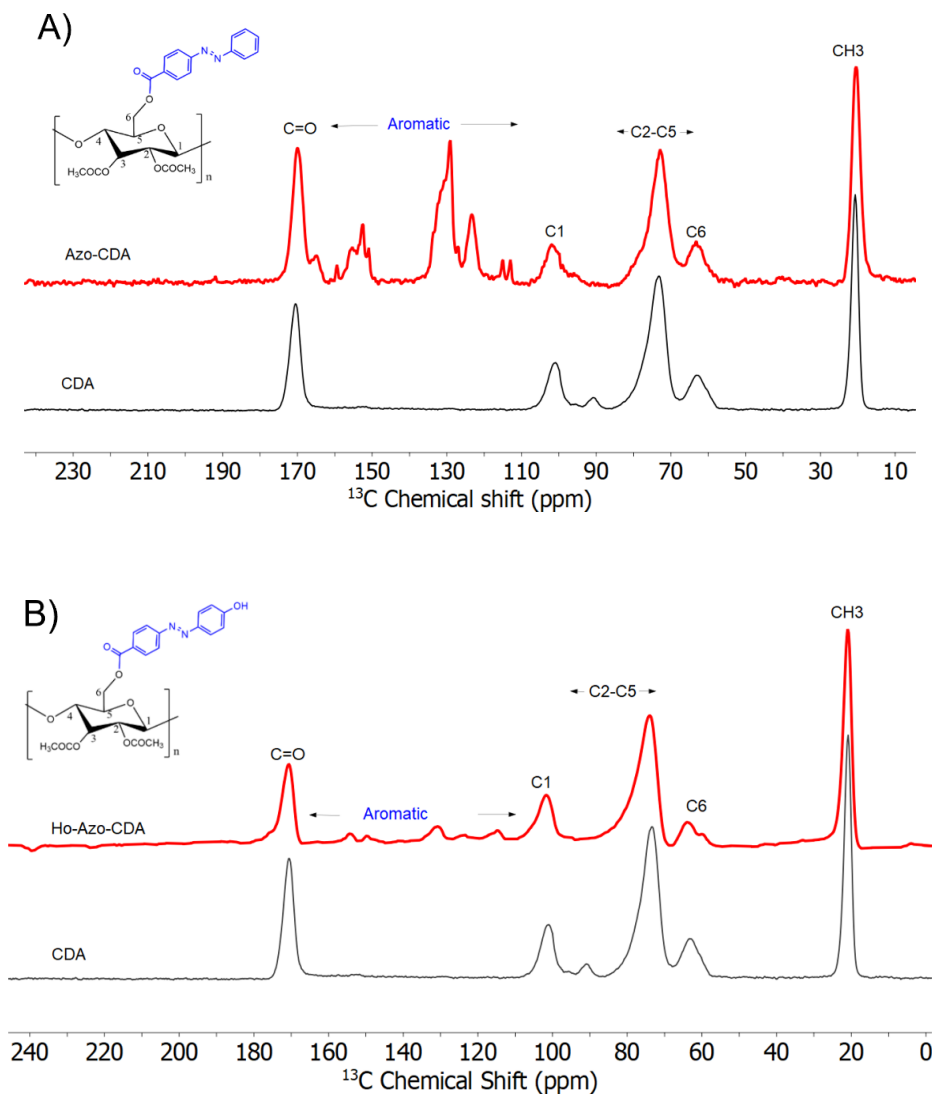


Figure 5.2 (A) ¹³C NMR of Azo-CDA in DMSO-d₆ solvent (red) and CDA in solid-state (black). (B) ¹³C NMR of Ho-Azo-CDA (red) and CDA (black) in solid-state.

The presence of peaks corresponding to the azo dye between 110–165 ppm was also observed for another azo grafted sample, Ho-Azo-CDA sample using solid-state NMR (**Figure 5.2b**). Solid-

State NMR was used since solubility of this polymer in DMSO was limited. The weaker intensity of the azo peaks in this spectrum might be due to lower grafting of the dye (2 % vs. 9 %) as described in the previous section.

5.3.2.3 FTIR spectroscopy

Another frequently used method to verify the grafting of azo dyes onto cellulose-based polymers is FTIR spectroscopy, owing to the distinctive aromatic (C=C) stretch that can be observed between 1400–1550 cm^{-1} (**Figure S5.3**). Additionally for methods involving the grafting of azo dyes onto cellulose *via* an esterification reaction, the appearance of an intense band at 1724 cm^{-1} and 1259 cm^{-1} corresponding to the ester's C=O and C–O stretching modes, respectively, is indicative of successful azo grafting.³¹ However, for the CA samples which already have ester groups this stretch will not provide much information on the success of the azo grafting. **Figure 5.3** shows the FTIR spectra of the unmodified CDA polymer and Azo-CDA polymer. For the Azo-CDA spectrum, the appearance of a peak at 1603 cm^{-1} corresponding to the aromatic carbon atoms of the azo dye (**Figure S5.3**) and the depression of the alcohol O–H stretching mode of the polymer observed for the CDA spectrum indicates successful attachment of the azo dye to CDA polymer (**Figure 5.3**). There were also two peaks observed between 600–800 cm^{-1} (**Figure 5.3**) which match the peaks observed in the fingerprint region of the Azo-COCl dye FTIR spectrum (**Figure S5.3**). For the other azo modified CA polymers, no observable changes were observed in the IR spectra.

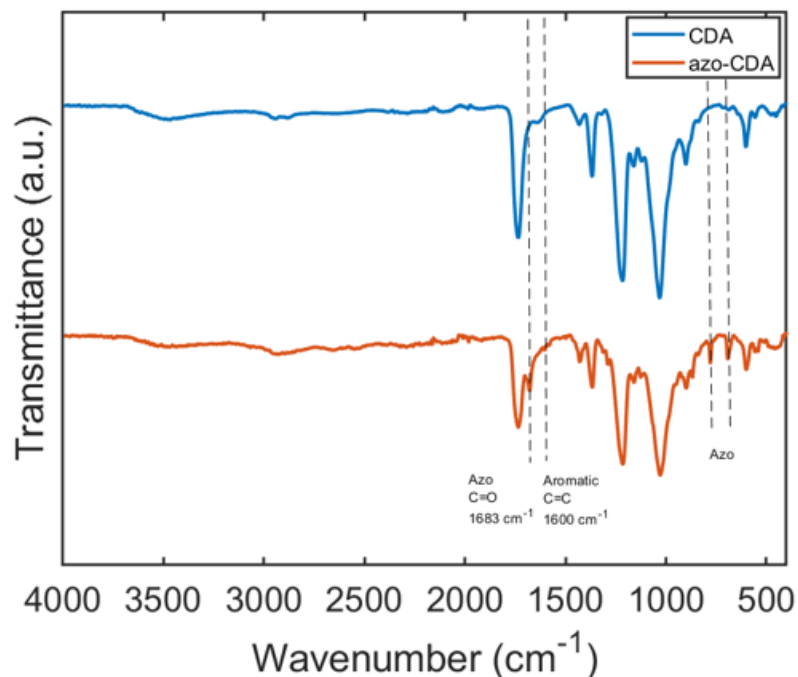


Figure 5.3 IR spectra of CDA (blue) vs. Azo-CDA (orange).

5.3.2.4 Surface imaging and azo content

Scanning electron microscopy (SEM) was used to visualize the surface of solvent cast or electrospun thin films of the various cellulose-based polymers (**Figure 5.4**). Energy dispersive spectroscopy (EDS) was used to provide an estimation of the % azo dye content grafted onto the polymer (N %, averaged over 3–6 different spots along the surface the same film). **Figure 5.4a** shows the surface of a thin film of CDA solvent cast from THF having a uniform surface with few imperfections. The thickness of the film was approximately 50 μm with negligible nitrogen measured in the sample (< 2 %). **Figure 5.4b** shows the surface of the Azo-CDA film which looks more uniform than the CDA film when solvent cast under the same conditions.

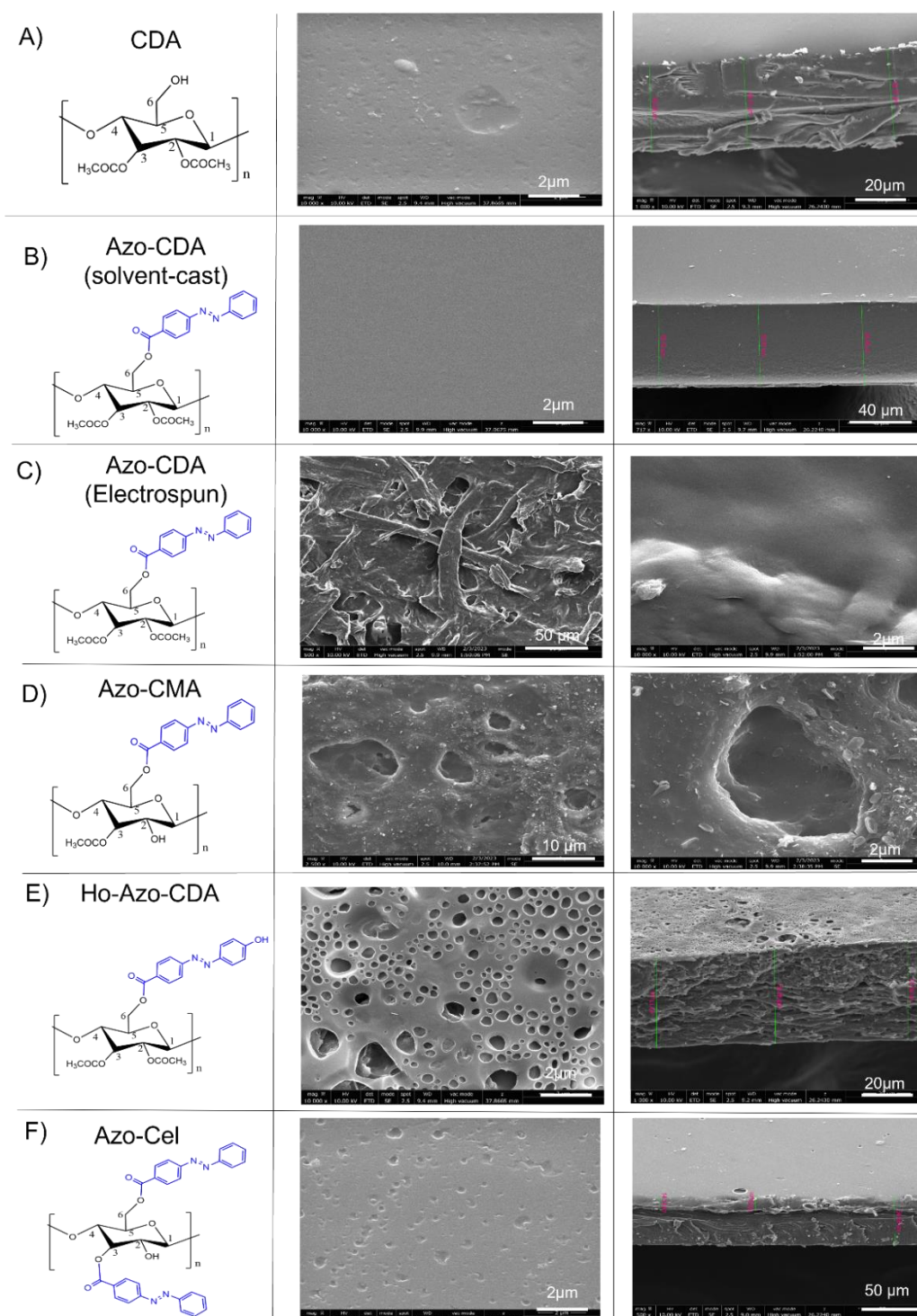


Figure 5.4 SEM images of planar and/or cross-sectional views of (A) CDA, (B) Azo-CDA (solvent-cast), (C) Azo-CDA (electrospun), (D) Azo-CMA (E) Ho-Azo-CDA, and (F) Azo-Cel.

The thickness of this film was approximately 70 μm , with an average nitrogen content of $9 \pm 3 \%$, indicating successful grafting of the azo dye, which contains the azo ($-\text{N}=\text{N}-$) bond, onto the CDA polymer. This value matched well with the value calculated using UV-Vis spectroscopy (9 %) in **Section 5.3.2.1**.

Figure 5.4c shows the surface of the electrospun Azo-CDA (15 wt.%) from the cosolvent acetone/DMF/water at two length scales. Compared to both solvent cast CDA and Azo-CDA films, the surface of the electrospun Azo-CDA film was observed to be more uneven and fibrous, with small air pockets observed along the surface. This unevenness in the surface of the electrospun film was expected since this technique generally is used to prepare a fibrous mesh network.^{31, 45, 46} However, it should be noted that well defined nanofibers were not observed for our electrospun film compared to previously reported results using the similar electrospinning conditions, which indicates that further optimization is needed to generate a well defined meshed network which results in a hydrophobic surface. From EDS mapping, the average nitrogen content was measured to be $11 \pm 2 \%$ which matches well to the solvent-cast Azo-CDA films, and the value calculated using UV-Vis spectroscopy (9 %) in **Section 5.3.2.1**. **Figure 5.4d** shows the surface of the solvent-cast Azo-CMA film from DMSO. Compared to Azo-CDA, the surface this film was observed to be very uneven with large micron-sized cavities. There also appeared to be small nano-sized particles dispersed all throughout the surface. EDS mapping showed that there was $> 3 \%$ sodium and chloride ions present along the surface, in addition to the expected C, O and N atoms. These small particulates could be aggregates of Azo-CMA containing salt and help contribute to the uneven surface observed. The average nitrogen content was measured to be $11 \pm 2 \%$ by EDS.

Figure 5.4e shows the surface of the Ho-Azo-CDA film solvent cast from THF, which had many small cavities on the surface which permeated throughout the layered cross section of the

film, with thickness approximately 50 μm . This side of the film was in contact with air during the drying process of the film. The other side of the film which was in contact with the glass dish also had holes and a flaky appearance. The very different morphology of this film compared to the Azo-CDA film could be due to a solubility effect, the different concentrations of the solutions used or hydrogen bonding of the hydroxyl groups on the azo dye, resulting in a patchy film formed during the evaporation process of the THF solvent. The EDS profile of Ho-Azo-CDA showed an average nitrogen content of $7 \pm 3 \%$, which was higher than the value measured by UV-Vis spectroscopy ($\sim 2 \%$). Lastly, **Figure 5.4f** shows the surface of a thin film solvent cast from the Azo-Cel sample in THF, which looked the most similar to the CDA sample, *i.e.*, overall uniform with periodic indentations on the surface. This is very different to the surface of the electrospun Azo-Cel (fibrous mesh) previously reported by the authors Otsuka and Barrett.^{31, 37} The thickness of this film was approximately 60 μm and the average nitrogen content was $6.8 \pm 0.4 \%$.

5.3.2.5 X-ray diffraction patterns

The changes in the crystallinity of cellulose following acetylation, and CAs when functionalized with the azo dyes, were assessed using powder X-ray diffraction (PXRD). Cellulose is known to have a very crystalline structure ($\text{CI} = \sim 80 \%$),^{25, 47, 48} with the ratio of the intensity of the peaks at $\sim 23^\circ$ and $\sim 17.5^\circ$ providing an estimation of the crystallinity of the polymer according to **Equation 9** in the **Supplementary Information**.⁴⁹ On the other hand it has been shown that cellulose triacetate has a much lower crystallinity ($\text{CI} = \sim 30 \%$) compared to cellulose, due to destruction in the crystalline regions of the native cellulose polymer by the acid used during esterification.²⁵ **Figure 5.5** shows the XRD pattern of cellulose kraft pulp with characteristic peaks of cellulose I: 23° (200 plane), 17.5° (110 plane) and, 14.5° ($1\bar{1}0$ plane).²⁵ The crystallinity of the cellulose kraft pulp was calculated to be $\text{CI} = 55 \%$. The characteristic peaks of cellulose I were

also present for the CMA and CTA samples, with CI = 69 % and 22 %, respectively. On the other hand, the XRD pattern of the commercial CDA from Sigma Aldrich matched better the XRD pattern of regenerated cellulose II: 21 ° (020 plane), 20 ° (110 plane) and, 12 ° (1 $\bar{1}$ 0 plane).⁵⁰ In contrast with the sharper diffraction peaks observed for the cellulose, CMA and CTA samples, CDA had very broad peaks indicating a significant decrease in crystallinity. The Azo-CDA and Ho-Azo-CDA films had similar XRD patterns to CDA, resembling that of cellulose II with broad peaks indicating low crystallinity. Lastly, the XRD pattern of the Azo-CMA film was similar to that of CMA, with CI = 54 %, indicating a crystalline film.

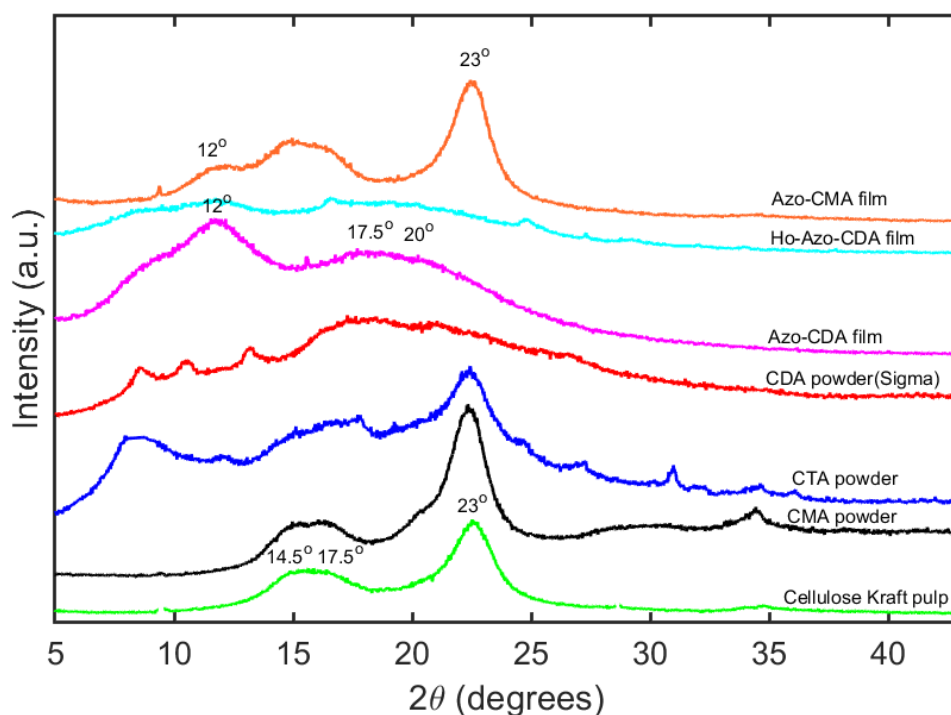


Figure 5.5 X-ray diffraction patterns of Cellulose (green), CMA powder (black), CTA powder (blue), CDA powder from Sigma Aldrich (red), Azo-CDA film (magenta), Ho-Azo-CDA film (cyan), and Azo-CMA film (orange).

5.3.2.6 Thermal stability

The thermal stabilities of the azo dyes, CA polymers, and Azo-CA polymers were determined using Thermogravimetric analysis (TGA) as shown in **Figure 5.6**. This is an important property to assess to determine the processing temperatures of a polymer. It has already been shown in the literature that the onset of the thermal decomposition temperature (T_d) of cellulose is ~ 300 °C.³¹ **Figure 5.6** shows that following acetylation of cellulose to CTA, the T_d decreased to 237 °C, while the T_d of CMA was observed to be similar to cellulose at 297 °C. This is in comparison to commercial CDA whose T_d of 349 °C was higher than that of cellulose. The much lower than expected T_d for the CTA prepared in this study could be due to degradation of the polymer chains from residual acetic acid.

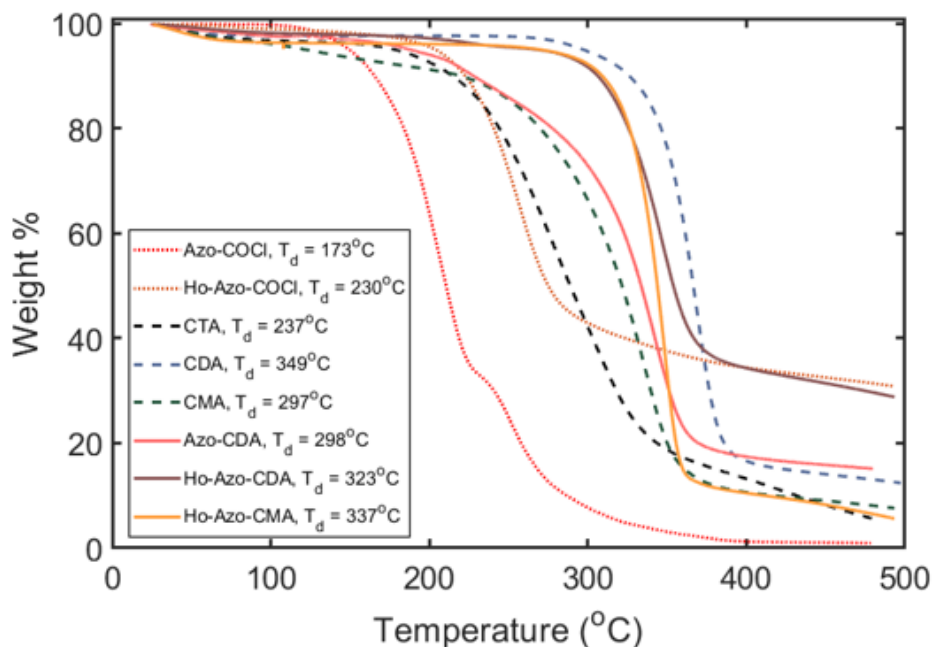


Figure 5.6 TGA traces showing the thermal decomposition temperature (T_d) of starting materials: azo dyes and CA, and azo functionalized CA (Azo-CA) samples.

As it relates to the azo dyes, the T_d of commercial Azo-COCl and the synthesized Ho-Azo-COCl were 173 °C and 230 °C, respectively (**Figure 5.6**). Compared to the commercial Azo-COCl, for Ho-Azo-COCl after 500 °C the weight % did not reduce to 0 % as expected, but was closer to 30 % at minimum. This may be due to impurities in the synthesized dye compared to the commercial dye. Functionalization of CDA with Azo-COCl to form Azo-CDA decreased the polymer's T_d from 349 °C to 298 °C, while functionalization with Ho-Azo-COCl to form Ho-Azo-CDA slightly decreased the polymer's T_d from 349 °C to 323 °C. Similar to Ho-Azo-COCl, for Ho-Azo-CDA about 30 % of the sample was still present at 500 °C (**Figure 5.6**). An increase in the T_d of the CMA polymer was observed when functionalized with Ho-Azo-COCl, where the T_d increased from 297 °C to 337 °C (**Figure 5.6**). These results indicate the possibility of the azo dye to either increase or decrease the thermal stability of the CA polymers.

5.3.3 Isomerization and kinetics of azo dyes and Azo-CA polymers

Azo dyes are a very interesting class of chromophores because in addition to their vibrant colours and intense absorption bands in the UV-Vis region, these dyes can undergo a reversible *trans*↔*cis* isomerization in response to the absorption of a photon of light, making them excellent photo-switches. As discussed in the introduction, the functionalization of an azobenzene dye with various electron donating- and electron-withdrawing groups, and attachment to polymers can drastically change the position of its absorption bands along the UV-Vis spectrum. Modification of azo dyes can also significantly affect the rate at which the *cis* isomer of the azo dye relaxes back to the more stable *trans* isomer while in the dark. The difference in the *cis* lifetime of different azo dyes can range from a few seconds to hours and knowing this decay rate can be useful when fabricating stimuli-responsive materials, for example when fabricating actuators, sensors, and self-cleaning devices. **Figure 5.7a** shows the time dependent UV-Vis spectrum of the hydroxy-azobenzene acyl

chloride dye (Ho-Azo-COCl) that was synthesized and subsequently covalently attached to the CDA polymer.

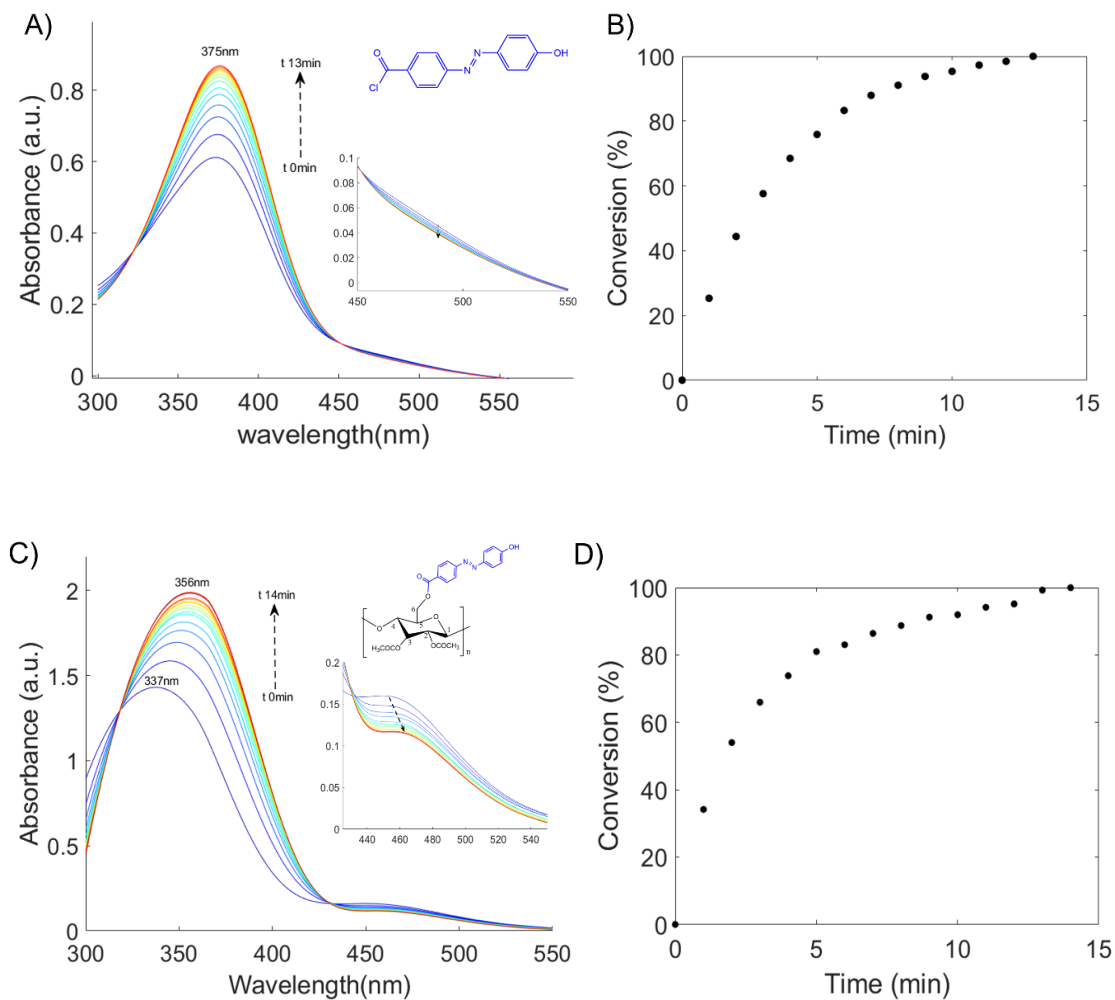


Figure 5.7 UV-Vis spectra and thermal back relaxation of (A) Ho-Azo-COCl and (C) Ho-Azo-CDA in THF. Absorbance measurements were taken at 1 min intervals in the dark. (B) and (D) show the conversion of the *cis* isomer of Ho-Azo-COCl and Ho-Azo-CDA back to its original *trans* state in the dark.

The dye has a maximum absorption band in the UV region (375 nm, represented by the orange line) with a much less pronounced band in the visible region (~ 490 nm) (**Figure 5.7a**).

During irradiation of the Ho-Azo-COCl azo dye with low intensity UV light (385–390 nm), the peak at 375 nm decreased significantly, while the peak at 490 nm increased slightly (**Figure 5.7a**). This was indicative of the *trans*-to-*cis* isomerization of the azo dye. To measure the kinetics of the *cis* decay, once the UV light was switched off the absorbance was measured at 1 min intervals until the absorbance returned to its original value. It was observed that within 13 min, 100% conversion back to the initial absorbance value at 375 nm was achieved when the dye was kept in the dark (**Figure 5.7b**). **Figure 5.7c** shows the time dependent UV-Vis spectrum of the Ho-Azo-COCl azo dye once grafted onto the CDA polymer. Unlike the free azo dye in solution, the maximum absorbance band was observed to be at 356 nm (19 nm blue shifted). During exposure to the UV light, the absorbance also decreased as observed before, but this time the maximum absorbance band shifted to 337 nm (19 nm blue shift) as seen in **Figure 5.7c**. Similarly, once the UV light was switched off and the sample kept in the dark, the absorbance increased back to its original value, and the maximum absorbance was shifted back to the initial wavelength of 356 nm (**Figure 5.7c**). Full conversion of the *cis* isomer back to the *trans* isomer was achieved in a similar time frame as for the unbound dye, after 14 min (**Figure 5.7d**).

Figure 5.8a shows the decay of the *cis* isomer of the Ho-Azo-COCl dye, which had an excellent fit to the monoexponential function (SI **Equation 3**), with the variable A (which corresponds to rate constant, k) having a value of 0.26 min^{-1} (or $4.3 \times 10^{-3} \text{ s}^{-1}$). On the other hand, **Figure 5.8b** shows the *cis* decay of the Ho-Azo-CDA polymer, which had an excellent fit to the biexponential function (SI **Equation 4**), with variables A and B (which correspond to two rate constants, k_a and k_b) having values of 0.28 min^{-1} and 0.41 min^{-1} , respectively.

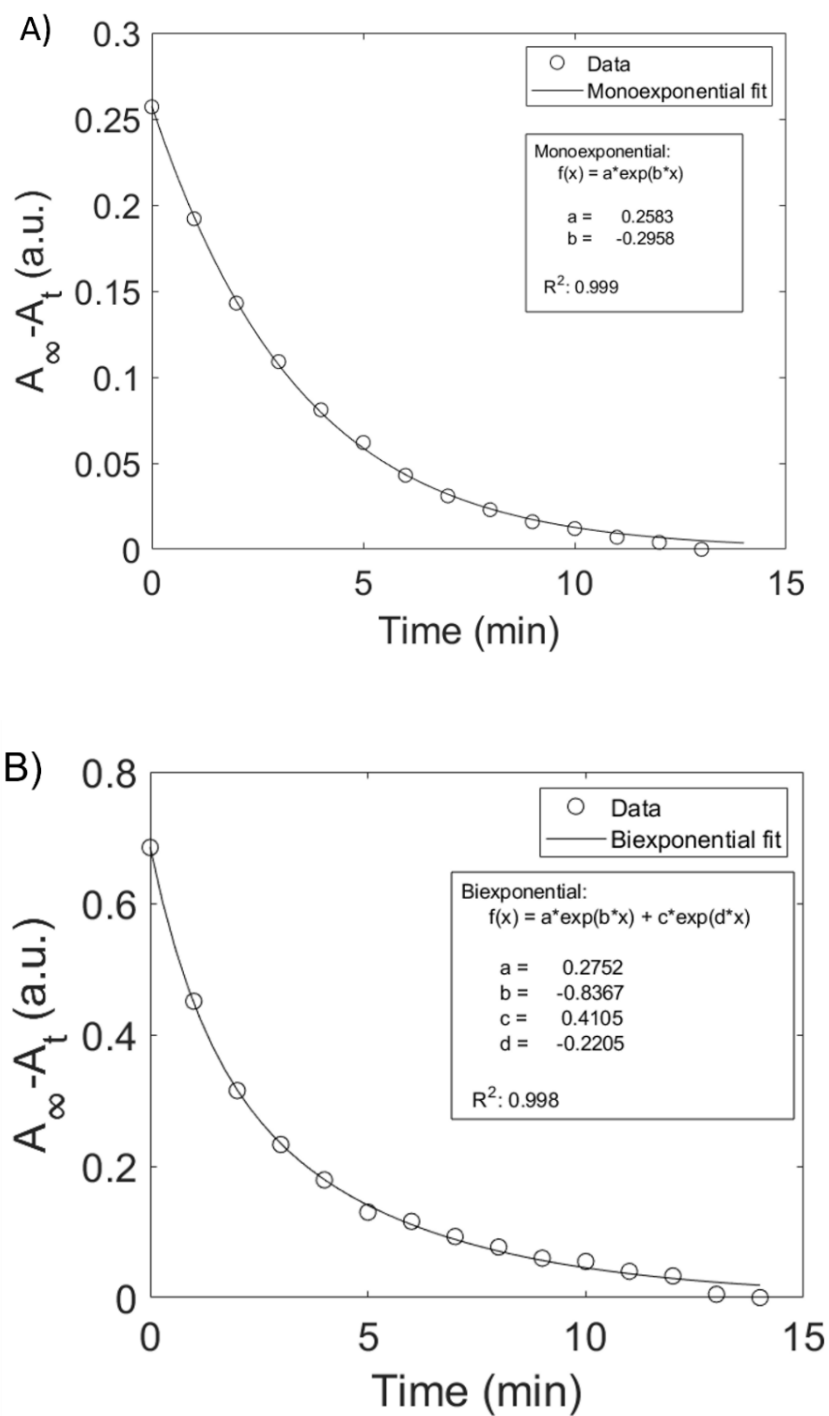


Figure 5.8 Decay of the *cis* isomers of (A) Ho-Azo-COCl azo dye fit with a monoexponential function and (B) Ho-Azo-CDA polymer fit with a biexponential function.

This indicated that there were two different isomerization processes occurring once the azo dye was bound to the CDA polymer. This dual rate behaviour has been observed in the literature for other polymer bound azo dyes such as Disperse Red 1, and generally the anomalous slower rate constant can be disregarded.^{51, 52} Therefore, the rate constant of this Ho-Azo-CDA polymer was 0.41 min^{-1} (or $6.8 \times 10^{-3} \text{ s}^{-1}$), slightly higher than the value of the unbound azo dye.

Table 5.1 shows a compilation of the maximum absorbance bands of the azo dyes and Azo-CA samples, as well as the rate constants, k , and their corresponding *cis* lifetime, τ . Also shown are the previously reported results for Azo-COCl and Azo-Cel, marked with (*).³¹ The *cis* lifetime of Azo-COCl was previously reported as $\tau = 83 \text{ min}$, while the *cis* lifetime of Azo-Cel was $\tau = 28 \text{ hr}$, showing that grafting of the azo dye to the polymer significantly slows down the *cis* decay.³¹ In this study, the synthesized Ho-azo-COCl dye had a *cis* lifetime of $\tau = 4 \text{ min}$ (**Table 5.1**), much shorter than the Azo-COCl dye. For the Azo-CDA polymer prepared in this study, the time dependent UV-Vis spectrum showing the isomerization is shown in **Figure S5.5a**. **Table 5.1** shows that the *cis* lifetime of Azo-CDA was $\tau = 9 \text{ hr}$, much longer than the unbound azo dye, but much shorter than the previously reported Azo-Cel.

Table 5.1 also shows the *cis* lifetime of Ho-Azo-CDA ($\tau = 2 \text{ min}$) which was slightly slower than the unbound azo dye ($\tau = 4 \text{ min}$). Researchers have reported both diminished and increased *cis* lifetimes once an azo dye is bound to a polymer.^{51, 52} In comparison to Ho-Azo-CDA, Ho-Azo-CMA had a longer *cis* lifetime of $\tau = 24 \text{ min}$ (**Table 5.1**). The full time-dependent UV-Vis spectrum of Ho-Azo-CMA is shown in **Figure S5.6a**. The switching of Azo-CMA in THF could not be observed, likely due to the poor solubility. In generally, it was observed that the *cis* lifetime of the unbound azo dye was much shorter than that of the dye once bound to the polymer.

Sample	k ($\times 10^{-3} \text{ s}^{-1}$)	τ
Azo-COCl*	0.20	83 min
Azo-Cel*	0.01	28 hr
Azo-CDA	0.03	9 hr
Azo-CMA	-	-
Ho-Azo-COCl	4.3	4 min
Ho-Azo-CDA	6.8	2 min
Ho-Azo-CMA	0.7	24 min

Table 5.1 Kinetics of the thermal back relaxation of the *cis* isomer of the azo dyes and Azo-cellulose-based polymers in THF following irradiation with UV light. (* from Ref: Otsuka and Barrett, 2019).³¹ No error analysis, measurements for 1 sample each.

5.3.4 Water contact angle measurements

For self-cleaning materials surface wettability is a very important parameter to assess. For hydrophilic surfaces, *e.g.*, on a surface of cellophane, a drop of water will spread out across the surface resulting in a water contact angle (WCA) typically $< 90^\circ$.¹⁰ On the other hand, hydrophobic and superhydrophobic surfaces, *i.e.*, surfaces with a WCA $> 90^\circ$ and $> 150^\circ$, respectively, will bead up and repel a water droplet from their surfaces, and will attract more hydrophobic compounds.^{11, 12} The WCA of a material, denoted by θ , is indirectly proportional to its SFE by the relationship $\cos \theta$ according to Young's model. Additionally, the SFE is affected by the roughness of the surface, where rougher surfaces result in higher contact angles and therefore lower surface energies.^{10, 16}

To fabricate a self-cleaning material, the SFE of the material needs to be reversibly altered in a significant way using an external stimuli.^{1, 37} The incorporation of a photo-switchable molecule

such as an azo dye onto the surface of a material is one way in which a photo-responsive self-cleaning material can be made.¹ As shown in the previous sections, CA can be easily functionalized with various azo dyes which are still able to undergo *trans* ↔ *cis* isomerization even when grafted onto the polymer. Previous reports on the azobenzene dye have shown that the *cis* isomer is significantly more hydrophilic than the *trans* isomer, since the *cis* isomer has a dipole moment of 3.0 D compared to the 0 D of the *trans* isomer.³⁶ It has already been shown by one of the authors that an electrospun Azo-Cel fabric's SFE can be controlled (toggled between more and less hydrophobic states) in response to UV/Vis light.³⁷ **Figure 5.9a** shows the schematic of how such a method could be applied to the polymer cellulose acetate (CA).

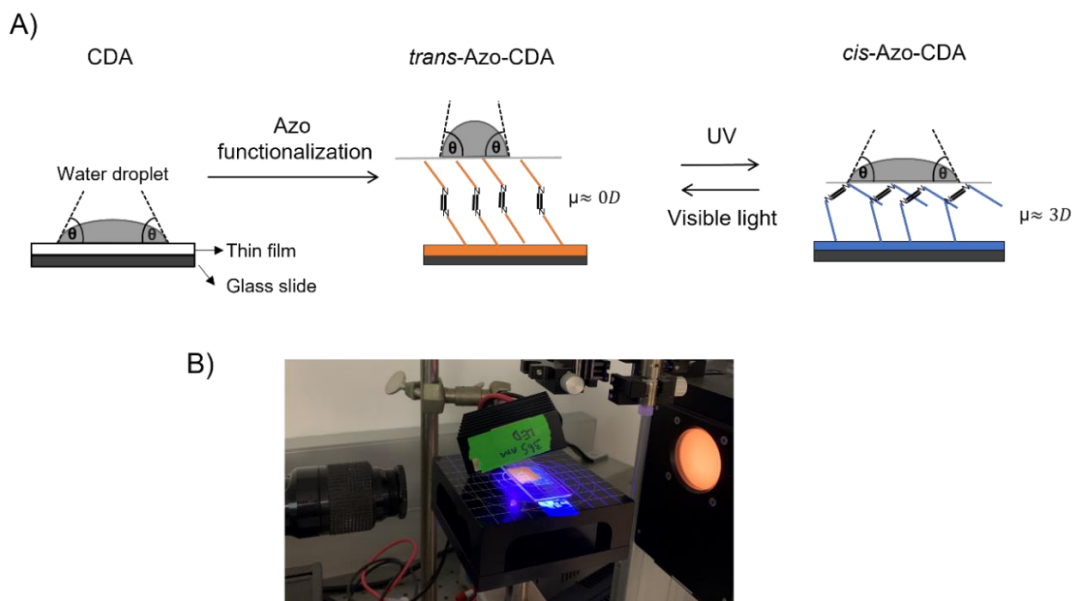


Figure 5.9 (A) Schematic showing the change in surface wettability of azo functionalized CDA films in response to light. (B) Photograph of the optical set up used to initiate a photo-response in thin film and contact angle set up used to measure water contact angle (WCA).

It was presumed that upon functionalization of the CA material with an azobenzene-type dye, the WCA should increase and the SFE should decrease, and after irradiation with UV light, conversion from the *trans* to *cis* state should decrease the WCA and increase SFE making the hydrophobic material now hydrophilic. Cycling between UV and Vis irradiation should result in cycling between hydrophobic and hydrophilic states of the material, dislodging any compounds which are adhered to the surface. **Figure 5.9b** shows the experimental set-up of the goniometer with a sample on top of the stage while being irradiated with a UV LED or laser.

The WCA of the various cellulose and CA films were first measured as shown in **Figure 5.10**. The cellulose-based material with the lowest WCA and which was the most hydrophilic was cellophane, with a WCA of $33 \pm 4^\circ$. Acetylation of the cellulose material resulted in an increase in the WCA and a decrease in the surface's hydrophilicity in the order of increasing WCA: CMA ($50 \pm 4^\circ$) < CDA ($59 \pm 2^\circ$) = CTA ($60 \pm 6^\circ$). This is expected since acetyl groups which are hydrophobic are replacing the hydrophilic hydroxyl groups of the cellulose polymer. While the results match well with other studies on CA materials,^{9, 53} the WCA of CTA was lower than expected (hydrophobic, 90°) since the CTA prepared in this study was not fully acetylated (DS 2.5 vs. 3). The remaining hydroxyl groups present on the structure likely resulted in the lowered WCA. **Figure 5.10** also shows that the azo modification of the various CA polymers further increased the WCA. This could be due to a decrease in the availability of hydrophilic groups on the surface, the more hydrophobic nature of the *trans*-azo dyes compared to the hydroxyl groups of the polymer, an increase in the surface roughness of the films, or a change in film porosity.

Figure 5.10 shows that the Azo-CMA film had a much higher WCA ($77 \pm 4^\circ$) compared to CMA, a 27-degree difference. Similarly Azo-CDA had a higher WCA ($70 \pm 3^\circ$) compared to CDA, a 11-degree difference. Despite having the same azo functional group, Azo-CMA had a

higher a WCA compared to Azo-CDA. The difference was possibly due to the large pores and uneven surface observed for Azo-CMA (**Figure 5.4d**) compared to Azo-CDA (**Figure 5.4b**), in the SEM images. Air can become trapped in these pores creating hydrophobic pockets along the film surface.

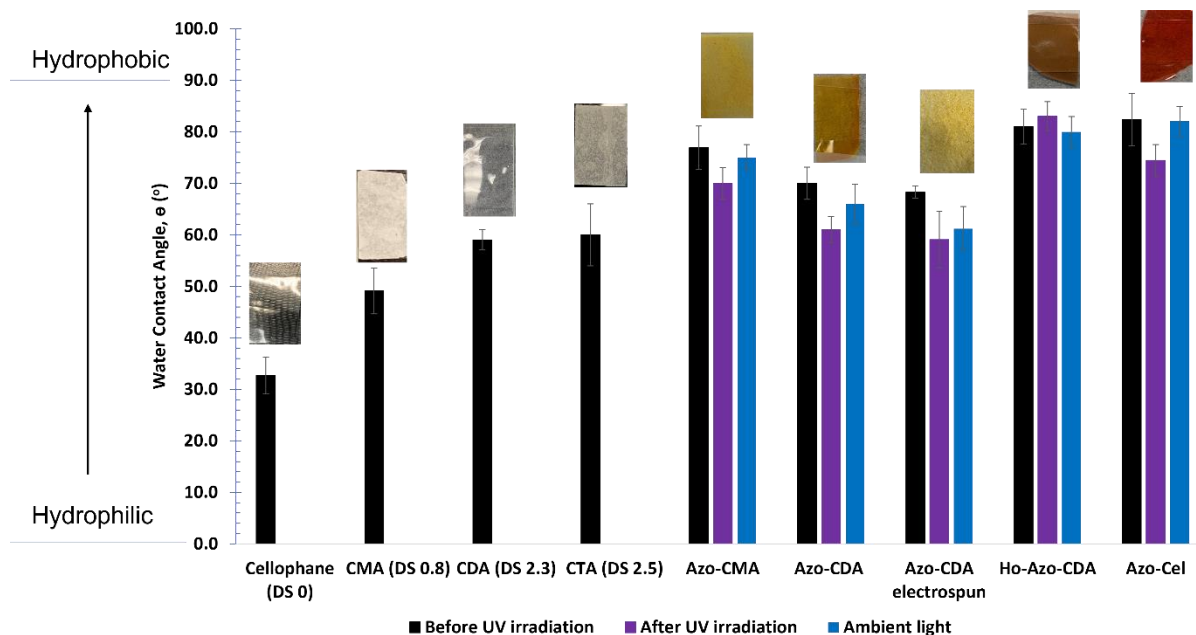


Figure 5.10 Effect of acetylation of cellulose and grafting of azo dyes onto cellulose and CA polymers on surface wettability (black bars). Purple bars indicate the water contact angle (WCA) of the film surface following UV irradiation for $t = 20$ min and blue bars represent the WCA following exposure to ambient visible light for $t = 20$ min.

The solvent cast and electrospun Azo-CDA film (15 wt.% from acetone/DMF/water) had similar WCA values ($70 \pm 3^\circ$ and $69 \pm 1^\circ$, respectively) (**Figure 5.10**). It should be noted that the

electrospun Azo-CDA film from acetic acid also had a WCA value $\sim 70^\circ$. The negligible difference between the WCAs of the solvent-cast and electrospun Azo-CDA films indicate that the electrospinning conditions used were not optimal in creating a film with a fibrous network capable of forming a hydrophobic surface. The Ho-Azo-CDA and Azo-Cel samples had the highest WCA values of $81 \pm 3^\circ$ and $82 \pm 5^\circ$, respectively, which was an increase in the WCA by 22° for the Ho-Azo-CDA sample from CDA, and 49° for the Azo-Cel sample from cellophane. The WCA of Ho-Azo-CDA was also higher than that of Azo-CDA, possible due to the presence of the small cavities along the surface of Ho-Azo-CDA (**Figure 5.4e**), which similarly to the Azo-CMA can trap air creating hydrophobic pockets along the film surface. Compared to the previously reported WCA of the electrospun Azo-Cel which had a value of 120° ,³⁷ the solvent-cast film had a much lower WCA, which shows how important the method of preparation and resultant surface morphology of the material is towards preparing hydrophobic surfaces.

Once the initial WCA values of the various azo functionalized cellulose-based films were measured under ambient light, the materials were exposed to high intensity UV light for $t = 20$ min and another series of WCA measurements were taken. The light was then switched off and the material was once again exposed to ambient visible light for $t = 20$ min and the measurements repeated. **Figure 5.10** shows that for all the samples, there was no significant change in the WCA of the materials before and after irradiation with UV and visible light. This unexpected lack of a significant change in the WCA might be due to several reasons, such as most of the azo dyes being located within the film and not on the surface, or restriction of movement of the azo dyes attached the polymer in this solid-state form. Attempts were made to measure the *trans-cis* isomerization of the azo dye in these films using high-powered laser pump-probe experiments, yet met with no success. These results indicate that another design approach may be needed to achieve significant

WCA changes of the azo modified CA materials in the solid-state. Perhaps crosslinking of the cellulose network with the azo dye as was done in a previous study using polydopamine and an amino azo dye,¹ or modification of only the surface of a premade cellulose acetate film could achieve better results.¹³

5.3.4 Water vapour permeability measurements

In addition to the surface wettability of Azo-CA materials, the water permeability of the material is an important factor to assess for self-cleaning materials. Generally cellulose-based materials are porous, hence their wide use as filtration membranes. The effect of the azo dye modification of the CA polymer on the water vapour permeability (WVP) was assessed, as well as any changes in this parameter in response to UV irradiation. **Figure 5.11** shows that WVTR and WVP of the unmodified CDA and CMA polymer films were very similar and the lowest of the series.

For both films the WVTR value was $< 100 \text{ cm}^3\text{m}^{-2}\text{day}^{-1}$, which places the films in the moderate WVTR range.⁵⁴ For the Azo-CDA films, the WVTR increased to about $100\text{--}240 \text{ cm}^3\text{m}^{-2}\text{day}^{-1}$, and upon UV irradiation the WVTR remained within this range at $120\text{--}180 \text{ cm}^3\text{m}^{-2}\text{day}^{-1}$ (**Figure 5.11**). There was also no significant effect of the UV irradiation on the WVP of the Azo-CDA films. The Azo-CMA films had the highest WVTR and WVP of all the samples (**Figure 5.11**), likely due to the presence of large pores throughout the films, not seen with the other samples (**Figure 5.4d**). Upon UV irradiation of the Azo-CMA films there was a slight increase in the WVTR (from $240\text{--}300$ to $260\text{--}350 \text{ cm}^3\text{m}^{-2}\text{day}^{-1}$) as well as the WVP (increased by factor of 1.6). This showed that the WVTR/WVP of the Azo-CMA films was affected by the UV irradiation, possibly due to the *trans-cis* isomerization of the azo dye. Measurements could not be performed

for the Ho-Azo-CDA and Azo-Cel samples, as the films were not large enough to fit the lids of the WVP set-up.

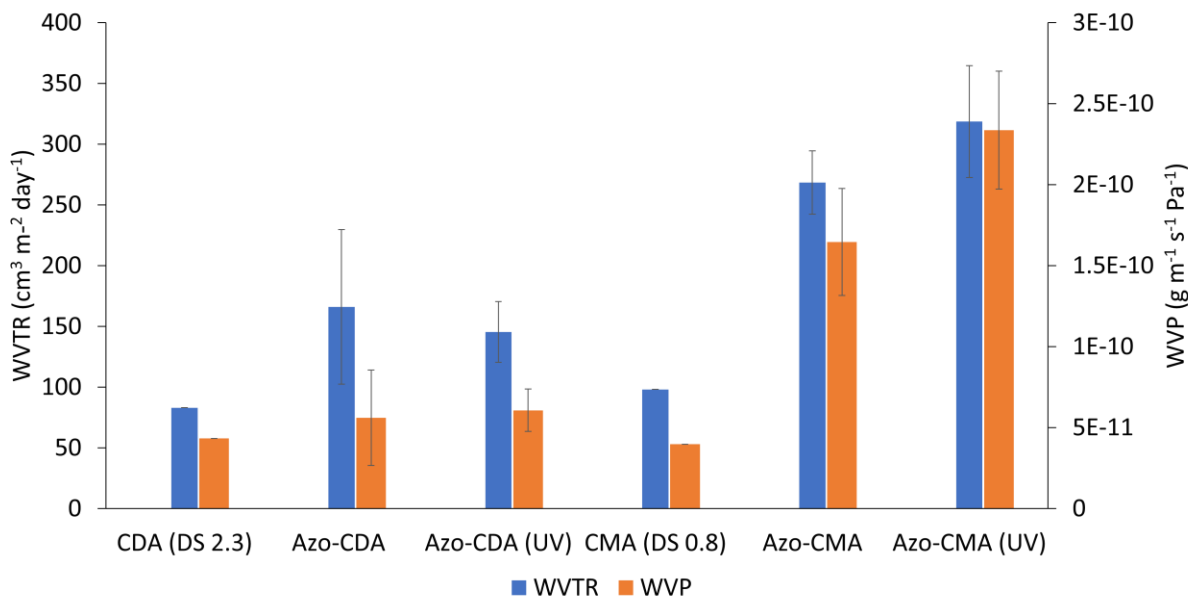


Figure 5.11 Change in water vapour transmission rate (WVTR) and water vapour permeability (WVP) of CA (CDA and CMA) and azo modified CA films (Azo-CDA and Azo-CMA) under ambient light and with exposure to UV light.

5.4 Conclusions

Photo-reversible azo modified CA polymers were prepared for the first time *via* an esterification reaction of CA with various azo dyes. The incorporation of the azo dye onto the cellulose-based polymer negatively affected the crystallinity of the polymer but in general improved the thermal stability. With UV-Vis spectroscopy it was observed that the azo dyes once bound to the polymer were still capable of undergoing *trans-cis* isomerization in response to UV light, with the rate of

the *cis* decay of the azo dye following a biexponential decay and generally relaxing more slowly once bound to the polymer. To assess the viability of the Azo-CA materials for use as self-cleaning devices, the change in the WCA upon exposure to UV/Vis light was measured. While the results showed that the WCA of the azo functionalized cellulose-based films were higher (less hydrophilic) than the unmodified cellulose and CA samples, there was no significant change detected in the WCA of the Azo-Cel and Azo-CA films following irradiation with UV light. However, measurements of the WVP of the Azo-CMA films showed a significant change in the water permeance of the films during UV irradiation compared to exposure to visible light. These results are promising and indicate that more work is needed to optimize a material whose WCA can effectively change in response to UV light. Future work may include the modification of cellulose and CA with an octa-fluoro azo dye, and electrospinning of the resulting polymer towards making these photo-reversible self-cleaning materials.

5.5 References

1. S. N. Ramanan, N. Shahkaramipour, T. Tran, L. Zhu, S. R. Venna, C.-K. Lim, A. Singh, P. N. Prasad and H. Lin, *Journal of Membrane Science*, 2018, **554**, 164–174.
2. D. Klemm, B. Heublein, H. P. Fink and A. Bohn, *Angewandte Chemie International Edition in English*, 2005, **44**, 3358–3393.
3. P. Sonkaew, A. Sane and P. Suppakul, *Journal of Agricultural and Food Chemistry*, 2012, **60**, 5388–5399.
4. Q. Tarrés, P. Mutjé and M. Delgado-Aguilar, *Cellulose*, 2019, **26**, 6917–6932.
5. J. Wang, D. J. Gardner, N. M. Stark, D. W. Bousfield, M. Tajvidi and Z. Cai, *ACS Sustainable Chemistry & Engineering*, 2017, **6**, 49–70.
6. F. Li, P. Biagioni, M. Bollani, A. Maccagnan and L. Piergiovanni, *Cellulose*, 2013, **20**, 2491–2504.

7. K. Torvinen, J. Sievänen, T. Hjelt and E. Hellén, *Cellulose*, 2012, **19**, 821–829.
8. Y. Wang, X. Wang, Y. Xie and K. Zhang, *Cellulose*, 2018, **25**, 3703–3731.
9. F. E. Bartell and B. R. Ray, *Journal of the American Chemical Society*, 1952, **74**, 778–783.
10. T. A. Dankovich and D. G. Gray, *Journal of Adhesion Science and Technology*, 2012, **25**, 699–708.
11. P. Samyn, *Journal of Materials Science*, 2013, **48**, 6455–6498.
12. T. Onda, S. Shibuichi, N. Satoh and K. Tsujii, *Langmuir*, 1996, **12**, 2125–2127.
13. C. Jin, R. Yan and J. Huang, *Journal of Materials Chemistry*, 2011, **21**, 17519–17525.
14. P. Khanjani, A. W. T. King, G. J. Partl, L. S. Johansson, M. A. Kostianen and R. H. A. Ras, *ACS Applied Materials & Interfaces*, 2018, **10**, 11280–11288.
15. M. M. Bashar, H. Zhu, S. Yamamoto and M. Mitsuishi, *RSC Advances*, 2017, **7**, 37168–37174.
16. A. Alam, E. Ewaldz, C. Xiang, W. Qu and X. Bai, *Polymers (Basel)*, 2020, **12**, 2092–2109.
17. T. Young, *Philosophical Transactions of the Royal Society of London*, 1805, **95**, 65–87.
18. M. A. Hubbe, Gardner, D. J., and Shen, W, *BioResources*, 2015, **10**, 8657–8749.
19. A. K. A. Mukherjee, R.K. Chaturvedi, H.K. Gupta, B.D., *Indian journal of textile research*, 1981, **6**, 120–123.
20. T. A. Wheatley, *Drug Development and Industrial Pharmacy*, 2007, **33**, 281–290.
21. H. Kono, H. Hashimoto and Y. Shimizu, *Carbohydrate Polymers*, 2015, **118**, 91–100.
22. O. Arslan, Z. Aytac and T. Uyar, *ACS Applied Materials & Interfaces*, 2016, **8**, 19747–19754.
23. J. Ganster and H. Fink, in *Bio-Based Plastics: Materials and Applications*, ed. S. Kabasci, John Wiley & Sons, Ltd, 1st Edn., 2014, pp. 37–62.
24. P. Sikorski, M. Wada, L. Heux, H. Shintani and B. T. Stokke, *Macromolecules*, 2004, **37**, 4547–4553.
25. X. Fan, Z. Liu, J. Lu and Z. Liu, *Industrial & Engineering Chemistry Research*, 2009, **48**, 6212–6215.
26. A. Liukkonen, *Scanning*, 1997, **19**, 411–415.

27. C. L. Bird and M. P. Harris, *Journal of the Society of Dyers and Colourists*, 1957, **73**, 199–202.
28. T. M. Baldwinson, *Journal of the Society of Dyers and Colourists*, 1961, **77**, 246–251.
29. O. Yoshio, S. Hideaki, H. Koichi and I. Masahiro, *Chemistry Letters*, 1986, **15**, 983–986.
30. K. Arai and H. Udagawa, *Die Makromolekulare Chemie, Rapid Communications*, 1988, **9**, 797–800.
31. I. Otsuka and C. J. Barrett, *Cellulose*, 2019, **26**, 6903–6915.
32. Z. Li, D. Zhang, J. Weng, B. Chen and H. Liu, *Carbohydrate Polymers*, 2014, **99**, 748–754.
33. L. Zhang, J. Li and H. Liu, *Cellulose*, 2016, **23**, 1177–1188.
34. V. Chandrasekaran, E. Johannes, H. Kobarg, F. D. Sonnichsen and T. K. Lindhorst, *ChemistryOpen*, 2014, **3**, 99–108.
35. J. Wang, B. Wu, S. Li, G. Sinawang, X. Wang and Y. He, *ACS Sustainable Chemistry & Engineering*, 2016, **4**, 4036–4042.
36. G. S. Hartley and R. J. W. Le Fèvre, *Journal of the Chemical Society (Resumed)*, 1939, **119**, 531–535.
37. H. Ahmadi-Nohadani, S. Nono-Tagne, C. J. Barrett and I. Otsuka, *Macromolecular Rapid Communications*, 2022, **43**, 2200063–2220070.
38. S. N. Fernandes, L. E. Aguirre, R. V. Pontes, J. P. Canejo, P. Brogueira, E. M. Terentjev and M. H. Godinho, *Cellulose*, 2015, **23**, 465–476.
39. W. Qin, Z. Li, J. Li, L. Zhang, R. Liu and H. Liu, *Cellulose*, 2014, **22**, 203–214.
40. X. Hu, P. J. Zheng, X. Y. Zhao, L. Li, K. C. Tam and L. H. Gan, *Polymer*, 2004, **45**, 6219–6225.
41. L. F. Pinto, S. Kundu, P. Brogueira, C. Cruz, S. N. Fernandes, A. Aluculesei and M. H. Godinho, *Langmuir*, 2011, **27**, 6330–6337.
42. N. Olaru, A. Andriescu and L. Olaru, *European Polymer Journal*, 2001, **37**, 865–867.
43. Sigma-Aldrich, Cellulose acetate, <https://www.sigmaaldrich.com/CA/en/product/aldrich/180955>, (accessed Feb 1st, 2022).
44. N. Böhm, A. Materny, W. Kiefer, H. Steins, M. M. Müller and G. Schottner, *Macromolecules*, 1996, **29**, 2599–2604.
45. Y. Zhang, C. Zhang and Y. Wang, *Nanoscale Advances*, 2021, **3**, 6040–6047.

46. W. Chen, H. Ma and B. Xing, *International Journal of Biological Macromolecules*, 2020, **158**, 1342–1351.
47. M. Moradian, M. N. Alam and T. G. M. van de Ven, *Industrial & Engineering Chemistry Research*, 2021, **60**, 13756–13763.
48. H. Yang, M. N. Alam and T. G. M. van de Ven, *Cellulose*, 2013, **20**, 1865–1875.
49. H. A. Foner and N. Adan, *Journal of the Forensic Science Society*, 1983, **23**, 313–321.
50. L. K. Tolonen, P. A. Penttilä, R. Serimaa, A. Kruse and H. Sixta, *Cellulose*, 2013, **20**, 2731–2744.
51. C. J. Barrett, A. Natansohn and P. Rochon, *Macromolecules*, 1994, **27**, 4781–4786.
52. L. L. Norman and C. J. Barrett, *Journal of Physical Chemistry B*, 2002, **106**, 8499–8503.
53. F. Mikaeili and P. I. Gouma, *Scientific Reports*, 2018, **8**, 12472–12480.
54. R. Shogren, D. Wood, W. Orts and G. Glenn, *Sustainable Production and Consumption*, 2019, **19**, 194–215.
55. J. Gao, Y. He, F. Liu, X. Zhang, Z. Wang and X. Wang, *Chemistry of Materials*, 2007, **19**, 3877–3881.
56. R. Mustapha, A. Zoughaib, N. Ghaddar and K. Ghali, *Energy*, 2020, **195**, 117057–117067.

5.6 Appendix 4: Supporting information for Chapter 5

5.6.1 Experimental

5.6.1.1 Materials

Cellulose kraft pulp was kindly provided by FP Innovations (Quebec, Canada). Cellulose acetate (39.3–40.3 % acetyl content, Mn ~30,000) was purchased from Aldrich (CAS # 9004-35-7). Cellophane sheets were purchased from ThermoFisher Scientific (Catalog # CM-20, 50 sheets, 24 × 24 cm). The azo dye 4-phenylazobenzoyl chloride (173452-1G) and thionyl chloride (230464-100mL) were purchased from Millipore Sigma. Hydrochloric acid (36 %) was purchased from ACP (LOT # H-6100) and ethanol (100 %) from Commercial Alcohols (# PO16EAAN). Sodium carbonate (CAS # 497-19-8) and petroleum ether (CAS # 8032-32-4) were purchased from Fisher Scientific. NaOH pellets (CAS # 1310-73-2), 4-aminobenzoic acid (CAS # 150-13-0), spectroscopic grade THF (CAS # 109-99-9), DMF ACS reagent grade (CAS # 227056), acetone ACS reagent (CAS # 67-64-1) and anhydrous pyridine (CAS # 110-86-1) were purchased from Sigma Aldrich. Phenol crystals (CAS # 108-95-2) and sodium nitrite (CAS # 7631-99-4) were purchased from VWR.

5.6.1.2 Preparation of cellulose triacetate

The preparation of cellulose acetate with varying degrees of acetylation was carried out based on previously reported methods with slight modification.^{19, 25} Cellulose triacetate (CTA) was prepared by the acetylation of cellulose kraft pulp with acetic anhydride. Cellulose was dried overnight in an oven at 60 °C. The dried cellulose (10.00 g, MW of glucose repeat unit (C₆H₁₀O₅) = 162.1 g/mol) was activated for 1 hr using a mixture of 25 mL glacial acetic acid and 0.5 mL

concentrated sulfuric acid (6 M) with occasional stirring. The activated cellulose was fully acetylated to CTA by adding 100 mL of a mixture of acetic anhydride and glacial acetic acid (1:3 v/v) and heating the mixture at 55 °C for 30 min. The mixture was cooled to RT and 100 % ethanol added to precipitate the polymer from solution. The fibrous polymer was dissolved in DCM, a good solvent for CTA selectively over cellulose, cellulose diacetate, and cellulose monoacetate. The mixture was filtered using No.1 Whatman filter paper and the solvent evaporated and recollected. CTA (7.72 g, yield = 77%) was dried for 72 hr in an oven at 60 °C under vacuum before analysis to remove residual water and solvents. The resulting CTA had a degree of substitution of 2.5–2.7 (~53 % acetyl content) depending on the batch, confirmed by H¹ NMR spectroscopy (**Figure S5.1a**), according to **Equation 1**.

$$DS = \frac{\frac{1}{3} \times \int 1.8-2.2ppm \text{ (acetyl protons)}}{\frac{1}{7} \times \int 3.4-5.2ppm \text{ (pyranose protons)}} \quad (1)$$

5.6.1.3 Preparation of cellulose monoacetate

Cellulose monoacetate (CMA) was prepared by the deacetylation of CTA *via* a hydrolysis reaction, according to previously established protocols with slight modifications.^{19, 21, 42} CTA was prepared as previously outlined using cellulose (10.00 g, MW of cellobiose unit = 342.3 g/mol, 14.6 mmol) and the generated CTA (DS = 2.5) was then deacetylated by adding a 100 mL mixture of water and glacial acetic acid (2:3 v/v) and heating the mixture at 75 °C. Aliquots were removed at $t = 24$ and 48 hr and the polymers were precipitated out using ethanol and then acetone. The CMA polymer (7.9 g, yield = 65 %) was dispersible and partially soluble in water, and it was confirmed that at $t = 48$ hr, CMA had a DS of 0.8, confirmed by H¹ NMR spectroscopy (**Figure S5.1a**), using **Equation 1**.

5.6.1.4 Synthesis of 4-(4-hydroxyphenylazo) benzoyl chloride

To synthesize the azo dye 4-(4-hydroxyphenylazo) benzoyl chloride (Ho-azo-COCl) the precursor 4-(4-hydroxyphenylazo) benzoic acid was first prepared according to previous reports, with slight modifications.⁵⁵ In a 100 mL round bottom flask, 50 mL 1:1 acetone: water, 4-aminobenzoic acid (2.084 g, 15 mmol), sodium nitrite (1.296 g, 18 mmol) and concentrated HCl (30 mL, 40 mmol) were added and allowed to pre-activate for 30 min. In a separate 500 mL round bottom flask, 100 mL 1:1 acetone: water, sodium carbonate (3.168 g, 60 mmol), NaOH (2.404 g, 30 mmol) and phenol (1.423 g, 15 mmol) were mixed. Both solutions were combined and left to stir overnight. The solvent was removed from the resulting red solution using a rotary evaporator. Water was added to the crude product which was acidified to produce a very fine precipitate which was filtered and dried. NMR and FTIR spectroscopies (**Figures S5.2 and S5.3**) confirmed the desired product which was brown in appearance (1.716 g). The acyl chloride form of this azo dye was then prepared by refluxing 4-(4-hydroxyphenylazo) benzoic acid (0.44g, 1.8mmol) with 5 mL thionyl chloride for 1.5 hr at 80 °C. The remaining thionyl chloride was removed by distillation to give an orange-brown crude product ($m = 0.32$ g) which was purified in hot ethanol, filtered, and dried ($m = 0.20$ g). NMR and FTIR spectroscopy confirmed the successful preparation of the desired product (**Figures. S5.2 and S5.3**).

5.6.1.5 Functionalization of CA with azo dyes

The functionalization of cellulose-based polymers with azo dyes is outlined in **Figure 5.1**. CDA (0.50 g) was dried overnight and then dissolved in 20 mL anhydrous pyridine. In a separate flask 4-phenylazobenzoyl chloride (2.25 g, 9.2 mmol) was dissolved in 20 mL anhydrous pyridine. The solutions were combined in a 3-neck round bottom flask, stirred, and refluxed at 100 °C for 48 hr

under a flow of nitrogen gas. The orange product (Azo-CDA) was precipitated out using 100% ethanol, filtered, and dried overnight ($m = 0.67$ g). Any physisorbed dye was removed from the polymer by mixing in ethanol overnight. The successful grafting of the azo dye onto CDA was confirmed by NMR spectroscopy (**Figure 5.2a**) and FTIR spectroscopy (**Figure 5.3a**). This process was repeated using the azo dye 4-(4-hydroxyphenylazo) benzoyl chloride (1.00 g) under the same conditions. The brown product (Ho-Azo-CDA) was precipitated out using 100 % ethanol, filtered, and dried overnight ($m = 0.52$ g, 53 %). To prepare azo functionalized CMA, CMA (0.17 g) was dissolved in 5 mL anhydrous pyridine and 4-phenylazobenzoyl chloride (0.10g) dissolved in 5 mL pyridine, combined in a 3-neck round bottom flask, stirred and refluxed at 100 °C for 48 hr under a flow of nitrogen gas, to give an orange product Azo-CMA ($m = 0.19$ g). Ho-Azo-CMA was prepared in a similar manner, using CMA (0.17 g) and 4-(4-hydroxyphenylazo) benzoyl chloride (0.1 g). Azo-Cel polymer was previously synthesized by Otsuka and Barrett (2019) by reacting cellulose (0.5 g) and 4-phenylazobenzoyl chloride ((2.25 g, 9.2 mmol) to yield a red product (Azo-Cel) which had a mass of 2.13 g.³¹

5.6.1.6 Kinetics of azo dye isomerization

The UV-Vis spectra of the unbound azo dyes (Azo-COCl and Ho-Azo-COCl) and azo functionalized polymers: Azo-Cel, Azo-CDA, Azo-CMA, Ho-Azo-CDA and Ho-Azo-CMA were measured in THF at RT. The sample solutions were irradiated with a UV (365–390 nm) LED light source (12 V, 700 mA) for 20 min followed by the spectral measurements. The solutions were kept in the dark and the absorbance taken at various time intervals to monitor the thermal back relaxation of the *cis* isomer. For a first order *cis* → *trans* thermal isomerization:

$$\text{Rate} = \frac{d[\textit{trans}]}{dt} = -\frac{d[\textit{cis}]}{dt} = k[\textit{cis}] \quad (2)$$

Where $[\textit{trans}]$ and $[\textit{cis}]$ are the concentrations of the *trans* and *cis* isomers, respectively at any time t , and k is the first order rate constant. The rate constant, k , for a monoexponential relaxation curve can be determined from the time dependent absorbance A_t , absorbance immediately after pumping A_0 , and absorbance at infinite time, *i.e.*, complete relaxation back to *trans* A_∞ , using the equation:

$$(A_\infty - A_t) = (A_\infty - A_0)e^{-kt} \quad (3)$$

A plot of $\ln(A_\infty - A_t)$ vs. t should be linear with a slope of $-k$. For samples which deviate from first order kinetics, the experimental A_t relaxation curves were fit to the biexponential equation with 4 fitting parameters:

$$(A_\infty - A_t) = Ae^{-k_a t} + Be^{-k_b t} \quad (4)$$

Like the first-order kinetics, A_∞ and A_t are the absorbance at infinite time and the time dependent absorbance after the pump beam is switched off. A and B are the weighting coefficients and normalization of these values gives the relative contributions associated with the processes having rate constant k_a and k_b , respectively. The lifetime of the *cis* isomer τ , was calculated using the **Equation 5** below, where k is the rate constant:

$$\tau = \frac{1}{k} \quad (5)$$

5.6.1.7 Preparation of free-standing CA films

CDA and Azo-CDA thin films were prepared by dissolving the polymers (0.5 g) in THF (20 mL, 0.89 g/mL) equating to a 3 w/w % solution, and solvent casting into glass petri dishes. The dishes were left uncovered at RT in a fume hood for 2 days. Thin films of Ho-Azo-CDA were prepared in a similar manner by dissolving (0.1 g) of the polymer in 10 mL THF solvent to make a 1 w/w % solution. Thin films of CTA (0.1 g) and Azo-CMA (0.1 g) were prepared by dissolving the polymers in 10 mL DMSO, while CMA (0.5 g) was dissolved in 20 mL DMSO. The films were placed in an oven and dried for 3 days under vacuum at 60 °C. The Azo-Cel thin films were prepared by solvent-casting the polymer 10 w/w % solution from THF and air drying for 2 days uncovered.

5.6.1.8 Electrospinning of Azo-CDA

Electrospinning of Azo-CDA was carried out based on previously established protocols for CDA with slight modifications.⁴⁵ A 10 wt % solution of Azo-CDA in acetic acid (80 % v/v) was prepared and electrospun into a mesh onto an aluminium drum 8 cm distant using a syringe with a #21 needle under a voltage of 10 kV.⁴⁵ A 7.5 wt % and 15 wt % solution of Azo-CDA in acetone/DMF/water (3:2:1) mixture were prepared and electrospun onto an aluminium drum 10 cm distant using a syringe with a #21 needle under a voltage 10 and 11 kV, respectively.⁴⁶

5.6.1.9 Water contact angle measurements

The water contact angle (WCA) of the various polymer films was measured using the sessile drop method, using an optical contact angle goniometer (Model OCA 20, Dataphysics, USA). A drop of water (20 μ L) was placed onto the surface of the film and an image of the drop captured using

a high-resolution camera. Images were taken at $t = 0, 1, 5,$ and 10 min. Measurements were performed in triplicate at different locations on the films. For photo-responsive WCA experiments, the azo-cellulose-based samples were irradiated with an UV LED (385–390 nm, 12 V, 700 mA) or a high-powered UV laser (375 nm, 50 mW/cm²) for 20 min, followed by a drop being placed onto the surface and the image captured. The film was then exposed to ambient visible light for 20 min and the WCA measured again. These measurements were performed in triplicate.

5.6.1.10 Water vapour transmission rate and permeability experiments

The thickness of the films was measured in triplicate using a micrometer gauge instrument (tmi® testing machine, model 49–70). The water vapour transmission rate (WVTR) and water vapour permeation (WVP) tests were performed according to the ASTM E96 upright cup test with slight modifications.⁵⁶ A vial was filled with dried calcium chloride and a strip of the thin film was placed between two circular disks on top of the flask. The initial mass was recorded, and the vial placed in a humidity chamber with saturated salt solution (22 °C, 60 % RH). The mass was taken every 24 hr for 1 week and WVTR calculated based on the **Equation 7**:

$$WVTR (cm^3m^{-2}day^{-1}) = \left(\frac{w}{t}\right)(A^{-1}) \quad (7)$$

where w is the weight loss (g) converted to volume loss (cm³) given that the density of water is 1 gcm⁻³, t is the time (days), and A is the area of the film (m²). The WVP can then be calculated using **Equation 8**:

$$WVP (gm^{-1}s^{-1}Pa^{-1}) = WVTR \cdot d \cdot (\Delta p^{-1}) \quad (8)$$

Here d is the thickness of the film (m), and Δp is the vapour pressure difference of saturated salt solution (2 kPa, at 295 K). For the azo-cellulose-based samples, measurements were also

performed while irradiated with UV light (365 nm, 12 V, 700 mA) and the WVTR and WVP calculated. For these measurements the $T = 24\text{ }^{\circ}\text{C}$ and $\text{RH} = 54\%$ due to slight heating from the UV light.

5.6.1.11 Spectroscopies and analyses

Fourier transform infrared (FTIR) spectroscopy

The Infrared (IR) spectra of all samples were recorded on an FTIR spectrometer (Spectrum II, PerkinElmer, USA) with a single bounce diamond attenuated total reflectance (ATR) accessory employed. The IR spectra was recorded in transmittance mode over the range 400 to 4000 cm^{-1} with a resolution of 1 cm^{-1} averaged over 24 scans.

Nuclear magnetic resonance (NMR) spectroscopy

H^1 NMR spectra of all samples were acquired using a Varian 500 MHz spectrometer with solvent DMSO- d_6 or D_2O . Solid-State C^{13} NMR of the CDA and Ho-Azo-CDA samples were carried on a Varian VNMRS 400 MHz NMR spectrometer, using a 4mm probe, with cross polarization at a magic angle spinning of 54.74° . Samples were spun at 13 kHz with 3092 scans with an acquisition time of 30 ms and a delay of 3 s.

X-ray diffraction (XRD)

The crystallinity of cellulose, CAs, and Azo-CAs were acquired on a Bruker Discover D8 two-dimensional diffractometer, with $\text{Cu K}\alpha$ radiation ($\lambda = 1.54\text{ \AA}$) and VANTEC 2D detector. Measurements were made for $2\theta = 5\text{--}50^{\circ}$, with a step interval of 0.02° . The characteristic planes

(200) and (110) of cellulose I were assigned according to other established protocols,⁴⁹ and the crystallinity determined using the **Equation 9**:

$$CI (\%) = \left(\frac{I_{max} - I_{min}}{I_{max}} \right) \times 100 \quad (9)$$

Where CI is the crystallinity index (%), I_{max} is the intensity of the maximum peak at plane 200, and I_{min} is the intensity of the minimum peak at plane 110.

Thermogravimetric analysis (TGA)

The thermal stabilities of the azo dyes, CA polymers and Azo-CA polymers were determined using a TA instruments TGA 5500 instrument where the samples were heated using ramp 10 °C/min to 500 °C/min, under N₂ gas, with flow rate of 90 mL/min.

Scanning electron microscopy- energy dispersive spectroscopy (SEM-EDS)

The surface (planar view) of the Azo-CA and Azo-Cel thin films was imaged by high resolution Field Emission Scanning Electron Microscopy (FE-SEM) using a FEI Quanta 450 Environmental Scanning Electron Microscope with EDAX Octane Super 60mm SDD. Elemental mapping was done using the TEAM EDS analysis system. The accelerating voltage used was 10 kV after sputter coating with platinum with a thickness of approximately 7 nm. The nitrogen content of the films was determined by averaging the weight % nitrogen, measured at 3–6 different spots along the surface the same film.

5.6.2 Spectroscopy data

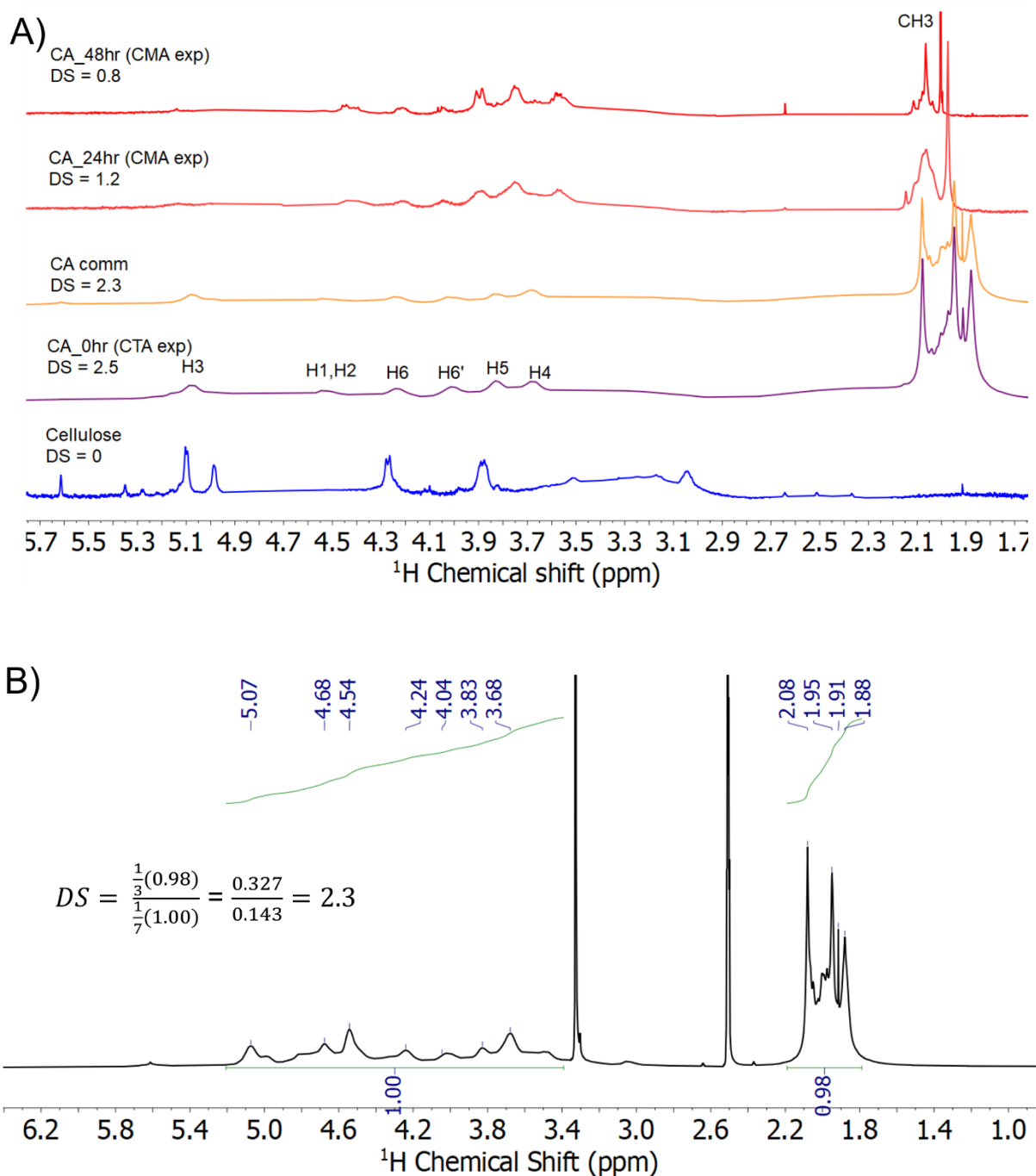


Figure S5.1 (A) ¹H NMR spectra of CA polymers in DMSO-d₆ or D₂O solvent at various time periods following acetylation of cellulose and consequent hydrolysis of cellulose triacetate (CTA). (B) Determination of degree of substitution (DS) of commercial CA using ¹H NMR spectroscopy, in DMSO-d₆ solvent.

Cellulose: ^1H NMR (500 MHz, DMSO) δ 5.10, 4.98, 4.28, 4.24, 3.91, 3.86, 3.51 ppm.

CTA (DS = 2.5): ^1H NMR (500 MHz, DMSO) δ 5.08, 4.61, 4.54, 4.24, 4.01, 3.82, 3.67, 2.08, 1.95, 1.91, 1.88 ppm.

CA_{24hr} (DS = 1.2): ^1H NMR (500 MHz, D₂O) δ 4.52, 4.18, 3.98, 3.88, 3.72, 3.50, 2.07, 1.97 ppm.

CA_{48hr} (DS = 0.8): ^1H NMR (500 MHz, D₂O) δ 4.46, 4.16, 4.05, 3.89, 3.75, 3.56, 2.06, 2.00 ppm.

CA comm (CDA) (DS = 2.3): ^1H NMR (500 MHz, DMSO) δ 5.07, 4.68, 4.54, 4.24, 4.04, 3.83, 3.68, 2.08, 1.95, 1.91, 1.88 ppm.

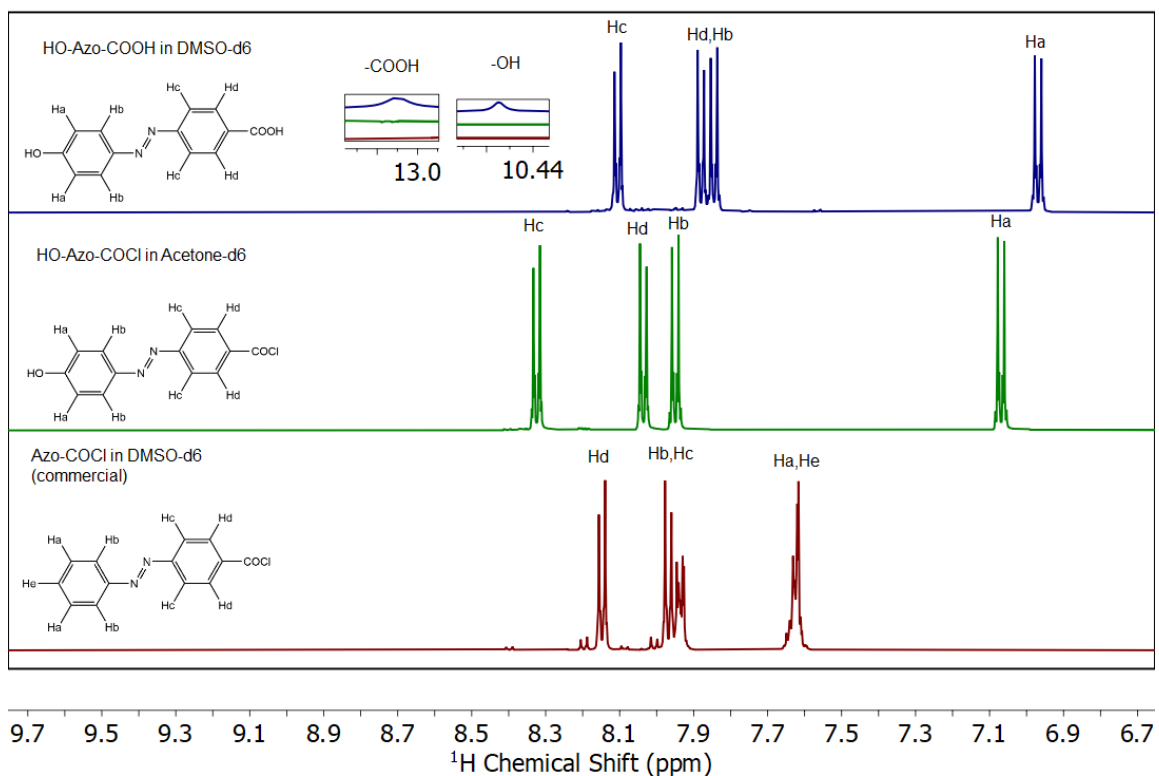


Figure S5.2 ^1H NMR of azo dyes: precursor Ho-Azo-COOH (blue), synthesized Ho-Azo-COCl and (green) and commercial Azo-COCl (red).

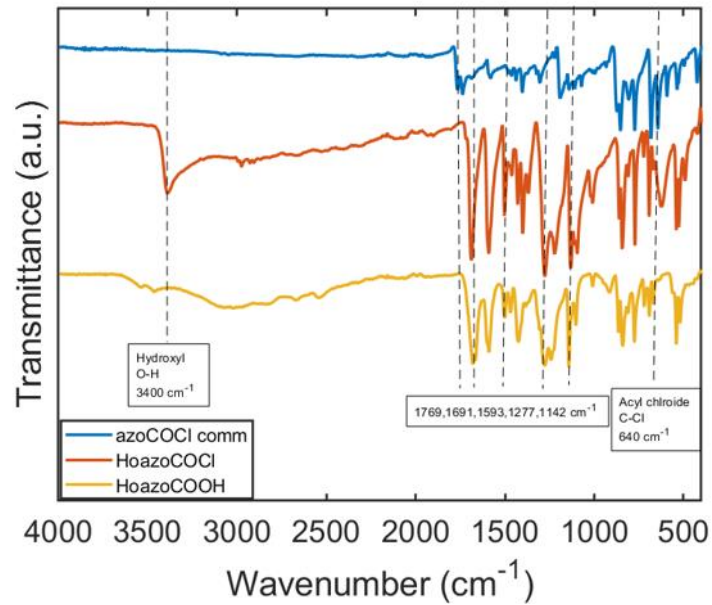


Figure S5.3 IR spectra of azo dyes: (blue) commercial Azo-COCl, (orange) synthesized Ho-Azo-COCl, and (yellow) precursor Ho-Azo-COOH.

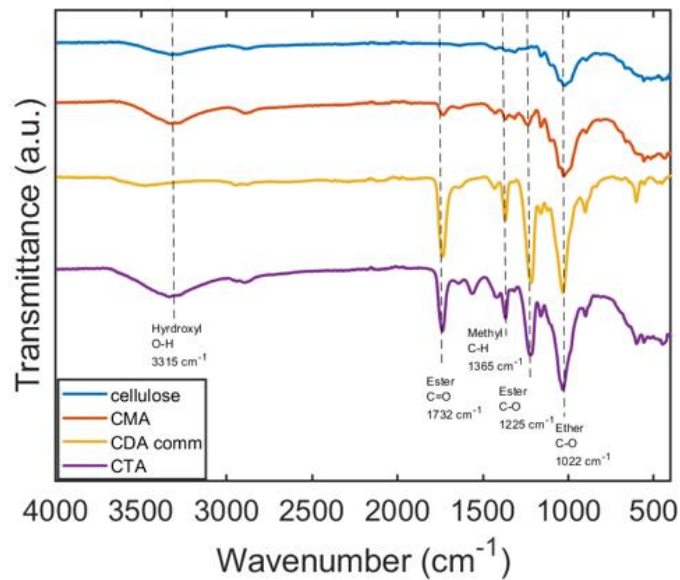


Figure S5.4 IR spectra of cellulose and cellulose acetate with varying % acetyl content.

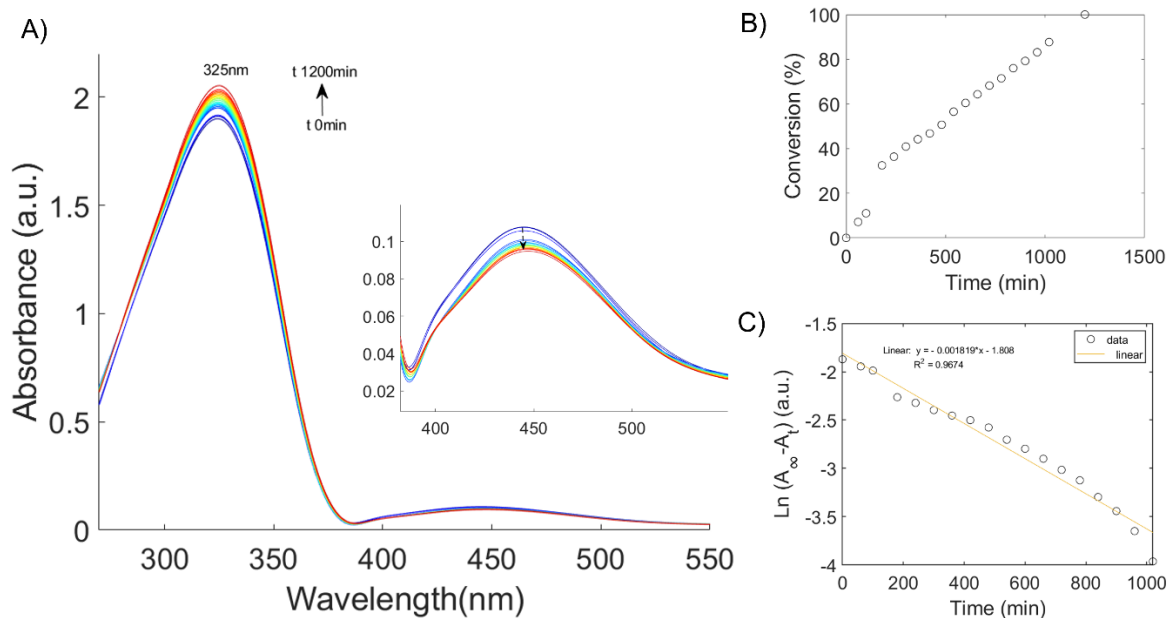


Figure S5.5 (A) UV-Vis spectra and thermal back relaxation of Azo-CDA in THF solution in the dark following irradiation with UV light for $t = 20$ min. Measurements were taken at $t = 60$ min intervals. Inset shows the decrease in the absorbance band at 450 nm during thermal back relaxation. (B) Conversion of Azo-CDA from *cis*-to-*trans* isomer in dark following irradiation with UV light. (C) Plot of first order kinetics $\text{Ln}(A_\infty - A_t)$ vs. t for Azo-CDA in THF during *cis* decay.

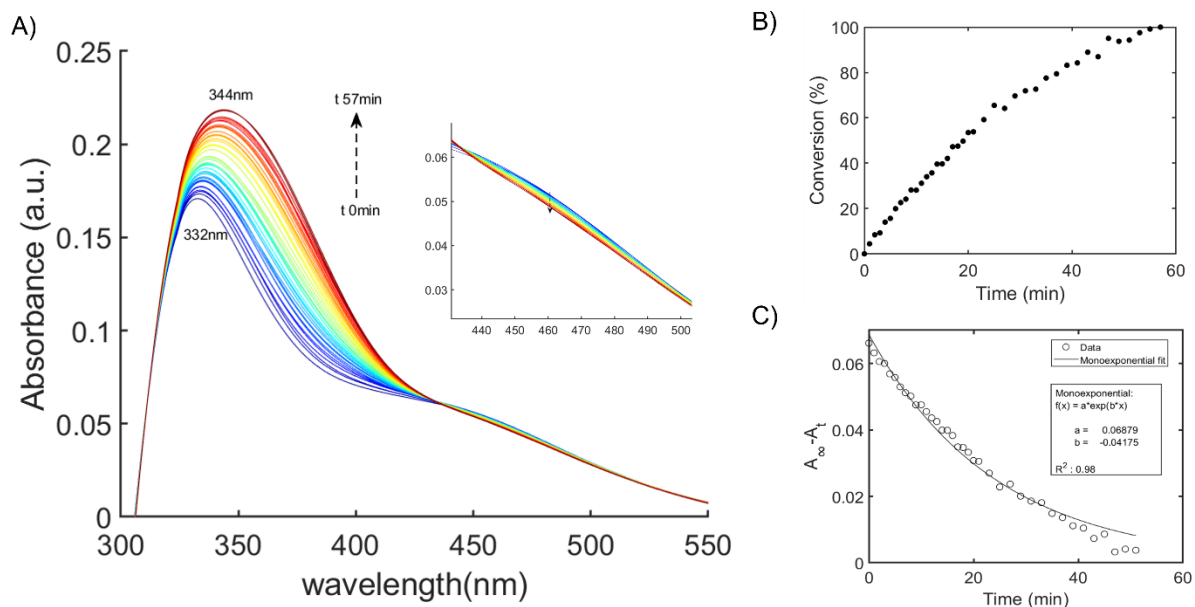


Figure S5.6 (A) UV-Vis spectra and thermal back relaxation of Ho-Azo-CMA in THF solution in the dark following irradiation with UV light for $t = 20$ min. Measurements were taken at $t = 60$ min intervals. Inset shows the decrease in the absorbance band at 460 nm during thermal back relaxation. (B) Conversion of Ho-Azo-CMA from *cis*-to-*trans* isomer in dark following irradiation with UV light. (C) Decay of the *cis* isomer of Ho-Azo-CMA in THF fit with a monoexponential function.

Chapter 6: Discussion, conclusions, and future outlook

6.1 Discussion

This Thesis outlined several methods to develop photo-reversible materials using azo dyes and natural polymers. Each Chapter showed how azo dyes can function as dynamically active molecular photo-switches when incorporated into a biopolymer network, be it *via* weak soft-bonded interactions (ionic bonding, hydrogen bonding) or strong covalent bonds. The assembly of these azo dyes into the polymer matrix or grafting of the azo dyes onto the polymer backbone greatly affected the properties of materials made from these biopolymers. Fabrication using biopolymers is of great interest as this presents an alternative method of preparing these photo-reversible materials in a more sustainable manner, by replacing the commonly used traditional petrol-based polymers, such as P4VP and PAA, with natural polymers such as alginate, cellulose, and its derivatives, which are bio-sourced and biodegradable.

Chapter 1 highlighted the potential of biopolymers such as cellulose, and starch, to replace traditional petrol-based polymers in various applications. It provided an overview of the field of photo-reversible soft-bonded azo/polymer complexes, showing that supramolecular chemistry can be used to develop robust materials for a wide array of varied applications *via* photo-driven disassembly of self-assembled layers, multilayers, and composite materials. Chapter 1 also highlighted the few previous instances where these photo-reversible materials have been prepared using natural polymers, achieving similar performance as their petrol-based counterparts. Within this Thesis, many of the objectives of developing photo-reversible materials using azo dyes and natural polymers have been achieved, *via* the self-assembly or covalent modification of natural polymers such as sulfated cellulose, cellulose acetates, and alginate. The use of (water-soluble) natural polymers in place of petrol-based polymers

addresses some of the 12 principles of Green Chemistry,^{1, 2} such as (i) the use of renewable feedstocks, (ii) design for degradation, (iii) compatibility with safer solvents and auxiliaries, and (iv) use of less hazardous chemical synthesis. It is hoped that these developments would help support the transition to a more sustainable production of photo-reversible materials in the future.

Chapter 2 introduced a facile and inexpensive method of preparing photo-reversible materials using azo dyes and natural polymers, utilizing self-assembly by means of a layer-by-layer (LbL) approach, to develop thin polyelectrolyte multilayer (PEM) films with precise control over film growth and properties. These new reversibly ‘soft-bonded’ assemblies could potentially serve as a new class of materials to replace some of the artificial plastics currently used for a variety of thin film or coating applications. These PEM films could function as competitive photo-reversible materials, yet also ones that can be photo-reversibly disassembled and re-solubilized, since the assembled films were insoluble in water once the azo dyes were in the *trans*-geometric configuration, but less stable and more water-soluble in the *cis* form. While PEM films have been prepared in the past using natural polymers such as silk and hyaluronic acid, the crosslinking of natural polymers solely using an azo dye *via* soft bonding interactions was yet to be undertaken. Chapter 2 showed the results of only one of the many natural polymers tested to make these PEM films, with the best results achieved using the natural polymer sodium cellulose sulfate (NaCS), which is a negatively charged water-soluble form of cellulose, with the positively charged water-soluble commercial azo dye, Bismarck Brown Y (BBY) as a bivalent cross-linker. On its own NaCS forms water-soluble films, which have previously been used to make films for packaging; however, once assembled into multilayers with the positively charged BBY azo dye, the resulting PEM films were insoluble in water. The films could withstand immersion in high temperatures, very acidic and

basic conditions, and up to 1 M salt concentration, allowing potential use in a wide range of packaging applications.

The NaCS/BBY thin films which had a vibrant red colour, were characterized using several techniques such as: (i) UV-Vis spectroscopy, to monitor the growth of the thin films during the deposition process by measuring the increase in the maximum absorption of the azo dye at $\lambda_{max} = 450\text{--}460$ nm; (ii) FTIR spectroscopy, to observe the changes in the amine vibrational stretching frequency upon formation of salt bridges, *i.e.* intermolecular ionic and hydrogen bonding between the polymer and azo dye; (iii) AFM to measure changes in film thickness, with the thickness of the NaCS/BBY films remaining at ~ 300 nm after exposure to water for 2 weeks under white light, but decreasing to 0 nm upon exposure to low intensity blue light with gentle washing with tap water; (iv) XPS and (v) SEM-EDS to confirm the presence of both the polymer and azo dye throughout the thin film; and (vi) contact angle measurements were performed to observe changes in the hydrophilicity of the film surface of the NaCS polymer only *vs.* the NaCS/BBY multilayered films.

Having thoroughly characterized the NaCS/BBY films, it was then necessary to confirm that the BBY azo dye could function as a photo-switch, capable of undergoing *trans-cis* geometric isomerization in response to visible light. Even though BBY is a commercial azo dye which has been around since the 1860s, there were no previous reports on the isomerization of this azo dye. For the first time, the *trans-cis* isomerization of the BBY azo dye was observed using two different spectroscopic techniques, confocal Raman spectroscopy and laser pump-probe experiments. Using a green laser as the light source, the *trans-to-cis* isomerization of the ‘free’ azo dye, and the azo dye embedded in the NaCS/BBY films was observed by confocal Raman spectroscopy. With the pump-probe experiments both the *trans-to-cis* isomerization and the *cis* decay of the azo dye back to *trans* could be monitored. Using

a green laser as the pump beam and a blue laser as the probe beam, the *trans*-to-*cis* isomerization of the azo dye in THF was observed, with the *cis* decay following an unexpected biexponential decay kinetics. The isomerization of the azo dye in other solvents and in the PEM films was explored in more detail in Chapter 3, both experimentally and using DFT theoretical modeling.

Once it was confirmed that the BBY azo dye could undergo *trans*-*cis* isomerization, the photo-induced disassembly of the material was tested using a novel simulated ‘sun and rainfall’ experiment designed in-house at McGill. For these experiments, the films were exposed to ‘sun’ which was chosen as low (solar) intensity blue light since the maximum absorption of the BBY azo dye was $\lambda_{max} = \sim 460$ nm, which should induce *trans*-to-*cis* isomerization. Exposure to the full spectrum of white light (400–700 nm) should promote both the *trans*-to-*cis* and *cis*-to-*trans* isomerization allowing the films to remain stable under ambient conditions for a prolonged period. For the simulated ‘sun and rainfall’ experiments, the films were clamped under a stream of flowing water and irradiated continuously, with the disassembly of the films tracked using UV-Vis spectroscopy by monitoring the decrease in the absorbance of the azo dye. The results showed that the films preferentially disassembled in the presence of blue light while being gently washed, in comparison to films washed in the dark or under ambient white light. However, it was observed that the NaCS/BBY films did not always completely disassemble while being washed with DI water and irradiated with blue light, probably due to the high stability of the multilayers held together by ‘strong’ electrostatic interactions. This over-stability could be rectified by the addition of salt (2 M NaCl solution) which can screen the electrostatic charges within the multilayers, or by increasing the pH above 11, which deprotonates the azo dye weakening the interactions between the dye and the polymer. To mimic ‘rainfall’ conditions, the films were also washed with tap water while being irradiated with blue light, and complete disassembly was observed after 1 day. The presence of

salts and other charged species in the tap water appeared to help speed up the rate of disassembly of the films.

LbL assembly was chosen as the technique to make these photo-reversible materials since it offered better control over the assembly of the components which resulted in films that were water resistant but could be re-solubilized once irradiated with blue light, yet also most easily studied and characterized. Initially, solvent-casting was employed to create these photo-reversible thin films, whereby an aqueous solution of the cellulose-based polymer and an aqueous solution of the azo dye were mixed, poured into a glass dish and the film allowed to form *via* solvent evaporation. This random bulk mixing of the polymer and azo dye either did not produce films which were insoluble in water under ambient conditions, or which produced films that were too stable and would not disassemble under blue light.

While Chapter 2 presented a successful case of developing photo-reversible PEM films using the NaCS polymer and BBY azo dye, there were other polymers and azo dyes which were also tested. For the NaCS polymer, other positively charged water-soluble commercial azo dyes containing an amine group (NH_2), such as 4,4'-azodianiline and acid yellow 9 (AY9), were used to make PEM films, however, these other 2 azo dyes did not form good PEM films with the polymer. Other water-soluble natural polymers were also tested, such as hydroxypropyl cellulose (HPC), dialdehyde cellulose (DAC) and cellulose monoacetate (CMA). HPC formed stable PEM films with the BBY azo dye, however, these films were not as uniform as the NaCS/BBY films, had lower loading of the azo dye during the dipping process, and did not fully disassemble when irradiated with blue light. Unlike NaCS which is a negatively charged polymer, HPC is neutral and therefore the main attractive force between HPC and BBY was hydrogen bonding which is much weaker than the electrostatic interactions present for NACS/BBY. PEM films were also formed with the DAC polymer and the BBY azo

dye, as well as 4,4'-azodianiline. In both cases a Schiff base reaction can occur between the aldehyde group of DAC and the protonated amine groups of the azo dye, resulting in the formation of a permanent imine bond, in addition to hydrogen bonding which can also form between the two functional groups.³ The resulting films were orange and yellow in colour, respectively. While both films were stable under ambient conditions, they did not disassemble significantly in the presence of blue or green light.

Chapter 3 provided some first insights into the *trans* (EE) \leftrightarrow *cis* (ZZ) isomerization of the photo-switch used to prepare the photo-reversible materials described in Chapter 2. It provided both an experimental and computational study of the isomerization of a well-used commercial bis-azo dye known as Bismarck Brown Y (BBY). Using an optical pump-probe set-up, the *trans-cis-trans* isomerization of BBY was monitored in various solvents such as THF and DMF (aprotic solvents), and water and ethanol (protic solvents), as well as embedded in the NaCS/BBY PEM films, *i.e.*, in the solid-state. These measurements showed that the BBY azo dye can isomerize using specific wavelengths of visible light (blue or green), even when incorporated into the PEM films. This would help support the mechanism of the disassembly of the NACS/BBY films being photo-driven. The results showed that the BBY azo dye could isomerize using visible light (close to 532 nm), and that the decay of the *cis* geometric isomer followed a highly unusual biexponential decay, on the timescale of milliseconds-seconds. This isomerization was also observed for the azo dye in the PEM films, with the *cis* decay observed to be slower once embedded in the film compared to in solution. Based on previous literature of bis-azo dyes, since BBY is a symmetrical molecule, both azo units should behave similarly and have equivalent *cis* decay kinetics; thus overall, the azo dye should follow a monoexponential decay.^{4,5} This was further supported by the DFT calculations performed by our collaborator Prof. William Pietro at York University, Toronto. DFT modeling is a powerful technique that can be used by other researchers to rationalize experiments, or who might not

have access to some of the specialized and expensive equipment required for pump-probe experiments (*e.g.*, lasers, shutters, lock-in electronics) needed to observe fast-switching azo dyes such as BBY.

Computational modelling was undertaken by our collaborators to predict the timescale of the *cis* relaxation of the BBY azo dye. DFT calculations were performed with Orca 5.0 software using the def2-TZVP (triple-split-valence with polarization) basis set and B3LYP functionals for DFT calculations. The B3LYP functional has previously been used to model other bis-azo dyes and provided useful predictions on the geometries and kinetics of these azo dyes, which matched well with the experimental results.⁵⁻⁸ Using DFT modeling, it was possible to obtain optimized equilibrium geometries of the three isomers of BBY (EE, EZ, and ZZ), as well as optimized *cis-trans* isomerization transition-state (TS) geometries (EZ-EE and ZZ-EZ). For geometry-optimized structures, many possible conformers of the benzene rings were investigated to estimate the global minima. The results showed that the geometries of both *cis* isomers were similar, with the *cis* isomers approximately 50 % shorter than the *trans* isomer. This significant length change of the photo-switch, predicted by DFT, supports the theory that the *trans-cis* isomerization of BBY was the main cause of the photo-driven disassembly of these PEM films. DFT modeling also provided information on the *cis-trans* isomerization mechanism which is identical for both the ZZ-EZ and EZ-EE processes, occurring through a combination of rotation and inversion. Generally, the rotation pathway results in a more polar transition state whose energy can be affected by the surrounding solvent molecules. Experimentally, it was observed that the faster isomerization process of BBY displayed a higher rate constant in aprotic solvents such as THF and DMF compared to that observed in protic solvents such as ethanol and water, which supports the rotation mechanism.

Additionally, DFT modeling predicted that the *cis* decay for both *cis* forms of BBY (*ZZ*) and (*EZ*) are approximately the same, with the decay on the timescale of seconds ($\tau = 4\text{--}5$ s, gas phase). Commercial BBY azo dye is only claimed by the manufacturer to be 50 % pure as sold. The mass spectra indicated that the majority of the impurity in the commercial BBY dye consists of another azo dye (2,3',4-triaminoazobenzene), likely produced during the diazonium coupling reaction, and with a very similar structure to BBY, making purification of this dye particularly challenging. The presence of this impurity in significant quantities is possibly a contributing cause of the anomalous shorter lifetime observed for the crude BBY commercial azo dye. Repeating the pump-probe experiments with the recrystallized BBY azo dye resulted in good fit to a monoexponential decay observed in water ($\tau = 0.5$ s) and ethanol ($\tau = 1.1$ s), while a good fit to a biexponential decay was still observed in DMF ($\tau = 0.3$ s and 1.1 s). The monoazo dye analog for BBY, Chrysoidine, had a similar trend with a good fit of the *cis* relaxation curve of Chrysoidine to a monoexponential function in water ($\tau = 0.6$ s) and ethanol ($\tau = 1.3$ s), and a biexponential function in DMF ($\tau = 0.3$ s and 0.8 s). This indicates that outside of the presence of impurities, other factors such as dimerization or aggregation from π - π stacking, hydrogen bonding, and poor solubility might also influence the relaxation rates observed for azo dyes. BBY is less soluble in DMF compared to water and ethanol, so this is likely the cause of the two rates which were observed even after purification of the dye. This effect has been observed previously in our research group for some azo dyes in poor solvents, where 2 distinct rates are observed.^{9, 10}

Chapter 4 provided several possible routes to valorize waste brown seaweed (*Sargassum spp.*): (i) it presented a facile and cheap method to extract two highly valued polysaccharides: alginate and cellulose, (ii) and led to the subsequent conversion of the extracted alginate to bio-based films and straws for packaging and food applications, (iii) as well as the fabrication of photo-reversible materials such as PEM films and capsules using the

extracted alginate, and (iv) demonstrated the use of the unprocessed seaweed as an alternative for traditional cat litter. While stationed in St. Vincent and the Grenadines from 2020–2021, large quantities of brown seaweed (*Sargassum spp.*) were observed littered across a beach close to my home. The seaweed was brought back to Montreal and used as a cheap raw material to extract up to 35 % alginate and 17 % cellulose, a total added value of 52 % polysaccharides extracted from the waste brown seaweed. The protocols used to extract these biopolymers from the brown seaweed were based on previous literature with slight modifications, from Caribbean researchers Mohammed *et al.*,¹¹ as well as international researchers Doh, Whiteside, and Lee,¹² based in the US and Korea. The extraction methods were all aqueous based, requiring only cheap and readily accessible chemicals such as soda ash, bleach, ethanol, and caustic soda. In comparison to previously reported methods, it was observed in this work that the omission of the acid treatment of the seaweed resulted in an increase of the cellulose yield from 3 % to 17 %. Both the alginate and cellulose yields were comparable or better than previously reported values.

Several spectroscopic techniques were used to characterize the extracted polysaccharides, including solid-state NMR and FTIR spectroscopies. PXRD analysis showed that the crystallinity of the extracted cellulose from the brown seaweed was similar to that of cellulose kraft pulp, extracted from terrestrial sources (trees). PLM was used to visualize the extracted polysaccharides, where fibres and microgels were observed for the sodium alginate, and microfibrils and fibres observed for cellulose. Alginate is commonly used as a gelling agent in food, in cosmetics, as wound dressings and as active food packaging. In Chapter 4, the extracted alginate was used to make bio-based films for packaging applications, whereby sodium alginate was blended with a natural plasticizer also acquired in St. Vincent, known as arrowroot starch. Arrowroot starch can serve as an alternative to the more commonly used corn starch as a plasticizer since arrowroot is very abundant in St. Vincent. Films made from blends

of alginate, arrowroot starch, and glycerol had tensile properties comparable to that of traditional petrol-based plastics such as HDPE and PS, and other bio-based polymeric films, *e.g.*, PLA. The barrier properties were also comparable to HDPE, EVOH, PGA, PVDC, and corn starch. The extracted alginate was also used to fabricate photo-reversible materials such as PEM films and capsules, by ionically linking the negatively charged alginate polymer with the positively charged azo dyes BBY and BBR. Additionally, water-insoluble alginate films and capsules could be prepared by submerging the sodium alginate materials in a solution of calcium chloride. Lastly, the unprocessed brown seaweed was observed to have a high-water absorption capacity > 300 % its weight, which is comparable to clay-based materials generally used as cat litter, which can allow the brown seaweed to be used as a cheap bio-based and biodegradable alternative for such high absorbent household materials.

Finally, Chapter 5 presented a second method of preparing more stable photo-reversible materials, by means of covalent modification of cellulose-based polymers with azo dyes, towards application as self-cleaning materials. This project was inspired by recent work on the functionalization of cellulose with azobenzene dye from Otsuka *et al.*,^{13, 14} from our research group, where Azo-dye-functionalized cellulose (Azo-Cel) materials were prepared and tested towards mechanical bending and photo-induced changes in surface wettability. During the first year of my PhD program, I began working on converting cellulose triacetate (CTA) and cellulose diacetate (CDA) which are insoluble in water, to the water-soluble cellulose monoacetate (CMA) form, which could then be used to make photo-reversible PEM films similar to those prepared in Chapter 2. However, LbL assembly of the CMA polymer with the azo dyes did not result in the formation of good quality PEM films, possibly due to the absence of any charged groups on the polymer and its limited solubility in water. As such, CMA and CDA were covalently modified with azo dyes, using the method outlined by Otsuka *et al.*,^{13, 14} towards photo-induced changes in surface wettability to serve as self-cleaning materials.

Cellulose acetates (CAs) are commonly used as coatings, to make lenses, LEDs, as well as filtration membranes. Photo-induced changes in the surface wettability of Azo-CA materials could allow these materials to clean themselves using an external stimulus such as light. Such materials in theory would be capable of more efficient and longer use, and reuse many times over, saving on resources, time, and money.

The covalent modification of the CA polymers with two azo dyes was accomplished by means of a nucleophilic substitution reaction, whereby the labile chlorine groups of the azobenzoyl chloride dyes are substituted with the deprotonated hydroxyl groups of the CA polymers. While this is the most common method used to synthesize these Azo-dye-functionalized cellulose-based materials, there are several drawbacks to this method compared to the LbL self-assembly used in the previous Chapters. These drawbacks include the inert conditions, high temperatures (100 °C), long reaction time (48 hr), and non-aqueous solvent (pyridine) needed for the reaction to proceed, to achieve adequate grafting of azo dye onto the polymer. Nonetheless, using this method up to 10 wt.% azo dye could be grafted onto the CA polymers, with the successful grafting confirmed by several spectroscopic techniques, such as UV-Vis, FTIR, and NMR spectroscopies. Most of the past research published on azo dye modified cellulose derivatives did not include any studies on the *trans-cis* isomerization of the azo dyes once grafted onto the polymers, with the only report on the kinetics of these azo dyes being from our research group, Otsuka *et al.* in 2019. In this Chapter, the isomerization of the azo dyes bound to the CA polymers was assessed in solution, where for most samples switching from the *trans*-Azo-CA to the *cis*-Azo-CA could be accomplished using a low power UV LED, with the *cis* lifetimes ranging from a few minutes (Ho-Azo-CA samples) to hours (Azo-CDA sample), showing the ability to tune the *cis* lifetime by altering the functional groups on the azo dye.

The Azo-CA polymers were solvent-cast and/or electrospun as thin films, and then characterized by SEM-EDS, PXRD, and TGA. The Azo-CMA and Ho-Azo-CDA solvent-cast films had many cavities throughout its surface as seen by SEM, with the solvent-cast Azo-CDA, Azo-Cel and CDA films, having no cavities and relatively smoother surfaces in comparison. The electrospun Azo-CDA film had a more uneven surface than the solvent-cast Azo-CDA film, with small cavities also observed on the film surface by SEM. Electrospinning is a technique which has been used to prepare hydrophobic fibrous networks of Azo-Cel and CA, due to the uneven surface and hydrophobic air pockets created during the electrospinning process.^{14, 15} In this study, Azo-CDA was electrospun from solvents previously reported for CDA which formed hydrophobic fibrous networks; however, a fully fibrous network was not achieved with Azo-CDA, indicating further optimization is needed for this process.

To assess the photo-induced changes in surface wettability of the Azo-CA films, as well as a solvent-cast Azo-Cel film previously prepared by Otsuka *et al.*, the water contact angle (WCA) of the films were measured under ambient visible white light and under UV irradiation. For all the azo modified cellulose and CA films, no significant change in the WCA was observed, averaged over 3 measurements. For some samples, 1 out of the 3 measurements would show a change in WCA of up to 10 degrees in response to UV irradiation, however, these changes were not reproducible. Even when a high-powered UV laser (375 nm) was used instead of a low powered UV LED, reproducible changes in the WCA could not be achieved. This unexpected lack of a significant change in the WCA might be due to most of the azo dyes being located within the film and not on the surface, or restriction of movement of the azo dyes attached the polymer in this solid-state form. Attempts were made to measure the *trans-cis* isomerization of the azo dye in these films using high-powered laser pump-probe experiments as outlined in Chapter 3, yet with no success.

Another important factor to assess for self-cleaning materials is the change in water permeance in response to the UV/Vis light stimulus. For these measurements, circular caps were 3D printed, in which the thin films were placed and capped on top of a vial containing calcium chloride. The vial was then placed in a high humidity chamber and the weight of the vial measured overtime as the films were exposed to ambient visible white light, followed by UV light. The results showed that the Azo-CMA films, which had the largest pores of the Azo-CA samples, were the only samples to have a significant change in its WVTR/WVP in response to UV irradiation. This result is promising and with further optimization of the synthesis of these Azo-CA samples we hope to achieve similar results with the other samples.

6.2 Conclusions

Photo-reversible materials for applications in controlled disassembly systems and self-cleaning materials, were prepared using natural polymers and azo dyes. In Chapter 2, stable multilayered films (NaCS/BBY) were reported to be successfully formed between photo-responsive layers, and layers containing a cellulose-based polymer were prepared, and their controlled disassembly when triggered by blue light was confirmed and characterized. These results demonstrate the utility of employing natural polymers in fabricating dynamic, visible light-reversible materials. The water soluble, biodegradable and bio-sourced polymer NaCS, and the water soluble azobenzene photo-switch BBY were assembled into multilayers to form robust, water-resistant, optically clear, and uniform thin films of 50 bilayers, 390 ± 15 nm thick, held together by weak intermolecular interactions between the hydroxyl and sulfonate groups of NaCS and the amino groups and amine salts of BBY. The disassembly of these LbL films however could be triggered on demand using 460 nm blue visible light, confirmed by time-

dependent UV-Vis spectroscopy of the photo-disassembly in blue light *vs.* dark. The isomerization of BBY in solution and thin films under irradiation was confirmed by pump-probe and Confocal Raman spectroscopy experiments, respectively. The isomerization of azobenzenes results in significant microstructural changes from a planar, nonpolar structure (E) to a polar, twisted conformation (Z), resulting in large changes in the material, leading to complete and controlled disassembly back into their water-soluble components reversibly, in principle ready for re-use. It is hoped that these new ‘reversibly soft-bonded’ materials can lead in future to a new class of materials that be easily and cheaply fabricated from water-soluble and low-toxicity ‘green’ components, recovered after dis-assembly under gentle environmental conditions, unchanged and ready for re-use, as potential replacements for many current single-use artificial plastics.

In Chapter 3 the thermal relaxation of BBY in solution and embedded in polymeric thin films was measured for the first time by means of pump-probe experiments, and the behaviour rationalized with computational DFT modelling. BBY was able to undergo *trans*→*cis* isomerization following irradiation with visible light, and thermally relaxed back to the *trans* isomer in the dark, with a *cis* lifetime on the timescale of milliseconds – seconds. It was observed that the *cis* decay was best fit to a biexponential model in most solvent systems and when embedded in the multi-layered cellulose-based thin films. Two rate constants were measured for the *cis* decay of crude BBY: a fast anomalous isomerization rate (k_a), and a slower more expected rate (k_b). The *cis* lifetime was slightly more prolonged when BBY was in the NaCS/BBY thin films *vs.* in solution. Upon recrystallization the more expected monoexponential decay was observed with a *cis* lifetime of $\tau = 1.1$ s in ethanol. This *cis* lifetime corresponded well to that of the monoazobenzene analogue, Chrysoidine ($\tau = 1.2$ s, in ethanol). The experimental value of the *cis* lifetime of crude and recrystallized BBY also corresponded well with the value predicted by DFT calculations for BBY ($\tau = 4\text{--}5$ s, gas phase).

It is hoped that these advanced purification techniques developed and reported here, and the associated spectroscopic behaviour observed for the various components, will aid some of the many researchers who employ Bismarck Brown azo dyes in their experiments and materials.

The work reported in Chapter 4 demonstrated the ability of waste brown seaweed (*Sargassum spp.*) to be used as the starting material to fabricate various bio-based materials such as films, straws and photo-reversible PEM films and capsules, to potentially be used for packaging applications. The unwanted influx of this pelagic *Sargassum spp.* (brown seaweed) into the Caribbean sea has resulted in many challenges for the region; however, as outlined above there are many ways in which this waste material can be valorized. The extraction of a high value hydrocolloid known as sodium alginate (~35 % yield) was achieved in a facile manner using readily available reagents such as soda ash and bleach. Materials made from this extracted alginate had the required physical and barrier properties to replace other bio-based and synthetic polymeric materials. In addition to the extracted alginate, cellulose, one of the most highly valued polymers on earth was extracted from a non-terrestrial source in adequate yield (~17 % yield), providing another avenue to harness this polymer. The incorporation of a photo switchable small molecule azo dye, *via* soft-bonding interactions with the alginate polymers resulted in the fabrication of photo-reversible materials which in the future can be tested for their potential use in controlled assembly/disassembly applications, such as drug delivery systems.

Lastly, in Chapter 5, photo-reversible azo modified CA polymers were prepared for the first time *via* an esterification reaction of CA with various azo dyes. The incorporation of the azo dye onto the cellulose-based polymer negatively affected the crystallinity of the polymer but in general improved the thermal stability. With UV-Vis spectroscopy it was observed that the azo dyes once bound to the polymer were still capable of undergoing *trans-cis*

isomerization in response to UV light, with the rate of the *cis* decay of the azo dye following a biexponential decay and generally relaxing more slowly once bound to the polymer. To assess the viability of the Azo-CA materials for use as self-cleaning devices, the change in the water contact angle (WCA) upon exposure to UV and Vis light was measured. While the results showed that the WCA of the azo functionalized cellulose-based films were higher (less hydrophilic) than the unmodified cellulose and CA samples, there was no significant change detected in the WCA of the Azo-Cel and Azo-CA films following irradiation with UV light. However, measurements of the WVP of the Azo-CMA films showed a significant change in the water permeance of the films during UV irradiation compared to exposure to visible light. These results are promising and indicate that more work is needed to optimize a material whose WCA can effectively change in response to UV light.

6.3 Future outlook

For the photo-reversible PEM films prepared in Chapter 2, future disassembly studies are required to determine exactly what role hydrogen bonding *vs.* ionic bonding play in the rate of disassembly of these materials. While the NaCS/BBY films could be fully disassembled using blue light while gently washed with tap water, high concentrated salt solutions, and very alkaline water, full disassembly in the absence of salts, *i.e.*, deionized (DI) water while irradiated with the blue light was not achieved. This might be an indicator that the ionic bonding between the NaCS polymer and BBY azo dye was too strong to disrupt solely from the geometric rearrangement of the azo dye (*trans* to *cis*) in response to blue light absorption. Another area that requires future work is the method of fabricating these photo-reversible materials. LbL assembly is relatively more time consuming and complicated to scale up

compared to bulk mixing and solvent-casting which would be a more preferable, accessible, easy and cost-effective way of preparing these photo-reversible materials. This work has been taken up by a junior PhD student, who thus far has achieved promising results by bulk mixing and solvent casting chitosan instead of NaCS as the polymer, and Allura Red and Amaranth azo dyes in place of BBY. For the pump-probe experiments, future work includes performing a temperature dependent study to determine the pre-exponential factor (A_{rr}) of BBY, to improve the accuracy of the calculation of the rate constant using the Arrhenius equation in the DFT modeling. A temperature dependent study was indeed attempted for the BBY azo dye, however, the current setup available in our labs could not produce accurate results with respect to temperature control, due to fogging, and T fluctuations. For temperature-dependent studies a much more complex flow cell (which we do not have currently) would need to ensure accurate temperatures are maintained. As it relates to the valorization of brown seaweed, future work might include performing disassembly studies of the azo dye/alginate PEM films and capsules that were prepared. Lastly for the Azo-CA materials, there was no significant change yet observed in the WCA of the materials, despite significant changes in the WVTR/WVP or the Azo-CMA sample. Perhaps crosslinking of the cellulose network with the azo dye, or modification of only the surface of a premade cellulose acetate film could achieve better results. Future work may include the modification of cellulose and CA with an octa-fluoro azo dye (since fluorinated cellulose has been shown to make superhydrophobic materials), and electrospinning of the resulting polymer towards making these photo-reversible self-cleaning materials.

6.4 References

1. P. T. Anastas and J. C. Warner, *Green Chemistry: Theory and Practice*, Oxford University Press, Oxford; New York, 1998.
2. ACS, 12 Principles of Green Chemistry, <https://www.acs.org/greenchemistry/principles/12-principles-of-green-chemistry.html>, (accessed March 6, 2023).
3. R. Koshani, M. Tavakolian and T. G. M. van de Ven, *ACS Sustainable Chemistry & Engineering*, 2021, **9**, 4487–4497.
4. C. Slavov, C. Yang, L. Schweighauser, C. Boumrifak, A. Dreuw, H. A. Wegner and J. Wachtveitl, *Physical Chemistry Chemical Physics*, 2016, **18**, 14795–14804.
5. C. Boumrifak, C. Yang, S. Bellotto, H. A. Wegner, J. Wachtveitl, A. Dreuw and C. Slavov, *ChemPhotoChem*, 2019, **3**, 411–417.
6. A. Georgiev, E. Bubev, D. Dimov, D. Yancheva, I. Zhivkov, J. Krajcovic, M. Vala, M. Weiter and M. Machkova, *Spectrochimica Acta Part A: Molecular and Biomolecular Spectroscopy*, 2017, **175**, 76–91.
7. J. Dokić, M. Gothe, J. Wirth, M. V. Peters, J. Schwarz, S. Hecht and P. Saalfrank, *Journal of Physical Chemistry A*, 2009, **113**, 6763–6773.
8. N. K. Joshi, M. Fuyuki and A. Wada, *Journal of Physical Chemistry B*, 2014, **118**, 1891–1899.
9. C. J. Barrett, A. Natansohn and P. Rochon, *Chemistry of Materials*, 1995, **7**, 899–903.
10. L. L. Norman and C. J. Barrett, *Journal of Physical Chemistry B*, 2002, **106**, 8499–8503.
11. A. Mohammed, R. Bissoon, E. Bajnath, K. Mohammed, T. Lee, M. Bissram, N. John, N. K. Jalsa, K. Y. Lee and K. Ward, *Carbohydrate Polymers*, 2018, **198**, 109–118.
12. H. Doh, M. H. Lee and W. S. Whiteside, *Food Hydrocolloids*, 2020, **102**, 105542–105551.
13. I. Otsuka and C. J. Barrett, *Cellulose*, 2019, **26**, 6903–6915.
14. H. Ahmadi-Nohadani, S. Nono-Tagne, C. J. Barrett and I. Otsuka, *Macromolecular Rapid Communications*, 2022, **43**, 2200063–2220070.
15. F. Mikaeili and P. I. Gouma, *Scientific Reports*, 2018, **8**, 12472–12480.